

**MONOLAYER FUNCTIONALIZATION OF SILICON AND METAL OXIDE
SURFACES WITH BORON- AND NITROGEN-CONTAINING PRECURSORS**

by

Dhamelyz Silva-Quinones

A dissertation submitted to the Faculty of the University of Delaware in partial fulfillment of the requirements for the degree of Doctor of Philosophy in Chemistry and Biochemistry

Winter 2024

© 2024 Dhamelyz Silva-Quinones
All Rights Reserved

**MONOLAYER FUNCTIONALIZATION OF SILICON AND METAL OXIDE
SURFACES WITH BORON- AND NITROGEN-CONTAINING PRECURSORS**

by

Dhamelyz Silva Quinones

Approved: _____
Joel Rosenthal, Ph.D.
Chair of the Department of Chemistry and Biochemistry

Approved: _____
Deborah H. Norris.
Interim Dean of the College of Arts & Sciences

Approved: _____
Louis F. Rossi, Ph.D.
Vice Provost for Graduate and Professional Education and
Dean of the Graduate College

I certify that I have read this dissertation and that in my opinion it meets the academic and professional standard required by the University as a dissertation for the degree of Doctor of Philosophy.

Signed:

Andrew V. Teplyakov, Ph.D.
Professor in charge of dissertation

I certify that I have read this dissertation and that in my opinion it meets the academic and professional standard required by the University as a dissertation for the degree of Doctor of Philosophy.

Signed:

Murray V. Johnston, Ph.D.
Member of dissertation committee

I certify that I have read this dissertation and that in my opinion it meets the academic and professional standard required by the University as a dissertation for the degree of Doctor of Philosophy.

Signed:

Sharon L. Neal, Ph.D.
Member of dissertation committee

I certify that I have read this dissertation and that in my opinion it meets the academic and professional standard required by the University as a dissertation for the degree of Doctor of Philosophy.

Signed:

Chaoying Ni, Ph.D.
Member of dissertation committee

ACKNOWLEDGMENTS

First and foremost, I want to extend my deepest gratitude and sincere appreciation to Professor Andrew Teplyakov for his unwavering support and invaluable guidance that played a pivotal role in providing the necessary foundation for my success throughout my Ph.D. study. Professor Teplyakov's commitment and encouragement were crucial in shaping me as an independent researcher. I am immensely grateful for the privilege of working under his guidance, and I attribute a significant portion of my accomplishments to his significant influence and support.

I would also like to thank the rest of my committee members, Dr. Murray Johnston, Dr. Sharon Neal, and Dr. Chaoying Ni for their helpful and insightful suggestions and for their support throughout the years.

I would also like to acknowledge all of our collaborators for their significant contributions to each of my Ph.D. projects. Dr. George T. Wang at Sandia National Laboratories, for his invaluable collaboration on the monolayer doping project. Dr. Robert E. Butera and Dr. Kevin J. Dawyer at the Laboratory for Physical Sciences, for their help with the STM measurements and their insightful suggestions for my research projects.

I gratefully acknowledge Dr. Shi Bai at the NMR Laboratory at the University of Delaware, for his enormous help and insightful suggestions with solid-state NMR, the training in liquid NMR, and the help with the ADF computational calculations.

I would also like to thank Dr. Mitchell S. Chinn and Zach Grzenda at the Chemours Company, for their fruitful collaboration in the surface modification of metal oxides project and for the help with the BET, OH/nm^2 , and ICP measurements.

I would gratefully thank Prof. Ni and his colleague Dr. Yong Zhao at the W. M. Keck Microscopy Facility for the training in SEM and for being always available when I had questions. Dr. Gerald Poirier, Dr. Jing Qu, and Dr. Chin Chen Kuo at the Advanced Material Characterization Laboratory for training me in AFM, BET, and Contact Angle and for the help provided in using the instruments.

Thank you to Dr. Xu Feng for the significant assistance and the training in ToF-SIMS at the Surface Analysis Facility and the interpretation of the multiple spectra with different types of samples. Thank you as well to Dr. Wenbo Wu and Tienna Deroy for training me in XPS and for all the help throughout these years.

I would also like to express my gratitude to Dr. Iulian Codreanu and Dr. Shyan-Tzong Horng at the University of Delaware Nanofabrication Facility for the help and training in the cleanroom, ALD, profilometry, and ellipsometry.

I want to thank the former and current fellow groupmates for all the help and the incredible work together. Dr. Chuan (River) He, Dr. Sana Rani, Dr. Mahsa Konh, Dr. Carly Byron, Tyler Parke, Marissa Pina, Asishana Onivefu, Sanuthmi Dunuwila, John Mason and Robert Norden.

I also extend my gratitude to Professor Juan Carlos F. Rodriguez-Reyes, he guided me through my undergrad thesis and encouraged me to pursue my graduate studies. Additionally, we collaborated during my Ph.D. years, continuing the studies in mining samples from the Peruvian Andes.

Special thanks go to my family in Peru, particularly my parents, Rosana and Alfredo, and my sister Karol, whose constant encouragement fueled my perseverance and gave me motivation from miles away during the completion of this journey, words cannot express how grateful I am to have them in my life. I want to dedicate this thesis to you. I am also thankful for the support of my boyfriend Ahmed, who has been there for me during challenging times and moments of joy.

Additionally, I would like to recognize two special friends, my best friend Daleska, who despite being miles away, was always there for me; and Micaih, my friend since the first day of the Ph.D. program. Thank you both for the laughter, extended conversations, and words of support that made every day brighter.

Finally, I would like to thank my furry friend: Dubi, who joined me on this journey and brought countless moments of joy and entertainment. I'm also thankful for his remarkable talent in waking me up early every morning.

I may not have sufficient space to mention everyone here, but each one of you holds a special place in my heart for the rest of my life.

TABLE OF CONTENTS

LIST OF TABLES	x
LIST OF FIGURES	xii
ABSTRACT	xx

Chapter

1	INTRODUCTION	1
1.1	Monolayer Functionalization of Semiconductor Surfaces	1
1.2	Ultra-shallow monolayer doping	3
1.3	Functionalization of Metal Oxide Surfaces	4
1.4	Area Selective-Atomic Layer Deposition (AS-ALD)	5
2	EXPERIMENTAL PROCEDURES AND CALCULATIONS	9
2.1	Surface Modification of Silicon	9
2.1.1	Materials	9
2.1.2	Preparation of hydrogen-terminated Si(100) surface	10
2.1.2.1	Modified Radio Corporation of America (RCA) cleaning method.....	10
2.1.2.2	HF dip method (Piranha clean).....	10
2.1.3	Preparation of chlorine-terminated Si(100) surface	11
2.1.4	Preparation of the Bromine-Terminated Si(100) Surface (in UHV) and Scanning Tunneling Microscopy (STM) Imaging.....	11
2.1.5	Reaction of boron trichloride with Cl- or H-terminated Si(100) surface.....	12
2.1.6	Reaction of Hydrazine with Cl-, H-, or Br-Terminated Si(100) Surfaces	12
2.1.7	Reaction of 4-Fluorophenylboronic Acid with the H- and Cl-Si(100) Surfaces.	13
2.1.8	Reaction of Boric Acid with the H- and Cl-Si(100) Surfaces	14
2.2	Surface Functionalization of Metal Oxide Nanomaterials	14

2.2.1	Reaction of 4-fluorophenylboronic acid with TiO ₂ rutile, TiO ₂ anatase and γ -Al ₂ O ₃	14
2.3	Analytical Techniques	15
2.3.1	X-ray Photoelectron Spectroscopy (XPS).....	15
2.3.2	Time-of-Flight Secondary Ion Mass Spectrometry (ToF-SIMS).....	16
2.3.3	Fourier Transform Infrared Spectroscopy (FT-IR)	19
2.3.4	Solid-state Nuclear Magnetic Resonance (ss-NMR).....	20
2.3.5	Atomic Force Microscopy (AFM).....	22
2.4	Computational Methods	24
2.4.1	Density Functional Theory computational details.....	24
3	REACTION OF BCl ₃ WITH H- AND Cl-TERMINATED Si(100) AS A PATHWAY FOR SELECTIVE, MONOLAYER DOPING THROUGH SOLUTION CHEMISTRY	30
3.1	Abstract.....	30
3.2	Introduction	31
3.3	Results and discussions	33
3.4	Conclusions	43
4	REACTION OF HYDRAZINE WITH SOLUTION- AND VACUUM-PREPARED SELECTIVELY TERMINATED Si(100) SURFACES: PATHWAYS TO THE FORMATION OF DIRECT Si-N BONDS	45
4.1	Abstract.....	45
4.2	Introduction	46
4.3	Results and discussions	49
4.4	Conclusion.....	67
5	SOLUTION CHEMISTRY TO CONTROL BORON-CONTAINING MONOLAYERS ON SILICON: REACTIONS OF BORIC ACID AND 4-FLUOROPHENYLBORONIC ACID WITH H- AND Cl-TERMINATED Si(100)	69
5.1	Abstract.....	69
5.2	Introduction	70
5.3	Results and discussions	72
5.4	Conclusions	85

6	ATTACHMENT CHEMISTRY OF 4-FLUOROPHENYLBORONIC ACID ON TiO ₂ AND Al ₂ O ₃ NANOPARTICLES.....	87
6.1	Abstract.....	87
6.2	Introduction	88
6.3	Results and discussions	91
6.4	Conclusions	109
7	INHIBITION OF ATOMIC LAYER DEPOSITION OF TiO ₂ BY FUNCTIONALIZING SILICON SURFACE WITH 4-FLUOROPHENYLBORONIC ACID.....	110
7.1	Abstract.....	110
7.2	Introduction	111
7.3	Results and discussion.....	113
7.3.1	XPS of growth and non-growth surfaces before and after ALD of TiO ₂	114
7.3.2	Ti/Si XPS intensity ratios, estimated TiO ₂ thickness, and selectivity on the growth and non-growth surfaces.	120
7.3.3	ToF-SIMS depth profile on growth and non-growth surfaces ..	126
7.4	Conclusions	131
8	SUMMARY AND FUTURE WORK.....	132
	REFERENCES	135
Appendix		
A	SUPPLEMENTARY INFORMATION FOR CHAPTER 3	156
B	SUPPLEMENTARY INFORMATION FOR CHAPTER 4.....	160
C	SUPPLEMENTARY INFORMATION FOR CHAPTER 5.....	165
D	SUPPLEMENTARY INFORMATION FOR CHAPTER 6.....	171
E	SUPPLEMENTARY INFORMATION FOR CHAPTER 7	181
F	COPYRIGHT PERMISSIONS	185

LIST OF TABLES

Table 4.1: Surface Coverage (Φ) Comparison for the Differently Terminated Si Surfaces before and after Their Reaction with Hydrazine Based on XPS measurements ^a	60
Table 4.2: Thermodynamic Requirements for the Reaction of Hydrazine with Single-Dimer (Si_9H_{12}), Two-Dimer ($\text{Si}_{21}\text{H}_{24}$), and Three-Dimer ($\text{Si}_{21}\text{H}_{20}$) Clusters.....	65
Table 5.1 Comparison of the Relative B/Si Coverage (Φ) on Cl-Si(100) after the Reaction with 4-Fluorophenylboronic Acid and Boric Acid at 50 °C, Calculated by Using the Overlayer Model; C/F and B/F Ratios after the Reaction with 4-Fluorophenylboronic Acid at 50°C.....	75
Table 5.2: Thermodynamic Requirements for the Reaction of 4-Fluorophenylboronic Acid with a Functionalized Si(100) Surface Represented by a $\text{Si}_{21}\text{H}_{24}$ Cluster.....	81
Table 5.3: Thermodynamic Requirements for the Reaction of Boric Acid with a Functionalized Si(100) Surface Represented by a $\text{Si}_{21}\text{H}_{24}$ Cluster	82
Table 6.1: Experimental Surface Coverage of the Intact Chemisorbed FPBA Molecule Measured by Solution Phase ^{19}F NMR, Experimental Concentrations of OH Groups on Metal Oxide before Modification, and BET Surface Area of Metal Oxide before Modification.....	96
Table 6.2: Calculated Theoretical Binding Energies of B 1s and F 1s for Structures Modeled with Gaussian09 Using B3LYP/LANL2DZ for Geometry Optimization and a Single Point Calculation Using B3LYP/6-311+g(d,p) for the Energy Calculation.....	98
Table 7.1: Relative B/Si coverage after the reaction of FPBA with Cl-Si(100) ¹¹	116
Table 7.2: Selectivity of FPBA calculated from equation (1) using Ti 2p/ Si 2p ratios obtained with XPS.....	122
Table 7.3: FPBA-Si (100) selectivity calculated from equation (1) using the estimated TiO_2 thickness obtained from equation (2)	125

Table 8.1 Thermodynamic requirements for the reaction of hydrazine with single-dimer (Si_9H_{12}), two-dimer ($\text{Si}_{21}\text{H}_{24}$) and three-dimer ($\text{Si}_{21}\text{H}_{20}$) clusters monochloride and monobromide-terminated.	163
Table 8.2. Thermodynamic requirements for the reaction of 4-fluorophenylboronic acid (SA and SB) and boric acid (SC and SD) with two-dimer cluster.	169
Table 8.3. Comparison of the thermodynamic requirements for the reaction of 4-fluorophenylboronic acid (A) and phenylboronic acid (B) with Cl-terminated Si(100).	169
Table 8.4. Calculated ^{13}C , ^{11}B , and ^{19}F chemical shifts (ppm) for monodentate 4FPBA on TiO_2	174
Table 8.5. Calculated ^{13}C , ^{11}B , and ^{19}F chemical shifts (ppm) for bidentate bridging 4FPBA on TiO_2	175
Table 8.6. Calculated ^{13}C , ^{11}B , and ^{19}F chemical shifts (ppm) for bidentate 4FPBA on TiO_2	176
Table 8.7. Calculated ^{13}C , ^{11}B , and ^{19}F chemical shifts (ppm) for monodentate 4FPBA on Al_2O_3	177
Table 8.8. Calculated ^{13}C , ^{11}B , and ^{19}F chemical shifts (ppm) for bidentate bridging 4FPBA on Al_2O_3	178
Table 8.9. Calculated ^{13}C , ^{11}B , and ^{19}F chemical shifts (ppm) for bidentate 4FPBA on Al_2O_3	179
Table 8.10. Calculated ^{13}C , ^{11}B , and ^{19}F chemical shifts (ppm) for 4FPBA molecule	180

LIST OF FIGURES

Figure 1.1: Schematic representation of the surface modification pathways.	2
Figure 1.2: Schematic representation of doping by monolayer doping (MLD) using the B- or N- containing precursors.	4
Figure 1.3: AS-ALD process schematic showing how a film is selectively deposited in the GA.	8
Figure 2.1: Schematic illustration of the working principle of X-ray photoelectron spectroscopy. a) General principle, and b) X-ray photoelectron excitation.	16
Figure 2.2: Schematic illustration of the working principle of ToF-SIMS.	18
Figure 2.3: Schematic illustration of the principle of IR adsorption.	20
Figure 2.4: Illustration of the working principle of the atomic force microscopy.	23
Figure 3.1: Comparison of the reactivity of the H-terminated and Cl-terminated Si(100) surfaces.	35
Figure 3.2: XPS spectra of Cl 2p, B 1s and Si 2p spectral regions for H-terminated Si(100) before reaction (a1), after BCl ₃ reaction (b1) at 35 °C for 3 h, (c1) at 50 °C for 3 h and (d1) at 70 °C for 3 h (the inset shows the zoomed-in region of the spectrum corresponding to the formation of Si-B _x and Si-O _x species) and for Cl-terminated Si(100) before reaction (a2), after BCl ₃ reaction (b2) at 35 °C for 3 h, (c2) at 50 °C for 3 h and (d2) at 70 °C for 3 h (the inset shows the zoomed-in region of the spectrum corresponding to the formation of Si-B _x and Si-O _x species). Each spectrum is the result of averaging three different experimental spectra.	37
Figure 3.3: Comparison of the peak position in the experimental XPS spectra of B 1s obtained from the reaction with BCl ₃ at 70 °C for 3 h (a) before the reaction (showing a Si 2 s plasmon feature) and (b) following the reaction and the computationally predicted values for the models indicated, shown as black bars underneath the experimental spectrum. .	39

Figure 3.4: Relative Cl/Si monolayer coverage after BCl ₃ reaction with Cl-Si(100) (dashed red line), relative B/Si monolayer coverage after BCl ₃ reaction with Cl-Si(100) (solid red line), relative Cl/Si monolayer coverage after BCl ₃ reaction with H-Si(100) (dashed blue line) and relative B/Si monolayer coverage after BCl ₃ reaction with H-Si(100) (solid blue line), calculated from the Briggs and Seah equation, as described in detail in reference. ¹¹⁰	40
Figure 3.5: XPS spectra of B 1s and Si 2p spectral regions for H-terminated and Cl-terminated Si(100) surface prepared by HF-dip method: H-Si(100) after BCl ₃ reaction at 50 °C (a1), after BCl ₃ reaction at 70 °C (b1) for 3 h; Cl-Si(100) after BCl ₃ reaction at 50 °C (a2), after BCl ₃ reaction at 70 °C (b2) for 3 h.	43
Figure 4.1: Schematic Comparison of the Reaction Sequences for the H-, Cl-, and Br-Terminated Si(100) Surfaces	50
Figure 4.2: XPS spectra of the Si 2p spectral region for (a) H-terminated Si(100) that is the starting point, (b) H-Si(100) following the reaction with hydrazine, (c) Cl-Si(100), (d) Cl-Si(100) following the reaction with hydrazine, (e) Br-Si(100) and (f) Br-Si(100) following the reaction with hydrazine. Each spectrum is the result of averaging three different experimental spectra. The fits include the features corresponding to Si-Cl and Si-Br surface species on Cl-Si(100) and Br-Si(100) surfaces (c and e) that do not appear on the same surfaces following their reaction with hydrazine (d and f). The same spectra are shown in the insets as zoomed-in versions.	51
Figure 4.3: XPS spectra of the Cl 2p spectral region for (a) Cl-Si(100) before surface modification and (b) Cl-Si(100) after surface modification with hydrazine.	54
Figure 4.4: XPS spectra of the Br 3d spectral region for (a) Br-Si(100) before surface modification and (b) Br-Si(100) following the surface modification with hydrazine.	55

- Figure 4.5: XPS spectra of the N 1s spectral region for (a) H-Si(100) surface before the reaction with hydrazine, (b) H-Si(100) surface following the reaction with hydrazine, (c) Cl-Si(100) before the reaction with hydrazine, (d) Cl-Si(100) following the reaction with hydrazine, (e) Br-Si(100) before hydrazine treatment and (f) Br-Si(100) following the reaction with hydrazine (each spectrum is the result of averaging three different experimental spectra). The computationally predicted values for the species indicated (A, B, C, D, E, F, G, H, and I) are shown as black solid bars in the right panel with the experimental features indicated by the red gradients..... 56
- Figure 4.6: Filled-state STM images (a): -2.5 V, 0.1 nA, (b): -2.0 V, 0.1 nA of fully Br-terminated Si(100)-(2 × 1) surfaces. Each Si dangling bond of the surface is passivated with one Br atom, preserving the dimer rows of the (2 × 1) reconstruction of the bar surface. A single atomic step runs across the center of (a). Several darker Si dimer vacancies are visible in (b). 59
- Figure 4.7: Left panels: AFM image of (a) hydrogen-terminated Si(100) and (b) H-Si(100) after the reaction with hydrazine and (c) chlorine-terminated Si (100) and (d) Cl-Si(100) after the reaction with hydrazine. Right panels: Line profiles of each of the AFM images. The RMS was determined for areas of 500 × 500 nm. 62
- Figure 5.1: Schematic Comparison of the Reaction of 4-Fluorophenylboronic Acid (4FPBA) and Boric Acid (BA) with Cl-Terminated and H-Terminated Si(100) Surfaces 73
- Figure 5.2: XPS spectra of B 1s spectral region (showing a Si 2s plasmon feature). The left panel shows the (a1) H-terminated Si(100) as the starting point, (b1) H-Si(100) after the reaction with boric acid (BA) at 50 °C for 3 h and, (c1) H-Si(100) after the reaction with 4-fluorophenylboronic acid (4FPBA) at 50 °C for 3 h; and the right panel shows the (a2) Cl-terminated Si(100) as the starting point, (b2) Cl-Si(100) after the reaction with boric acid at 50 °C for 3 h, and (c2) Cl-Si(100) after the reaction with 4-fluorophenylboronic acid at 50 °C for 3 h. 74

- Figure 5.3: XPS spectra of Si 2p spectral region. The left panel shows the (a1) H-terminated Si(100) as the starting point, (b1) H-Si(100) after the reaction with boric acid (BA) at 50 °C for 3 h, and (c1) H-Si(100) after the reaction with 4-fluorophenylboronic acid (4FPBA) at 50 °C for 3 h; and the right panel shows the (a2) Cl-terminated Si (100) as the starting point, (b2) Cl-Si(100) after the reaction with boric acid at 50 °C for 3 h, and (c2) Cl-Si(100) after the reaction with 4-fluorophenylboronic acid at 50 °C for 3 h..... 76
- Figure 5.4: The left panel shows the XPS spectra of C 1s spectral region for the H- and Cl-Si(100) surfaces after the reaction with 4-fluorophenylboronic acid (4FPBA) at 50 °C for 3 h. The right panel shows the XPS spectra of F 1s spectral region for the H- and Cl-Si(100) surfaces after the reaction with 4-fluorophenylboronic acid at 50 °C for 3 h. The computationally predicted result is shown as a solid vertical bar underneath the experimental data..... 78
- Figure 6.1. DFT models of the 4FPBA attachment on TiO₂ (left) and Al₂O₃ (right) simple clusters in three configurations: Monodentate, bidentate, and bridging bidentate..... 93
- Figure 6.2: XPS spectra of boron 1s (left) and fluorine 1s (right) regions for the 5 wt % loading of 4FPBA on (a,e) anatase TiO₂ nanopowder, (b,f) rutile TiO₂ nanopowder, (c,g) γ -Al₂O₃ nanopowder, as well as (d,h) pure 4FPBA for comparison..... 97
- Figure 6.3. Solid-state ¹¹B NMR of (a) 5 wt % 4FPBA on anatase TiO₂, (b) 5 wt % 4FPBA on rutile TiO₂, (c) theoretical ¹¹B NMR spectrum for monodentate 4FPBA on the TiO₂ cluster, (d) theoretical ¹¹B NMR spectrum for bidentate 4FPBA on the TiO₂ cluster, (e) theoretical ¹¹B NMR spectrum for bidentate bridging 4FPBA on the TiO₂ cluster, (f) 5 wt % 4FPBA on γ -Al₂O₃, (g) theoretical ¹¹B NMR spectrum for monodentate 4FPBA on the Al₂O₃ cluster, (h) theoretical ¹¹B NMR spectrum for bidentate 4FPBA on the Al₂O₃ cluster, (i) theoretical ¹¹B NMR spectrum for bidentate bridging 4FPBA on the Al₂O₃ cluster, (j) pure 4FPBA powder, and (k) theoretical ¹¹B NMR spectrum for molecular 4FPBA..... 100
- Figure 6.4. Solid-state ¹⁹F NMR of (a) 5 wt % 4FPBA on anatase TiO₂, (b) 5 wt % 4FPBA on rutile TiO₂, (c) 5 wt % 4FPBA on γ -Al₂O₃, (d) pure 4FPBA powder, and (e) ADF-predicted chemical shift for molecular 4FPBA. 102

Figure 6.5. Solid-state ^{13}C NMR of (a) 5 wt % 4FPBA on anatase TiO_2 , (b) 5 wt % 4FPBA on rutile TiO_2 , (c) theoretical NMR spectrum for monodentate 4FPBA on the TiO_2 cluster, (d) theoretical NMR spectrum for bidentate 4FPBA on the TiO_2 cluster, (e) theoretical NMR spectrum for bidentate bridging 4FPBA on the TiO_2 cluster, (f) 5 wt % 4FPBA on $\gamma\text{-Al}_2\text{O}_3$, (g) theoretical NMR spectrum for monodentate 4FPBA on the Al_2O_3 cluster, (h) theoretical NMR spectrum for bidentate 4FPBA on the Al_2O_3 cluster, (i) theoretical NMR spectrum for bidentate bridging 4FPBA on the Al_2O_3 cluster, (j) pure 4FPBA powder, and (k) theoretical NMR spectrum for molecular 4FPBA..... 104

Figure 6.6: FTIR spectra of (a) 5 wt % 4FPBA on anatase TiO_2 , (b) 5 wt % 4FPBA on rutile TiO_2 , (c) theoretical IR spectrum for monodentate 4FPBA on the TiO_2 cluster, (d) theoretical IR spectrum or bidentate 4FPBA on the TiO_2 cluster, (e) theoretical IR spectrum for bidentate bridging 4FPBA on the TiO_2 cluster, (f) 5 wt % 4FPBA on $\gamma\text{-Al}_2\text{O}_3$, (g) theoretical IR spectrum for monodentate 4FPBA on the Al_2O_3 cluster, (h) theoretical IR spectrum for bidentate 4FPBA on the Al_2O_3 cluster, (i) theoretical IR spectrum for bidentate bridging 4FPBA on the Al_2O_3 cluster, (j) pure 4FPBA powder, and (k) theoretical IR spectrum for molecular 4FPBA. 107

Figure 7.1: Steps followed in the preparation of OH-, H-, and FPBA-Si(100) surfaces used in the comparison of TiO_2 growth by ALD. 114

Figure 7.2: B 1s, F 1s, Si 2p, Ti 2p XPS spectral regions of FPBA-Si(100); as prepared (a), and after 5 (b), 10 (c), 20 (d), 30 (e), and 50 (f) ALD cycles of TiO_2 115

Figure 7.3: Si 2p, Ti 2p XPS spectral regions of OH-Si(100) as prepared (a), and after 5 (b), 10 (c), 20 (d), 30 (e) and 50 (f) ALD cycles of TiO_2 117

Figure 7.4: O 1s XPS spectral region of FPBA-Si(100) (1); as prepared (a1), after 5 (b1), 10 (c1), 20 (d1), 30 (e1), and 50 (f1) cycles of TiO_2 ALD, and OH-Si(100) (2); as prepared (a2), after 5 (b2), 10 (c2), 20 (d2), 30 (e2), and 50 (f2) cycles of TiO_2 ALD..... 119

Figure 7.5: Ti 2p/ Si 2p ratios recorded as a function of the number of ALD cycles. 121

Figure 7.6: Estimated TiO_2 thickness (nm) as a function of the number of ALD cycles. 123

Figure 7.7: ToF-SIMS depth profile showing the intensity of the TiO^- , F^- , B^- , Si_2^- , and SiO^- ions vs depth of a) FPBA-Si(100) after 50 cycles, b) FPBA-Si(100) after 200 cycles. And the intensity of TiO^- , Si_2^- , and SiO^- ions vs depth of c) OH-Si (100) after 50 cycles and d) OH-Si(100) after 200 cycles. All the intensities were normalized to Si_2^- at saturation.....	127
Figure 7.8: ToF-SIMS depth profile showing the intensity of the F^- and B^- ions vs depth of FPBA-Si(100) after 50 cycles a), and FPBA-Si(100) after 200 cycles b).....	129
Figure A1: XPS spectra of Cl 2p, B 1s and Si 2p for the optimization of the time of the BCl_3 reaction with Cl terminated-Si (100) for 1, 3 and 5 hours.	156
Figure A2. The top three panels show the XPS spectra of Cl 2p, B 1s and Si 2p results of the sputtering with Ar^+ monoatomic mode on the Cl-terminated Si (100) after reaction with BCl_3 for a) 0 seconds, b) 21 seconds, c) 35 seconds, and d) 49 seconds of sputtering. And the bottom three panels show the peak area versus the time of sputtering for a) Boron, b) Carbon and c) Chlorine.	157
Figure A3. XPS spectra of O 1s for the reaction of BCl_3 at 70°C with a) H terminated-Si(100), and b) Cl terminated-Si(100).....	158
Figure A4: Scheme A1. Models used for the DFT calculations performed with Gaussian 09 suite utilizing B3LYP functional and 6-311G+(d,p) basis set.....	159
Figure B1. XPS spectra of the N 1s spectral region for H-Si(100) surface before (a) and after (b) reaction with hydrazine. The computationally predicted values for the oxidized species indicated are shown as black solid bars underneath the experimental spectra.	161
Figure B2. XPS spectra of Si 2p and N1 spectral regions comparing the reactivity of a) OH terminated-Si (100) before reaction with hydrazine, b) OH terminated-Si (100) after reaction with hydrazine, c) Cl terminated-Si(100) after reaction with hydrazine followed by a dip in H_2O and d) Cl terminated-Si(100) after reaction with hydrazine.	162
Figure B3. Nitrogen-containing species attached to the silicon surface modeled in Gaussview and used for the DFT calculations performed with Gaussian 09 suite utilizing B3LYP functional and 6-311G+(d,p) basis set.	164

Figure C1: The top two panels show the XPS spectra of B 1s and Si 2p spectral region for reaction of boric acid with H-Si(100) at a) 25°C, b) 50°C and c) 70°C. And the two bottom panels shows the XPS spectra of B 1s and Si 2p spectral region for reaction of boric acid with Cl-Si(100) at a) 25°C, b) 50°C and c) 70°C.....	165
Figure C2. Top two panels show the XPS spectra of B 1s and Si 2p spectral region for reaction of 4-fluorophenylboronic acid with H-Si(100) at a) 35°C, b) 50°C, and c) 70°C. And the two bottom panels show the XPS spectra of B 1s and Si 2p spectral region for reaction of 4-fluorophenylboronic acid with Cl-Si(100) at a) 35°C, b) 50°C, c) 70°C and d) 110°C.....	166
Figure C3. XPS spectra of Cl 2p spectral region for the a) Cl-terminated Si(100) as the starting point, b) Cl-Si(100) after the reaction with boric acid at 50°C for 3h and, c) Cl-Si(100) after the reaction with 4-fluorophenylboronic acid at 50°C for 3h.....	167
Figure C4. AFM images of the a) H-terminated Si(100), b) Cl-terminated Si(100), c) Cl-terminated Si(100) after the reaction with boric acid and d) Cl-terminated Si(100) after the reaction with 4-fluorophenylboronic acid with Cl-Si(100).....	168
Figure D1. XPS spectra of boron 1s (left) and fluorine 1s (right) regions for weight loadings (a, f) 10wt%, (b, g) 5wt%, (c, h) 1wt%, and (d, i) 0.5wt% of 4-fluorophenylboronic acid on anatase TiO ₂ , as well as (e, j) pure 4-fluorophenylboronic acid for comparison. The peak recorded at 683.7 eV for F 1s spectral region is the result of XPS-induced decomposition.	171
Figure D2. XRD spectra of anatase TiO ₂ as received a), FPBA/anatase TiO ₂ b), rutile TiO ₂ as received c), FPBA/rutile TiO ₂ d), γ -Al ₂ O ₃ as received e), and FPBA/ γ -Al ₂ O ₃ . Distinct peaks for anatase TiO ₂ (*), rutile TiO ₂ (•), and γ -Al ₂ O ₃ (◆) are indicated.	173
Figure D3. Structure of monodentate 4FPBA on TiO ₂	174
Figure D4. Structure of bidentate bridging 4FPBA on TiO ₂	175
Figure D5. Structure of bidentate 4FPBA on TiO ₂	176
Figure D6. Structure of monodentate 4FPBA on Al ₂ O ₃	177
Figure D7. Structure of bidentate bridging 4FPBA on Al ₂ O ₃	178

Figure D9. Structure of 4FPBA molecule	180
Figure E1: Si2p, Ti2p, and O 1s XPS spectral regions of (a) H-Si(100) as prepared, (b) H-Si(100) after 10, (c) 20, (d) 30, and (e) 50 ALD cycles of TiO ₂ .	181
Figure E2: B 1s, F 1s and Si 2p XPS spectral regions of FPBA-Si(100) as prepared a), and after 48 hours b).....	182
Figure E3: Si 2p XPS spectral region of H-Si(100) as prepared a), after 1 hour b), 3 hours c), 5 hours d), and 48 hours e).	183
Figure E4: AFM images of the a) FPBA-Si(100), b) FPBA-Si(100) after 50 TiO ₂ ALD cycles, c) OH-terminated Si(100), and d) OH-terminated Si(100) after 50 TiO ₂ cycles.....	183
Figure E5: ToF-SIMS depth profile showing the intensity of the F ⁻ , CF ⁻ , B ⁻ , FC ₆ H ₄ BO ₂ ⁻ and C ₆ H ₄ ⁻ fragments at the interface of TiO ₂ layer and FPBA-Si(100) after 200 ALD cycles.	184

ABSTRACT

As the dimensions of electronic device components shrink, there is a growing need for innovative methods and chemical modification strategies to fabricate nanometer-sized features. The work outlined in this dissertation focuses on two main strategies: the ultra-shallow monolayer doping, and area selective deposition. These strategies necessitate a detailed understanding of the interactions between different precursors and substrates, as well as the development of innovative techniques for governing and manipulating these interactions.

In the following chapters, a novel chemical method for the monolayer functionalization of silicon surfaces with boron- and nitrogen-containing precursors is discussed and proposed as a pathway for ultra-shallow monolayer doping.

Secondly, the monolayer functionalization of metal-oxide surfaces with an organic precursor with unique spectroscopic labels was investigated in order to understand the attachment chemistry of these materials and to develop spectroscopic labels for surface characterization.

And lastly, the use of an organic molecule with unique spectroscopic labels is proposed as an effective resist to block the growth of materials in area selective deposition.

The goals for the research contained in this dissertation are:

- 1) Modify the surface of the semiconductor to form direct dopant (B, N)-Si bonds and control the concentration of the dopant.

2) Explore and control the attachment of the boron-containing precursor that contains unique spectroscopic labels (F, B) with the metal-oxide surfaces.

3) Modify the chemical reactivity of the surfaces with respect to a metal-organic precursor to inhibit or promote the deposition of TiO₂ films.

To achieve these goals, a combination of spectroscopic, microscopic and computational investigations was performed to study the surface chemical modifications processes. X-ray photoelectron spectroscopy (XPS), Fourier-transform infrared spectroscopy (FTIR), time-of-flight secondary ion mass spectrometry (ToF-SIMS) and solid-state nuclear magnetic resonance spectroscopy (ss-NMR) were used to elucidate the chemical environment and to determine the binding modes of the attached compounds on the surfaces. Atomic force microscopy (AFM) was utilized to evaluate the surface morphological changes after the surface chemical modifications. Also density functional theory (DFT) calculations were utilized to supplement the analysis, interpret the results of spectroscopic measurements and to interrogate surface stability of possible surface species.

Chapter 1

INTRODUCTION

1.1 Monolayer Functionalization of Semiconductor Surfaces

Surface modification to control the electronic properties of different semiconductor materials, especially silicon, has been studied in recent decades, and new methodologies to improve and control such modifications are being developed.^{1,2} As the size of the components in electronic devices is shrinking as predicted by Moore's law, new approaches are needed for the semiconductor industry towards nanometer dimensions that improve the performance and decrease the cost of the devices. Achieving control at the molecular scale is integral to these advancements, with surface and interface modifications playing a crucial role.^{1,3}

One important motivation for the functionalization of semiconductors, such as silicon, with molecular monolayers is to fine-tune the properties of the material toward a desired application. Some of the applications expand in a number of fields including electronics, sensing, bio-sensing and energy conversion.⁴

Surface functionalization schemes used in this work are summarized in Figure 1.1. The surface modification usually starts with the introduction of hydrogen^{5,6}, hydroxyl groups,⁷⁻⁹ or halogens^{6,10} (more commonly Cl and Br). These atoms or groups of atoms change the reactivity of the semiconductor surface which will influence the reactions with the selected boron- and nitrogen-containing precursors that are studied in this thesis.¹¹⁻¹⁴ If a covalent bond with the selected boron- and nitrogen-containing

precursors is formed, this procedure can be followed by capping and rapid thermal annealing (RTA), and an ultra-shallow doped surface can be obtained.¹⁵⁻¹⁷

Another pathway, also shown in Figure 1.1, happens when the reaction with the boron- or nitrogen-containing precursors is selective. In this case, with further modification, one can obtain a surface with two different reactivities, which is important in processes like area-selective deposition.¹⁸ Therefore, surface functionalization with monolayers of atoms or molecules can serve as a preliminary step for further modification protocols.

The two approaches shown in Figure 1.1 are important for the scaling down of devices, and the importance of the ultra-shallow doping and area-selective deposition will be discussed in sections 1.2 and 1.3, respectively.

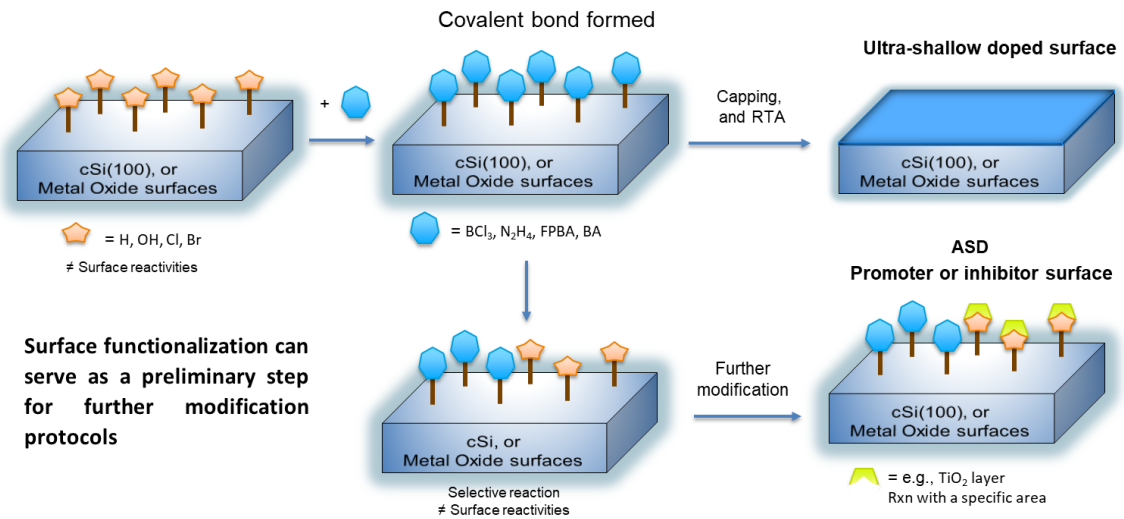


Figure 1.1: Schematic representation of the surface modification pathways.

1.2 Ultra-shallow monolayer doping

To control the electronic properties of semiconductors, a process called doping is used, which consists of adding impurities to alter these properties and to create p-n junctions. This is normally done with trivalent (B, As) and pentavalent (N, P) elements.¹⁹ This process can be achieved using different techniques including ion implantation and plasma doping.²⁰ These are conventional techniques, and their principal limitations are the severe crystal damage and issues related to the control of the dopant amount required to have an ultra-shallow doping, which is required to make devices smaller.^{17,21,22} Other techniques, including atomic layer deposition (ALD) or chemical vapor deposition (CVD), have also been used. They are based on exposing the substrate to gas-phase doping precursors. One important drawback of these techniques is the expensive equipment required to use, the ultra-high vacuum conditions and the toxic gases used in some cases.^{23,24}

Doping silicon surfaces, especially ultra-shallow doping with high dopant concentrations, plays a crucial role in tuning the electrical properties of the semiconductor materials.^{3,17} In 2008, Javey et. al. proposed the technique called monolayer doping, that has been used to achieve shallow doping ($< 5\text{nm}$) of silicon with high dopant concentrations ($>10^{20}\text{ cm}^{-3}$). The process consists of two main steps, by which the silicon surface is first functionalized with a dopant-containing molecule followed by a rapid thermal annealing (RTA) to drive dopant into the substrate as shown in Figure 1.2.³

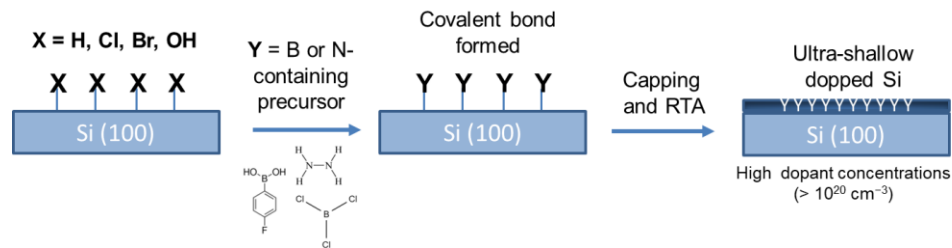


Figure 1.2: Schematic representation of monolayer doping (MLD) using the B- or N-containing precursors.

This thesis addresses a solution-based route to form direct Si-B bonds by the reaction of BCl₃ with a Cl-terminated Si (100) surface, described in chapter 3; a solution-based route to form direct Si-N bonds by the reaction of hydrazine with H-, Br- and Cl-terminated Si (100) surfaces, described in chapter 4; and a solution-based route to form Si-O-B bonds, by the reaction of 4-fluorophenyl boronic acid (FPBA) and boric acid (BA) with Cl-terminated Si (100) surfaces, described in chapter 5. This study provides potential pathways for ultra-shallow and supersaturated monolayer doping of the technologically important silicon (100) surface using B- and N-containing precursors.

1.3 Functionalization of Metal Oxide Surfaces

Metal oxide nanostructures have unique properties that are becoming important for applications such as catalysis of chemical reactions, drug delivery, water treatment, textile industries, polymer composites, adhesives, and coatings. Metal oxides are usually chemically stable; however, the use of some of these materials is limited by their wide band gap that reduces their light adsorption in the visible range.²⁵ Another challenge in relation to metal oxide nanoparticles is their high tendency to aggregation.

Chemical functionalization of metal oxide nanoparticles has gained interest to control their dispersion and aggregation.²⁶

Various classes of organic compounds can be used as metal oxide modifiers, among them are thiols, carboxylates, phosphonates and silanes.²⁷⁻²⁹ A highly promising, but not fully explored choice for the attachment group is the boronic functionality (R-B(OH)₂). This functionality may form multiple binding configurations with different metal oxides that are not well understood, the types of attachments can be monodentate, bidentate chelating, and bidentate bridging.

New chemical modification strategies of metal oxide surfaces are always in demand; however, the chemistry itself is often difficult to follow without specifically designed spectroscopic labels. In this thesis, a boronic functionality (R-B(OH)₂, specifically 4-fluorophenylboronic acid, was tested as a molecular probe that has unique spectroscopic labels (F, B) in reaction with common oxide nanomaterials (TiO₂ and Al₂O₃),¹⁴ described in chapter 6. The attachment chemistry was investigated by XPS, IR and ss-NMR. The spectroscopic measurements were supplemented by DFT investigations to define the binding modes for 4-fluorophenylboronic acid on oxide surfaces. The well-defined surface modification chemistry and a set of spectroscopic labels distributed within this molecule can then be further used to probe the surface reactivity of other nanomaterials.

1.4 Area Selective-Atomic Layer Deposition (AS-ALD)

Atomic Layer deposition (ALD) relies on self-limiting surface reactions that take place between surface functional groups and gas-phase precursors. The precursor and co-reactant are alternated during the dosing and an inert gas or pump down steps

are followed between each dosing step. This process enables uniform thin film growth, conformality and atomically precise thickness control.³⁰

Figure 1.3 shows a representation of an ALD cycle to deposit a TiO₂ film, using Tetrakis(dimethylamino)titanium (TDMAT) as the precursor for Ti and water as a co-reactant. In the first half-cycle, the TDMAT reacts with the hydroxyl sites on a OH-terminated Si surface. In the second half-cycle, the H₂O reacts with the remaining dimethylamino groups, which leads to the hydroxylation process and the formation of Ti-O-Ti bonds in the deposited film. After the completion of the entire cycle, a TiO₂ layer is formed on the surface. The thickness of the TiO₂ film depends on the number of ALD cycles.

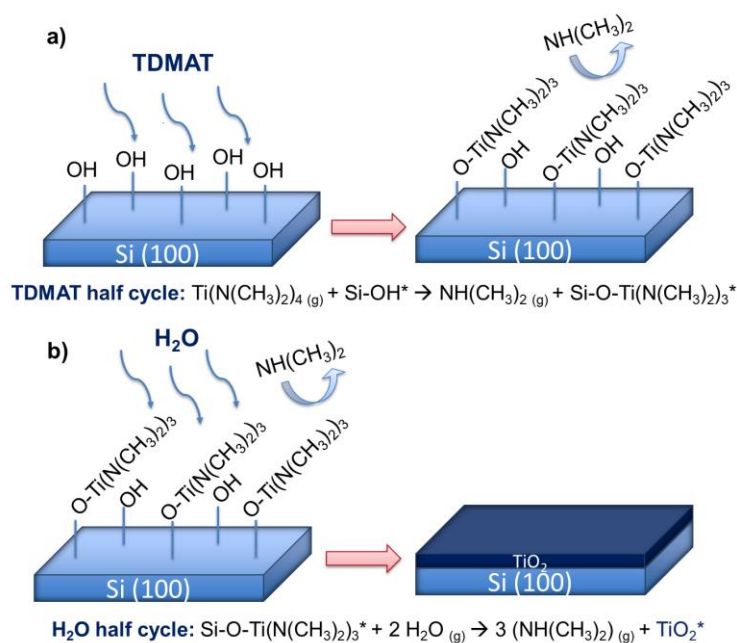


Figure 1.3: Representation of the ALD process using TDMAT and water as precursors to deposit TiO₂. a) Half-cycle reaction of TDMAT with hydroxyl sites, and b) reaction of water molecules with the remaining dimethylamino groups.

In Area-Selective Atomic Layer Deposition (AS-ALD) the chemical nature of the surfaces allows to control where the reactions take place. This can be achieved by chemically modifying the surface, as shown in Figure 1.1, the efficiency of the chemisorption of a specific precursor depends on its affinity with specific surface functional groups. For instance, it is well known that OH groups on the surface favor the growth of TiO₂ when using precursors like TDMAT or TiCl₄, this surface is called the ‘growth area (GA)’. On the other hand, passivating the surface with self-assembled monolayers of functional alkyl molecules or recently studied small molecule inhibitors (SMIs) are being developed to create ‘non-growth areas (NGA)’. SMIs are very effective to block or delay the growth of TiO₂ that uses TDMAT or TiCl₄ as precursors.^{31–35}

Figure 1.4 shows the schematic of AS-ALD process, this can be achieved by modifying the surface to create the GA and NGA or area activation and area deactivation.³⁶ Ideally, the deposition occurs only in the desired GA, however a more realistic AS-ALD process will form unwanted nuclei in the NGA, causing the loss of selectivity.¹⁸ A solution to this problem is to implement correction steps like 1) repeating the functionalization step to protect the NGA and 2) etching selectively to remove the deposited material on the NGA.³⁷

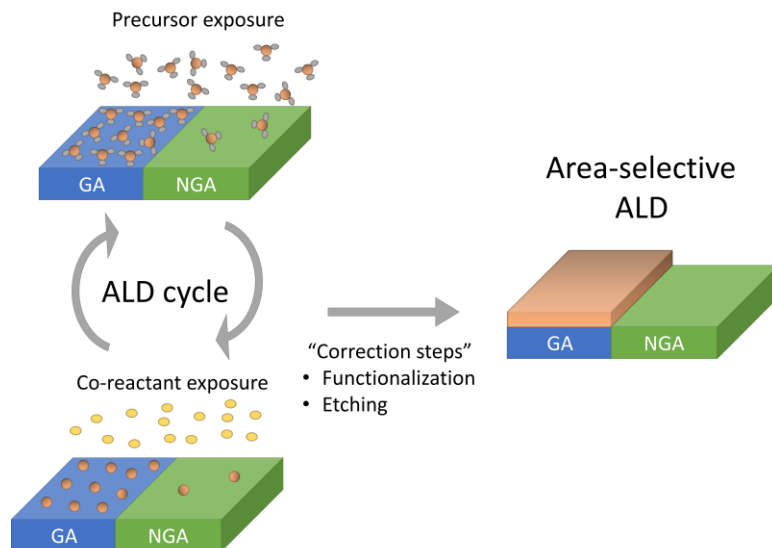


Figure 1.4: AS-ALD process schematic showing how a film is selectively deposited in the GA

In chapter 7 of this thesis, 4-fluorophenylboronic acid (FPBA) molecule was used as an SMI to passivate the Si (100) surface. FPBA on silicon forms a stable passivated surface that efficiently inhibits the deposition of TiO_2 , up to 20 cycles, in an ALD process based on sequential tetrakis(dimethylamido)titanium (TDMAT) and water doses. A detailed spectroscopic investigation with XPS confirms the formation of a stable monolayer, and ToF-SIMS profiles of this surface confirm that the FPBA functionality is still intact at the interface.

Chapter 2

EXPERIMENTAL PROCEDURES AND CALCULATIONS

This chapter describes the experimental and computational methods performed in this dissertation, including detailed information on the materials, surface modifications and the characterization techniques with experimental data collection and data fitting parameters.

2.1 Surface Modification of Silicon

2.1.1 Materials

In chapter 3, 4 and 5 p-type one-side polished Si(100) wafers (Prolog Semicor Ltd., 380 mm thickness, 5–10 Ω -cm resistivity) were used as substrates, and in chapter 7 single-side polished Si(100) wafers (p-doped, Virginia Semiconductors, 400 mm \pm 25 mm, 1-10 Ω -cm resistivity) were used as substrates. All chemicals in chapter 3, 4, 5 and 7 were reagent grade or better: N₂ (research purity), hydrogen peroxide (Fisher, 30% certified ACS grade), ammonium hydroxide (Fisher, 29% certified ACS plus grade), hydrochloric acid (Fisher, 37.3% certified ACS grade), buffer-HF improved (Transene Company, Inc.), chlorobenzene (99+%, Acros), phosphorus pentachloride (\geq 98.0% Sigma-Aldrich), benzoyl peroxide (Acros), boron trichloride 1.0 M in toluene (Sigma-Aldrich), toluene (99.8%, Fisher), anhydrous hydrazine (98%, Sigma-Aldrich), THF (Fisher, distilled from Na/benzophenone), 4-fluorophenylboronic acid (\geq 95.0% Sigma-Aldrich), boric acid (\geq 99.5% Sigma-Aldrich), toluene (Fisher, 99.9% certified ACS), and reagent alcohol (Fisher, 99.9% certified ACS ethanol, catalog number A962-4). The

deionized water used to rinse the surfaces and containers was from a first-generation Milli-Q with 18 M Ω ·cm resistivity.

2.1.2 Preparation of hydrogen-terminated Si(100) surface

2.1.2.1 Modified Radio Corporation of America (RCA) cleaning method

The hydrogen-modified Si(100) surface was prepared by the RCA cleaning procedure. Standard Cleaning-1 (SC-1) solution was freshly prepared by mixing Milli-Q water, hydrogen peroxide, and ammonium hydroxide (volume ratio 4:1:1), Standard Cleaning-2 (SC-2) solution was freshly prepared by Milli-Q water, hydrogen peroxide, and hydrochloric acid (volume ratio 4:1:1). The Teflon beakers and Si(100) wafers were cleaned in SC-1 solution for 30 and 10 min, respectively, in an 80 °C water bath and under N₂ stream. After rinsing with Milli-Q water, the clean wafers were etched in HF buffer solution for 2 min and rinsed again with Milli-Q water. Then, the wafers were placed in SC-2 solution for 10 min to grow a silicon oxide layer. After that, the rinsed silicon wafers were etched in HF buffer solution again for 1 min, followed by a 6 min etching process in ammonium fluoride solution to form a hydrogen-terminated Si(100) surface.

2.1.2.2 HF dip method (Piranha clean)

The HF-dip method was used as an alternative to the RCA cleaning procedure described above in selected experimental investigations for a quick preparation of H-terminated silicon surface that is less well-defined chemically than the surface prepared according to the procedure described above in section 2.1.2.1. The Si(100) wafer was cleaned at room temperature in a 1:4 mixture of hydrogen peroxide and sulfuric acid for 5 min, followed by 5 min Milli-Q water rinsing. After that, the rinsed silicon wafer was

dipped into a 10% HF aqueous solution for 2 min, followed by rinsing with Milli-Q water once to form the H-terminated Si(100) surface.

2.1.3 Preparation of chlorine-terminated Si(100) surface

The chlorine-terminated Si(100) surface was prepared by a well-established procedure using PCl_5 that was initially proposed for Si(111).³⁸ Phosphorus pentachloride powder was dissolved in chlorobenzene solvent, with a trace amount of benzoyl peroxide as a reaction initiator. This solution was purged with nitrogen gas under N_2 atmosphere for at least 30 min to remove gaseous impurities. A hydrogen-terminated Si(100) wafer was placed into this solution immediately after the etching procedure. The entire setup was placed in an oil bath at 110 °C for 1 h to prepare the stable chlorine-terminated Si(100) sample.

2.1.4 Preparation of the Bromine-Terminated Si(100) Surface (in UHV) and Scanning Tunneling Microscopy (STM) Imaging

Br-terminated Si(100) samples were prepared by a collaborating team in the research group of Dr. Robert Butera (The Laboratory for Physical Sciences, MD) in a UHV STM system with a base pressure of $P < 2.6 \times 10^{-9}$ Pa (2.0×10^{-11} Torr) using a ScientaOmicron VT-STM with a ZyVector STM Lithography control system. The Si(100) wafers used were p-type, B-doped with resistivity $\rho = 0.07$ to $0.09 \Omega \cdot \text{cm}$, and were oriented within 0.5° of (100). Si samples were cut to 4×12 mm in size, cleaned via sonication in acetone, methanol, and isopropanol, mounted on a ScientaOmicron XA sample plate, and loaded into an UHV chamber. Clean Si(100)- 2×1 surfaces were then prepared by a standard flash-annealing technique in UHV to 1200 °C, following the procedure found in Reference 39.³⁹ This (2×1) surface reconstruction results in one remaining dangling bond on each Si atom. The clean samples were then exposed to a

flux of Br₂ to achieve a Br-terminated surface with each Si atom bonding with a single Br atom. Br₂ was generated from a solid-state, electrochemical cell consisting of AgBr doped with 8 wt % CdBr₂.⁴⁰ Br exposures were done with the sample at ~250 °C to minimize water contamination. After exposure, Br-terminated samples were annealed at 375 °C to desorb physisorbed species without activating etching and roughening processes.⁴¹ During Br₂ exposure, the pressure in the chamber remained below 5.3×10^{-9} Pa (4×10^{-11} Torr). After confirming a fully Br-terminated surface in the STM, samples were removed from the UHV chamber and exposed to air for less than 5 min before being stored in dry N₂.

2.1.5 Reaction of boron trichloride with Cl- or H-terminated Si(100) surface

The freshly prepared Cl- or H-terminated Si(100) sample was transferred into a clean Schlenk flask filled with nitrogen gas, then evacuated. This fill-evacuate procedure was repeated three times. Boron trichloride 1.0 M in toluene solution was injected into the Schlenk flask, which was placed in an oil bath at 35, 50, 70 and 114 °C, using a clean and dry syringe. The silicon wafer was stirred in the boron trichloride solution for 1, 3 and 5 h to form a boron-modified Si(100) surface. After the reaction, the boron trichloride-modified Si(100) surface was rinsed with toluene to remove any residues from the surface, dried with nitrogen gas, and then immediately transferred into the vacuum chamber to perform the XPS measurements.

2.1.6 Reaction of Hydrazine with Cl-, H-, or Br-Terminated Si(100) Surfaces

The freshly prepared hydrogen- and chlorine-terminated Si(100) samples were transferred into a clean Schlenk flask filled with N₂(g) and then evacuated. The Br-terminated Si(100) sample was transported from the Laboratory for Physical Sciences

to the University of Delaware in a custom-built sample carrier filled with nitrogen and transferred into a clean Schlenk flask with minimal exposure to ambient conditions. Then, the anhydrous hydrazine was injected into the Schlenk flask using a clean and dry syringe and placed in an oil bath at 35 °C. The terminated silicon wafer was reacted in the anhydrous hydrazine for 1 h to form a hydrazine-modified Si(100) surface. After the reaction, the hydrazine-modified Si(100) surface was rinsed with THF to eliminate any residues from the surface, dried with nitrogen gas, and then immediately transferred into the vacuum chamber to perform the X-ray photoelectron spectroscopy (XPS) measurements; there was a brief exposure to the ambient atmosphere during the transportation of the sample.

In order to confirm that the Br–Si(100) samples are not altered substantially by the transport, which took approximately 2 h in a sample carrier, STM was used to verify that the surface passivation of a similarly UHV-prepared Br–Si(100) sample was unaltered after exposure to ambient conditions. In addition, once transferred for the experiments at the University of Delaware, a part of the Br–Si(100) sample was immediately checked for surface oxidation with XPS.

2.1.7 Reaction of 4-Fluorophenylboronic Acid with the H- and Cl–Si(100) Surfaces.

The 4-fluorophenylboronic acid was dissolved in toluene (30 mM) and mixed for 1 h at 100 °C under N₂(g) stream. Then, the Cl–Si(100) or H–Si(100) substrate was introduced into the flask with the solution and reacted for 3 h at 35, 50, 70, and 110 °C under N₂(g) stream. Then the sample was cleaned with toluene 3 times, dried with N₂(g), and immediately transferred to the XPS setup. Toluene was demonstrated not to react with these surfaces within the range of conditions tested, similar to previous work.^{12,13}

2.1.8 Reaction of Boric Acid with the H- and Cl-Si(100) Surfaces

The boric acid was dissolved in reagent alcohol in a concentration of 1.0 M and kept under N₂(g) stream. Once the powder was completely dissolved, the Cl-Si(100) or H-Si(100) sample was introduced into the flask and reacted with the solution for 3 h at room temperature (25), 50, and 70 °C. Then the sample was cleaned in the same solvent used to prepare the solution three times, dried with N₂(g), and immediately transferred to the XPS sample chamber. Reagent alcohol was demonstrated not to react with these surfaces within the range of conditions tested, similar to previous work.^{12,13}

2.2 Surface Functionalization of Metal Oxide Nanomaterials

2.2.1 Reaction of 4-fluorophenylboronic acid with TiO₂ rutile, TiO₂ anatase and γ -Al₂O₃

Solutions with varying weight percentages (0.5, 1, 5, 10 wt %) of 4-fluorophenylboronic acid were prepared in ethanol. A 25 mL aliquot of the 4FPBA solution was combined with 0.1 g of metal oxide dispersed in an equal volume of DI water. The metal oxides used were titanium (IV) oxide rutile nanopowder (Sigma Aldrich, <100 nm, 99.5%), titanium oxide(IV) anatase nanopowder (Alfa Aesar, 32 nm, 99.9%), and gamma aluminum oxide nanopowder (Sigma Aldrich, <50 nm). The particle sizes were confirmed by transmission electron microscopy (TEM) and it was confirmed that the metal oxide nanoparticle sizes were consistent with manufacturer specifications. The mixture was stirred at room temperature for 24 h, the resulting solid was retrieved by centrifugation and rinsed with ethanol in triplicate, and finally, the powder was dried under N₂ gas at room temperature.

2.3 Analytical Techniques

2.3.1 X-ray Photoelectron Spectroscopy (XPS)

X-ray Photoelectron Spectroscopy (XPS) is one of the most widely used surface analytical techniques. This technique is also known as ESCA (electron spectroscopy for chemical analysis). XPS provides the compositional and chemical information of the top few nanometers of solid samples.

Figure 2.1 represents the general principle of the XPS. The surface to be analyzed is irradiated with an X-ray beam. When a photon of $h\nu$ energy interacts with an electron in a level with binding energy E_B , the entire photon energy is transferred to the electron, therefore a photoelectron is ejected with a kinetic energy. The binding energy E_B can be calculated using the equation (1)

$$E_B = h\nu - E_{\text{kinetic}} - \Phi \dots (1),$$

where Φ is the work function of the spectrometer. The $h\nu$ energy must be greater than E_B . XPS is focused on the electrons in the core-levels, but an electron can also come from the occupied portion of the valence band.⁴²

All elements, except H and He can be measured by XPS, and every element has a unique set of electronic binding energies, which enables the elemental surface analysis of solid samples.

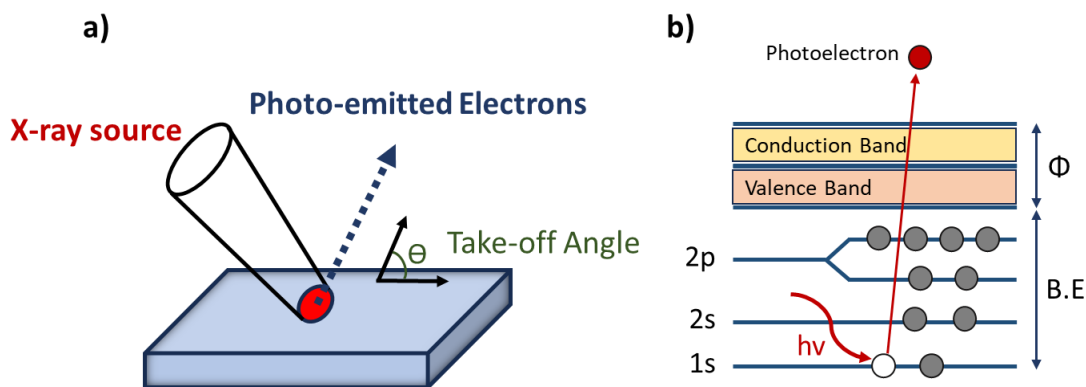


Figure 2.1: Schematic illustration of the working principle of X-ray photoelectron spectroscopy. a) General principle, and b) X-ray photoelectron excitation.

In chapters 3-7 the XPS analysis was performed on a Thermo Scientific K-Alpha+ instrument in the Surface Analysis Facility at the University of Delaware equipped with an Al K-alpha source ($h\nu = 1486.6$ eV) with a 35.3° take-off angle. The measurements were performed with a base pressure of 5×10^{-9} mBar. Survey spectra were collected over a binding energy range of 0–1000 eV, with a pass energy of either 100 eV (Chapter 3-6) or 200 eV (Chapter 7), step size of 1 eV, and dwell time of 10 ms. High resolution spectra were collected with a pass energy of either 20 eV (Chapter 3-5), 60 eV (Chapter 6) or 50 eV (Chapter 7), step size of 0.1 eV, and dwell time of 50 ms. The data were processed by CasaXPS software (version 2.3.16). The carbon 1s peak at 284.6 eV was used to calibrate all the spectral features.

2.3.2 Time-of-Flight Secondary Ion Mass Spectrometry (ToF-SIMS)

Another mature and highly sensitive surface analytical technique is ToF-SIMS. It provides information about the composition of a solid sample within the top 1-2 nm. The basic information gathered by the ToF-SIMS is the mass spectrum of the secondary

ions generated from a pulsed beam of primary ions (such as Bi^+ , Bi_3^+ , Bi_3^{++}) as shown in Figure 2.2. The mass m of each ion with charge q is measured via its time of flight through an analyzer of length L after an acceleration voltage U_e , according to equation (2).⁴³

$$t = L \times \sqrt{\frac{m}{2qU_e}} \dots (2)$$

ToF-SIMS can be operated in positive or negative ion mode (determined by the polarity of the electric field applied between the extractor and the sample stage), in which only positively or negatively charged fragments, respectively, are collected. The calibration of the masses is usually done with H^+ , H_2^+ , H_3^+ , C^+ , CH^+ , CH_2^+ , CH_3^+ , C_2H_3^+ , C_3H_5^+ , C_4H_7^+ , C_5H_9^+ , C_6H_9^+ , and C_7H_7^+ in positive ion mode, and H^- , H_2^- , C^- , CH^- , CH_2^- , CH_3^- , C_2^- , C_2H^- , C_3^- , C_4^- , C_5^- , C_6^- , C_7^- , and C_8^- in negative ion mode.

One of the most important capabilities of this technique is the ultra-shallow depth profile, which consists of the continuous monitoring of the secondary ions as a crater is made. In most cases the crater generated is measured using a profilometer, so the depth can be calibrated. Reactive ions such as Cs^+ and O_2^+ are commonly used for elemental depth profiling of metal and semiconductor layers. While Cs, a strong electron donor, helps to enhance the ionization of negative ions, oxygen enhances the positive ion yields thanks to its electronegativity.⁴⁴

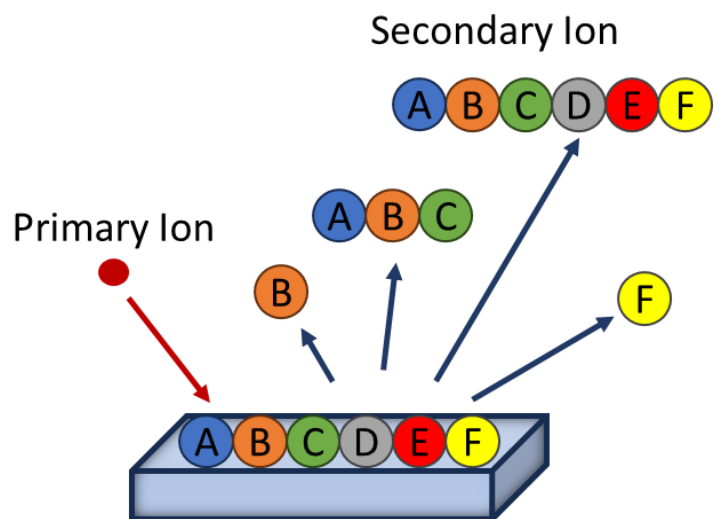


Figure 2.2: Schematic illustration of the working principle of ToF-SIMS.

The ToF-SIMS analysis shown in chapter 7 was performed on a TOF.SIMS 5 instrument (ION-TOF USA, Inc.) equipped with a Bi_n^{m+} ($n=1-5$, $m=1,2$) liquid metal ion gun, Cs, and O_2 dual-source ion column for ultra-low energy sputtering, and low energy electron flood gun for charge compensation. For the depth profiles, a 500 eV Cs^+ sputter ion beam with a 30 nA current was applied to create a $200 \mu\text{m} \times 200 \mu\text{m}$ area. The analysis area was a $50 \mu\text{m} \times 50 \mu\text{m}$ area in the center of the sputter crater, which was analyzed by using a pulsed 30 keV, 0.13 pA Bi^+ primary ion beam. The negative ions were collected, and the sputtering depths were measured with a profilometer to obtain corresponding sputtering rates of the Si (100) substrate as described in chapter 7, and the thickness of the TiO_2 layer deposited by ALD was measured with ellipsometry as described in chapter 7 to obtain the corresponding sputtering rate. The ToF-SIMS measurements were performed in collaboration with John Mason and Robert Norden in the Surface Analysis Facility in the University of Delaware.

2.3.3 Fourier Transform Infrared Spectroscopy (FT-IR)

Fourier Transform Infrared Spectroscopy is an important analytical technique that can identify particular functional groups present in a molecule. FTIR spectroscopy takes advantage of how IR light changes the dipole moments in molecules that correspond to a specific vibrational energy. Infrared spectra result from transitions between quantized vibrational energy states. Molecular vibrations can range from the simple coupled motion of the two atoms of a diatomic molecule to the much more complex motion of each atom in a large polyfunctional molecule. For many vibrational modes, only a few atoms have large displacements, and the rest of the molecule is almost stationary. The frequency of such modes is characteristic of the specific functional group in which the motion is centered and is minimally affected by the nature of the other atoms in the molecule. Thus, the observation of spectral features in a certain region of the spectrum is often indicative of a specific chemical functional group in the molecule.^{45,46}

Figure 2.3 shows the principle of IR absorption with an example water molecule. When IR radiation is incident on a sample (solid, liquid or gas), it absorbs radiation at frequencies similar to its molecular vibration frequencies and transmits other frequencies. Frequencies of absorbed radiation are detected by infrared spectrometer, and a plot of absorbed energy against frequency can be obtained.

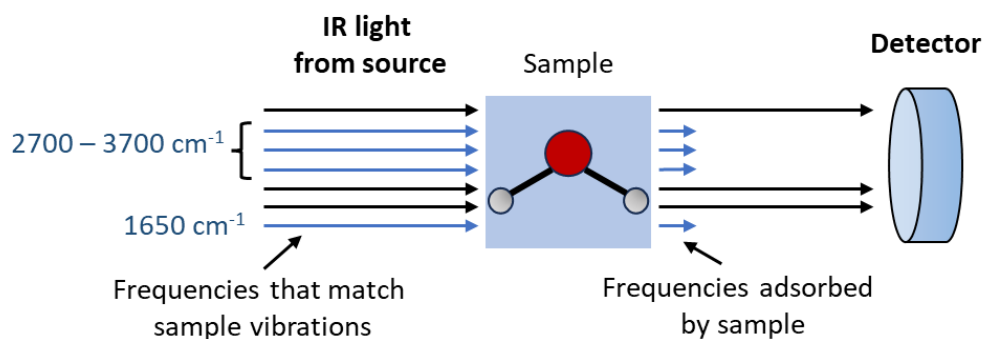


Figure 2.3: Schematic illustration of the principle of IR adsorption.

The FTIR spectroscopy shown in chapter 6 was performed using a Nicolet 860 ESP FTIR at room temperature and pressure using KBr as a background. Sample powder was mixed with KBr and pressed into a thin pellet, and transmission IR spectra were collected.

2.3.4 Solid-state Nuclear Magnetic Resonance (ss-NMR)

Solid-state NMR spectroscopy is a technique that provides information about the atomic level structure in solid materials. The NMR principle is based on a physical phenomenon in which a nuclei in an uniform magnetic field absorb and re-emit electromagnetic radiation. To gain solid-state NMR spectra with higher resolution, additional hardware needs to be used, such as magic-angle spinning (MAS) probe which spins the sample rapidly at an angle of 54.7° with respect to the external magnetic field and averages the chemical shifts to their isotropic value. The principles behind solid-state NMR are similar to those of liquid-state, and it is a useful method of characterization when a sample cannot be dissolved. The peaks reflect the chemical environment that a specific type of nucleus exists in. Similar to liquid-state NMR where

the instrument can identify ^{11}B , ^{13}C , ^{19}F , etc. Solid-state NMR is capable of looking at the same types of nuclei.⁴⁷

In chapter 6, the solid-state ^{11}B and ^{19}F NMR measurements were carried out on a Bruker Avance III 500 MHz NMR spectrometer (Bruker, Billerica, MA) operating at the Larmor frequency of 160.46 MHz for ^{11}B and 470.59 MHz for ^{19}F , respectively. A Bruker 4.0 mm multinuclear HX double resonance magic-angle spinning (MAS) probe was used to acquire ^{11}B spectra at a spinning rate of 14 kHz within ± 3 Hz. The reported ^{11}B chemical shifts were referenced externally to NaBH_4 at -42.06 ppm.⁴⁸ A Bruker 1.3 mm triple resonance (HFX) MAS probe was used to collect the ^{19}F MAS spectra at a spinning rate of 60 kHz within ± 5 Hz. The ^{19}F chemical shift referencing was done with the secondary standard of mefloquine at -40.7 ppm, with respect to Trifluoroacetic acid (TFA) at 0 ppm. The solid-state cross-polarization (CP) ^{13}C NMR spectra were acquired using a Bruker AVIII 600 MHz spectrometer with a Bruker 3.2 mm HXY probe. The MAS rate was regulated at 14 kHz within ± 3 Hz. The relaxation delay was 3 s, and the CP contact time was 2 ms. The chemical shifts were reported by referencing externally via a peak at 43.5 ppm for α -carbon of glycine relative to tetramethylsilane (TMS) at 0 ppm. The sample temperature of all measurements was regulated at 300 K unless otherwise noted. The ss-NMR data were collected by Dr. Shi Bai in the NMR Laboratory at the Department of Chemist and Biochemistry, University of Delaware.

Solution ^{19}F NMR was performed using a Bruker AVIII 600 MHz spectrometer (Bruker, Billerica, MA) equipped with a BBFO probe using standard proton decoupling ^{19}F data acquisition parameters. For the calibration curve, a stock solution of FPBA (100 mM) was prepared, and then serial dilutions were done to obtain concentrations of 50, 30, and 15 mM. To quantify the number of molecules adsorbed on each surface, 1 g of

each nanomaterial was reacted with 10 mL of each diluted solution for 24 h. Then, it was centrifuged and washed three times with ethanol. The solutions for the calibration curve, the supernatant after the reaction, and the washes were measured in the solution ^{19}F NMR. The fluorine concentration before and after the reaction was measured to find the chemisorbed and physisorbed molecules after the reaction of each nanomaterial with FPBA. Then, the concentration obtained in each of the ethanol washes was subtracted to obtain only the chemisorbed molecules.

2.3.5 Atomic Force Microscopy (AFM)

Atomic Force Microscopy is a method used to characterize the morphology of the surface of a sample. The AFM principle is based on the cantilever/tip assembly that interacts with the sample to produce atomic scale resolution images.

A schematic illustration of the main components of an atomic force microscope is shown in Figure 2.4. Imaging is accomplished by measuring the interaction force via deflection of a soft cantilever while raster - scanning the tip across the surface.⁴² The up/down and side to side motion of the AFM tip as it scans along the surface is monitored through a laser beam reflected off the cantilever. This reflected laser beam is tracked by a position-sensitive photo-detector (PSPD) that picks up the vertical and lateral motion of the probe.

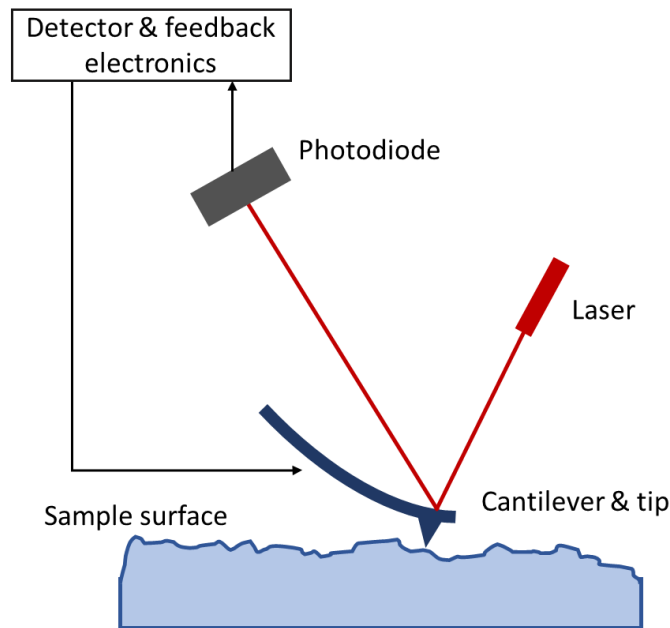


Figure 2.4: Illustration of the working principle of the atomic force microscopy.

The AFM images in chapter 4 and 5 were obtained using a tapping mode with a J-scanner scanning probe microscope (Multimode Nanoscope V). The sensing tips used were aluminum coated (BudgetSensors), which had a frequency of 300 kHz and a force constant of 40 N/m.

The AFM images in chapter 7 were obtained using tapping mode with an Anasys Nano IR2 system. The Bruker gold-coated, microfabricated silicon probes that were ~225 microns long and came pre-mounted on half-washer mounts were used. All the images obtained were processed with Gwyddion software (version 2.62) and the line profiles were processed with Origin 2019.

2.4 Computational Methods

2.4.1 Density Functional Theory computational details

To complement the information obtained with experimental techniques described above, computational calculations with DFT were performed in the studies described in this thesis. DFT is a versatile computational quantum mechanical modelling method. The computational calculations performed with DFT provides fundamental understanding and allows to optimize structures of interest, calculate energies of adsorptions between the substrate and the B- and N-containing precursors, comparison between experimental and theoretical core-level energies of 1s elements, and the theoretical vibrational frequencies. This theoretical information helps to support peak assignments in XPS and FTIR, as well as the thermodynamics of the reactions performed with the selected precursors in this thesis.

In chapter 3, the DFT calculations were performed using the Gaussian 09⁴⁹ suite of programs in order to determine the binding energy of different boron-containing species bonded to the Si(100) surface. The Si₂₁H₂₀ cluster model was used to simulate the Si(100) surface with different boron-containing species attached (see Figure A3 in Appendix A). The geometry was optimized with the B3LYP functional and the 6-311G+(d,p) basis set.^{50,51} In order to compare experimental and computationally predicted results for B 1s, additional calibration had to be performed. Koopmans' theorem was used to evaluate the core binding energies for the boron-containing species analyzed as the negative of corresponding orbital energies. The approach used in this work to calibrate predicted binding energies for a number of light elements had been reported by several groups.⁵²⁻⁵⁵ Briefly, the negative values of the predicted orbital energies are compared for well-known (mostly molecular) species whose XPS spectra

are recorded experimentally. The difference between experimental and computationally predicted values includes the solid-state work function and depends on the specific computational method (functional and basis set). This difference is included as a calibration factor for comparing the computationally predicted binding energies for possible proposed surface species and experimental XPS results. This approach has been successfully applied to nitrogen^{52,55} and carbon,⁵³ and a good correlation was observed for other elements.^{53,54} In chapter 3, the absolute values of the binding energies were calibrated by the comparison of the computationally predicted values with reference XPS data for boric acid⁵⁶ and trimethylborane.⁵⁷ The correction factor used based on the calibration was + 7.52 eV, which is the average difference between the binding energies predicted for B 1s level for these two molecules computed by the same method as shown above (B3LYP/6-311G+(d,p)) and experimentally recorded XPS spectra of these two molecules.

In chapter 4, geometry optimization calculations were performed using the B3LYP functional and 6-311 + G(d,p) basis set.^{50,51} Three different clusters were investigated in order to compare the energy required for the reaction of target surfaces with hydrazine. The Si₉H₁₂ cluster represents a single dimer on the Si(100)-2 × 1 surface. A two-dimer cluster Si₂₁H₂₄ represents two neighboring dimers belonging to two rows on the Si(100)-2 × 1 surface. It was investigated in order to understand the hydrazine binding between two rows of silicon dimers and the influence of neighboring silicon atoms on the energy of the systems of interest. A three-dimer Si₂₁H₂₀ cluster represents three dimers within the same row on this surface. For discussion purposes, these clusters will be referred to as one-, two-, and three-dimer clusters even if the dimer bond is broken (e.g., by SiCl₂ species formation). The Si and H atoms in the silicon

cluster models were kept frozen from the third layer down to the last layer in the cluster during the optimization to prevent unrealistic distortion of the cluster models. The models were used to simulate the Si(100) surface with different terminations (H, Cl, and Br, including the formation of dihydrogenide and dihalide species) and different nitrogen-containing species attached to the silicon surface. In order to estimate the possible differences in energies predicted by the different model clusters, selected reactions have been investigated on all three clusters, and the energetics of these reactions are summarized in Table B1 in Appendix B. Despite some minor discrepancies, the conclusions in this chapter are not affected by these differences. N 1s core-level energy was predicted using Koopman's theorem, and the correction factor to the predicted core-level energy for N 1s was 10.03 eV.⁵⁵ To predict the stability of surface species formed, the energy predicted for the cluster models and molecular reactants was subtracted from the energy predicted for the adsorbate attached to the cluster model.

In chapter 5, optimization calculations for geometry were conducted employing B3LYP functional and 6-311+G(d,p) basis set^{50,51} with Grimme's D3 dispersion corrections (Empirical dispersion = GD3).⁵⁸ A silicon cluster was studied in order to evaluate the energy required for the reaction of boric acid and 4-fluorophenylboronic acid with H and Cl-terminated Si(100) surfaces. The two-dimer cluster $\text{Si}_{21}\text{H}_{24}$ represents two neighboring dimers belonging to two rows on the Si(100)- 2×1 surface. The silicon and hydrogen atoms in the silicon cluster models were kept frozen from the third layer down to the last layer in the cluster during the optimization to prevent unrealistic distortion of the cluster models. The models were used to simulate the Si(100) surface with different terminations (dihydride and dichloride species) and

different boric- and boronic species attached to the silicon surface. In order to simulate the dihydride and dichloride terminations, the Si–Si bond of the two top dimers was broken in order to saturate it with two hydrogen or two chlorine atoms. B 1s and F 1s core-level energy was predicted using Koopman's theorem, and the calibration for each element was performed by the comparison of the computationally predicted values with reference XPS data.⁵⁵ For the calibration of computationally predicted B 1s features in model clusters, previously reported XPS investigations of boric acid⁵⁶ and trimethylborane⁵⁷ were used as references; and for the calibration of F 1s features, the XPS measurements of fluorobenzylphosphonic acid,⁵⁹ hexafluoroacetylacetone,⁶⁰ and tetrafluoropropanol^{55,61} were used as references. The calibration was performed similarly to the previously reported C 1s and N 1s features to obtain an average correction factor translating the computationally predicted values for the 1s orbitals into the experimentally observed XPS features.^{52,53,55} The correction factors to the predicted core-level energy for B 1s and F 1s were +7.52 and +15.16 eV, respectively; these values were obtained by averaging the difference between the binding energies predicted of the reference molecules by the same method mentioned above (B3LYP/6-311G+(d,p)) and the experimentally recorded XPS spectra of the reference molecules.^{52,53,55} In order to evaluate the thermodynamics of surface reactions, the energies predicted for the cluster models representing reactive surface sites and molecular reactants were subtracted from the energy predicted for the products of the reactions, as discussed in detail below and in Tables 5.2 and 5.3.

In chapter 6, the TiO₂ and Al₂O₃ surfaces were modeled by cluster models: Ti₂O₇H₆ for TiO₂ and Al₂O₅H₄ for Al₂O₃. The geometry was optimized with the B3LYP functional^{49,62} and LANL2DZ^{51,63} basis set. The 6-311+g(d,p)^{50,51,63–66} basis set was

used for single point energy calculations with Grimme's d3 dispersion correction⁶⁷ and was chosen to calculate the core-level 1s binding energies of the boron and fluorine atoms. The FPBA molecule was optimized at monodentate, bidentate, and bridging bidentate attachment positions, with the removal of two hydrogens and an oxygen in the form of H₂O for each B–O–Ti bond formation. Core-level 1s energies of the models were predicted using Koopmans' theorem,^{68,69} which states that the binding energy of one electron, measured by XPS, is a negative of the orbital energy of that electron. This approach was used to predict the theoretical binding energies of the FPBA attachment to the Ti and Al clusters at the B3LYP/6-311+g(d,p) level. The absolute values for fluorine 1s were calibrated by comparing the computationally predicted values of core-level energies in molecular species predicted by the same method with the experimentally measured F 1s spectra of fluorobenzylphosphonic acid,⁵⁹ hexafluoroacetylacetone,⁶⁰ and tetrafluoropropanol,⁶¹ resulting in a correction term of +15.16 eV, and the boron was calibrated with experimental data for boric acid⁵⁶ and trimethyl borane,⁵⁷ which produced a correction term of +7.5 eV. The validity of such an approach for calibrating core-level energies with computational methods has been discussed extensively.^{11,52,53,70}

Amsterdam DF (ADF) package⁷¹ was used to predict ¹¹B, ¹⁹F, and ¹³C chemical shifts for all of the FPBA-attached structures: monodentate, bidentate, and bidentate bridging. The full set of predicted chemical shifts can be found in Tables D1–D6. The revised Perdew–Burke–Ernzerhof (revPBE)⁷² functional was used for ¹¹B and ¹³C, the hybrid PBE0 functional⁷³ with 50% HF exchange was used for ¹⁹F, and the Slater-type TZ2P57 all-electron basis set (no frozen core) was used for all elements. The numerical quality was set to “very good” for each calculation using the Becke integration. The

chemical shifts of the ^{13}C model structures were calculated according to $\delta = (\sigma_{\text{ref}} - \sigma)/(1 - \sigma_{\text{ref}})$, where the constant ($\sigma_{\text{ref}} = 189.05$ ppm) was obtained from an optimized structure of tetramethylsilane (TMS). The chemical shifts of the ^{11}B model structures were calculated according to $\delta = (\sigma_{\text{ref}} - \sigma)/(1 - \sigma_{\text{ref}})$, where the constant ($\sigma_{\text{ref}} = 80.4$ ppm) was obtained from an optimized structure of boric acid. Chemical shifts of the ^{19}F model structures were calculated according to $\delta = (\sigma_{\text{ref}} - \sigma)/(1 - \sigma_{\text{ref}})$, where the constant ($\sigma_{\text{ref}} = 195.72$ ppm) was obtained from an optimized structure of trichlorofluoromethane.

Chapter 3

REACTION OF BCl₃ WITH H- AND Cl-TERMINATED Si(100) AS A PATHWAY FOR SELECTIVE, MONOLAYER DOPING THROUGH SOLUTION CHEMISTRY

3.1 Abstract

This chapter explores the interaction of boron trichloride with H- and Cl-terminated Si(100) surfaces, aiming to comprehend how this molecule interacts with the surface. The objective is to design a solution chemistry-based silicon surface doping processes using a precursor that is free of carbon and oxygen. The process was followed with X-ray photoelectron spectroscopy (XPS). Within the reaction conditions investigated, the reaction is highly effective on Cl-Si(100) for temperatures below 70 °C, at which point both surfaces react with BCl₃. The XPS investigation followed the formation of a B 1s peak at 193.5 eV corresponding to (B-O)_x species. Even the briefest exposure to ambient conditions lead to hydroxylation of surface borochloride species. However, the Si 2p signature at 102 eV allowed for a confirmation of the formation of a direct Si-B bond. Density functional theory was utilized to supplement the analysis and identify possible major surface species resulting from these reactions. This work provides a new pathway to obtain a functionalized silicon surface with a direct Si-B bond that can potentially be exploited as a means of selective, ultra-shallow, and supersaturated doping. The material in this chapter is based on a published manuscript¹².

3.2 Introduction

As described in section 1.1, silicon surfaces that are selectively terminated (or functionalized) are considered a benchmark for the chemical modification of semiconductors, encompassing both fundamental and applied perspectives. Several reviews have emphasized the essential aspects of how these single-crystalline surfaces undergo modification and are used in practical applications.^{1,74-76} Doping silicon surfaces, especially ultra-shallow doping with high dopant concentrations, is at the core of many of these applications.^{17,77} Recently, monolayer doping has been used to achieve shallow doping (< 5 nm) of silicon with relatively high dopant concentrations ($> 10^{20}$ cm⁻³) through a process by which the silicon surface is functionalized with a dopant-containing molecule followed by a rapid thermal anneal (RTA) to drive the dopant into the substrate.³ Monolayer doping provides a relatively quick and low-cost solution chemistry-based method to dope silicon substrates without having to work in high vacuum environments and to control the dopant concentration by chemical design.⁷⁸ Recent studies have even demonstrated the use of boron-containing and phosphorous-containing molecular precursors with self-capping properties.⁷⁹⁻⁸² However, the use of carbon and oxygen containing precursor molecules, as well as a commonly used oxide capping layer to prevent desorption, leads to significant amounts of undesirable contaminants diffusing into the substrate along with the dopant.⁸³ Additionally, the high annealing temperatures (typically > 900 °C) required to break the Si-C bonds formed during traditional monolayer doping chemistries lead to diffusion-limited doping levels and may be incompatible with existing device features or structures on the chip. To circumvent these issues, in this chapter we propose that a more ideal monolayer doping

process would instead utilize carbon- and oxygen-free precursors that form a direct Si-dopant bond, e.g. Si–B or Si–P, thereby reducing contaminants, significantly lowering the thermal budget, and providing a route towards supersaturation ultra-shallow doping. These characteristics have been demonstrated with advanced manufacturing techniques that use gas-phase surface chemistry in ultra-high vacuum environments,^{84,85} but a more accessible solution chemical pathway holds considerable promise to accelerate discovery of device functionality and process flexibility in microelectronics unavailable to conventional doping pathways.⁸⁶

Many solution chemistry-based silicon functionalization schemes leverage the formation of a halogen-terminated surface from an initial hydrogen terminated surface to drive a desired chemical reaction.^{87–89} This implies some level of selectivity between the target reactant and the chosen substrate termination, i.e. a favorable reaction occurs on a halogen terminated surface, while no reaction occurs on a hydrogen terminated surface. Several reports have investigated the ordering of mixed hydrogen/halogen adsorbates on silicon surfaces,^{90–92} the halogen-halogen interaction of halogen-terminated Si(100),⁹³ and the ability to place halogen adatoms within patterned, de-passivated areas on an otherwise fully hydrogen passivated Si (100) surface has been demonstrated.^{93,94} With proper substrate patterning to achieve the desired termination in a predefined area, one could envision a selective-area monolayer doping process in which the dopant-containing precursor was chosen not only for its ability to foster a direct Si-dopant bond, but also for its selective reaction with the substrate termination. One of the issues with selectively terminated silicon surfaces is that the primary target of those investigations has been the well-defined Si(111) single crystal face. At the same time, the more technologically relevant Si(100) crystal face has received substantial

attention mostly in ultra-high vacuum studies (see review ⁷⁴ and references therein) supported by computational investigations,^{76,95,96} and relatively little work has investigated the reactions of the type of condensation on H-terminated Si(100).^{97,98} In general, the modification of the Si(100) surface by using solution chemistry appears to yield more complex species compared to those on Si(111).^{6,89,99,100}

The study in this chapter compares the reactivity of boron trichloride (BCl₃) with Cl-Si(100) and H-Si(100) surfaces as the basis for developing future processing for a selective area monolayer doping that forms direct Si-dopant bonds and that also utilizes an O- and C-free dopant precursor. The entire process is performed using wet chemistry (solution) methods. We find that under a relatively wide range of experimental conditions, BCl₃ exhibits very high selectivity towards a reaction with Cl-Si(100) at temperatures below 70 °C. The reaction in an oxygen-and water-free atmosphere could clearly yield an unoxidized surface and lead to the formation of direct Si-B bonds.

3.3 Results and discussions

All substrates and chemicals used in this chapter can be found in chapter 2, section 2.2.1. The preparation of H-, Cl-Si(100) and the reaction with boron trichloride can be found in sections 2.1.2, section 2.1.3 and section 2.1.5 respectively.

The XPS analysis was performed as described in chapter 2, section 2.1.1. To quantify surface coverages of boron and chlorine, an overlayer model was used ⁶ with the following assumptions:

- (1) chlorine- or boron-containing molecules are on the silicon substrate, and the adventitious hydrocarbon and oxygen layer is on top of that overlayer;
- (2) all the chlorine and boron atoms in the overlayer are in the solid state.

The equivalent monolayer coverage of an overlayer species was calculated from the equation:

$$\Phi = \left[\left(\frac{\lambda \sin\theta}{a_{ov}} \right) \left(\frac{SF_{Si}}{SF_{ov}} \right) \left(\frac{\rho_{Si}}{\rho_{ov}} \right) \left(\frac{I_{ov}}{I_{Si}} \right) \right] \quad (1)$$

Where Φ is the overlayer coverage; λ is the penetration depth (4.0 nm in this instrument); θ is the photoelectron takeoff angle with respect to the analyzer (35.3°); a_{ov} is the atomic diameter of the overlayer species. The value of a_{ov} was obtained using the following equation:

$$a_{ov} = \left(\frac{A_{ov}}{\rho_{ov} N_A} \right)^{1/3} \quad (2)$$

A_{ov} is the atomic weight of the overlayer species: 35.45 g/mol and 10.81 g/mol for Cl and B atoms, respectively. N_A is Avogadro's constant. I is the integrated area under the overlayer or substrate peaks, determined by Casa XPS software (version 2.3.16).

The objective of this chapter is to compare the reactivity of boron trichloride with H- and Cl-terminated Si(100) surfaces, for designing solution chemistry-based Si surface doping processes using a carbon- and oxygen-free precursor. Figure 3.1 summarizes the preparation of and possible reaction pathways for BCl_3 with H-Si(100) and Cl-Si(100) surfaces.

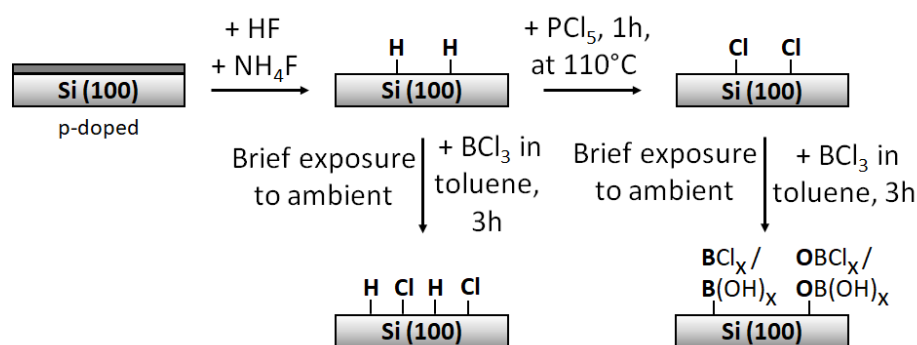


Figure 3.1: Comparison of the reactivity of the H-terminated and Cl-terminated Si(100) surfaces.

As will be demonstrated in this chapter, the reaction of BCl_3 with H-Si(100) is only initiated at elevated temperatures and yields largely partial chlorination of this surface and partial oxidation. In contrast, Cl-Si(100) is very efficient in reacting with BCl_3 , and it will be shown that direct Si-B bonds are formed on this surface. However, any boron-chloride species formed on this surface are highly susceptible to oxidation even following very brief exposure to ambient conditions upon sample transfer, such that a number of possible boron-containing oxidized surface species are formed. Possible species are discussed later. The top two panels of Fig. 3.2 show the B 1s, Cl 2p, and Si 2p XPS spectral regions of the H-terminated surface carefully prepared by the so-called modified RCA procedure (as described in section 2.1.2.1) before and after reaction with BCl_3 at three different temperatures. At 35 °C and 50 °C there is no indication of boron being present, which suggests that boron trichloride does not react with the H-terminated Si(100) at these lower temperatures to introduce boron, and only some chlorination is observed. However, when the reaction is performed at 70 °C a distinct B 1s peak at 193.5 eV corresponding to $(\text{BO})_x$ ^{101–103} is observed, indicating that boron is introduced. As will be discussed below, these boron-containing species may

also contain chlorine atoms, but will be referred to as $(\text{B-O})_x$ within this chapter. It should be noted that the chlorine presence on the surface increases with temperature and is the highest for the reaction performed at 70 °C, which suggests that the chlorine comes from the BCl_3 ¹⁰¹ since this surface was not in contact with the PCl_5 reagent used to prepare the Cl-terminated surface (see details in the experimental section). The Si 2p spectral region shows a peak corresponding to the SiO_x species at approximately 103 eV^{104,105} in addition to the bulk signature, indicating that the surface is susceptible to oxidation even upon very brief exposure to ambient upon transfer to the XPS instrument.

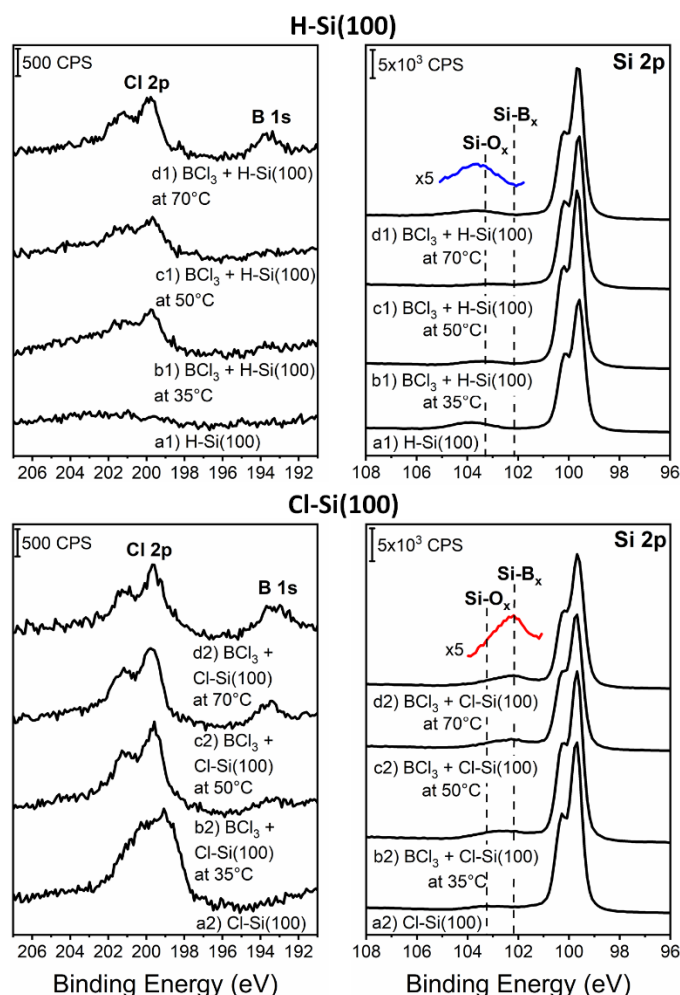


Figure 3.2: XPS spectra of Cl 2p, B 1s and Si 2p spectral regions for H-terminated Si(100) before reaction (a1), after BCl_3 reaction (b1) at 35 °C for 3 h, (c1) at 50 °C for 3 h and (d1) at 70 °C for 3 h (the inset shows the zoomed-in region of the spectrum corresponding to the formation of Si-B_x and Si-O_x species) and for Cl-terminated Si(100) before reaction (a2), after BCl_3 reaction (b2) at 35 °C for 3 h, (c2) at 50 °C for 3 h and (d2) at 70 °C for 3 h (the inset shows the zoomed-in region of the spectrum corresponding to the formation of Si-B_x and Si-O_x species). Each spectrum is the result of averaging three different experimental spectra.

The reaction of BCl_3 with Cl-terminated Si(100) surface (prepared starting with the H-Si(100) surface prepared by the RCA procedure (see experimental section

2.1.2.1)) is summarized in the bottom two panels of Fig. 3.2. For all the reaction temperatures tested, there is a peak of B 1s present at around 193.5 eV corresponding to the (B-O)_x species. The intensity of the B 1s peaks increases at higher temperatures, having the highest intensity at 70 °C. Additionally, it is observed that the Cl 2p feature decreases with reaction temperature. Another interesting feature observed in the Si 2p region is the peak at 102.1 eV corresponding to the Si-B bond.¹⁰⁶⁻¹⁰⁸ This feature is very prominent and is clearly distinguishable from the SiO_x signature around 103 eV, which is indeed observed but is minimal at the optimized reaction conditions at 70 °C. Surface B-Cl groups are expected to rapidly oxidize upon even brief exposure to ambient conditions during sample transfer following the reaction to the XPS instrument. Previous studies demonstrated the deposition of B₂O₃ films formed by atomic layer deposition on Si surfaces using BCl₃/H₂O and BCl₃/O₂, where the B 1s feature is also observed at ~ 193 eV and chlorine contamination is recorded at high temperatures.^{101,103} Even at room temperature, it was shown that a complex mixture of species including B-Si, BCl, BCl₂ and BCl₃ formed on silicon.¹⁰⁶ In fact, boron trichloride gas reacts with the Si(100) causing both etching and boron introduction, with the deposition rate of boron higher at lower temperatures and etching of silicon more favorable at higher temperatures.¹⁰⁹ Most importantly, however, the Si-B bond in the set of investigations presented here is preserved and oxygen is not incorporated into the silicon wafer when BCl₃ reacts with Cl-Si(100). Thus, boron trichloride does react preferentially with the Cl-terminated vs the H-terminated surface, where a peak for B 1s around 193.5 eV corresponding to (B-O)_x¹⁰¹⁻¹⁰³ is present at all the temperatures tested for the Cl-Si(100) surface and the highest intensity for the B 1s is obtained for the reaction performed at 70 °C.

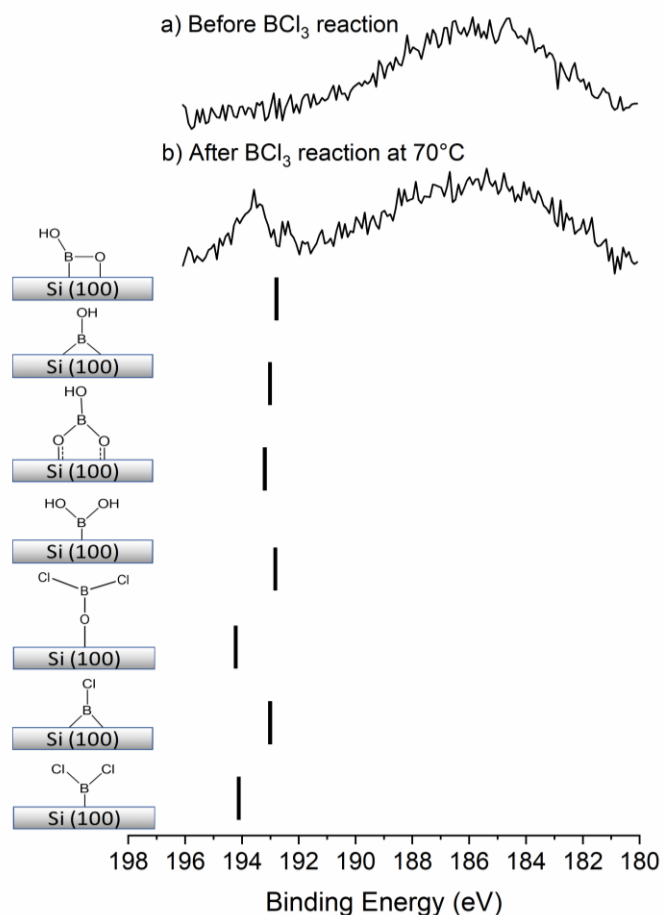


Figure 3.3: Comparison of the peak position in the experimental XPS spectra of B 1s obtained from the reaction with BCl_3 at 70°C for 3 h (a) before the reaction (showing a Si 2s plasmon feature) and (b) following the reaction and the computationally predicted values for the models indicated, shown as black bars underneath the experimental spectrum.

The possible species formed on the surface during the reaction of boron trichloride with Cl-terminated Si(100) followed by a brief exposure to ambient were modeled using the Gaussian 09 suite of programs⁴⁹ utilizing the B3LYP functional and 6-311G+(d,p) basis set (section 2.4.1).^{50,51} The results for the calculated binding energies of the modeled species are shown in Fig. 3.3 where the different species are

projected to have their XPS signature very close to the experimental peak position obtained after the reaction with BCl_3 at 70°C for 3 h. The expected positions of the B 1s features were calibrated as described in the computational methods section 2.4.1. The experimental data are fully consistent with boron introduction, but the nature of the attached boron species is difficult to determine based on these calculated binding energies alone, since the expected position of the B 1s features all fall within the experimentally observed peaks.

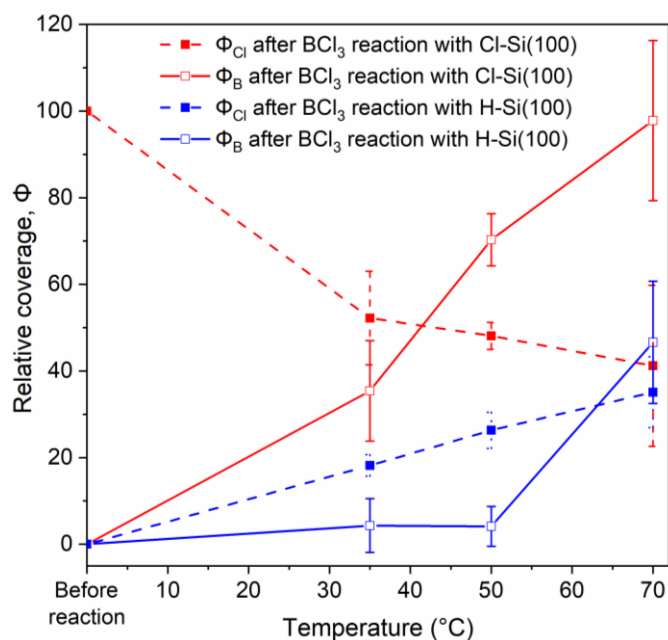


Figure 3.4: Relative Cl/Si monolayer coverage after BCl_3 reaction with Cl-Si(100) (dashed red line), relative B/Si monolayer coverage after BCl_3 reaction with Cl-Si(100) (solid red line), relative Cl/Si monolayer coverage after BCl_3 reaction with H-Si(100) (dashed blue line) and relative B/Si monolayer coverage after BCl_3 reaction with H-Si(100) (solid blue line), calculated from the Briggs and Seah equation, as described in detail in reference.¹¹⁰

Fig. 3.4 shows the surface coverage of boron and chlorine on Cl-Si(100) and H-Si(100) surfaces after reaction with BCl_3 as a function of reaction temperature, as estimated according to the calculations obtained from equation (1) in the experimental section 3.3.5. These results clearly show that for the Cl-Si(100) surface the chlorine coverage decreases significantly after the reaction with BCl_3 at any temperature studied, with a slight temperature dependence, while the presence of boron increases significantly as the temperature increases. Opposite to that, for H-Si(100) the amount of chlorine increases with temperature, but the presence of boron is only appreciable at 70 °C. It appears that the BCl_3 does react preferentially with the Cl-terminated surface, and only introduces chlorine to the H-Si(100) surface. We surmise that once the amount of chlorine on that surface is substantial, the reaction proceeds similarly to how it would proceed on Cl-Si(100). However, surface chlorine concentration produced on the H-Si(100) surface by BCl_3 at temperatures below 70 °C (e.g. $< \sim 20\%$) at these reaction conditions is not sufficient for the boron-introducing reaction to occur at significant rates.

The reaction of BCl_3 with H-Si(100) and Cl-Si(100) surfaces prepared with a simple HF-dip method, rather than the careful RCA procedure, was also investigated. It has been shown that a simple dip into a 10% HF solution (see details of the HF-dip method in the experimental section 2.1.2.2) can produce an H-terminated silicon surface that is poorly defined chemically but has superior electrical properties.^{5,111,112} Fig. 3.5 summarizes the results. Similar to the results presented above for the Si(100) surfaces carefully prepared by the RCA procedure, there is a clear selectivity for the reaction of BCl_3 with Cl-Si(100) compared to H-Si(100) at 50 °C, and the reaction loses its selectivity at 70 °C. However, one noticeable difference is that the Si-B peak at around

102 eV is not observed for the simple HF-dip prepared samples. Silicon surface oxidation is observed, as clearly evidenced by the presence of the SiO_x peak in the Si 2p region recorded for all the samples, regardless whether they are H- or Cl-terminated. This difference between the reactivities of differently prepared H- and Cl-terminated Si(100) surfaces implies that better defined RCA-prepared surfaces, likely consisting mostly of dihydride/dichloride species,⁹⁹ show better propensity towards formation of Si-B bond in a reaction with BCl_3 , and/or better resistance to subsequent oxidation of any initial Si-B bonds formed during the exposure to ambient. The HF-dip prepared surfaces, which likely have a wider variety of surface species both in H-terminated and in Cl-terminated samples, also form B-containing surface species; however, the position of boron in those species appears to quickly shift towards arrangements that do not contain a direct Si-B bond, possibly Si-O-B, upon exposure to ambient.

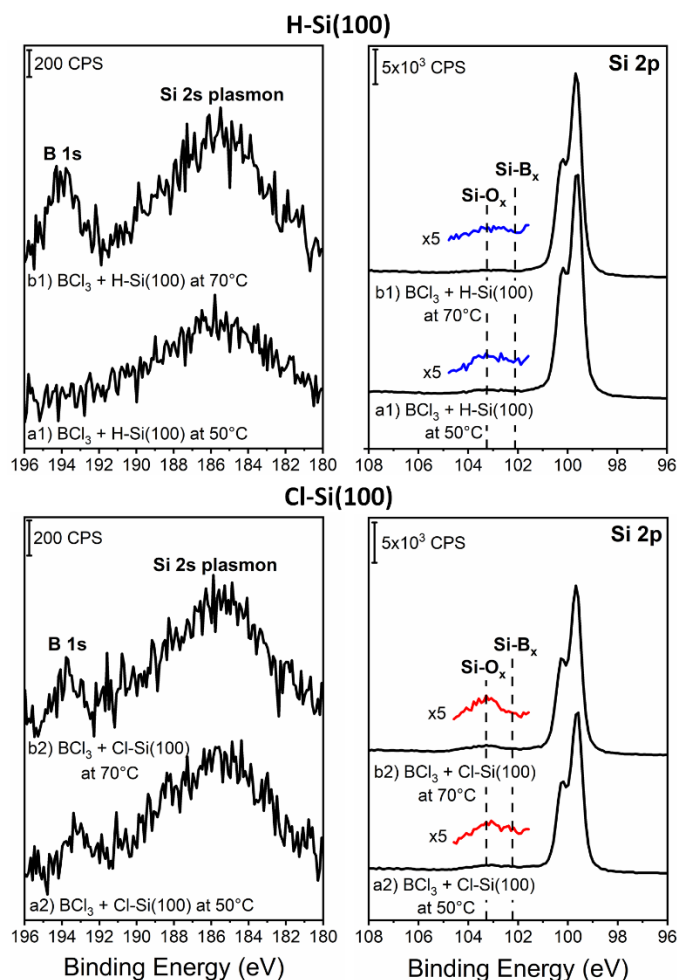


Figure 3.5: XPS spectra of B 1s and Si 2p spectral regions for H-terminated and Cl-terminated Si(100) surface prepared by HF-dip method: H-Si(100) after BCl_3 reaction at 50 °C (a1), after BCl_3 reaction at 70 °C (b1) for 3 h; Cl-Si(100) after BCl_3 reaction at 50 °C (a2), after BCl_3 reaction at 70 °C (b2) for 3 h.

3.4 Conclusions

In this chapter a solution chemistry-based route to form direct Si-B bonds by the reaction of BCl_3 with a Cl-terminated Si(100) surface was demonstrated. This provides a potential pathway for ultra-shallow and supersaturated monolayer doping of the technologically important silicon (100) surface using a carbon- and oxygen-free

precursor. Additionally, the results indicate that BCl_3 reacts preferentially with the Cl-Si(100) surface compared to H-Si(100), providing a potential method for selective functionalization with BCl_3 of surfaces co-patterned with both Cl and H terminations. The doping level can be controlled by the reaction conditions, and a number of post-processing reduction schemes^{101,103,106,113} can be potentially used to remove remaining contaminants. An example of the use of low energy Ar^+ sputtering to remove carbon contamination resulting from a brief exposure of the sample to ambient conditions during the transfer to the XPS instrument is provided in the supporting information section. A fully enclosed glove box can also be used to maintain an oxygen- and water-free atmosphere during the experiments to minimize oxidation.

Chapter 4

REACTION OF HYDRAZINE WITH SOLUTION- AND VACUUM- PREPARED SELECTIVELY TERMINATED Si(100) SURFACES: PATHWAYS TO THE FORMATION OF DIRECT Si-N BONDS

4.1 Abstract

In this chapter, the reactivity of liquid hydrazine (N_2H_4) toward H-, Cl-, and Br-terminated Si(100) surfaces was explored to unveil the principles governing nitrogen incorporation into the surface. This process has important implications in a wide variety of applications, including semiconductor surface passivation and functionalization, nitride growth, and many others. The use of hydrazine as a precursor allows for reactions that exclude carbon and oxygen, the primary sources of contamination in processing. In this chapter, the reactivity of N_2H_4 with H- and Cl-terminated surfaces prepared by traditional solvent-based methods and with a Br-terminated Si(100) prepared in ultrahigh vacuum was compared. The reactions were studied with X-ray photoelectron spectroscopy, atomic force microscopy, and scanning tunneling microscopy, and the observations were supported by computational investigations. The H-terminated surface led to the highest level of nitrogen incorporation; however, the process proceeds with increasing surface roughness, suggesting possible etching or replacement reactions. In the case of Cl-terminated (predominantly dichloride) and Br-terminated (monobromide) surfaces, the amount of nitrogen incorporation on both surfaces after the reaction with hydrazine was very similar despite the differences in preparation, initial structure, and chemical composition. Density functional theory was used to propose the possible

surface structures and to analyze surface reactivity. The material in this chapter is based on a published manuscript¹³.

4.2 Introduction

The fundamental concept underlying numerous industrial processes, such as doping, etching, catalysis, and film growth, involves the insertion of atoms or small fragments into the lattice of a substrate. As discussed in chapter 1, emerging molecular-level technologies and advanced manufacturing demand novel approaches to govern the mechanisms of these surface reactions. These new approaches in the field of semiconductor surface modification, specifically for silicon functionalization, have been regularly reviewed in the literature, and a number of important points about them are highlighted in references^{1,74,114–116}. Reactions of nitrogen-containing molecules with silicon surfaces have been a subject of substantial research over several decades (see, for example, references^{114,115,117} and multiple references therein). In addition to the fundamental intricacies of surface reactions in ultrahigh vacuum,^{118–120} more recently, a number of condensation processes on selectively terminated silicon surfaces with nitrogen-containing compounds have been investigated by solution-based approaches. The condensation reactions included investigations of the reactivity of nitro- and nitroso-compounds with H-terminated silicon and amine reactions with halogen-terminated silicon surfaces.^{97,121} Both efforts have been inspired by surface functionalization; however, the key target has been the formation of a direct Si–N bond for the ultimate formation of silicon nitride (SiN) layers. SiN layers on Si surfaces are very effective in suppressing interface reactions between Si and a metal oxide layer (high-k gate dielectrics), such as in ultra-large-scale integration (ULSI) technology.¹²² They are widely used as passivating and dielectric thin films in semiconductor

technology.^{123,124} However, it is extremely difficult to form atomically flat and uniform interfaces based on the Si–N bonds, which is necessary for scaling down and improving the performance of miniaturized devices.^{122,125,126}

There are a number of fundamental and practical issues that need to be addressed in order to control the Si–N bond formation. The first problem is contamination, especially with carbon or oxygen, an integral part of many proposed nitrogen-containing precursor molecules,^{97,121,127} which affects the electrical and optical properties of silicon; the second is the often necessary use of ultrahigh vacuum (UHV);^{127,128} and the third is that model reactions are often performed on a convenient Si(111) surface that is stable following hydrogen or halogen termination, but Si(100) is rarely used in model studies outside the UHV conditions, despite the fact that it is the most commercially relevant surface.

In order to address the first issue, O- and C-free precursors can be used. Among them, certainly ammonia (NH₃)^{120,129–133} has received the most attention; but hydrazine (N₂H₄) has also been investigated.^{110,134–136} In some of the previous studies, the nitridation of silicon surfaces and interfaces employed thermal reactions of N₂, NH₃, or mixtures of N₂/H₂ in the gas phase.^{124,129,137,138} By and large, these reactions require high temperatures and UHV conditions. Solution-based chemistry, on the other hand, can be performed at much lower temperatures, and it has been shown recently to produce easily controlled interfaces at relatively low expense.^{139,140} Ammonia and hydrazine can be used at these conditions both neat and in a variety of solvents,^{132,141} and H- or halogen-terminated silicon surfaces can be produced to passivate the silicon after oxide removal and can survive outside UHV for the time needed for further surface modification. In fact, H and halogen-terminated silicon surfaces have been shown to be stable in several

solvents during reactions with BCl_3 ,¹² ammonia,¹³² and alkyl silanes.³⁸ Compared to the reaction with ammonia and its derivatives, the reaction of hydrazine on semiconductor surfaces has been studied to a much lesser extent. The reaction of modified silicon with anhydrous hydrazine requires lower processing temperatures than that needed for ammonia as a nitriding agent for silicon surfaces.¹¹⁰ In addition, hydrazine has two nitrogen atoms that can act as electron donors and can form more stable surface species compared to those formed with ammonia.^{110,135}

It should be noted that a number of studies have computationally investigated reactions of a chlorine-terminated Si(100) surface with ammonia^{142,143} or phosphine (PH_3)¹⁴⁴ molecules and compared the results with selected experimental data available for ammonia reacting with Cl-covered Si(100) surfaces in ultrahigh vacuum (UHV).¹⁴⁵ There is also some mechanistic insight available for the interaction of ammonia with H-covered Si(100), again under UHV conditions.^{145,146} The previous computational work on the PH_3 reaction with ideally monochloride-terminated Si(100) surface explicitly attempted to investigate this process without the presence of surface defects and found only very weak interaction, so the rest of that work focused on reactions with the defective surface.¹⁴⁴ However, accomplishing the reaction in liquid phase not only allows for the kinetically hindered processes to occur but also changes the thermodynamics of the process by introducing the interaction of the HCl molecule, the key product of the reaction with Cl-Si(100), with excess ammonia (or in our case with hydrazine).

The work presented in this chapter demonstrates that a well-defined interface can be formed in a reaction of appropriately terminated Si(100) surfaces with hydrazine via solution-based chemistry. The results show that the nitrogen incorporation into the

H-Si(100) surface can exceed monolayer coverage, possibly at the expense of surface roughening or subsurface insertion. We also investigate and compare the reaction of hydrazine with a solution chemistry-prepared Cl-Si(100) (which is mostly covered with silicon dichloride species^{99,147}) and on a Br-Si(100) prepared in UHV (which is primarily covered with silicon monobromide species¹⁴⁸). Finally, we show that despite different surface preparations, the halogen-terminated Si(100) surfaces react with hydrazine to produce similar surface species and coverage, suggesting that a technological bridge can be formed between UHV processing and solution-based chemistry of silicon.

4.3 Results and discussions

All materials used in this chapter can be found in chapter 2, section 2.2.1. The XPS analysis was performed as described in chapter 2, section 2.1.1. And the AFM images were obtained as described in section 2.1.5

The objective of this chapter is to showcase the creation of a well-defined interface through a reaction involving H-, Cl- and Br-terminated Si(100) surfaces and hydrazine using solution-based chemistry.

Figure 4.1 summarizes the preparation of the Br-, H-, and Cl-Si(100) surfaces followed by the reaction with hydrazine, starting with a clean Si(100) surface in UHV and with silicon covered with a native oxide layer in solution chemistry experiments (the details of each preparation are described in chapter 2).

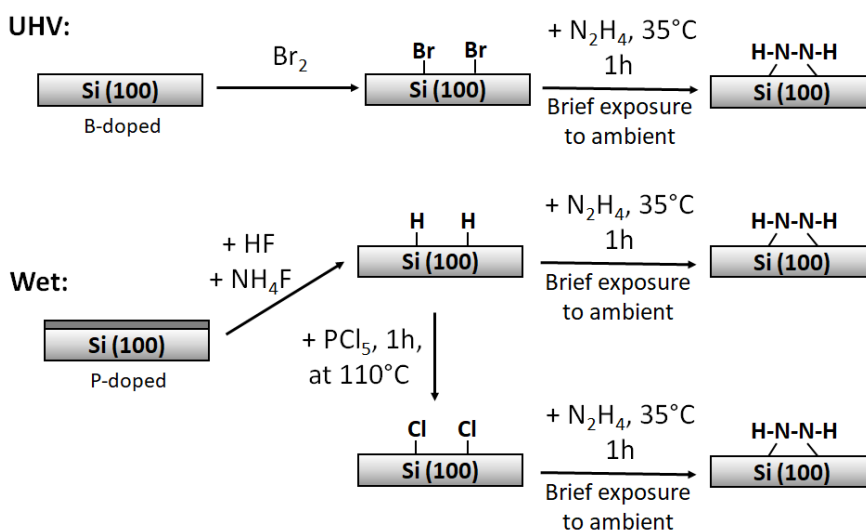


Figure 4.1: Schematic comparison of the reaction sequences for the H-, Cl-, and Br-terminated Si(100) surfaces

As will be shown in this chapter, hydrazine reacts with all the surfaces investigated, and a direct Si–N bond is formed. Note that the product shown in the scheme is only used to illustrate that the reaction has occurred. It is well known that the solution chemistry-prepared H-terminated Si(100) surface consists mostly of the dihydride species,¹⁴⁹ so it is expected that the chlorinated surface prepared starting with this H-Si(100) substrate would be mostly covered with silicon dichloride species, as previously reported.^{12,99} Comparing the H- and Cl-terminated silicon surfaces prepared by the solution chemistry with a Cl–Si(100) surface prepared in UHV would have been ideal to uncover the differences between silicon monochloride and silicon dichloride surface species; however, in the tests, the Cl–Si(100) surface did not survive outside UHV for a time that would be sufficient to transfer it from the Laboratory for Physical Sciences for further modification at the University of Delaware. Thus, the more stable monobromide-terminated Si(100) surface prepared in UHV was used.

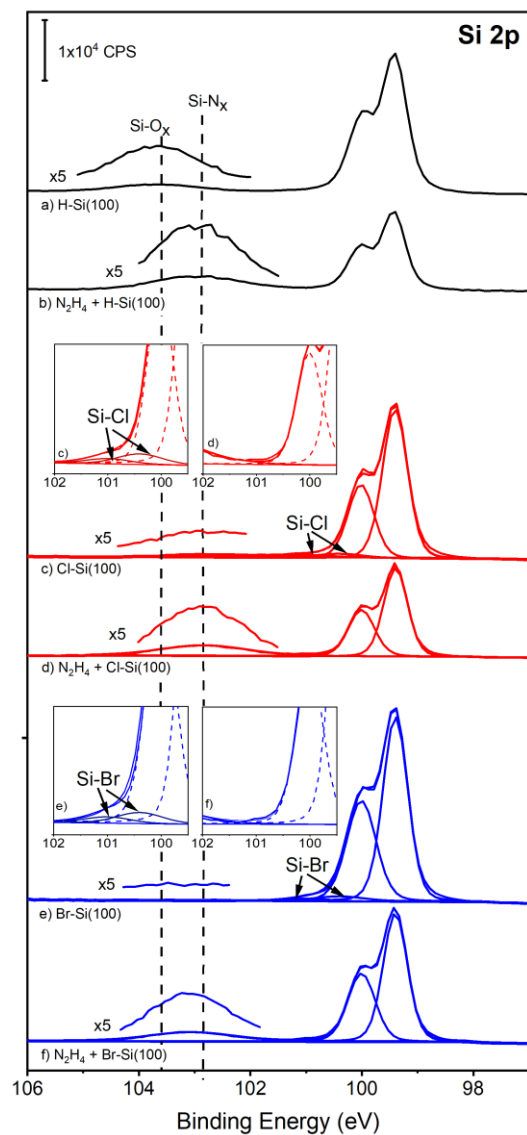


Figure 4.2: XPS spectra of the Si 2p spectral region for (a) H-terminated Si(100) that is the starting point, (b) H-Si(100) following the reaction with hydrazine, (c) Cl-Si(100), (d) Cl-Si(100) following the reaction with hydrazine, (e) Br-Si(100) and (f) Br-Si(100) following the reaction with hydrazine. Each spectrum is the result of averaging three different experimental spectra. The fits include the features corresponding to Si-Cl and Si-Br surface species on Cl-Si(100) and Br-Si(100) surfaces (c and e) that do not appear on the same surfaces following their reaction with hydrazine (d and f). The same spectra are shown in the insets as zoomed-in versions.

Figure 4.2 shows the XPS spectra of the H-, Cl-, and Br-Si(100) surfaces before and after the reaction with hydrazine. Based on the Si 2p spectra shown in this figure, the H-terminated Si(100) has an intense Si 2p_{3/2} feature at 99.4 eV corresponding to elemental silicon and a small peak at 103.7 eV corresponding to (Si-O)_x species from brief exposure to the ambient conditions upon its transfer to the XPS chamber.¹⁵⁰ Following the reaction of this surface with hydrazine, there is a clear spectroscopic difference observed for the higher binding energy peak, which now appears at 102.7 eV and corresponds to (Si-N)_x species. This shift to a lower binding energy is due to the lower electronegativity of nitrogen compared to oxygen, and it can be clearly differentiated on the silicon surface.^{110,132,151} It should be noted that on H-Si(100) reacted with hydrazine (Figure 4.2 b)), the intensity of the peak that corresponds to partial oxidation at 103.7 eV is much smaller than that on H-Si(100) before the reaction with hydrazine (Figure 4.2 a)). This may be the result of shorter exposure time for transferring the H-Si(100) sample for the hydrazine reaction compared to that required to transfer it to the XPS chamber or may indicate oxide removal during hydrazine modification. Although specific reactions of hydrazine with H-Si(100) are very difficult to pinpoint within the framework of this investigation, this compound is a known reducing agent, and it is possible that some reduction processes involving surface oxide or Si-OH groups could proceed in series of reactions similar to those reported by Gao et al.¹⁵² The Cl-terminated Si(100) in Figure 1c shows a very small feature corresponding to oxidation, and after the reaction with hydrazine the position of the higher binding energy peak is at approximately 102.7 eV, indicating the formation of (Si-N)_x. The spectrum shown in Figure 4.2 c) for the Cl-Si(100) surface can be fitted with a pair of the spin-orbit coupled peaks corresponding to the Si-Cl species, based on

literature data,¹⁵³ in addition to the main silicon 2p features. These additional features disappear after the reaction with hydrazine, as shown in the corresponding insets in Figure 4.2. There have been previous attempts to identify and quantify the types of Si-Cl species formed on Si(100), for example, with soft X-ray photoelectron spectroscopy in a two-step chlorination/alkylation process^{99,154} or by angle-resolved XPS for Cl₂ plasma etching;¹⁵⁴ however, for this study, the weak signals and possible inhomogeneity of the surfaces make it difficult to perform the quantitative assignment, although the position of the Si-Cl peaks shown in Figure 1c is consistent with the dichloride formation.¹⁵⁵ The Cl 2p spectra may be much more informative in the quantification of chlorine amount on this surface.

Finally, for the Br-Si(100) surface shown in Figure 1e, no oxidation is observed despite brief exposure of the samples to ambient conditions and transporting them to a different location under nitrogen. We attribute the stability of the UHV-prepared Br-Si(100) surface to its nearly defect-free character in combination with steric hindrance associated with the relatively large halogen adatom that inhibits the accessibility of Si-Si and Si-Br bonds by impinging oxygen-containing molecules. After the reaction with hydrazine, this surface clearly exhibits the formation of the Si-N_x species indicated by the peak at 102.7 eV as shown in Figure 4.2 f). Similarly to the chlorinated surface, the spectrum shown in Figure 4.2 e) for the Br-Si(100) surface can be fitted with a pair of the spin-orbit coupled peaks corresponding to the Si-Br species, based on literature data,¹⁵³ in addition to the main silicon 2p features. These additional features disappear after the reaction with hydrazine, as clearly shown in the corresponding insets for Figure 4.2 e,f. Again, examining the Br 3d spectra instead of

quantifying these weak signals may be more informative, especially when compared with independent Br coverage determination by STM.

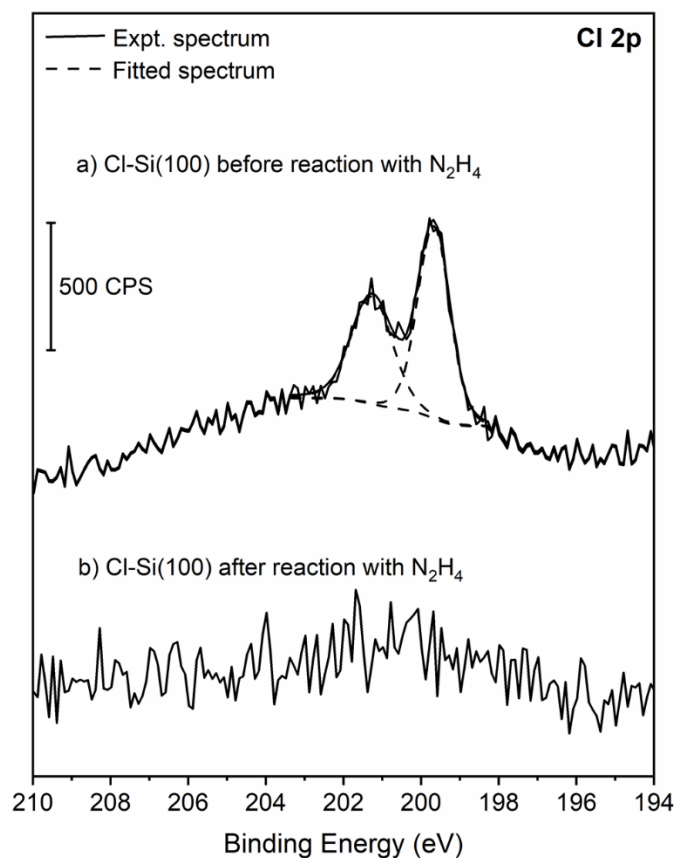


Figure 4.3: XPS spectra of the Cl 2p spectral region for (a) Cl-Si(100) before surface modification and (b) Cl-Si(100) after surface modification with hydrazine.

The H-, Cl-, and Br-terminated surfaces all show the formation of direct Si-N bonds; however, they show different N coverages and they form different N-containing species, as will be discussed below.

Figure 4.3 shows the XPS spectra of the Cl 2p region of the chlorine-terminated silicon surface prepared with a saturated solution of PCl₅. Before the reaction with

hydrazine, the Cl 2p region exhibits the $2p_{3/2}$ and $2p_{1/2}$ features at 199.6 and 201.1 eV, respectively. The small width of the peaks suggests that there is only one type of Cl-containing surface species formed on this sample. It is most likely that the peaks observed correspond to dichloride species since they would be expected to form on a solution chemistry-prepared surface.¹⁵³ After the hydrazine treatment of this surface, chlorine is removed completely, confirming that it has been consumed by a chemical reaction and is likely replaced by nitrogen.

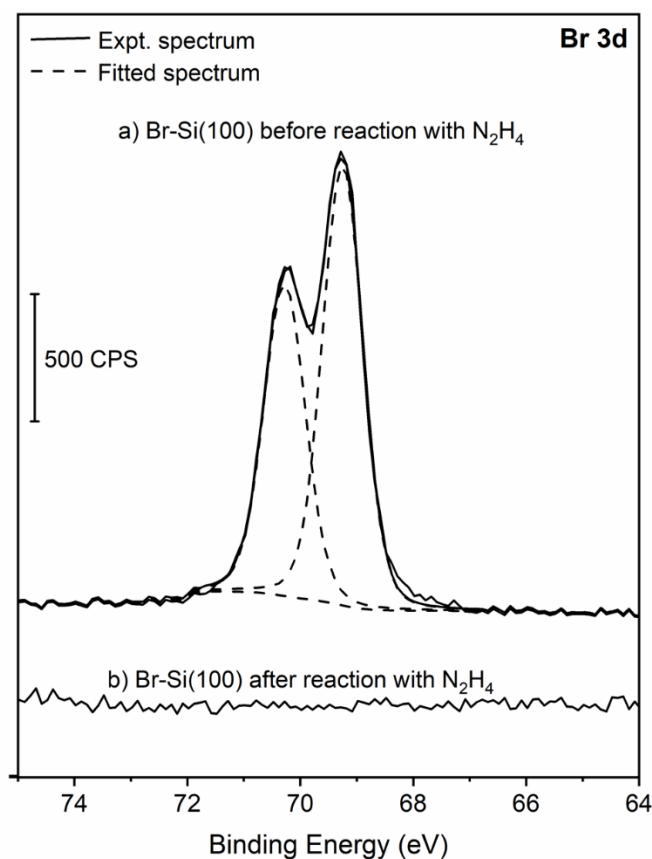


Figure 4.4: XPS spectra of the Br 3d spectral region for (a) Br-Si(100) before surface modification and (b) Br-Si(100) following the surface modification with hydrazine.

Figure 4.4 shows the XPS spectra of the Br 3d region of the bromine-terminated silicon surface prepared in UHV. Before the reaction with hydrazine, the Br 3d region shows the $3d_{5/2}$ and $3d_{3/2}$ features at 69.1 and 70.1 eV, respectively.¹⁵³ With the preparation in UHV, monobromide sites are mostly present on the surface, as was confirmed with STM and discussed below. After the reaction of this surface with hydrazine, the bromine is removed completely.

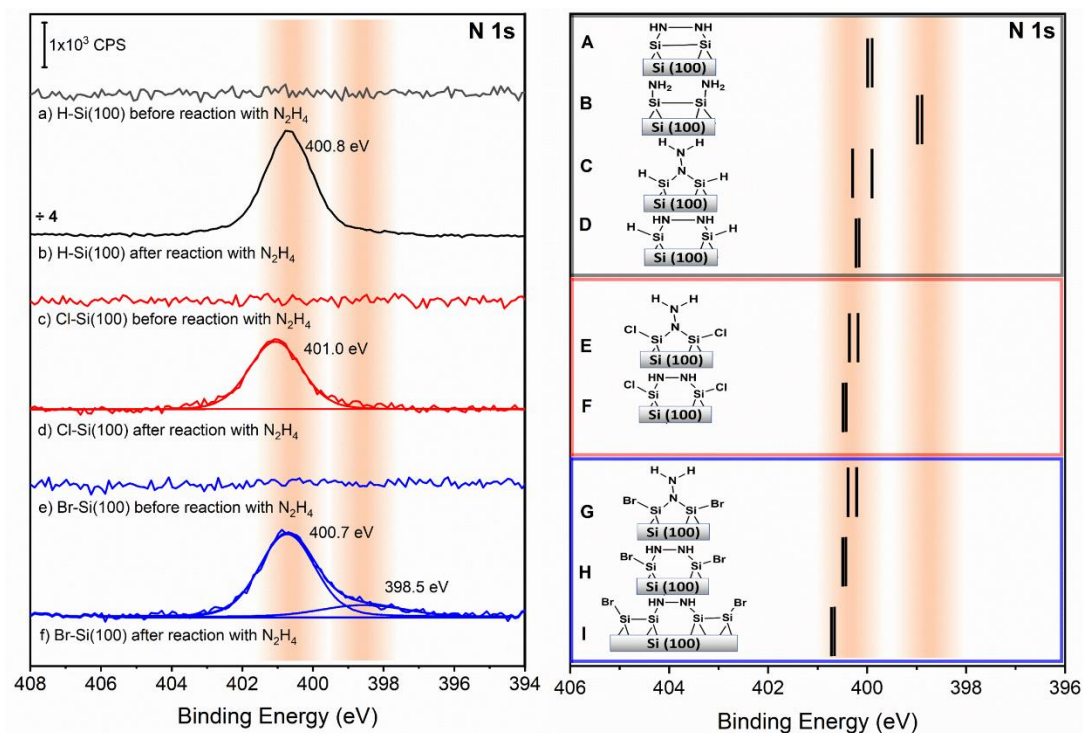


Figure 4.5: XPS spectra of the N 1s spectral region for (a) H-Si(100) surface before the reaction with hydrazine, (b) H-Si(100) surface following the reaction with hydrazine, (c) Cl-Si(100) before the reaction with hydrazine, (d) Cl-Si(100) following the reaction with hydrazine, (e) Br-Si(100) before hydrazine treatment and (f) Br-Si(100) following the reaction with hydrazine (each spectrum is the result of averaging three different experimental spectra). The computationally predicted values for the species indicated (A, B, C, D, E, F, G, H, and I) are shown as black solid bars in the right panel with the experimental features indicated by the red gradients.

The N 1s experimental spectrum shown for the H-Si(100) surface following the reaction with hydrazine in Figure 4.5 exhibits a single-peak N-containing functionality at 400.8 eV in spectrum 4.5 b). The chlorine-terminated surface after the reaction with hydrazine also shows a single peak in spectrum 4.5 d) for N-containing functionality at 401.0 eV. The experimental spectrum in Figure 4.5 f) shown for the Br-Si (100) surface reacted with hydrazine indicates a predominant N-containing functionality at 400.7 eV and a minor species at 398.5 eV. The experimental binding energies that correspond to the observed features were compared to selected computationally predicted models (A, B, C, D, E, F, G, H, and I) from the DFT study, which is shown in Figure 4.5 with corresponding binding energies indicated by solid bars. The models correspond to the possible reaction paths leading to the N-containing products following the reaction with hydrazine. The main products of the reaction can be bonded to the surface with a N-N bond arranged vertically or horizontally with respect to the surface or hydrazine can dissociate forming two NH₂ species.¹¹⁰ The presence of chlorine in species E and F after the treatment with hydrazine was considered, as well as the presence of bromine in species G, H, and I; however, these species are not expected to be present on the final surfaces reacted with hydrazine, since the XPS investigations confirm that the halogens are removed. Nevertheless, it is important to understand the role of halogen atoms possibly remaining on the surface in the appearance of the XPS spectra obtained. Models A through D describe the most likely species that could form on Si(100) during its reaction with hydrazine. Among these models, A, which is formed without breaking the Si-Si bond of the underlying dimer, is the least likely to form on the Cl-Si(100) or H-Si(100) surface, since these surfaces are likely primarily covered with dichloride or dihydride species, respectively. The position of the features corresponding to model B

is the most consistent with the minor feature experimentally observed at 398.5 eV and suggests the presence of surface -NH_2 species following the N–N dissociation. This feature is only observed for the Br–Si(100) surface. Similar features have been reported for reactions of ammonia¹³² and hydrazine¹¹⁰ with the Cl-terminated Si(111) surface and were also assigned to the presence of -NH_2 species. Thus, species of type C or D would be expected to be the most likely on H–Si(100) and Cl–Si(100) based on this subset of XPS studies; however, species C contains two very different nitrogen atoms and should result in a broad feature in the N 1s spectral region, which is not the case. In other words, among models A–D, species D is the most consistent with the observations reported in Figure 4.5. Additional surface chlorine or bromine could potentially shift the N 1s peaks of the proposed species toward higher binding energies, as suggested by the computed peaks predicted for species E through I; however, as noted above, there is no chlorine or bromine remaining on the surfaces following the reaction with hydrazine.

It is also known that the N 1s signal can be shifted toward higher binding energies by surface oxidation^{110,132} but with minimal surface oxidation that would not be expected. Nevertheless, selected models containing oxygen are presented in Figure B1 in Appendix B for comparison. Of these models, only the model that includes the selective oxygen insertion into the N–N bond of the surface-bound hydrazine resembles the experimentally recorded spectra; however, this model is also the least likely to form, since N–H dissociation or oxygen insertion into Si–Si surface bonds would be much more thermodynamically favorable. Thus, according to all these results, it is most likely that the hydrazine is bonded to the surface with its N–N bond parallel to the surface and without substantial oxidation. It is interesting, however, that the surface that appears to exhibit the most inhomogeneous behavior in the reaction with hydrazine is the one that

is the most ordered and covered with the most well-defined monohalide species, Br–Si(100). The detailed investigation of the reaction mechanisms causing this discrepancy may not be possible solely based on the results presented in this work; however, some conclusions on the reactivity of Si–Cl and Si–Br in a reaction with hydrazine can be reached based on the coverage analysis and computational investigation summarized in this chapter.

Before proceeding to evaluate surface coverages of halogens and nitrogen using XPS following a surface modification, it is important to calibrate the absolute coverage based on an independent measurement. STM provides an opportunity to use such an approach.

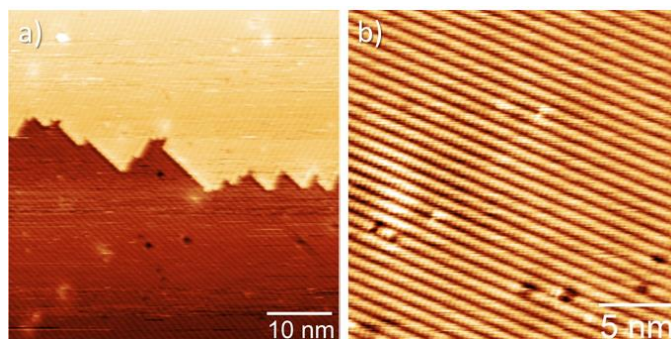


Figure 4.6: Filled-state STM images (a): -2.5 V, 0.1 nA, (b): -2.0 V, 0.1 nA of fully Br-terminated Si(100)- (2×1) surfaces. Each Si dangling bond of the surface is passivated with one Br atom, preserving the dimer rows of the (2×1) reconstruction of the bare surface. A single atomic step runs across the center of (a). Several darker Si dimer vacancies are visible in (b).

Figure 4.6 shows representative filled-state images of a fully Br-terminated Si(100)- 2×1 surface from one of the samples used in this study. A single atomic step is visible running through the image in (a), while (b) shows a magnification of a terrace

in a different area of the surface. The images were acquired after the atomically clean Si(100) surface was exposed to Br₂. Br₂ dissociatively chemisorbs on the surface with each Br atom passivating the single dangling bond of each Si atom and maintaining the (2 × 1) reconstruction of the bare Si surface. The appearance of continuous dimer rows on the surface indicates that the surface is fully Br-terminated as remaining Si dangling bonds would appear bright in comparison. Dark features visible on single-dimer rows in (b) are Si dimer vacancies that were present in the starting Si surface.

Most importantly, this microscopic technique allows us to compare the absolute coverages for halogens and nitrogen on the surfaces investigated.

H-Si(100)	Φ N/Si	7.0 ± 1.0
Cl-Si(100)	Φ Cl/Si	1.0 ± 0.3
	Φ N/Si	1.2 ± 0.1
Br-Si(100)	Φ Br/Si	0.4 ± 0.1
	Φ N/Si	1.4 ± 0.1

Table 4.1: Surface Coverage (Φ) Comparison for the Differently Terminated Si Surfaces before and after Their Reaction with Hydrazine Based on XPS measurements^a

^aOne monolayer refers to the model ideally terminated with the dichloride Si(100) surface.

Table 4.1 summarizes these studies. It assumes that the absolute Cl signal in XPS measurements corresponds to a monolayer of chlorine-containing SiCl₂ species on a Si(100) surface. In other words, this signal is used to indicate the surface structure where one silicon surface atom is bonded to two chlorine atoms. This approach to evaluate the surface coverage results in a relative coverage of 0.5 monolayers for a perfect Br-terminated and fully reconstructed Si(100)-2 × 1 surface prepared in UHV. This is due to half of the Si dangling bonds being eliminated in the formation of the Si

dimers. The absolute signal intensity in the XPS may depend on a number of factors; however, the relative signals (Br/Cl/N) should be very reliable, as long as the recorded spectra reflect the formation of surface species approximately within a monolayer. Based on the results shown in Table 4.1, the chlorine coverage on a Cl-Si(100) surface used in this work is approximately twice that for bromine on Br-Si(100) (confirmed to correspond to one Br to one surface Si by STM), as would be expected for dichloride termination of the Cl-Si(100) surface used in this work. Interestingly, the Cl-Si(100) surface reacted with hydrazine results in an almost perfect one-for-one replacement of every surface chlorine atom with nitrogen. This would correspond to every silicon surface atom being bound to two nitrogen atoms. Even more important is the observation that the Br-Si(100) surface, which has half the halogen centers as Cl-Si(100), after reacting with hydrazine, results in the attachment of approximately the same amount of nitrogen as Cl-Si(100). Although this does not necessarily mean that the species formed on both surfaces are identical (and certainly, the mechanisms could be completely different for monobromide and dichloride interaction with hydrazine), it does show that the reaction of both surfaces with hydrazine leads to the same level of nitrogen incorporation. This last point leads to an important parallel between wet chemistry processing and UHV-prepared surfaces in a reaction with hydrazine: The amount of nitrogen introduced onto the surface in both sets of experiments is approximately the same, despite the differences in surface preparation, initial structure, and chemical composition. This bridge between UHV-preparation surface schemes and solution-based chemistry may be extremely important for monolayer doping.

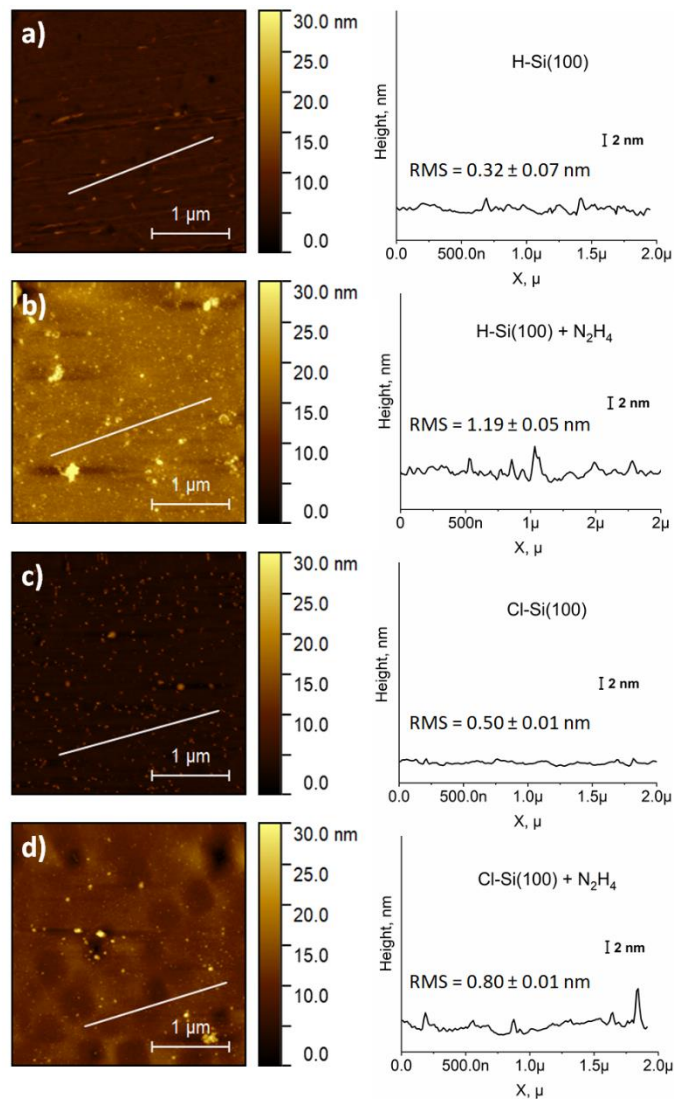


Figure 4.7: Left panels: AFM image of (a) hydrogen-terminated Si(100) and (b) H-Si(100) after the reaction with hydrazine and (c) chlorine-terminated Si(100) and (d) Cl-Si(100) after the reaction with hydrazine. Right panels: Line profiles of each of the AFM images. The RMS was determined for areas of 500×500 nm.

Significantly, the incorporation of nitrogen from hydrazine on the H-Si(100) surface leads to a large increase by nearly an order of magnitude compared to the

halogenated surfaces. This suggests that the reaction of hydrazine with the H-Si(100) surface is more complex and results in additional insertion pathways likely based on etching processes. In order to investigate this possibility, AFM evaluation of the resulting surfaces was undertaken and is summarized in Figure 4.7.

The AFM images in Figure 4.7 a,b) show that the RMS roughness of the H-Si(100) increases after the reaction with hydrazine, indicating that the surface has been altered, probably by etching processes, during the reaction with hydrazine. For comparison, the changes in the morphology of the Cl-Si(100) surface after its reaction with hydrazine are shown in Figure 4.7 c,d). The RMS roughness of the Cl-Si(100) increases only from 0.50 to 0.80 nm, which is consistent with the observation that coverage of chlorine on a Cl-Si(100) surface is approximately the same as coverage of nitrogen on the same surface reacted with hydrazine (in other words, the nearly atomically flat surface remains flat following the reaction, suggesting the displacement or condensation reactions as opposed to etching). The mechanism of possible etching of the H-Si(100) surface by hydrazine is outside the scope of this work. It could involve steps described in previous investigations of high-temperature processes,³⁹ electrochemical etching,¹⁵⁶ possible involvement of partially hydrated surface species,¹⁵⁷ and subsurface nitrogen insertion.¹⁵⁸⁻¹⁶¹ Nevertheless, the end result of incorporating a larger amount of nitrogen in this process as compared to the reaction of hydrazine with the halogenated silicon surfaces may be important for practical applications.

Reactivity of hydrazine with the native oxidized silicon surface is outside the scope of this work, but it is important to note that this reaction does occur and was briefly tested as summarized in Figures B1 and B2 in Appendix B; however, as noted

in this chapter, there is minimal oxidation of the starting surfaces used in this work; therefore, it is not expected to significantly affect the results reported. In addition, to test the stability of the hydrazine-modified Cl– Si(100) surface, it was dipped in deionized water, and the majority of nitrogen remained bound to this surface, although some oxidation did occur as would be expected. This set of experiments is also summarized in Figure B2 in Appendix B.

To provide some molecular-level understanding of the possible chemical processes leading to nitrogen incorporation into halogen-terminated silicon surfaces from hydrazine, a set of computational studies analyzing possible surface species and their stability were performed. The formation and some reactivity of monohalogenide or dihalogenide species on a Si(100) surface have been previously considered in a number of studies including energetics evaluation by STM¹⁶² and first-principle calculations,¹⁴⁷ and interaction of an ideal mono-chloride-terminated surface with ammonia.¹⁴² The brief investigation summarized below focuses on the monobromide species of Br–Si(100) and dichloride species of Cl–Si(100), which were suggested by the experimental investigation. In this analysis, the formation of HCl (which could be possible in a gas phase process) leads to the immediate formation of the ionic complex with excess hydrazine. This additional reaction step results in extra stabilization (exothermicity) for each reaction considered.

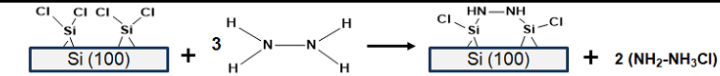
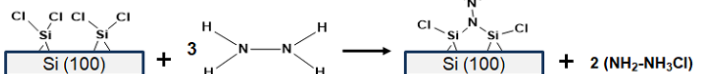
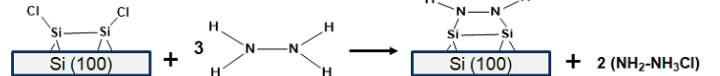
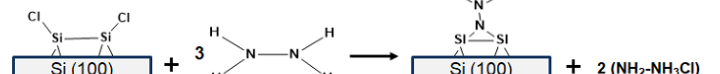
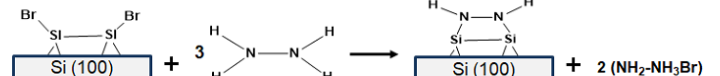
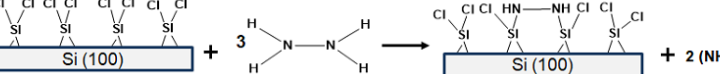
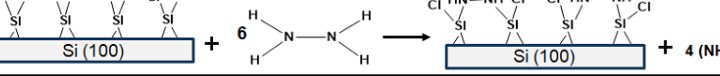
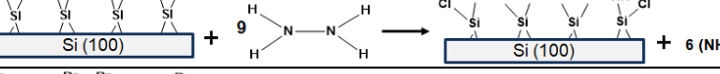
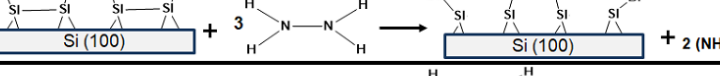
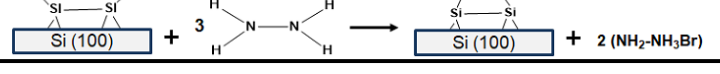
Reaction		Cluster model	Energy (KJ/mol)
A)		Si ₉ H ₁₂	-91.8
B)		Si ₉ H ₁₂	-127.0
C)		Si ₉ H ₁₂	72.0
D)		Si ₉ H ₁₂	140.3
E)		Si ₉ H ₁₂	161.4
F)		Si ₂₁ H ₂₄	-165.1
G)		Si ₂₁ H ₂₄	-216.3
H)		Si ₂₁ H ₂₄	-306.5
I)		Si ₂₁ H ₂₄	235.7
J)		Si ₂₁ H ₂₀	159.0

Table 4.2: Thermodynamic Requirements for the Reaction of Hydrazine with Single-Dimer (Si₉H₁₂), Two-Dimer (Si₂₁H₂₄), and Three-Dimer (Si₂₁H₂₀) Clusters.

From the results summarized in Table 4.2, it is immediately apparent that the reaction of hydrazine is more favorable when the surface is terminated with dichloride (see reactions A, B, F, G, and H) than when the surface is terminated with monochloride (reactions C and D) or monobromide (reactions E, I, and J) where endothermic energy changes are predicted. In addition, these model calculations show that the energy required to attach one, two, and three molecules of hydrazine simultaneously to the Cl-Si(100) surface as -165.1 KJ/mol with one hydrazine attached (reaction F), -216.3

KJ/mol with two hydrazine molecules attached (reaction G), and -306.5 KJ/mol with three hydrazine molecules attached to the silicon surface (reaction H), respectively. Thus, there is a profound thermodynamic driving force for the formation of the surface fully covered with hydrazine starting from the dichloride-terminated Si(100) surface. The hydrazine can be attached to the surface with its N–N bond parallel to the Si–Si dimer (reactions A and C) or perpendicular to it (reactions B and D), based on the results in Table 4.2, with both possibilities ultimately leading to the formation of a surface where each chlorine atom is replaced with a nitrogen atom of a hydrazine molecule. In other words, these models are fully consistent with the XPS observations reported above. Again, although both species are predicted to be thermodynamically stable, XPS suggests that the model with the N–N bond parallel to the surface (reaction A) is most likely the dominant one on these Si(100) surfaces.

As noted above, it is unlikely that the reaction of hydrazine with Br–Si(100) surfaces proceeds by a simple substitution of every two surface bromine atoms with nitrogen atoms from a single hydrazine molecule, since the coverage of nitrogen in the case of a monobromide-covered surface is the same as in the case of dichloride on a Cl–Si(100) surface. This suggests that the reaction mechanism on a Br–Si(100) surface is different from that on a Cl–Si(100) surface. In fact, all the computational attempts to evaluate the energy required to make the hydrazine-reacted Si(100) surface starting with monobromide resulted in strongly endothermic processes (E, I, J), perhaps suggesting that fundamentally different reactions drive the interaction of hydrazine with a Br–Si(100) surface. However, one interesting point of this computational set of studies is that the Si–Cl bonds in similar structures to those with the Si–Br bond are more

reactive and lead to less endothermic processes (for example, one can compare reactions C and E).

Importantly, there are a number of exothermic reactions with Cl–Si(100) models consistent with the products observed in this work, as opposed to the products previously reported for ammonia^{110,132} and hydrazine reactions¹¹⁰ with the Cl-terminated Si(111) surface, where all the proposed species were the results of endothermic processes.

4.4 Conclusion

Within this chapter, silicon surfaces terminated with H, Cl, and Br underwent reaction with anhydrous hydrazine through solution-phase chemistry. In all cases, the reaction resulted in the formation of a direct Si-N bond. Even though the chlorine-terminated surface and bromine-terminated surface followed different preparation procedures that resulted primarily in the formation of dichloride- and monobromide-covered surfaces, respectively, they lead to a similar surface coverage of nitrogen following the reaction with hydrazine. The H–Si(100) surface apparently undergoes more complicated reactions rather than condensation processes resulting in surface roughening. According to the DFT investigations, the energy requirement for the hydrazine reaction with halogen-terminated silicon is more favorable when the surface is terminated with dichloride, and there is a substantial thermodynamic driving force for the formation of a fully reacted surface where each silicon surface atom is connected with two nitrogen atoms from the hydrazine. Despite the differences in preparation, initial structure, and chemical composition for Br–Si(100) and Cl–Si(100) surfaces used in this work, both surfaces exhibit similar nitrogen coverage following the reactions with hydrazine. Thus, the mechanism of nitrogen incorporation in monohalide- and

dihalide-covered silicon surfaces requires further investigation; however, the goal of controlled nitrogen introduction to the silicon surface for further practical applications is achieved and can provide a bridge for engineering processes that utilize solution chemistry and UHV methods for the preparation of selectively terminated silicon surfaces.

Chapter 5

SOLUTION CHEMISTRY TO CONTROL BORON-CONTAINING MONOLAYERS ON SILICON: REACTIONS OF BORIC ACID AND 4-FLUOROPHENYLBORONIC ACID WITH H- AND Cl-TERMINATED Si(100)

5.1 Abstract

In this chapter, the interactions between boric acid and 4-fluorophenylboronic acid with H- and Cl-terminated Si(100) surfaces were explored using solution-phase chemistry. X-ray photoelectron spectroscopy (XPS) studies reveal that both molecules react preferentially with Cl-Si(100) and not with H-Si(100) at identical conditions. On Cl-Si(100), the reactions introduce boron onto the surface, forming a Si-O-B structure. The quantification of boron surface coverage demonstrates that the 4-fluorophenylboronic acid leads to ~2.8 times higher boron coverage compared to that of boric acid on Cl-Si(100). Consistent with these observations, density functional theory studies show that the reaction of boric acid and 4-fluorophenylboronic acid is more favorable with the Cl- versus H-terminated surface and that on Cl-Si(100) the reaction with 4-fluorophenylboronic acid is ~55.3 kJ/mol more thermodynamically favorable than the reaction with boric acid. The computational studies were also used to demonstrate the propensity of the overall approach to form high-coverage monolayers on these surfaces, with implications for selective-area boron-based monolayer doping. The material in this chapter is based on a published manuscript¹¹.

5.2 Introduction

The process of organic modification of inorganic surfaces holds significant relevance and versatility across diverse applications. Among these applications are ultra-shallow doping, materials design, sensing, photovoltaics, and many others.^{2,74,75,163} The majority of current surface modification approaches rely on anchoring the organic molecules to the desired surface via specific functional groups.¹⁶⁴ For example, carboxylic and phosphonic acids, nitro- and nitroso functional groups, as well as various silicon-based functionalities, such as silanes or siloxanes, have been employed for surface modification of a wide variety of materials.^{98,121,165–167} Additionally, in some recent investigations, boron-containing functional groups have also been explored, especially when the electrical properties of the interfaces created are targeted.^{81,168} Many of these approaches have also been used to introduce high surface concentrations of desired elements for ultra-shallow doping using monolayer doping. In this case, a precise concentration of an element needed for the application is introduced chemically by the monolayer reactions and then treated thermally or photochemically to produce ultra-shallow doping profiles required for microelectronics.^{3,77,80,81} Monolayer reactions of N-,¹⁶⁹ P-,¹⁶⁵ and B-containing^{12,81} molecules have been explored for this purpose.

The investigations of the chemistries of boron-containing molecules on chemically functionalized semiconductor surfaces are limited. Dilute solutions of boric acid have been utilized for solar cell applications, where boron doping is required;^{170,171} however, in these reports boric acid was used only as a component for spin coating, and the process was followed by high-temperature annealing, with no surface reactions investigated. A molecular-level investigation of boric and boronic acids was reported to direct growth of thin films of polydopamine on solid surfaces, including commercial

Si(111) wafers.¹⁷² However, this investigation was focused on the interaction of boric acid with catechol moieties of dopamine rather than with the surfaces themselves. Phenylboronic and fluorinated phenylboronic acids can serve as attractive spectroscopic and chemical labels. These compounds in solution have been used to modify organic monolayers prepared on silicon,^{173,174} metal oxides,^{175,176} and metals.^{177,178} The boronic acid functionality ($-B(OH)_2$) has high affinity for diols and can be used for selective biosensing in nucleic acid recognition and sugar or glycoprotein detection.^{173,175,177,178} The fluorinated phenylboronic acid can enhance the electron transport properties because of the presence of π -conjugated structure of the phenyl group, and the boronic acid group can be easily chemically bonded to the surface of oxide materials, such as TiO_2 .¹⁷⁵ However, understanding the chemical interaction of the $-B(OH)_2$ functionality with modified silicon surfaces leading to the direct formation of B–Si or B–O–Si linkages is lacking. Among other sources of boron for ultra-shallow doping processes, BCl_3 has been considered. Recently, the solution chemistry of BCl_3 has been investigated on silicon surfaces terminated with hydrogen or chlorine.¹² A mechanistic understanding of that process was, however, complicated by partial oxidation of surface species in ambient and also possible etching processes. The reactions of boric and boronic acids on silicon surfaces may also shed light onto the formation of oxidized surface boron species that are produced in other boronation approaches.

This chapter compares the reactivity of solutions of boric acid ($B(OH)_3$) and 4-fluorophenylboronic acid ($F-C_6H_4-B(OH)_2$) with Si(100) surfaces terminated with chlorine (Cl–Si(100)) or hydrogen (H–Si(100)). The presence of fluorine atoms in 4-fluorophenylboronic acid allows for quantitative experiments using X-ray photoelectron spectroscopy and allows for an additional tracking label.¹⁷⁹ The reactivity, efficiency,

and thermodynamics of the reactions of boric and boronic compounds with H-Si(100) and Cl-Si(100) are investigated. The reaction conditions allowing controlled introduction of boron-containing functionalities to differently terminated silicon surfaces are compared, suggesting a pathway for selective-area monolayer doping.

5.3 Results and discussions

All materials used in this chapter can be found in chapter 2, section 2.2.1.

The AFM images were obtained as described in section 2.1.5. And the XPS analysis was performed as described in section 2.1.1. To quantify surface coverages of boron, an overlayer model was used, using the same equation as in section 3.4, with the following assumptions:

(1) A monolayer is defined for Cl-Si(100) as a surface covered by dichloride species (2 chlorine atoms per 1 silicon surface atom);¹³

(2) Following the reaction with boric acid and 4-fluorophenylboronic acid, two atoms of chlorine are replaced by a molecule of boric or boronic acid to form an ideal termination. This will be equivalent to one atom of boron per one atom of silicon, therefore forming nominally half a monolayer.

This chapter aims to investigate the reactivity, efficiency, and thermodynamics of the reactions involving boric and boronic compounds with H-Si(100) and Cl-Si(100). Furthermore, this research explores the reaction conditions that enable the controlled introduction of boron-containing functionalities to differently terminated silicon surfaces, suggesting a pathway for selective-area monolayer doping.

Figure 5.1 summarizes the experimental procedure followed for the preparation of the H- and Cl-terminated surfaces (described in sections 2.1.2 and 2.1.5 respectively)

and the subsequent reactions with 4-fluorophenylboronic acid and boric acid (described in sections 2.1.7 and 2.1.8 respectively) by solution chemistry.

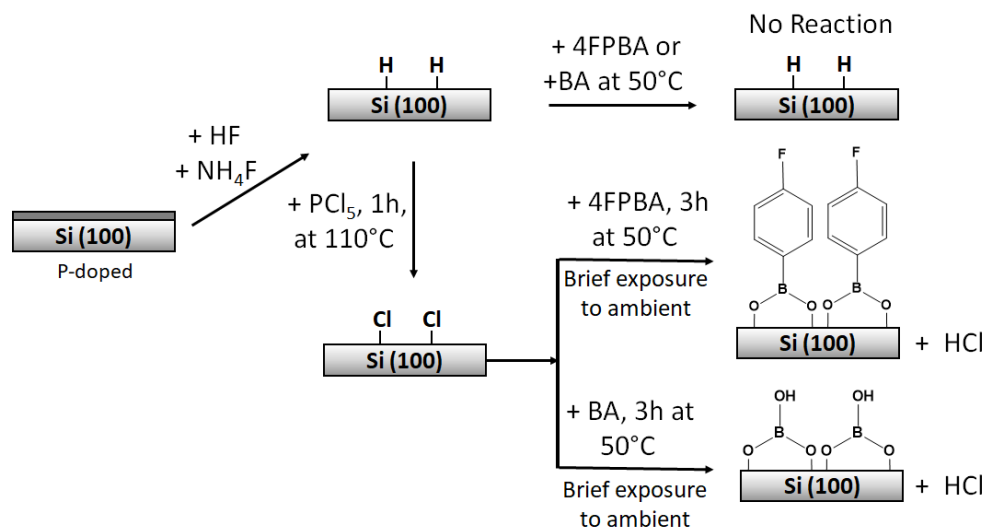


Figure 5.1: Schematic Comparison of the Reaction of 4-Fluorophenylboronic Acid (4FPBA) and Boric Acid (BA) with Cl-Terminated and H-Terminated Si(100) Surfaces

For the reaction of boric and boronic acids with Cl-Si(100), an optimization of conditions was performed (summarized in Figures C1 and C2 in Appendix C) with 50 °C selected as the best temperature for both reactions and HCl as the byproduct. At this optimized temperature, the reactions show the highest intensity of boron and fluorine (in the 4-fluorophenylboronic acid) XPS signals on the surface of the Cl-terminated Si(100) and also indicate lowest surface oxidation. A comparison between the reactivity of the H- and Cl-terminated surfaces was studied for both reactions, and it was shown that the H-terminated surface does not react with the boric and 4-fluorophenylboronic

acids, as there was no evidence of boron introduction in both cases within the range of reaction conditions investigated, as shown later in this chapter.

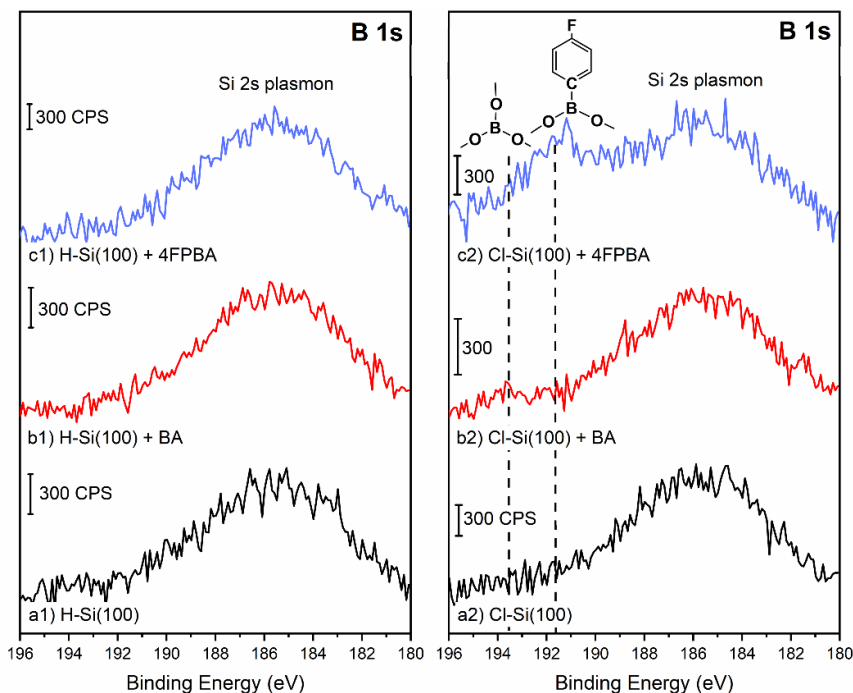


Figure 5.2: XPS spectra of B 1s spectral region (showing a Si 2s plasmon feature). The left panel shows the (a1) H-terminated Si(100) as the starting point, (b1) H-Si(100) after the reaction with boric acid (BA) at 50 °C for 3 h and, (c1) H-Si(100) after the reaction with 4-fluorophenylboronic acid (4FPBA) at 50 °C for 3 h; and the right panel shows the (a2) Cl-terminated Si(100) as the starting point, (b2) Cl-Si(100) after the reaction with boric acid at 50 °C for 3 h, and (c2) Cl-Si(100) after the reaction with 4-fluorophenylboronic acid at 50 °C for 3 h.

Figure 5.2 compares the B 1s spectral regions before and after the reaction of H- and Cl-terminated Si(100) surfaces with boric acid and 4-fluorophenylboronic. The left panel summarizes the reactions on H-Si(100) in plots a1, b1, and c1. Only the broad peak corresponding to the Si 2s plasmon is present at 186 eV with no evidence of boron

observed after the reaction of H-Si(100) with boric acid or 4-fluorophenylboronic acid. In the right panel, the Si 2p plasmon is also observed at approximately 186 eV on unreacted Cl-Si(100) (a2). Following the reaction with boric acid, in addition to the plasmon feature, there is also a clearly recorded B 1s feature at 193.5 eV corresponding to B-O_x species.^{12,101-103} After reaction with 4-fluorophenylboronic acid, the B 1s peak is also observed, but it is shifted to lower binding energy at 191.8 eV. This difference can be explained by the reactions summarized in Figure 5.1. Specifically, the surface species expected to form during the reaction of boric acid with Cl-Si(100) have a general structure with a BO₃ fragment. The reaction of the same surface with 4-fluorophenylboronic acid molecules is expected to produce surface species with one C-B bond and two O-B bonds. The higher electronegativity of an oxygen atom is expected to shift toward a higher binding energy of the resulting species compared to the species containing C-B bond. Qualitatively, this shift in binding energy is also confirmed in the computational models where the position of the B 1s feature in the model systems with boric acid and 4-fluorophenylboronic acid molecules was found to be ~193.8 and ~193.1 eV, respectively. The computationally predicted difference is smaller than that experimentally recorded, but that could probably be explained by a limited number of available experimental and calibration points for B1s.

	Relative B/Si coverage (Φ) on Cl-Si(100)	Ratio C/F	Ratio B/F
4-Fluorophenylboronic Acid	0.57 ± 0.07	6.20 ± 0.20	0.70 ± 0.07
Boric acid	0.20 ± 0.02

Table 5.1 Comparison of the Relative B/Si Coverage (Φ) on Cl-Si(100) after the Reaction with 4-Fluorophenylboronic Acid and Boric Acid at 50 °C, Calculated by

Using the Overlayer Model; C/F and B/F Ratios after the Reaction with 4-Fluorophenylboronic Acid at 50°C.

The relative B/Si surface coverage was calculated with the overlayer model described elsewhere,^{6,12} and the results of this analysis are summarized in Table 5.1. This comparison shows that the boron coverage is approximately 2.8 times higher for the reaction of Cl-Si(100) with 4-fluorophenylboronic acid compared to boric acid.

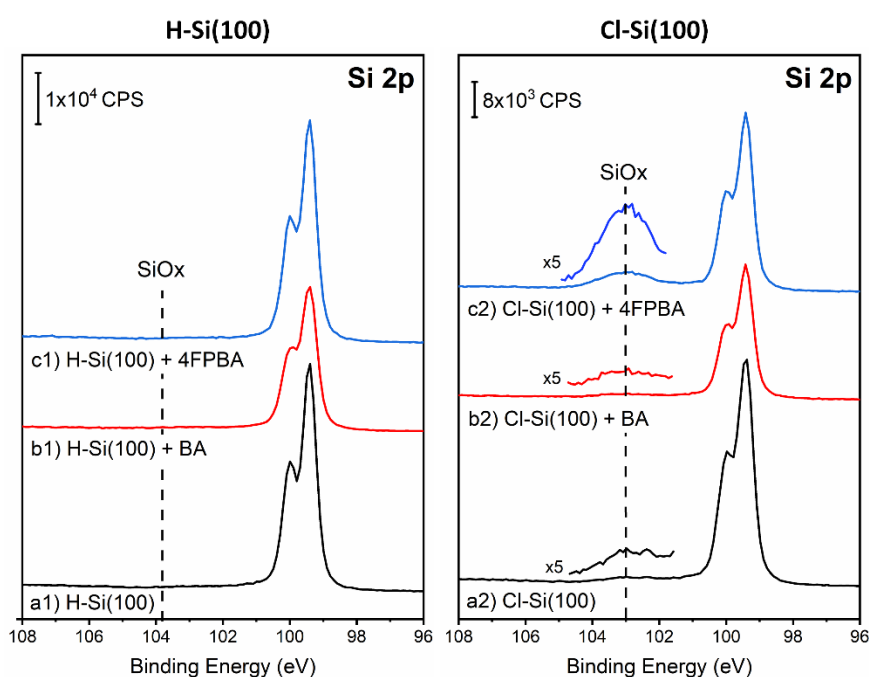


Figure 5.3: XPS spectra of Si 2p spectral region. The left panel shows the (a1) H-terminated Si(100) as the starting point, (b1) H-Si(100) after the reaction with boric acid (BA) at 50 °C for 3 h, and (c1) H-Si(100) after the reaction with 4-fluorophenylboronic acid (4FPBA) at 50 °C for 3 h; and the right panel shows the (a2) Cl-terminated Si (100) as the starting point, (b2) Cl-Si(100) after the reaction with boric acid at 50 °C for 3 h, and (c2) Cl-Si(100) after the reaction with 4-fluorophenylboronic acid at 50 °C for 3 h.

Figure 5.3 shows the XPS spectra of the Si 2p spectral region for the H- and Cl-terminated Si(100) surfaces before reaction and after the reactions with boric acid and 4-fluorophenylboronic acid. The H-terminated surface (a1) shows the characteristic Si 2p_{3/2} bulk peak at 99.4 eV and the absence of oxidation. Following the reaction of H-Si(100) with boric acid (a2) and 4-fluorophenylboronic acid (a3), the spectra do not change noticeably within the range of conditions studied. The Cl-terminated Si(100) surface also shows the intense Si 2p_{3/2} feature at 99.4 eV corresponding to the silicon crystal and a very small peak at around 103 eV corresponding to the Si-O_x species from the brief exposure to ambient conditions upon transfer to the XPS chamber after the monolayer formation. The formation of Si-Cl_x species can be confirmed by fitting the spectra according to previous investigations within the Si 2p spectra region;^{13,153} however, the Cl 2p region is more informative to confirm the reaction (Figure C3 in Appendix C shows a nearly complete removal of surface chlorine from the Cl-Si(100) surface in reactions with both boric acid and with 4-fluorophenylboronic acid). Following the reaction of this surface with boric acid (plot b2 in Figure 5.3), it can be noticed that the peak at higher binding energy corresponding to SiO_x species at approximately 103 eV is slightly increased and is significantly higher in intensity for the same surface reacted with 4-fluorophenylboronic acid (plot c2 in Figure 5.3). This is consistent with high coverage of 4-fluorophenylboronic acid on this surface following the reaction, as discussed further. Specifically, at this high coverage the reaction described in Figure 5.1 leads to the formation of Si-O linkages, similar to the formation of surface oxide. Some of the potential processes will be discussed with the help of computational investigations described in Tables 5.2 and 5.3.

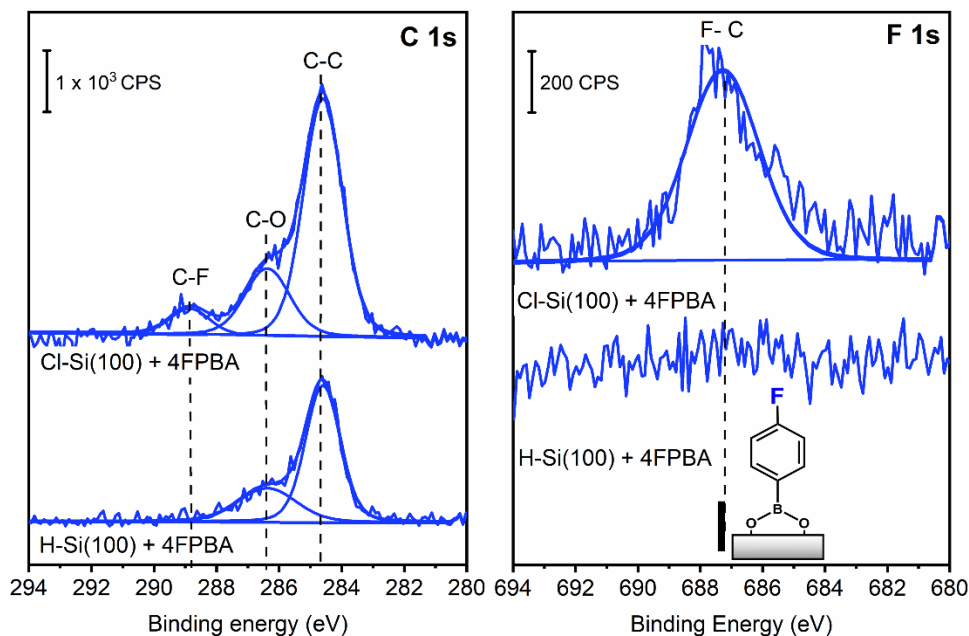


Figure 5.4: The left panel shows the XPS spectra of C 1s spectral region for the H- and Cl-Si(100) surfaces after the reaction with 4-fluorophenylboronic acid (4FPBA) at 50 °C for 3 h. The right panel shows the XPS spectra of F 1s spectral region for the H- and Cl-Si(100) surfaces after the reaction with 4-fluorophenylboronic acid at 50 °C for 3 h. The computationally predicted result is shown as a solid vertical bar underneath the experimental data.

The structure of 4-fluorophenylboronic acid offers an opportunity to complement the surface coverage studies based on the B 1s spectral region with an investigation of the carbon and fluorine chemical environments. Figure 5.4 shows the representative XPS spectra of C 1s and F 1s for H and Cl-Si(100) following the reaction with 4-fluorophenylboronic acid. Although the C 1s spectral region may be affected by the presence of adventitious carbon that could be accumulated during the brief exposure of the sample to ambient conditions during its transfer to the XPS setup, the left panel of Figure 5.4 shows three main peaks for Cl-Si(100) and two main peaks for H-Si(100).

The peak at 284.6 eV corresponds to the C–C bonds, and the feature at 288.9 eV, present only on Cl–Si(100), indicates the presence of a C–F functionality in a fluorophenyl group in this molecule.^{61,174,180–182} The peak at 286.2 eV also corresponds to adventitious carbon. The F 1s spectral region can be fitted with a single peak at 687.1 eV, consistent with the typical value for C–F species^{174,182,183} for the Cl-terminated surface, while this feature is not present on the H-terminated surface. The computationally predicted (in this work) F 1s peak for the models describing the 4-fluorophenylboronic acid molecule attached to the Si(100) is at 687.3 eV, which agrees well with the experimental results and is in agreement with fluorine label bound to organic functional group.¹⁸⁴ In order to know if the fluorine atom in the 4-fluorophenylboronic acid affects the reactivity with the Cl–Si(100), computational calculations with a molecule of phenylboronic acid attached to a dichloride terminated Si(100) were performed (Table 8.3 in Appendix C), and the results show that fluorine substitution does not substantially affect the reactivity of the 4-fluorophenyl boronic acid compared to the phenylboronic acid in this process. The molecular coverage calculated based on B concentration can be reevaluated independently based on the presence of C, B, and F in the 4-fluorophenylboronic acid molecule reacting with Cl–Si(100). The C/F and B/F ratios are provided in Table 5.1. The C/F ratio is expected to be 6, because the 4-fluorophenylboronic acid molecule has 6 carbon atoms in the phenyl ring and 1 fluorine atom, and the B/F ratio is expected to be 1 because there is only 1 boron atom per molecule. The experimental ratios obtained are fully consistent with these expectations, with the C/F ratio being just slightly higher than 6, likely because of adventitious carbon present, as discussed previously, and the B/F ratio was found to be slightly lower than expected. The small underestimation is

possibly due to screening of the B atoms attached directly to the surface by the phenyl groups.

It is interesting to note that the reaction of Cl-Si(100) with both boric acid and 4-fluorophenylboronic acid leads to nearly complete removal of surface chlorine (Figure C3 in Appendix C) despite the fact that the boron coverage following the reaction with boric acid is nearly three times lower than that with 4-fluorophenylboronic acid, suggesting that the overall reaction mechanisms are quite different. Given complete chlorine removal in both cases, it appears that in the case of boric acid, the reaction is more complicated and leads to surface oxidation and chlorine removal even without attachment of boron-containing functionalities. The AFM images summarized in Figure C4 in Appendix C demonstrate that surface roughness does not change substantially following the chemical modification of the surface investigated here, supporting the absence of etching processes. To better understand the basic thermodynamics of the simplest reactions of H-Si(100) and Cl-Si(100) with boric and boronic acids, a set of computational studies were performed. This investigation is summarized below in Tables 5.2 and 5.3 and targets the dihydride species for H-Si(100) and dichloride species for Cl-Si(100), which are expected to be the major species on the respective solution-prepared surfaces.^{12,99,149} This computational modeling is also fully consistent with the previously described computational characterization of BCl₃¹² and N₂H₂¹³ reactions with selectively terminated Si(100) surfaces.

Reaction		Energy (KJ/mol)
A		-86.2
B		-180.5
C		-209.8
D		-246.5
E		-18.2

Table 5.2: Thermodynamic Requirements for the Reaction of 4-Fluorophenylboronic Acid with a Functionalized Si(100) Surface Represented by a Si₁₂₁H₂₄ Cluster

Reaction		Energy (KJ/mol)
F		-65.8
G		-125.2
H		-166.5
I		-186.7

Table 5.3: Thermodynamic Requirements for the Reaction of Boric Acid with a Functionalized Si(100) Surface Represented by a Si₂₁H₂₄ Cluster

Tables 5.2 and 5.3 show the model reactions of boric acid and 4-fluorophenylboronic acid with H-Si(100) and Cl-Si(100) leading to the formation of stable surface species and a loss of H₂ or HCl, respectively. The dehydration reaction that would eliminate water and form direct Si-B bonds was not considered, because in that case the experimental B 1s and Si 2p signatures of boron-containing species would be much more shifted toward lower binding energy,^{12,108,185} which is not observed. However, additional studies of the more complex reactions of boric acid with

Cl-Si(100) may be needed to understand the substantially lower boron coverage compared with the 4-fluorophenylboronic acid reaction. Given that the XPS measurements are performed not in situ in ultrahigh vacuum but following solution chemistry reactions and subsequent transfer in air, the silicon surface reacted with boric acid may be a subject to further oxidation (without substantial silicon oxidation) and boron removal by the time the measurement is performed in this work. This process could be more efficient than in the case of stable and bulky 4-fluorophenylboronic surface adduct. Nevertheless, a number of important conclusions can be reached based on the proposed, exothermic reactions summarized in Tables 5.2 and 5.3. Upon comparison of reactions A and B, the reaction of 4-fluorophenylboronic acid on Cl-Si(100) surface is significantly more thermodynamically favorable than on H-Si(100); the energy required for the attachment of one molecule of 4-fluorophenylboronic acid is -180.5 kJ/mol on the chlorinated surface compared to the -86.2 kJ/mol on H-Si(100). A structure where a boronic acid functional group reacts with a single dichloride species on Cl-Si(100) surface (structure E in Table 5.2) has also been examined; however, this structure is much less stable than the other ones considered, with the stabilization of only 18.2 kJ/mol. Thus, it was not considered further. Given the similarities in the bond strengths of H-H (435.99 D^o₂₉₈/kJ/mol) and H-Cl bonds (431.62 D^o₂₉₈/kJ/mol),¹⁸⁶ most of the thermodynamic driving force for the formation of the surface species originates from the difference in Si-H and Si-Cl bond strengths for initial H-Si(100) and Cl-Si(100) surfaces, respectively. The same comparison can be done with the reactions F and G, in this case with one molecule of boric acid attached to hydrogenated and chlorinated surfaces, where both processes are also exothermic, and the chlorinated surface leads to a more thermodynamically favored

reaction. In the case of boric acid, the thermodynamic driving force is much lower than that for 4-fluorophenylboronic acid on both H-Si(100) and Cl-Si(100). These computational results agree with the experimental results described above. On the chlorinated surfaces, under the same conditions, the amount of boron introduced is higher when the surface is reacted with 4-fluorophenyl boronic acid than when it is reacted with boric acid. This is consistent with the observation that the reaction with 4-fluorophenylboronic acid is 55.3 kJ/mol more favorable than the reaction with boric acid. The difference can most likely be explained by the electron-withdrawing nature of the fluorophenyl group; however, the effect may require further investigations.

It should be noted that the reactions A, B, F, and G provide some information about the proposed reactions at low coverage; however, given the high coverage estimates provided in Table 5.1, it is expected that attached surface species will interact and change the thermodynamic driving force for subsequent attachment. Reactions C, D, H, and I in Tables 5.2 and 5.3 show the relative energies of dichloride-terminated surfaces reacted with two and three molecules. These model calculations show that the exothermicity of a reaction to attach two and three molecules of 4-fluorophenylboronic acid is -209.8 and -246.5 kJ/mol, respectively, and the exothermicity of a similar process for boric acid is -166.5 kJ/mol for two molecules and -186.7 kJ/mol for three. Of course, the limited size of the cluster models may raise issues with the “high coverage” comparison, especially because these models already show the difference between attachment thermodynamics toward the middle of the cluster compared to the replacement at the end. To address this problem, a number of additional calculations have been performed to follow the attachment process to different dimers of the same cluster, and the summary of this work is presented in Table 8.2 in Appendix C. On the

basis of this comparison, it is clear that despite some differences in modification of different reactive sites on Cl-Si(100) model cluster, the general trends highlighting the more exothermic reaction for 4-fluorophenylboronic compared to that of the boric acid and also the thermodynamic propensity for high coverage formation for both of these compounds are confirmed. Further studies will be required to investigate the kinetic requirements for both modifications; however, it is clear that relatively high coverages of B-containing functionality can be obtained in both cases, especially with a boronic functional group. This observation is important both for a direct modification of silicon with B-containing compounds and for further work in using boronic functional group to functionalize silicon surfaces. If a high coverage of boronic acids is possible on Si(100), this chemical approach can be generalized to include other functionalities instead of a fluorination that was used in this work as a spectroscopic label.

5.4 Conclusions

The findings presented in this chapter demonstrate that both 4-fluorophenylboronic acid and boric acid exhibit selective reactivity with the Cl-terminated Si(100) surface in contrast to the H-terminated Si(100) surface. The 4-fluorophenylboronic acid reaction with Cl-Si(100) results in boron coverage ~ 2.8 times higher compared to the similar process with boric acid within the range of conditions investigated. The structure of the 4-fluorophenylboronic acid molecule allows for an efficient quantification of surface coverage based on F and C spectral regions and confirms the findings obtained based on the presence of boron on the surfaces. Furthermore, the computational studies show and confirm that the reactions of boric acid and 4-fluorophenylboronic acid are more thermodynamically favorable with the Cl-Si(100) surface compared to the H-Si(100) surface and that the thermodynamic

driving force is greater for the reaction of 4-fluorophenylboronic acid than that of boric acid. In addition, computational studies suggest that the thermodynamics favors high coverages resulting from the reactions of both molecules with Cl-Si(100).

Based on this work, pathways for boron-based monolayer doping, surface chemical passivation, and secondary functionalization of silicon surfaces can be proposed:

(1) Boron-containing functionalities may be attached selectively at Cl-Si surface sites versus H-Si sites on the same substrate, providing a path for selective-area monolayer doping;

(2) The surface boron concentration can be controlled (although further work on removing carbon-containing fragments from the surface modified with boronic acids will be needed);

(3) The reactivity of surfaces modified with boronic acid can be manipulated;

(4) Silicon surface functionalization using boronic acids can be used for further functionalization by replacing the -F functionality used in this work for spectroscopic identification with a different reactive entity.

Overall, this work helps to pave a path to novel applications of B-containing functionalities for modification of silicon surfaces.

Chapter 6

ATTACHMENT CHEMISTRY OF 4-FLUOROPHENYLBORONIC ACID ON TiO₂ AND Al₂O₃ NANOPARTICLES

6.1 Abstract

This chapter explores the surface modification of nanoparticulate TiO₂ and Al₂O₃ materials using 4-fluorophenylboronic acid. The objective is to assess novel surface modification schemes and develop spectroscopic labels for characterizing the modified surfaces. The chemistry of the modification is followed on all these surfaces using X-ray photoelectron spectroscopy, multinuclear (¹¹B, ¹⁹F, and ¹³C) solid-state and solution NMR, and infrared spectroscopy to determine the binding modes of this compound using boron and fluorine as probe atoms. Density functional theory model calculations are utilized to visualize predicted surface species and to interpret the results of spectroscopic measurements. A comparison is made among TiO₂ rutile, TiO₂ anatase, and γ -Al₂O₃. On all three materials, the modification proceeds via the boronic functional groups, with metal oxide-controlled surface chemistry. The bonding configuration depends on the material and is dominated by a monodentate species for titania and by bidentate species for alumina. The surface structures determined to form on all the oxide semiconductors investigated suggest that sensitization or monolayer doping approaches with a well-defined chemical interaction via a boronic functionality can be developed. The material in this chapter is based on a published manuscript¹⁴.

6.2 Introduction

The quantitative characterization of surface chemistry heterogeneity in particle systems continues to be a challenge. The exploration of new advanced particle systems, featuring controlled composition, mixed materials, and diverse surface patchiness, requires the development and characterization of innovative surface chemical probes. Metal oxide particles are produced at the highest volumes and are also employed in the most diverse cross-section of applications compared to other commercial particle types. These applications span from microelectronics, energy and aerospace technologies to biomedical and agricultural applications. Because of such a variety of applications, new surface chemical modification schemes are always in demand for these materials; however, the chemistry itself is often difficult to follow without specifically designed spectroscopic labels. Ideally, this chemistry is expected to be robust and at the same time selective with respect to the specific surfaces and materials, and the spectroscopic probes are required to be easily identifiable. Overall, different approaches using molecular probes are a useful tool for investigating the surface properties of materials. For example, among the universal surface probes for metal oxides is the reaction with alcohols. Methanol chemisorption has been used to quantify the surface active sites of metal oxide catalysts¹⁸⁷ as well as to determine their surface area.¹⁸⁸ Surface carboxylate formation has been extensively studied on TiO₂ as well.^{189–191} However, since these carbon-based molecular probes have the same elements as common impurities and solvents, it is also often difficult both to pinpoint the chemical mechanisms of surface modification and to quantify the formation of surface species. Thus, a search for the solutions for both of these issues is always ongoing. One of the

approaches would be to combine a functional group that contains a unique spectral identifier with an independently identifiable spectroscopic “tail” label for the same molecule.

In developing novel labeling approaches to understand the chemistry of nanomaterials, one may consider the number of analytical tools, and most of the time, several of those have to be used simultaneously for unambiguous assignment of chemical interactions. Among those spectroscopic tools, X-ray photoelectron spectroscopy (XPS) and infrared (IR) spectroscopy have been used extensively.¹⁹² However, they often can only provide limited chemical information that has to be supplemented by other techniques. Recently, solid-state NMR (ss-NMR) has emerged as a reliable tool that can be used to understand the surface chemistry of nanomaterials. For example, ¹⁹F NMR labeling is often used in biological systems.^{193–195} Fluorine is an excellent probe due to its nuclear spin of 1/2, high sensitivity, and high natural abundance.¹⁹⁶ Another reliable and unique NMR probe is based on boron. ¹¹B is undoubtedly an excellent spectroscopic probe, being a high-abundant quadrupolar nucleus, which has been used extensively to follow complex transformations of heterogeneous catalytic systems.¹⁹⁷ Based on this brief assessment, it would be useful to utilize a functional group containing boron and a “tail” structure containing fluorine to probe the surface chemistry of nanomaterials and to propose novel surface binding functionalities.

A highly promising but not fully explored choice for the attachment group would be boronic functionality (R-B(OH)₂). Boronic acid has traditionally been used in organic halide cross-coupling reactions to form carbon–carbon bonds, most notably the Suzuki–Miyaura reaction.¹⁹⁸ It has also proved useful in the catalytic transformations

of organic molecules with various functionalities such as carboxylic acids, amines, and alcohols.¹⁹⁹ In recent studies, boronic acid applications have been expanded to include metal oxide attachments.²⁰⁰ Boric and boronic acids can be used both to deliver boron as a desired dopant and to sensitize the oxide nanomaterials. The attachment of boric acid ($\text{B}(\text{OH})_3$) to TiO_2 has been a topic of interest for applications in dye-sensitized solar cells. Boron doping of TiO_2 has been shown to lead to a higher photocatalytic activity compared to that of bare TiO_2 .^{201,202} A computational study from Raghunath and Lin²⁰³ explored various bidentate and monodentate attachments of $\text{B}(\text{OH})_3$ to a clean TiO_2 anatase (101) surface. The functionalized boronic acids, such as phenylboronic derivatives, have been shown to improve the properties of organic solar cells.^{204–206} They appear to enhance the electronic contact between the TiO_2 layer and the conductive organic layer in solar cells. Boronic acids overall are quite attractive chemical modifiers because they tend to have low toxicity, are inexpensive, and are insoluble under aqueous environments, all of which are beneficial characteristics for solar cell applications. However, their attachment chemistry on TiO_2 has not been investigated.

Anatase TiO_2 is heavily studied for photocatalysis because of its high activity as an indirect band-gap semiconductor.^{207–210} Rutile TiO_2 , while less investigated, is promising due to its superior thermal stability²¹¹ and photocatalytic activity for water splitting.²¹² In order to maximize the photocatalytic effect, modifications are being made such as morphological changes²¹³ and doping methods.^{214,215} Among other oxide nanomaterials, the properties of boron-modified alumina are of interest,²¹⁶ primarily as efficient catalysts in hydrocarbon reforming.^{217,218} However, further applications would

be much more developed if the chemistry of boronic acid attachment were understood better.

The objectives in this chapter are two-fold. First, we will test a molecular probe that has unique spectroscopic labels in its functional group (boron) and in its “tail” (fluorine) in a reaction with common oxide nanomaterials (TiO_2 and Al_2O_3). Such an approach should allow for independent verification of attachment chemistry on different materials and spectroscopic label introduction that is expected to depend on surface chemistry, paving the way to what is sometimes referred to as multimodal probes of surfaces. We will confirm that the attachment chemistry of this molecular probe can be investigated by XPS and IR spectroscopy and by ss-NMR spectroscopy with multiple nuclei (^{11}B , ^{19}F , and ^{13}C). We will then use these spectroscopic measurements supplemented by density functional theory (DFT) investigations to define the binding modes for phenylboronic acid on oxide surfaces. The well-defined surface modification chemistry and a set of spectroscopic labels distributed within this molecule can then be further used to probe the surface reactivity of other nanomaterials.

6.3 Results and discussions

All materials used in this chapter can be found in chapter 2, section 2.2.1. The reaction of 4-fluorophenyl boronic acid with the metal-oxide surfaces is described in section 2.2.1.

The XPS analysis was performed as described in chapter 2, section 2.1.1. The scans for fluorine 1s were observed to be affected by an experiment-induced decomposition to show lower binding energy peaks consistent with fluorine attached directly to the metal oxide surface for samples modified with FPBA. This decomposition was correlated to the longer XPS experiment runtime and is likely an

electron-stimulated effect that is more prevalent on metal oxides with distinct photochemical properties such as TiO₂. Therefore, the fluorine 1s scans reported in this chapter were collected immediately following loading the samples into the instrument to minimize this XPS-induced decomposition.

The solid-state ¹¹B and ¹⁹F NMR measurements and solution ¹⁹F NMR are described in chapter 2, section 2.1.4.

In order to understand the surface chemistry of the FPBA attachment, it is important to identify the main types of species that can be formed on a surface following the reaction. Albeit the high-level computational investigation would be outside the scope of this work, the initial comparison of possible surface species formed could be made based on very simplistic cluster calculations. The functionalities initially available on TiO₂ and γ -Al₂O₃ surfaces are mostly hydroxyl groups, which can be represented by Ti₂O₇H₆ and Al₂O₅H₄ cluster models, respectively. These clusters and their possible reactions with 4FPBA are described in Figure 6.1. The use of these models does not imply that the TiO₂ and γ -Al₂O₃ surfaces are represented correctly; however, they do allow for a comparison of possible formation of the key types of surface species: bidentate with both B–O groups attached to one metal atom, bidentate with each B–O group attached to adjacent metal atoms, and monodentate with only one B–O group attached to one metal atom. In addition, these models can be used to compare the key spectroscopic signatures of the corresponding functionalities attached to the surface, including the core-level energies that can be compared with the results of XPS studies, vibrational signatures to be compared with IR spectroscopy experiments, and chemical shifts to be compared with experimental NMR spectral features. Thus, the spectroscopic comparison with these key types of surface models will be essential in this chapter.

In the first set of experimental characterization, the surface chemistry of attached FPBA was probed with XPS. A set of boronic acid solutions were tested on TiO_2 to determine surface saturation. Analysis of the B 1s and F 1s regions in XPS indicated that saturation was reached at 5 wt % 4FPBA in ethanol and doubling the percentage to 10 wt % did not increase surface boron or fluorine concentrations further (Figure D1 in Appendix D).

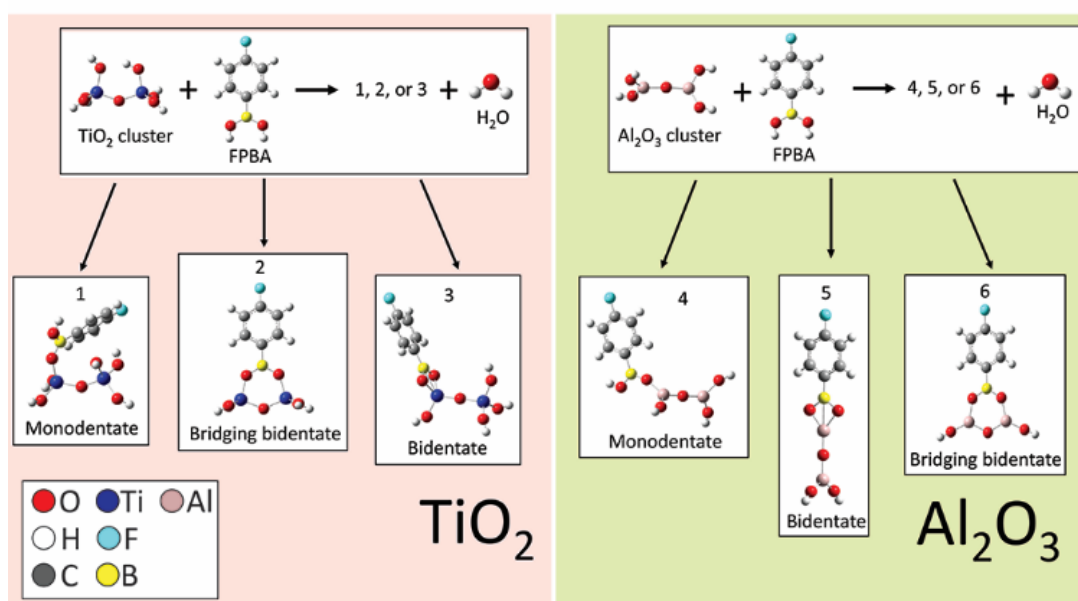


Figure 6.1. DFT models of the 4FPBA attachment on TiO_2 (left) and Al_2O_3 (right) simple clusters in three configurations: Monodentate, bidentate, and bridging bidentate.

Further characterization of the solvent washes showed that high levels of surface saturation were achieved. Analysis of the solvent washes can be used to quantify the amount of physisorbed FPBA, which was removed from the surface in the ethanol wash, and the remaining FPBA was assumed to be chemisorbed FPBA which remained on the

surface. Using this method of subtracting the physisorbed FPBA from the physisorbed and chemisorbed FPBA measured by solution ^{19}F NMR, the nanoparticle surface coverage of FPBA was determined (Table 6.1). With average surface coverages ranging from 1.21 to 1.75 molecules/nm², the FPBA molecule achieved excellent attachment and dispersion, without a proliferation of weakly adsorbed species after washing.

The theoretical surface coverage (molecules of FPBA/nm²) was calculated using the minimum projection radius (3.38 Å) of the FPBA molecule, obtained from the online software Chemicalize (accessed August, 2022, <https://chemicalize.com>) developed by ChemAxon.²¹⁹

The protocol used for surface hydroxyl titration follows a similar approach to that used in the Sears method. Titrations were performed using a Tiamo Titrand 809 autotitrator (Metrohm AG, Switzerland), with 0.1 N HNO₃ and 0.1 N KOH used as the titrants. To prepare the dispersions for each measurement, a set mass of powder (5 g for titanium dioxide samples, 1.5 g for alumina samples) was added to 100 g of the 1 M KNO₃ buffer solution. Before the titration, the dispersion was adjusted to either pH 4 or pH 9, depending on the initial dispersion pH, after which the dispersions were titrated using constant volume additions until reaching pH 9 or pH 4, respectively. The reported value used to calculate the surface hydroxyl content is mL of 0.1 N KOH/HNO₃ used to titrate the sample from pH 4 to pH 9. This value is normalized by particle mass and corrected for the buffer capacity of the salt solution by subtracting the volume required to titrate a blank 1 M KNO₃ solution from pH 4 to pH 9. The experiment to obtain molecules of OH/nm² was performed in collaboration with Zach Grzenda at the Chemours Company.

Surface areas were determined using the BET method on a Micromeritics TriStar II PLUS (Micromeritics Instrument Corporation, Norcross, GA). Samples were de-gassed under 15 psi of vacuum pressure at 150 °C for 3 h before the measurement. The experiment to obtain the surface areas was performed in collaboration with Zach Grzenda at the Chemours Company.

FPBA/TiO₂ rutile [denoted as FPBA/TiO₂ (R)] had the highest number of hydroxyl molecules per square nanometer, though FPBA/γ-Al₂O₃ has the highest BET surface area, and the highest experimental surface coverage of FPBA, shown in Table 6.1. Interactions between the surface OH group and the B–OH group on FPBA were an integral part of the proposed attachment mechanism (Figure 6.1). While the increase in experimental FPBA surface coverage from anatase TiO₂ [denoted as FPBA/TiO₂ (A)] to γ-Al₂O₃ was not as sharp as the roughly 3-fold increase in the BET surface area, it was likely that the increased surface area allowed for a slightly higher surface coverage of FPBA. There was no direct correlation between the experimental surface coverage and number of OH groups per square nanometer, which would point to the importance of the distance between the surface OH groups over the quantity of OH groups, where closely spaced hydroxyl groups would promote stronger bidentate adsorption.

X-ray powder diffraction was performed to confirm the nanopowder crystal structure, as shown in Figure D2 in Appendix D. Each of the nanopowders was confirmed to have the expected morphologies with no morphology change following the reaction with FPBA, though there was a very small amount of rutile contaminant in the anatase TiO₂ sample, which is typical for commercial powders. TEM was also performed to confirm that the reported commercial nanoparticle sizes were consistent and accurate, and the experimental details are reported in Appendix D.

Modified surface	Experimental surface coverage (molecules/nm ²)	Molecules of OH/nm ²	BET surface area (m ² /g)
FPBA/TiO ₂ (A)	1.56 ± 0.14	1.50	52.95
FPBA/TiO ₂ (R)	1.21 ± 0.13	2.77	25.89
FPBA/ γ -Al ₂ O ₃	1.75 ± 0.10	1.99	173.98
FPBA theoretical	2.20	-	-

Table 6.1: Experimental Surface Coverage of the Intact Chemisorbed FPBA Molecule Measured by Solution Phase 19F NMR, Experimental Concentrations of OH Groups on Metal Oxide before Modification, and BET Surface Area of Metal Oxide before Modification

Figure 6.2 shows the representative high-resolution XPS spectra for FPBA-modified anatase TiO₂ nanopowder (Figure 6.2 a,e), rutile TiO₂ nanopowder (Figure 6.2 b,f), γ -Al₂O₃ nanopowder (Figure 6.2 c,g), and pure 4FPBA (Figure 6.2 d,h). Comparing the pure FPBA powder and the boronic acid-modified metal oxides in the left panel of Figure 6.2, the B 1s binding energies are aligned at ~191.7 eV, which suggests that the local environment for boron attached to the metal oxide surface was similar to that of the FPBA molecule. This adds to the hypothesis that the organic fragment of the FPBA molecule remains largely intact on the metal oxide surface. The binding energy of this peak is between metal–boron and B₂O₃.^{103,220} It also aligns well with theoretical B 1s peaks calculated from simple FPBA/TiO₂ clusters with three different modes of B–OH attachment to Ti: monodentate, bidentate, and bidentate bridging.

In the right panel of Figure 6.2, the F 1s region of FPBA is compared to that of surface FPBA on rutile TiO₂, anatase TiO₂, and γ -Al₂O₃. The F 1s peak at higher binding energies was assigned to phenyl fluorine in FPBA in comparison with that of pure FPBA powder (Figure 6.2h). The F 1s peak at lower binding energies was assigned to a

decomposed surface Ti–fluorine species, which is believed to be induced in situ by the high-energy XPS beam because only one fluorine species was detected by ^{19}F NMR, which is a non-destructive technique, *vide infra*. It is important to note that comparing the absolute intensities of the high-resolution spectral regions for different nanomaterials is not quantitative, and separate spectroscopy experiments commonly show differences in peak intensity.

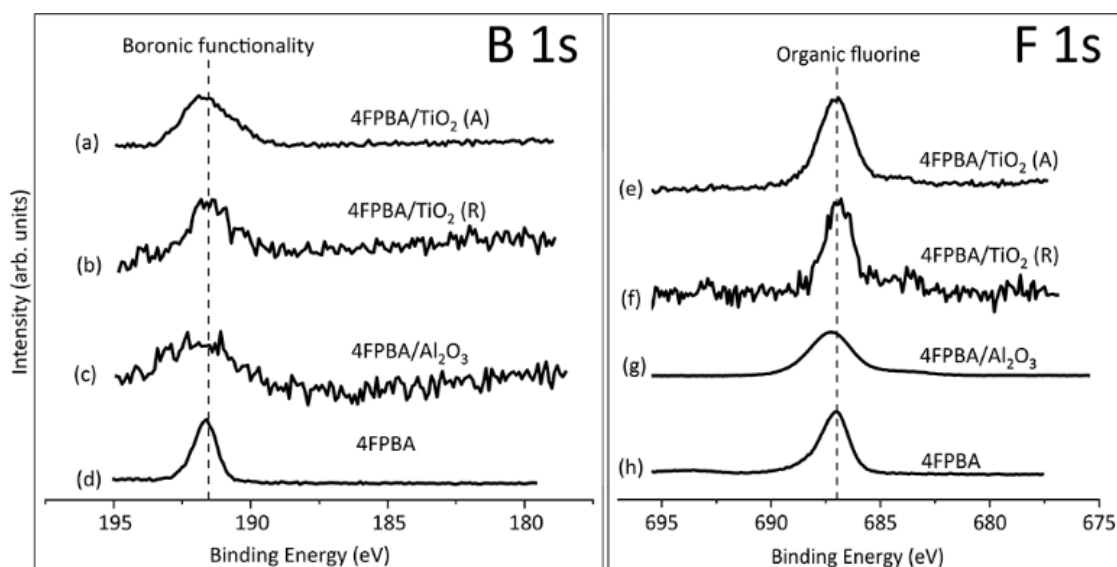


Figure 6.2: XPS spectra of boron 1s (left) and fluorine 1s (right) regions for the 5 wt % loading of 4FPBA on (a,e) anatase TiO_2 nanopowder, (b,f) rutile TiO_2 nanopowder, (c,g) $\gamma\text{-Al}_2\text{O}_3$ nanopowder, as well as (d,h) pure 4FPBA for comparison.

Theoretical binding energies were calculated using Koopmans' theorem, as shown in Table 6.2. The predicted positions of core-level energies for possible surface models, whether monodentate, bidentate, or bidentate bridging, do not appear to be sufficiently different to identify the experimentally observed species of either B 1s or F

1s features. However, these calculations suggest that the experimentally observed features are consistent with boronic functionality being intact following oxide surface modification. One more important piece of information can be deduced from the predicted F 1s binding energy of the metal–F species. The lower binding energy for such species is consistent with metal–F bond formation,²²¹ which was consistent with the surface fluorine peak following decomposition induced by the XPS experiment.

Structure	Calculated theoretical binding energy (eV)	
	B 1s	F 1s
4FPBA-TiO ₂ monodentate	192.4	687.3
4FPBA-TiO ₂ bidentate	192.5	687.2
4FPBA-TiO ₂ bidentate bridging	192.3	687.0
F-Ti	-	685.9
F-O-Ti	-	687.8
4FPBA-Al ₂ O ₃ monodentate	192.3	686.9
4FPBA- Al ₂ O ₃ bidentate	192.0	686.8
4FPBA- Al ₂ O ₃ bidentate bridging	192.1	686.7

Table 6.2: Calculated Theoretical Binding Energies of B 1s and F 1s for Structures Modeled with Gaussian09 Using B3LYP/LANL2DZ for Geometry Optimization and a Single Point Calculation Using B3LYP/6-311+g(d,p) for the Energy Calculation

To gain a more detailed understanding of the local environment of boron, several sets of solid-state NMR experiments were performed. In Figure 6.3, the ¹¹B NMR spectra are shown for 5 wt % loading on anatase (Figure 6.3 a), and rutile (Figure 6.3 b) TiO₂, 5 wt % loading on γ -Al₂O₃ (Figure 6.3 f), theoretical ¹¹B NMR chemical shifts on TiO₂ (Figure 6.3 c–e), theoretical ¹¹B NMR shifts on Al₂O₃ (Figure 6.3 g–i) 4FPBA (Figure 6.3 j), and theoretical ¹¹B NMR shifts for the 4FPBA molecule (Figure 6.3 k). ¹¹B is a quadrupolar nucleus, which typically results in complicated quadrupolar NMR line-shapes even for a single boron site. However, since a single major boron peak is

observed in the XPS of Figures 6.1 and 6.2, it is safe to assume that only one type of boron site is expected on the surface; thus, it is not necessary to deconvolute the ^{11}B spectra. Each of the FPBA-modified oxides shows a distinct ^{11}B signal with a similar lineshape to that of the pure FPBA powder. This observation suggests that the chemical environment of the boron atom remains very similar to that in a FPBA molecule following adsorption on all the materials studied despite their different structures. The NMR spectra in Figure 6.3 a,b,f all have similar lineshapes and intensities, but for the FPBA on rutile TiO_2 (Figure 6.3 b) the peak appears somewhat broader, which was confirmed by multiple replicate scans, and may be largely due to the inhomogeneous broadening for FPBA adsorbed on rutile TiO_2 despite overall similarities of the structures produced on this surface. One additional contribution may be from the possible minor pathway for C–F dissociation on this surface as was suggested by XPS measurements (Figure 6.2). In order to address these differences and to possibly assign the specific surface structures to the experimentally observed spectra, ADF theory was used to predict the chemical shifts for boron in FPBA attached to TiO_2 and Al_2O_3 cluster models. The predicted chemical shifts for boron aligned well with experimental values, therefore utilizing the ADF program for chemical structure prediction which has been proven useful in a previous study for boron sites.¹⁹⁷ This exercise confirms that boronic functionality could be used as an identifiable spectroscopic label; however, distinguishing the proposed surface structures based on this approach alone was not possible as all the models exhibited very similar calculated spectral properties.

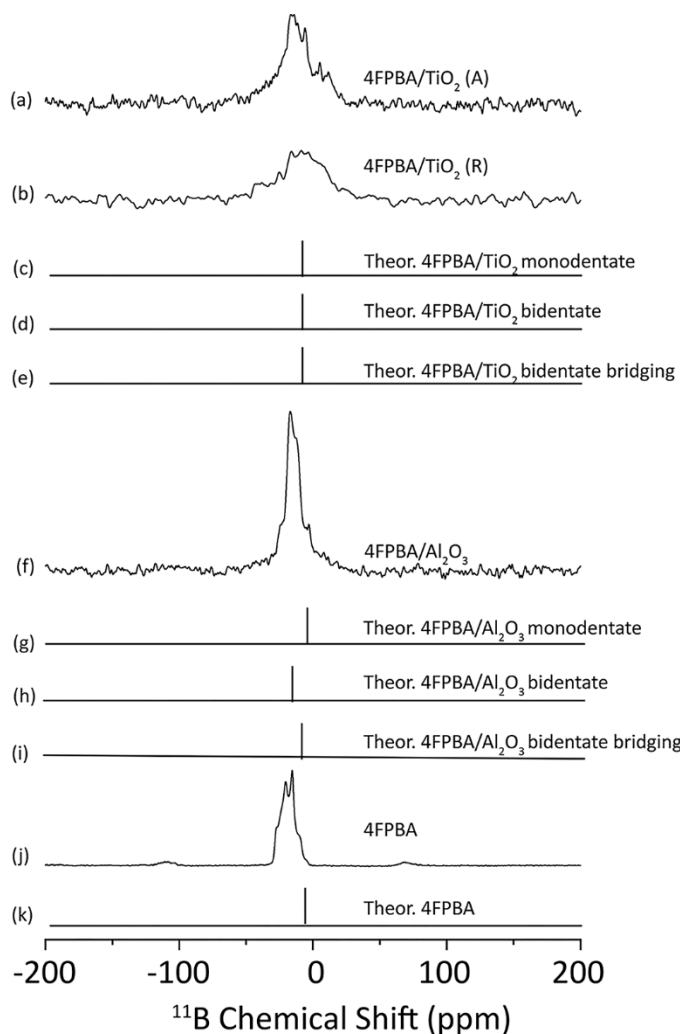


Figure 6.3. Solid-state ^{11}B NMR of (a) 5 wt % 4FPBA on anatase TiO_2 , (b) 5 wt % 4FPBA on rutile TiO_2 , (c) theoretical ^{11}B NMR spectrum for monodentate 4FPBA on the TiO_2 cluster, (d) theoretical ^{11}B NMR spectrum for bidentate 4FPBA on the TiO_2 cluster, (e) theoretical ^{11}B NMR spectrum for bidentate bridging 4FPBA on the TiO_2 cluster, (f) 5 wt % 4FPBA on $\gamma\text{-Al}_2\text{O}_3$, (g) theoretical ^{11}B NMR spectrum for monodentate 4FPBA on the Al_2O_3 cluster, (h) theoretical ^{11}B NMR spectrum for bidentate 4FPBA on the Al_2O_3 cluster, (i) theoretical ^{11}B NMR spectrum for bidentate bridging 4FPBA on the Al_2O_3 cluster, (j) pure 4FPBA powder, and (k) theoretical ^{11}B NMR spectrum for molecular 4FPBA.

As a probe, ^{19}F NMR is incredibly sensitive to changes in surface structure. Figure 6.4 a–e depicts the solid-state ^{19}F NMR spectra for 5 wt % loading on anatase TiO_2 (Figure 6.4 a), rutile TiO_2 (Figure 6.4 b), and $\gamma\text{-Al}_2\text{O}_3$ (Figure 6.4 c), as well as for pure solid 4FPBA (Figure 6.4 d) and theoretical ^{19}F NMR chemical shifts for molecular 4FPBA (Figure 6.4 e). The multiple peaks observed for pure solid FPBA (Figure 6.4 d) indicate the existence of potentially multiple polymorphs due to variations in the crystal packings in the solid powder; however, a singular dominant ^{19}F peak (~ -121 ppm) was observed for the 5 wt % loading samples on all the materials studied, although in several cases, a very small feature was also recorded around -190 ppm, which can be attributed to surface F formation following minor organic fragment decomposition pathways and is not correlated to the boronic acid ligand.^{222,223} The peak around -121 ppm lies in the expected range for organic fluorine^{224,225} and was consistent for each modified sample. Thus, for all the surface-modified oxide materials investigated, the presence of a single dominant ^{19}F peak indicates that in the monolayers formed fluorine atoms were not spatially close and were well-dispersed on the surface and that their chemical environments were very similar in all the cases studied. ADF calculations were used to predict the chemical shifts for fluorine on 4FPBA attached to TiO_2 and Al_2O_3 similarly to the assessment of ^{11}B features discussed above. The predicted ^{19}F chemical shift for the molecular compound is shown in Figure 6.4 e. ADF predicted the molecular ^{19}F chemical shift to be downfield compared to the surface-adsorbed molecule, again confirming that fluorine can serve as a robust and identifiable spectroscopic label²²⁶ and may potentially serve as an indicator of surface chemistry.

The use of ^{11}B or ^{19}F chemical labels allowed us to pinpoint three features of the adsorbed species on all the surfaces: (1) despite the fact that anatase TiO_2 , rutile TiO_2 ,

and polycrystalline γ -Al₂O₃ have vastly different surfaces, the similarity in the experimental ¹¹B or ¹⁹F spectra suggested that the chemical environment of all probes is very similar in all the cases; (2) the molecules are well-dispersed on each surface (with no unreacted agglomerate structures present, which would lead to the spectra similar to that of the solid powder); (3) comparison with computational models does not necessarily pinpoint the exact structures produced on surfaces but is fully consistent with the =B-(C₆H₄)-F entity being intact.

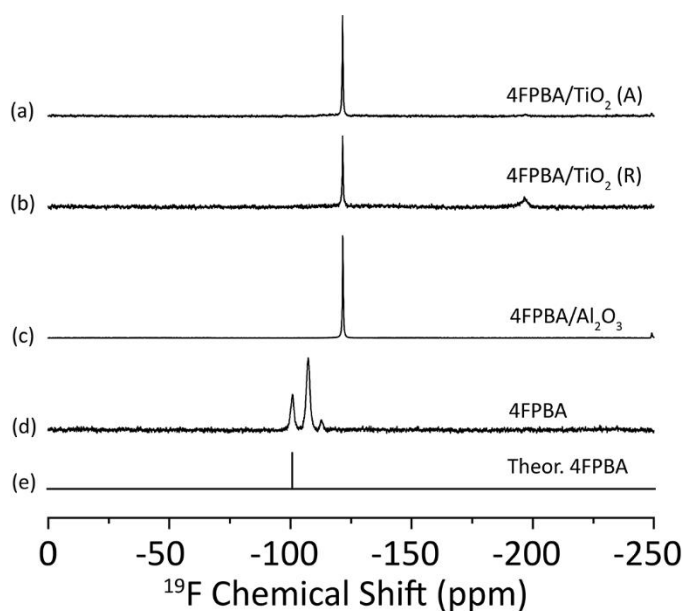


Figure 6.4. Solid-state ¹⁹F NMR of (a) 5 wt % 4FPBA on anatase TiO₂, (b) 5 wt % 4FPBA on rutile TiO₂, (c) 5 wt % 4FPBA on γ -Al₂O₃, (d) pure 4FPBA powder, and (e) ADF-predicted chemical shift for molecular 4FPBA.

One more piece of structural information can be obtained based on ¹³C NMR spectroscopy to probe the local chemical environment of the phenyl carbon atoms, as

summarized in Figure 6.5. All the assignments have been verified using ADF calculations, as shown in Figure 6.5. While slightly shifted compared with the experimental data, the ADF predictions for all the key functional groups were consistent with experimental observations. C–F groups were clearly identified as a single peak around 168 ppm and are aligned well with the spectral characteristics of pure FPBA powder (Figure 6.5 j). The spectra of chemically modified TiO₂ were also consistent with the expected features of molecular FPBA. Although the NMR signal for FPBA on anatase TiO₂ was not as strong as on rutile, the chemical shifts appear at the same positions. There appeared to be an array of overlapping peaks between 128 and 137 ppm, which aligned well with the pair of C–H peaks and the C–B peak predicted by the monodentate ADF model. Following the trend, the experimental peak at 116 ppm would align with overlapping C–H peaks on all of the theoretical models.

The spectra of the modified γ -Al₂O₃ surface were also consistent with the expected features but suggest that the local environment of the phenyl ring may be different on this material compared with that of TiO₂. The chemical shifts are similar to those of molecular FPBA and theoretically predicted bidentate FPBA (Figure 6.5 h,i), with a single strong peak around 138 ppm that aligned with the two overlapping C–H peaks predicted by ADF. Additionally, the strong peak around 115 ppm corresponds to the C–H peaks present in all theoretical models. A comparison of the predicted and experimental spectrum for the molecular structure suggests that this approach can be used for quantitative investigation and also that despite some local differences in FPBA attachment on TiO₂ and Al₂O₃ surfaces, the adsorbates are expected to be overall very similar, with the structure of the surface-bound moiety corresponding to the =B–(C₆H₄)–F being intact.

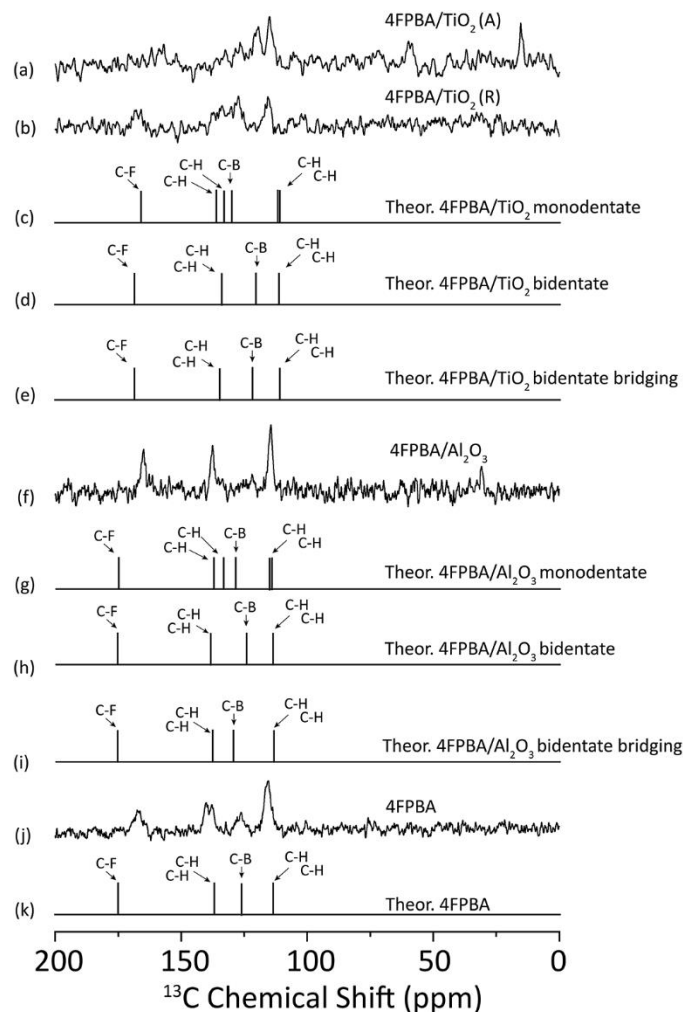


Figure 6.5. Solid-state ^{13}C NMR of (a) 5 wt % 4FPBA on anatase TiO_2 , (b) 5 wt % 4FPBA on rutile TiO_2 , (c) theoretical NMR spectrum for monodentate 4FPBA on the TiO_2 cluster, (d) theoretical NMR spectrum for bidentate 4FPBA on the TiO_2 cluster, (e) theoretical NMR spectrum for bidentate bridging 4FPBA on the TiO_2 cluster, (f) 5 wt % 4FPBA on $\gamma\text{-Al}_2\text{O}_3$, (g) theoretical NMR spectrum for monodentate 4FPBA on the Al_2O_3 cluster, (h) theoretical NMR spectrum for bidentate 4FPBA on the Al_2O_3 cluster, (i) theoretical NMR spectrum for bidentate bridging 4FPBA on the Al_2O_3 cluster, (j) pure 4FPBA powder, and (k) theoretical NMR spectrum for molecular 4FPBA.

FTIR spectroscopy was performed as described in chapter 2, section 2.1.3. Fourier-transform IR spectroscopy would be expected to produce quite complicated results but may also be able to confirm some of the assessments provided above. As shown in Figure 6.6, a comparison of the vibrational spectra predicted for the proposed computational models with the experimental ones can be used to pinpoint specific molecular features present on the surfaces modified with FPBA. Specifically, the peaks at ~ 1600 and $\sim 1500\text{ cm}^{-1}$ were assigned to the unique vibrations involving multiple atoms (simultaneously B, C, and H atoms) within the $=\text{B}-(\text{C}_6\text{H}_4)-\text{F}$ group. A distinct peak was observed at $\sim 1500\text{ cm}^{-1}$ on TiO_2 (Figure 6.6 a,b) and $\gamma\text{-Al}_2\text{O}_3$ (Figure 6.6 f), and a shoulder observed at $\sim 1600\text{ cm}^{-1}$ was present on all metal oxides (Figure 6.6 a,b,f). The broad peak observed at $\sim 1620\text{ cm}^{-1}$ is characteristic of surface water. When compared to theoretically predicted values and the spectrum of pure 4FPBA powder for identification, this experimental observation fully confirms the intactness of the $=\text{B}-(\text{C}_6\text{H}_4)-\text{F}$ functionality following the modification of all oxide surfaces investigated with FPBA.

Since all the investigations described above suggest the presence of the $(-\text{O}-)_2\text{B}-(\text{C}_6\text{H}_4)-\text{F}$ functional group following oxide surface modification with FPBA, it would be expected that surface hydroxyl sites act as the anchor point for the condensation reaction, which is predicted to govern the $\text{B}-\text{OH}$ group attachment. There are two main types of hydroxyl groups that are formed on titania, which are terminal OH groups and bridging OH groups. Terminal OH groups, bonded to only one Ti^{4+} atom, are electron-rich and act as basic sites. Bridging OH groups are bonded to two Ti^{4+} atoms, which causes the hydrogen to become more acidic due to the decrease in electron density on the oxygen.²²⁷ Because of the higher basicity of the terminal OH

group, it is probable that the mechanism of boronic acid attachment involves the electron-rich oxygen-donating electrons to the electrophilic boron, and the OH group attached to the boron combines with the hydrogen atom from the attacking OH group to form water. However, we cannot rule out the possibility of alternate reaction mechanisms.

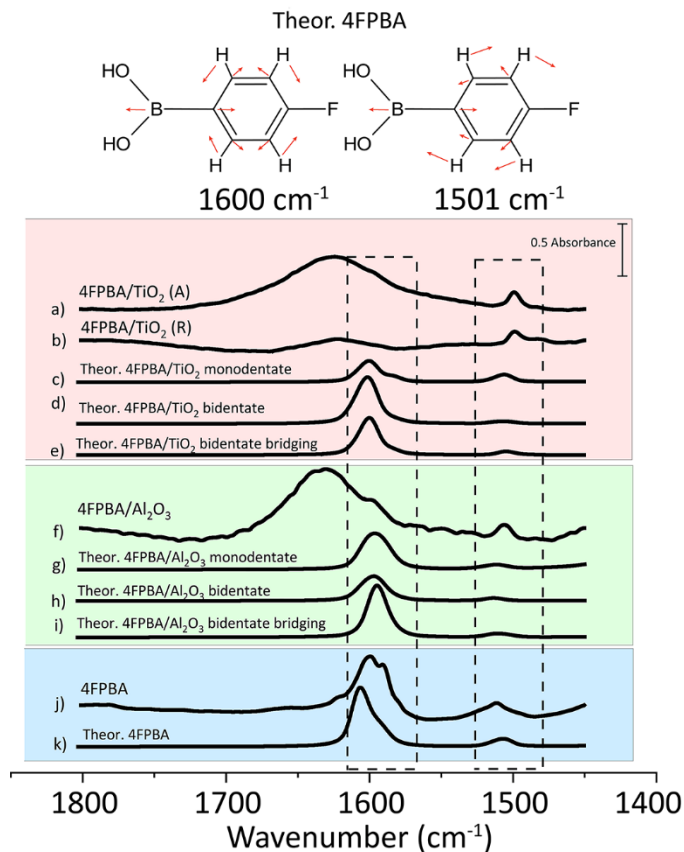


Figure 6.6: FTIR spectra of (a) 5 wt % 4FPBA on anatase TiO_2 , (b) 5 wt % 4FPBA on rutile TiO_2 , (c) theoretical IR spectrum for monodentate 4FPBA on the TiO_2 cluster, (d) theoretical IR spectrum or bidentate 4FPBA on the TiO_2 cluster, (e) theoretical IR spectrum for bidentate bridging 4FPBA on the TiO_2 cluster, (f) 5 wt % 4FPBA on $\gamma\text{-Al}_2\text{O}_3$, (g) theoretical IR spectrum for monodentate 4FPBA on the Al_2O_3 cluster, (h) theoretical IR spectrum for bidentate 4FPBA on the Al_2O_3 cluster, (i) theoretical IR spectrum for bidentate bridging 4FPBA on the Al_2O_3 cluster, (j) pure 4FPBA powder, and (k) theoretical IR spectrum for molecular 4FPBA.

While all the materials investigated may form terminal and bridging OH groups, the surfaces of rutile TiO_2 , anatase TiO_2 , and $\gamma\text{-Al}_2\text{O}_3$ have notable differences. Rutile TiO_2 has shorter Ti–Ti distances than anatase, which causes the formation of Ti–OO–Ti groups in water.²²⁸ This titanium peroxide functionality is predicted to be less reactive

than terminal OH groups, which might explain why, though still highly efficient in reaction with FPBA, rutile TiO₂ had the lower comparative surface coverage.

The hydroxylated Al₂O₃ surface has also been explored previously, with a wide array of OH orientations found on the surface. The two main categories are described as singly coordinated and doubly coordinated, similar to the terminal and bridging OH groups for TiO₂, and doubly coordinated OH groups on γ -Al₂O₃ have been reported to have lower deprotonation energies.²²⁹ The Al atom can also be coordinated to more than one OH, forming geminal Al(OH)₂ groups on the surface.^{228,229} This effect would encourage the formation of bidentate attachment to boronic acid by providing two spatially close OH groups for reaction with the B–OH groups. Overall, this observation helps rationalizing the differences between alumina and titania bonding of the boronic acid observed by NMR, as summarized in Figure 6.5. The bidentate attachment of the boronic functional group to the γ -Al₂O₃ surface would be supported by the similarities of the experimental and computationally predicted spectra. On titania, the ¹³C NMR spectra are clearly different and appear to be more consistent with the presence of monodentate attachment. However, quantitative assignment based on this study alone is not feasible and will deserve further investigations.

The experimentally determined hydroxyl surface density (Table 6.1) showed that FPBA attachment was not directly dependent on the quantity of available hydroxyls; however, taking into account the trends stated above, the spatial distance and orientation of the surface hydroxyls become much more significant for the binding modes than the average surface concentration of hydroxyl groups.

In this chapter, the comparison of the FPBA reaction with the surfaces of different nanoparticulate oxide materials suggests that this molecule can indeed be used

as an efficient modifier, with (1) boron label providing important information both about the efficiency of surface modification and the type of surface species formed; (2) fluorine label serving as a highly sensitive indicator of surface reactivity and surface coverage of molecular modifiers; and (3) the combination of spectroscopic methods providing a great insight into the surface chemistry of TiO_2 and Al_2O_3 , which can be expanded to include other oxides and also more complex nanomaterials.

6.4 Conclusions

In this work, 4-fluorophenylboronic acid was attached to rutile TiO_2 , anatase TiO_2 , and $\gamma\text{-Al}_2\text{O}_3$ nanoparticles with a simple low-temperature one-pot chemistry method, resulting in high surface concentrations. Several spectroscopic probes were developed to characterize the FPBA chemistry based on NMR, XPS, and IR spectroscopies, and the assignment of the binding configurations in the resulting surface structures was made based on the combination of these analytical techniques. This work will pave the way for further investigations of surface modification processes for a variety of complex materials using multiple spectroscopic probes as identifiers of chemistry, coverage, and changes in materials properties.

Chapter 7

INHIBITION OF ATOMIC LAYER DEPOSITION OF TiO₂ BY FUNCTIONALIZING SILICON SURFACE WITH 4- FLUOROPHENYLBORONIC ACID

7.1 Abstract

In this chapter, the chemistry of 4-fluorophenylboronic acid is investigated as a potentially effective resist to block the growth of materials on non-growth substrates in area-selective deposition methods. Choosing the appropriate surface modification requires knowledge of the corresponding chemistry and also a detailed investigation of the behavior of the functionalized surface in realistic deposition schemes. The 4-fluorophenylboronic acid (FPBA) is used as a model to investigate the possibility of utilizing the Si(100) surface functionalized with this compound as a non-growth substrate in a titanium dioxide (TiO₂) deposition scheme based on sequential doses of tetrakis(dimethylamido)titanium (TDMAT) and water. A combination of X-ray photoelectron spectroscopy (XPS) and time-of-flight secondary ion mass spectrometry (ToF-SIMS) allows for a full understanding of the process. The resulting surface is shown to be as effective a resist to TiO₂ deposition as currently used H-terminated silicon surfaces, but to exhibit much higher stability in ambient conditions. The material in this chapter is based on a submitted manuscript [Inhibition of atomic layer deposition of TiO₂ by functionalizing silicon surface with 4-fluorophenylboronic acid, Dhamelyz

Silva-Quinones, John Mason, Robert Norden, Andrew V. Teplyakov, Submitted to J. Vac. Sci. Technol A].

7.2 Introduction

Modern requirements for microelectronic devices to be developed past Moore's law into the so-called more-than-Moore direction²³⁰ require both miniaturization of the device features and exceptional conformality, which can only be delivered by bottom-up self-aligned nanofabrication. This approach is rooted in area-selective atomic layer deposition (AS-ALD) or area-selective deposition (ASD) techniques that have become the subject of intense research in recent years.^{18,37} They address the challenge of limiting the growth on specific areas by taking advantage of the differences in local surface chemistry. In other words, by changing the surface reactivity of the substrate one can favor or prevent the growth of a specific material on the target surface.^{30,37,231} Thus, the growth is expected on the growth area (GA), where the surface is modified using promotor-type molecules, but delayed or avoided on the non-growth area (NGA), where the surface is modified using inhibitor-type molecules, so that atomic level accuracy can be achieved.³⁶ The measure of efficiency of this difference in reactivity is characterized by selectivity, which is discussed later.

Although sometimes combinations of GA and NGA with high intrinsic selectivity can be utilized directly as prepared, most of the time, the intricate patterns used for modern applications and especially for 3D components, require some sort of chemical patterning, where passivated areas serve as NGA. In the past, polymer masks and self-assembled monolayers of functional alkyl molecules were used with a high degree of success,²³²⁻²³⁷ however, with the size of the target features quickly approaching single nanometer scale, the need for alternative materials for surface

modification became apparent. In silicon-based production, the most common approach is to use H-terminated silicon surface for patterning that can be achieved with as high resolution as a single atom (with scanning tunneling microscopy) or alternative atomic monolayer systems (Cl-, Br-, I-),¹⁰ but stability of these systems and the difficulty to prepare them consistently outside expensive ultra-high vacuum conditions brought up a demand for the use of small molecule inhibitors (SMIs),²³² with dimensions of just a few angstroms. SMIs can be introduced in the midst of the deposition cycle to refresh the NGA and suppress the defects appearing during the deposition. Moreover, the same general strategy can be applied to create an NGA at the start of the deposition process. There are certain requirements for the design and the selection of a good SMI for this purpose. They include chemical stability on a specific surface, steric hindrance, strength of adsorption, fast attachment reaction kinetics, and a minimal number of various binding modes, but most importantly, increased selectivity between GA and NGA.²³⁸

The 4-fluorophenylboronic acid (FPBA) molecule can be a promising SMI that satisfies the aforementioned requirements. The chemical reaction of the FPBA with a chlorine-terminated silicon surface follows the general condensation scheme, in which a chemical functionality of the incoming molecule combines with the surface functionality to produce a stable chemical bond and to release a side product. Similar processes have been demonstrated previously for introducing nitrogen-containing functionalities to silicon by reacting nitro- or nitroso- compounds with H-terminated silicon surfaces producing water as a side product^{98,121} and for amines reacting with Cl-terminated silicon surfaces, releasing hydrochloric acid (HCl) as a side product.^{132,179} Not only does FPBA form a condensation product with Cl-terminated silicon releasing HCl, but this reaction is also highly selective compared to the H-terminated silicon

surfaces.¹¹ It leads to the formation of very stable bidentate species with two Si-O-B bonds, which allows for the passivation of the surface and prevents further oxidation.¹¹ In addition, the FPBA molecule has boron and fluorine elements, which can serve as convenient spectroscopic labels.

This chapter will demonstrate that the passivation of silicon with FPBA results in the creation of a stable surface that effectively inhibits the deposition of titanium dioxide (TiO₂) in an atomic layer deposition (ALD) process utilizing sequential doses of tetrakis(dimethylamido)titanium (TDMAT) and water. This inhibitory effect persists for up to 20 cycles, demonstrating a selectivity of 71%. This selectivity is nearly identical to that of H-terminated silicon reacted under the same conditions, but FPBA-terminated surface is exceptionally stable, even in ambient. A detailed spectroscopic investigation confirms the formation of a stable monolayer, and ToF-SIMS profiles of this surface after the eventual loss of selectivity (covered with TiO₂ layer) confirms that the starting substrate is still intact and even identifies the differences in F and B positions at the interface.

7.3 Results and discussion

The XPS analysis was performed as described in chapter 2, section 2.1.1. ToF-SIMS analysis is described in section 2.3.2, and AFM images were obtained as described in section 2.3.5.

Figure 7.1 shows the steps followed for the preparation of OH-Si(100), H-Si(100), and FPBA-Si(100) described in chapter 2, sections 2.1.2 and 2.1.7. These three surfaces were loaded at the same time in the ALD chamber for each separate run, and 5, 10, 15, 20, 30, 50 and 200 cycles of TDMAT and H₂O were dosed at 130 °C to compare the growth of TiO₂ on all surfaces. After each set of ALD cycles, the samples

were loaded into the XPS chamber with minimal exposure to ambient for analysis as described in this chapter.

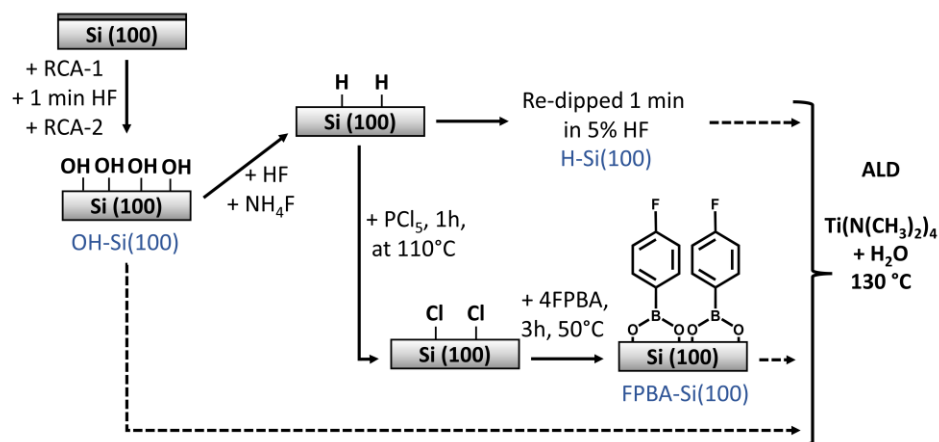


Figure 7.1: Steps followed in the preparation of OH-, H-, and FPBA-Si(100) surfaces used in the comparison of TiO₂ growth by ALD.

7.3.1 XPS of growth and non-growth surfaces before and after ALD of TiO₂

Figure 7.2 shows the B 1s, F 1s, Si 2p, and Ti 2p XPS spectral regions for the FPBA-modified Si(100) surface before and after 5, 10, 20, 30, and 50 ALD cycles of TiO₂. The initial surface (Figure 7.2 a) shows the presence of B 1s feature at around 191.9 eV and F 1s at around 687.1 eV which correspond to the B and F signal from the FPBA molecule as reported in previous studies.^{11,14} The Si 2p shows the Si bulk signal at 99.4 eV and the higher binding energy peak around 103.0 eV corresponding to Si-O-B bonds.¹¹ No presence of Ti is recorded on any of the surfaces before the deposition. The relative B/Si coverage obtained after the reaction of FPBA with Cl-Si(100) surface was 0.42 ± 0.01 (Table 7.1), which corresponds to 74 % of a monolayer equivalent to one boron atom per one silicon surface atom based on previous work.¹¹ This coverage corresponds to the saturation on this surface. It is also important to highlight the FPBA-

Si(100) surface stability which will be discussed and compared to a H-Si(100) surface in the next section.

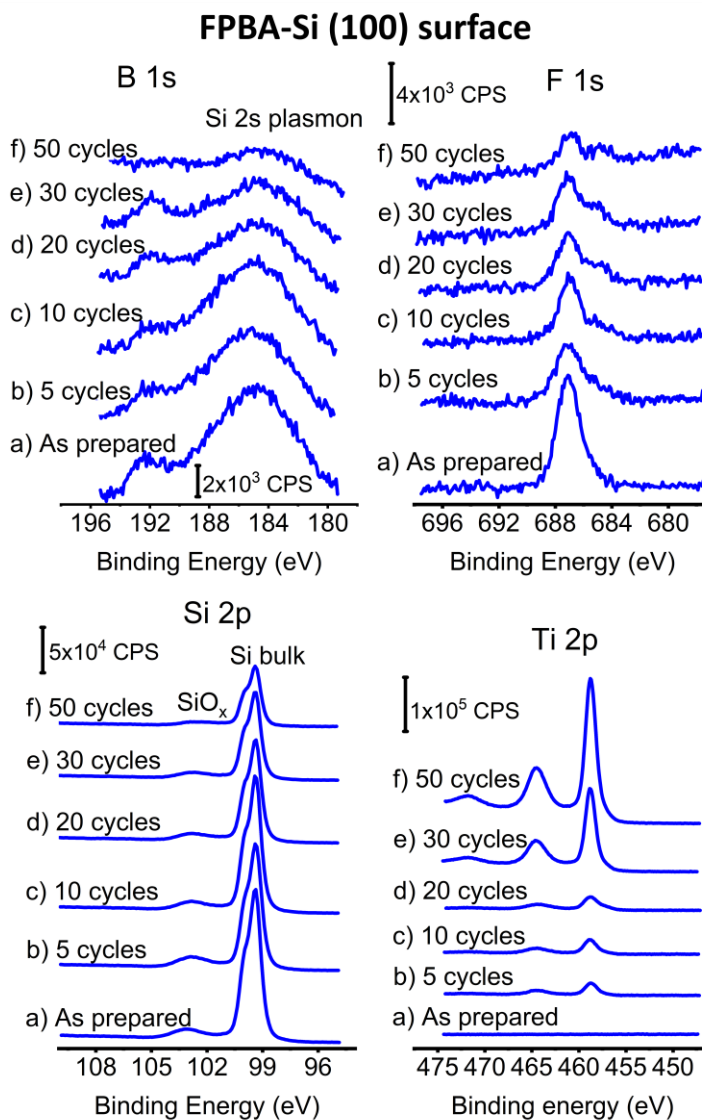


Figure 7.2: B 1s, F 1s, Si 2p, Ti 2p XPS spectral regions of FPBA-Si(100); as prepared (a), and after 5 (b), 10 (c), 20 (d), 30 (e), and 50 (f) ALD cycles of TiO₂.

Relative B/Si coverage (Φ) on Cl-Si (100)	
FPBA-Si (100)	0.42 ± 0.01

Table 7.1: Relative B/Si coverage after the reaction of FPBA with Cl-Si(100)¹¹

Following 5 to 50 ALD cycles onto the FPBA-modified silicon surface (Figure 7.2 b, c, d, e, and f), the B 1s signal is clearly observed and decreases substantially only at 50 cycles, and the B 1s peak position is maintained indicating that the chemical environment of boron is not changing substantially. The F 1s signal also clearly decreases, especially by 50 cycles, an additional peak appears at lower binding energy around 684.9 eV, which likely corresponds to the interaction of F with Ti. The Si 2p signal also decreases with an increasing number of ALD cycles, which is expected since the surface is being covered by the TiO₂ layer causing the attenuation of the Si signal.²³⁹ The Ti 2p spectral region shows how the Ti 2p signal increases slightly after 5 to 20 ALD cycles (likely indicating the presence of surface defects) and increases substantially after 50 ALD cycles.

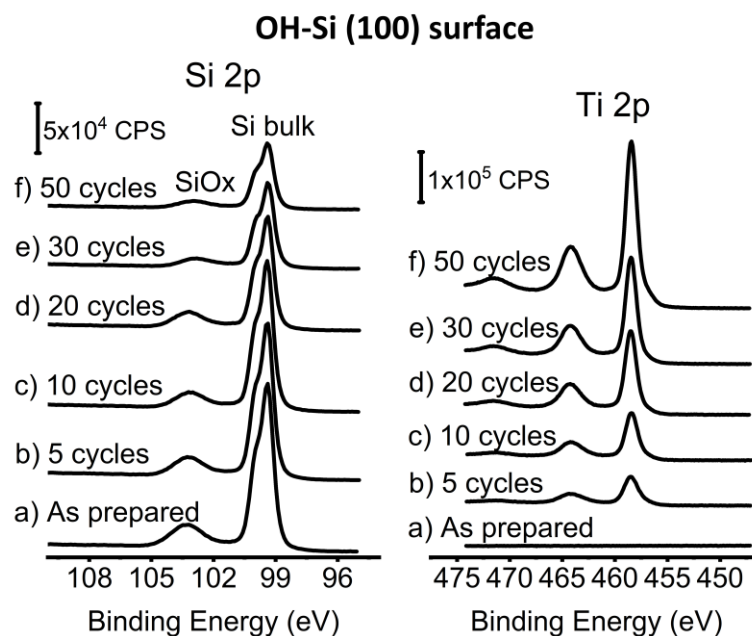


Figure 7.3: Si 2p, Ti 2p XPS spectral regions of OH-Si(100) as prepared (a), and after 5 (b), 10 (c), 20 (d), 30 (e) and 50 (f) ALD cycles of TiO₂.

In order to evaluate the selectivity of the TiO₂ deposition, we performed the same procedure on oxidized, OH-terminated silicon surface, where both half-cycles of the ALD process are expected to be very efficient. Figure 7.3 shows the Si 2p, and Ti 2p XPS spectral regions for the OH-terminated Si (100) surface before and after 5, 10, 20, 30, and 50 ALD cycles of TiO₂. The initial surface (Figure 7.3 a) shows a substantial oxidation in the Si 2p region at 103.5 eV.²⁴ After 5 to 50 cycles (Figure 7.3 b, c, d, e, and f) the Si 2p peak intensities decrease with the increasing number of ALD cycles, due to the surface being covered by the growing TiO₂ layer. In the Ti 2p region, the Ti signal intensity increases with the number of ALD cycles, this growth appears to be linear, which is different from what was observed for the FPBA-Si(100) surface. To have a better comparison of the TiO₂ growth on both non-growth surface (FPBA-Si

(100)) and growth surface (OH-Si (100)) the Ti 2p/Si 2p ratios, estimated TiO₂ thickness and selectivity were calculated and discussed further.

Figure E1 in the Appendix E section shows the Si 2p and Ti 2p XPS spectral regions of the H-Si(100) before and after 10 to 50 ALD cycles for comparison. It is important to note that the reactivity of H-Si(100), which is related largely to the defects on this surface,^{33,34} is extremely sensitive to the surface preparation procedure. The reports range from exceptionally high surface stability up to 45 ALD cycles²⁴⁰ to the immediate (albeit slower than on HO-terminated silicon) growth of TiO₂ in similar conditions.³¹ The efficiency of the TiO₂ deposition in the studies summarized in this chapter is between these two extremes and is used largely for comparison with the FPBA-terminated silicon. The observed intensity of the Ti signal is nearly linear up to 20 cycles (with a slope analyzed later in more detail) and the attenuation of the Si 2p signal, especially following 30 or more ALD cycles is clearly recorded, as would be expected.

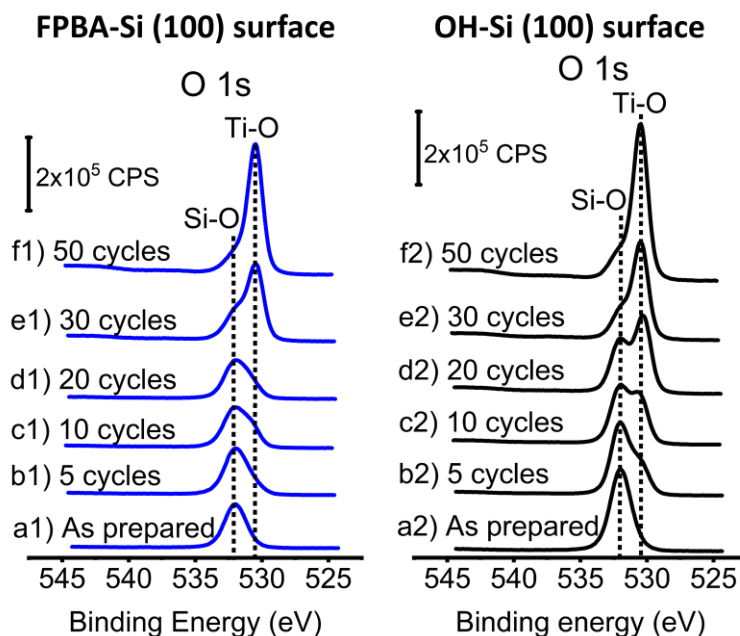


Figure 7.4: O 1s XPS spectral region of FPBA-Si(100) (1); as prepared (a1), after 5 (b1), 10 (c1), 20 (d1), 30 (e1), and 50 (f1) cycles of TiO₂ ALD, and OH-Si(100) (2); as prepared (a2), after 5 (b2), 10 (c2), 20 (d2), 30 (e2), and 50 (f2) cycles of TiO₂ ALD.

Since spectroscopic signature of oxygen is quite distinct in TiO₂, Figure 7.4 shows the O 1s XPS spectral region of the OH-Si (100) and FPBA-Si (100) surfaces before and after 5, 10, 20, 30, and 50 ALD cycles. Initially, on both surfaces, a single O 1s peak is observed around 532.0 eV corresponding mostly to the O-Si bonds.³³ After the ALD, noticeable differences on both surfaces are recorded. On the FPBA-Si (100) surface it is observed that from 5 to 20 cycles the predominant peak is still the one around 532.0 eV. Only a small shoulder at lower binding energy appears following 10 ALD cycles corresponding to the formation of O-Ti bonds.³³ After 30 ALD cycles, this feature becomes dominant in the O 1s spectra. On the OH-Si(100) surface, the O 1s peak at 530.5 eV corresponding to O-Ti is clearly observed even after 5 ALD cycles,

this O-Ti peak increases in intensity after 10 cycles and clearly dominates the spectrum after 10 ALD cycles.

This observation indicates that the nucleation of TiO_2 is much faster on the OH-Si(100) surface compared to the FPBA-Si(100) surface, as the latter delays the nucleation of TiO_2 at least up to 20 cycles. Figure E1 in Appendix E also shows the O1s peak for the H-Si(100) before and after 10 to 50 ALD cycles of TiO_2 for comparison. Here we can see that after 10 cycles the predominant peak appears at 532.0 eV, corresponding to O-Si, and after 20 cycles the peak at 530.5, corresponding to O-Ti becomes the more predominant and it increases as the ALD cycles increase, a behavior similar to that observed for the FPBA-Si(100) surface.

Based on the O-Ti peak at 530.5 eV measured on each surface, it can be concluded that the nucleation of TiO_2 is slower on the FPBA-modified silicon, especially up to 20 ALD cycles. This can be due to the extra protection that the FPBA-passivated silicon surface provides, as the $(-\text{O}-)_2\text{B}-(\text{C}_6\text{H}_4)-\text{F}$ functional groups provide steric hindrance that makes the surface inaccessible to react with TDMAT.

7.3.2 Ti/Si XPS intensity ratios, estimated TiO_2 thickness, and selectivity on the growth and non-growth surfaces.

Figure 7.5 shows the Ti 2p and Si 2p intensity ratios as a function of the number of ALD cycles on the FPBA-Si(100), OH-Si(100), and H-Si(100) surfaces. The OH-terminated Si(100) favors the growth of TiO_2 . As can be observed in the graph, the growth of Ti 2p is nearly linear (in fact, the observed deviation is expected for thicker films, due to the attenuation of Si signal). The FPBA-functionalized Si(100) is the non-growth surface and shows a delay in the growth of TiO_2 , this delay is evident up to 20 cycles and then a more linear growth is observed for 30 and 50 ALD cycles. A similar

behavior can be observed on the H-Si(100) surface, which shows a delay in the growth of TiO₂ up to 20 cycles, and then the growth is linear after 30 and 50 ALD cycles.

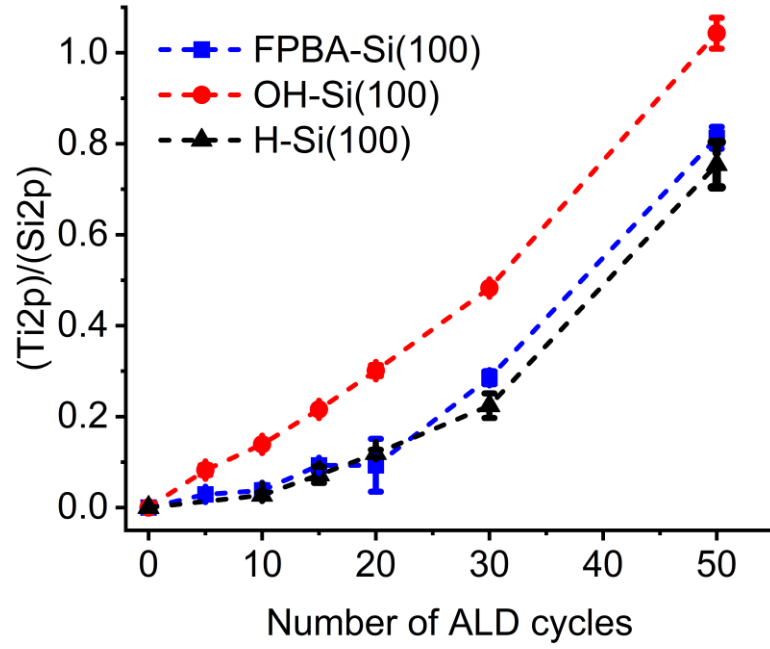


Figure 7.5: Ti 2p/ Si 2p ratios recorded as a function of the number of ALD cycles.

The selectivity was calculated using the ratios obtained on the growth and non-growth surfaces according to equation (1).²³²

$$S_x = \frac{R_{GS} - R_{NGS}}{R_{GS} + R_{NGS}} \quad (1)$$

where S_x is the selectivity after x number of ALD cycles and R represents the amount of deposited material on either GA or NGA. The growth surface for this experiment was OH-Si(100) and the non-growth surface was either H-Si(100) or FPBA-Si(100).

Table 7.2 shows that the FPBA-Si(100) surface delays the growth of TiO₂ up to 20 cycles with a selectivity of 0.5 ± 0.2 and after 50 cycles the selectivity is lost. The selectivity was also calculated for the H-Si(100) surface as shown in Table 7.2. It is maintained for up to 10 cycles with 0.6 ± 0.02 . Then, as the number of cycles increases, the selectivity decreases until it is lost after 50 cycles. The selectivity calculated for FPBA- and H-Si surfaces is similar. However, the FPBA-Si surface has the advantage of being stable in ambient conditions even after 48 hours as shown by comparing key spectral regions as a function of time for these two substrates in Figures E2 and E3 in Appendix E.

Cycles	FPBA-Si(100) Selectivity	H-Si(100) Selectivity
5	0.6 ± 0.10	-
10	0.6 ± 0.10	0.6 ± 0.02
15	0.4 ± 0.01	0.5 ± 0.10
20	0.5 ± 0.20	0.4 ± 0.04
30	0.3 ± 0.02	0.4 ± 0.05
50	0.1 ± 0.02	0.2 ± 0.10

Table 7.2: Selectivity of FPBA calculated from equation (1) using Ti 2p/ Si 2p ratios obtained with XPS.

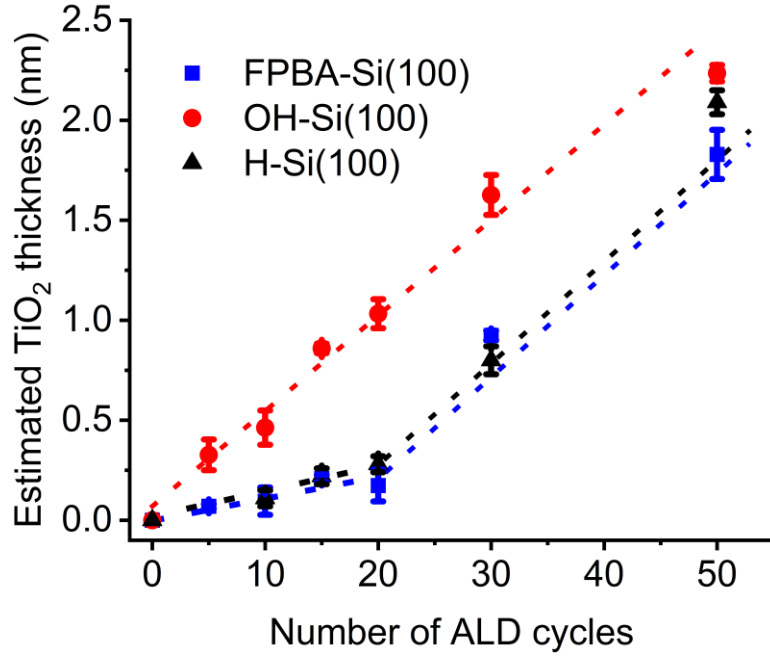


Figure 7.6: Estimated TiO₂ thickness (nm) as a function of the number of ALD cycles.

For a more direct comparison, Figure 7.6 plots the estimated thickness of the TiO₂ film deposited on different surfaces as a number of ALD cycles. It shows the estimated TiO₂ thickness calculated from equation (2)³¹

$$d_{TiO_2} = -\lambda_{TiO_2} \ln\left(\frac{I_{Si}}{I_{Si,0}}\right) \quad (2)$$

where d_{TiO_2} is the thickness of the TiO₂ layer, λ_{TiO_2} is the photoelectron mean free path in TiO₂, and $I_{Si,0}$ and I_{Si} are the Si 2p peak intensities before and after ALD. A mean free path of 2 nm for the Si 2p electron passing through the TiO₂ overlayer was used. The estimated TiO₂ thickness was calculated for the FPBA-, OH-, and H-Si(100) surfaces for different number of ALD cycles. The OH-terminated Si(100) surface shows a nearly perfect linear growth of TiO₂ with increasing number of ALD cycles with an $R^2 = 0.98$.

On the other hand, the FPBA-Si(100) shows a slower TiO₂ growth which is smaller than 0.25 nm in total up to 20 ALD cycles. After 30 and 50 cycles the TiO₂ growth rate increases, and shows a more linear behavior, indicating that the selectivity is lost at this point. To compare with a standard non-growth surface, the H-Si (100) was also considered. After 20 cycles the growth of TiO₂ is similar to that on the FPBA-Si(100) surface, and after 30 and 50 cycles the growth of TiO₂ is linear. This shows that the growth of TiO₂ on the H-Si(100) surface is similar to the growth of TiO₂ on the FPBA-Si(100). It is important to emphasize that the H-Si(100) was re-dipped in HF before loading in the ALD chamber to guarantee that it has minimal oxidation, while the FPBA-Si(100) surface did not need any additional treatment steps. Overall, it appears that FPBA-Si(100) is just as efficient as the H-Si(100) surface in its role as a NGA. However, it also has a number of advantages. The FPBA-Si(100) can be easily handled in ambient conditions and is exceptionally resistant to further oxidation. It is passivated by the Si-O-B bonds and is protected with the (-O-)₂B-(C₆H₄)-F functional groups that apparently delay the growth of TiO₂. This surface does not undergo any noticeable changes for days according to XPS. The stability of the FPBA-Si(100) and H-Si(100) surfaces in ambient compared in the Appendix E (Figures E2 and E3) indicates that unlike FPBA-Si(100) surface, H-Si(100) oxidizes very substantially within hours.

The selectivity was also calculated using the estimated TiO₂ thickness on each surface instead of the Ti 2p/Si 2p ratios. Table 7.3 shows the results obtained using equation (1). It shows that the selectivity on FPBA-Si(100) is maintained for up to 20 cycles and after 30 cycles the selectivity decreases substantially. Additionally, the selectivity on H-Si(100) subject to identical ALD cycles as those of FPBA-Si(100) surface is also reported, the selectivity trend for both surfaces is nearly the same.

Number of ALD Cycles	FPBA-Si(100) Selectivity	H-Si(100) Selectivity
5	0.64 ± 0.03	-
10	0.69 ± 0.02	0.62 ± 0.11
15	0.61 ± 0.04	0.58 ± 0.09
20	0.71 ± 0.11	0.58 ± 0.04
30	0.27 ± 0.03	0.32 ± 0.06
50	0.11 ± 0.03	0.03 ± 0.01

Table 7.3: FPBA-Si (100) selectivity calculated from equation (1) using the estimated TiO₂ thickness obtained from equation (2)

To further confirm the TiO₂ thickness estimated from XPS and complement the obtained chemical information using F and B as spectroscopic labels, ToF-SIMS depth profiles was used to analyze the OH-, and FPBA-Si (100) surfaces after 50 and 200 ALD cycles, which is described in the following section 7.3.3. 50 and 200 cycles were chosen as representative points, since these samples exhibited consistent and reliable properties determined by combining ToF-SIMS, ellipsometry and profilometry measurements and also in both cases the films deposited were very smooth according to AFM. According to the AFM measurements shown in Appendix E (Figure E4), after 50 cycles a uniform layer is deposited on both surfaces, with RMS of 0.23 nm for the FPBA-Si(100) surface and RMS of 0.25 nm for the OH-Si(100) surface.

7.3.3 ToF-SIMS depth profile on growth and non-growth surfaces

The calibration of the sputtering rate was done with two techniques: Ellipsometry for the TiO₂ layer deposited with ALD and profilometry for the Si(100) substrate.

The ellipsometry analysis was performed on a J. A Woolam M-2000VI. A three-layer (film/ native oxide/ silicon) Cauchy model was used to determine the film thickness of the TiO₂ layer on the OH-Si(100) after 200 cycles of TiO₂ ALD. In the model, the thickness of the native oxide was 20 Å. The thickness obtained by ellipsometry was used to calibrate the sputtering rate of the TiO₂ layer in ToF-SIMS depth profile. The sputtering rate for TiO₂ based on this calibration was 0.112 nm/s.

The profilometry analysis was completed with a Bruker Dektak XT profilometer, range of 6.5 µm, 3 mg force, and a tip width of 5 µm, run on valley settings. The craters made on the Si(100) by ToF-SIMS depth profiling were measured with profilometry, and this measurement was used to establish a sputtering rate for the depth calibration of the Si(100) substrate. The sputter rate used for this calibration of silicon removal was 0.125 nm/s.

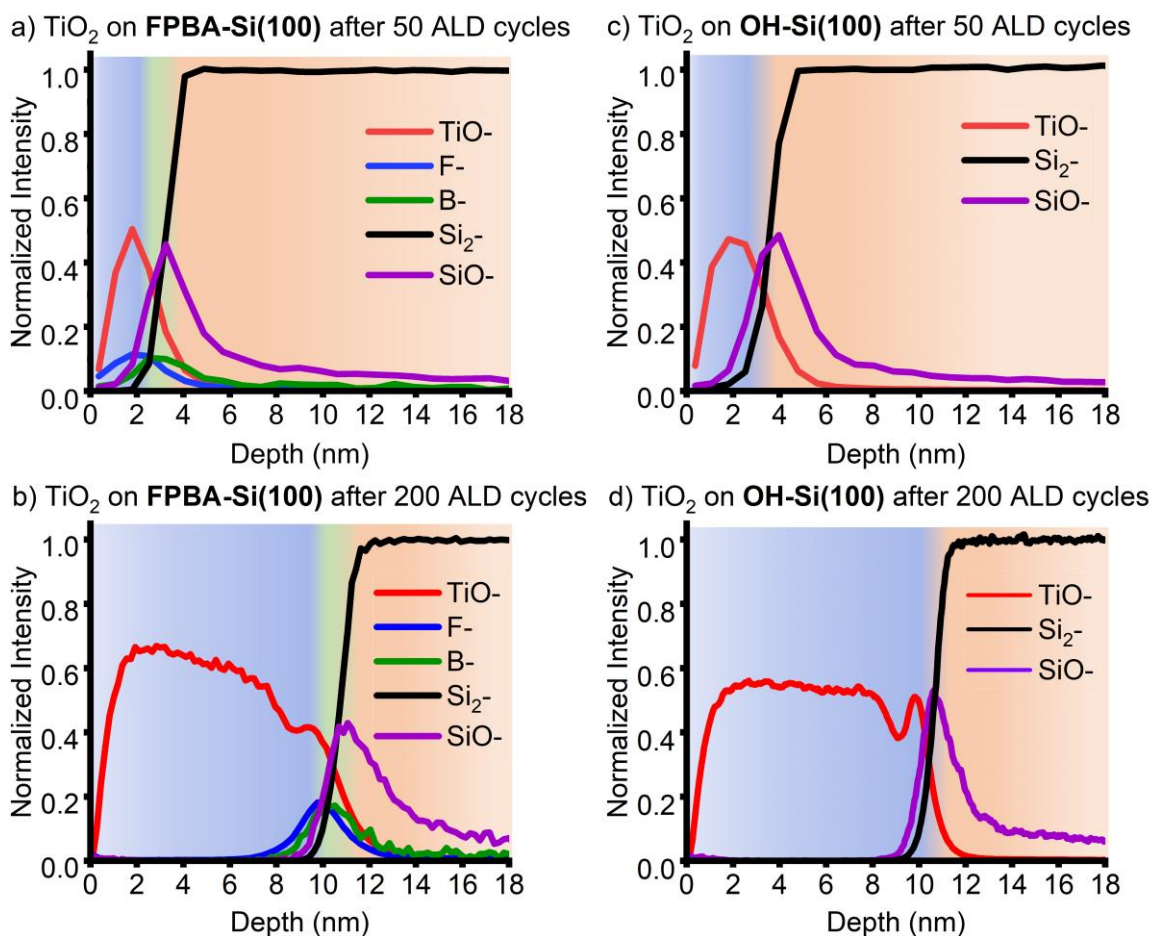


Figure 7.7: ToF-SIMS depth profile showing the intensity of the TiO^- , F^- , B^- , Si_2^- , and SiO^- ions vs depth of a) FPBA-Si(100) after 50 cycles, b) FPBA-Si(100) after 200 cycles. And the intensity of TiO^- , Si_2^- , and SiO^- ions vs depth of c) OH-Si(100) after 50 cycles and d) OH-Si(100) after 200 cycles. All the intensities were normalized to Si_2^- at saturation.

On the FPBA-Si(100) surface after 50 ALD cycles (Figure 7.7 a), the interface between titania and silicon is observed at approximately 2.9 nm in depth, if the depth is calibrated as described above in section 7.3.3 and the appropriate sputtering rates are obtained to convert the sputtering time scale into the depth scale. Right at the interface, the F^- and B^- are present, and a small shift of about 6 Å between F^- and B^- negative ions

is observed, which corresponds to the length of the FPBA molecule according to the computational models reported in our previous studies.¹¹ The FPBA molecule binds to the Si surface forming B-O-Si bonds, which was confirmed with XPS, therefore the SiO⁻ fragment which is also at the interface corresponds to the O-Si bond formed after the FPBA reaction.

After 200 ALD cycles on the FPBA-Si(100) surface, the interface between titania and silicon is recorded at approximately 10.5 nm in depth, and it is also observed that the SiO⁻, F⁻ and B⁻ ions remain at the interface at their original positions, as a small shift of about 6 Å between F⁻ and B⁻ negative ions also remains in place. This observation is consistent with the FPBA molecule staying at the interface without any of its constituents diffusing into the TiO₂ layer. The difference in depth location for F and B elements is also fully consistent with the entire fluorophenylboronic functionality being intact.

On the OH-Si(100) surface after 50 cycles, it is observed that the interface between titania and silicon is just above 3.5 nm in depth (reflecting nearly the same TiO₂ thickness as that estimated in XPS experiments). For this sample, SiO⁻ ion at the interface corresponds to the oxidized silicon surface as confirmed with XPS with the peak at ~103 eV.

After 200 cycles on the OH-Si (100) surface, the interface between titania and silicon is at approximately 10.6 nm.

Thus, following 50 cycles of ALD onto FPBA-Si(100) surface, the thickness of TiO₂ according to ToF-SIMS measurements is ~2.9 nm, and the TiO₂ layer on the OH-Si(10) surface is ~ 0.6 nm thicker, which matches with the results obtained for the estimated TiO₂ thickness calculated with equation (2).

After 200 ALD cycles, the TiO₂ thickness on both FPBA- and OH-Si(100) surfaces appears to be similar. At this point the selectivity is completely lost, the interface is buried, and the accuracy of pinpointing it precisely is limited. However, it is more important for the thicker TiO₂ layer to interrogate the structure of the interface between oxide and silicon substrate. As was mentioned above, B and F are used as spectroscopic labels in XPS and ToF-SIMS experiments, providing information about the intactness and stability of the molecule at the interface.

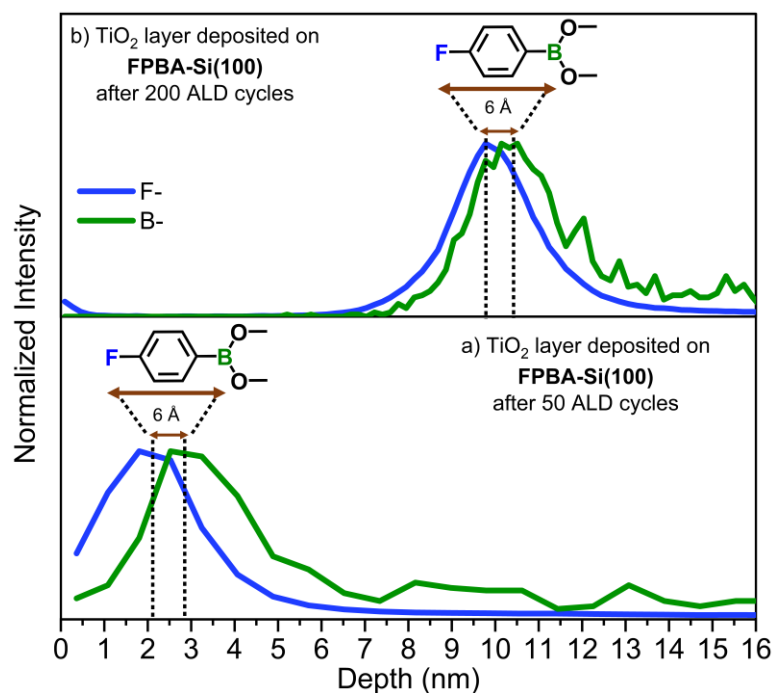


Figure 7.8: ToF-SIMS depth profile showing the intensity of the F⁻ and B⁻ ions vs depth of FPBA-Si(100) after 50 cycles a), and FPBA-Si(100) after 200 cycles b).

Figure 7.8 provides a zoomed-in comparison of the F⁻ and B⁻ ions intensity vs depth obtained by ToF-SIMS depth profile of the FPBA-Si(100) surface after 50 and 200 TiO₂ ALD cycles. It is clear that the 4-fluorophenylboronic functionality remains

at the interface following the process and that the distance between F⁻ and B⁻ labels is maintained at both depths. This set of measurements also suggests that this chemical group remains intact, as a clear and reproducible shift of 6 Å between F⁻ and B⁻ is observed. The theoretically predicted distance between B⁻ and F⁻ in the FPBA molecule after the attachment to the Si(100) is 5.7 Å as calculated from the computational models reported in our previous studies.¹¹ To further confirm the intactness of the (-O-)₂B-(C₆H₄)-F functional group, the CF⁻, FC₆H₄BO₂⁻ and C₆H₄⁻ fragments were also identified at the interface of the TiO₂ layer and the FPBA-modified Si(100) as shown in Figure E5 in Appendix E. Although some of these fragments exhibit very low intensity and thus low signal-to-noise ratios, it is apparent that the CF⁻ depth profile largely coincides with the F⁻ depth profile, confirming the presence of the C-F bond at the TiO₂/Si(100) interface, consistent with the XPS observations that were discussed above for the sample prepared by 50 cycles of ALD. On the other hand, the peak position of the B⁻ appears to precede the small signals corresponding to the aromatic ring and to the entire molecular fragment (FC₆H₄BO₂⁻), thus confirming the high sensitivity of the ToF-SIMS technique and reinforcing the hypothesis that the 4-fluorophenylboronic functionality remains intact following the loss of selectivity of the functionalized surface and eventual TiO₂ deposition.

This behavior and stability may be important not only to the use of FPBA-modified surfaces as NGA, but also brings up an important issue of modifying electronic and physical properties of the interfaces obtained on SMI-modified substrates following the eventual loss of selectivity.

7.4 Conclusions

The research detailed in this chapter reveals that the FPBA-treated Si(100) surface effectively inhibits the deposition of TiO₂ for up to 20 cycles, exhibiting a selectivity of 71% when compared to the GA OH-treated Si(100) in the ALD process utilizing TDMAT and water. This behavior is very similar to a traditional H-Si(100) surface acting as NGA in the same deposition scheme, but FPBA-Si(100) substrate exhibited exceptional stability in ambient, being stable for days compared to hours or even minutes for H-Si(100). F- and B- served as tracking labels in XPS and ToF-SIMS investigations to calculate coverage and evaluate the intactness and stability of the 4-fluorophenylboronic functional group at the interface with silicon following the ALD process. It appears that the entire chemical functionality remains intact in this system, which may be very important not only for the use of FPBA-Si(100) as a NGA, but also in designing interfaces with tunable electronic properties.

Chapter 8

SUMMARY AND FUTURE WORK

This dissertation provides fundamental understanding of reacting functionalized semiconductor surfaces with boron- and nitrogen-containing molecules. In the case of flat surfaces, these reactions can be used for monolayer doping or as a deposition resist. For oxide nanomaterials, the same approach can be used for spectroscopic labeling or for further functionalization.

The monolayer doping of semiconductors is a strategy that allows ultra-shallow doping with high dopant concentrations, which plays a crucial role in tuning the electrical properties of the semiconductor materials. The process involves chemical functionalization of the semiconductor surface with a monolayer of the dopant-containing precursor followed by the subsequent diffusion of the dopant by a rapid thermal annealing step. In chapters 3-5, the monolayer functionalization of Si(100) single crystal surface with boron- and nitrogen-containing compounds, including boron trichloride, hydrazine, boric acid, and 4-fluorophenylboronic acid, were studied in order to understand the interactions of these molecules with the different terminated surfaces (H-, Br-, and Cl-Si(100)) for designing possible silicon doping processes. We have confirmed selective reactions between boron trichloride, boric acid and 4-fluorophenylboronic acid and Cl-Si(100) surface. In addition it was also shown that different amounts of B, which can lead to p-type doping after an RTA step, can be introduced to the surface depending on the precursor chosen, since each reaction has different energy requirements, making some reactions more favorable than others.

It is also important to study other precursors that introduce atoms from the group 5A of the periodic table, such as N, P, and As. In this dissertation, the introduction of N was studied using hydrazine as the precursor. It was shown that the amount of N introduced to the surface can be controlled depending on the termination of the Si surface, while hydrazine can introduce amounts of nitrogen well above a monolayer saturation on a H-Si(100), it will only form a monolayer on a Cl- and Br-terminated Si surface even if the halogen-terminated surfaces were prepared in vacuum or in solution. For future work, the monolayer doping approach can also be applied to the study of other precursors, such as PCl_3 , and AlCl_3 , to investigate the potential to form P-Si or Al-Si direct bonds and selectivity with different terminations on Si(100). The use of XPS in combination with DFT calculations is key to identifying the species formed on the surface as well as to evaluating the thermodynamics of the reactions.

In chapter 6, monolayer functionalization of metal oxide surfaces such as TiO_2 and Al_2O_3 nanoparticles with 4-fluorophenylboronic acid in solution was investigated in order to understand the attachment chemistry and to develop spectroscopic labels for surface characterization. The use of solid-state NMR in combination with XPS and FTIR was critical in this study to elucidate the type of attachment in each metal oxide substrate. In addition to that, the DFT theoretical spectra complemented the study and were essential to determine and confirm different attachment types. For future work, further investigations can be done with complex materials using multiple spectroscopic probes as identifiers. Furthermore, this approach can be applied to area selective deposition (ASD), since it is key to know the attachment chemistry of the small molecule inhibitor (SMI) on different substrates. This will help with the selection and/or design of the SMI, improving the efficiency of the ASD process.

In chapter 7, the knowledge acquired in the previous studies was combined to use the 4-fluorophenylboronic acid (FPBA) as an SMI to block the growth of TiO_2 and design an ASD process. The FPBA was used to passivate the Si(100) surface and the F and B from the molecule served as spectroscopic labels to confirm the passivation and to evaluate the intactness of the molecule on the interface after the deposition of TiO_2 . A combination of XPS and ToF-SIMS were crucial to evaluate the growth of TiO_2 on the non-growth area (FPBA-Si(100) surface), and the growth area (OH-Si(100)). The selectivity obtained was 71 %, which was similar to the selectivity obtained with the standard non-growth surface H-Si(100). The advantage of using the FPBA as a small molecule inhibitor is that the surfaces modified with this molecule are very stable in ambient compared to the H-Si(100) surface and the spectroscopic labels can be used to evaluate the changes during the ASD process.

REFERENCES

- (1) Teplyakov, A. V.; Bent, S. F. Semiconductor Surface Functionalization for Advances in Electronics, Energy Conversion, and Dynamic Systems. *Journal of Vacuum Science & Technology A: Vacuum, Surfaces, and Films* **2013**, *31* (5), 050810. <https://doi.org/10.1116/1.4810784>.
- (2) Gao, F.; Teplyakov, A. V. Challenges and Opportunities in Chemical Functionalization of Semiconductor Surfaces. *Appl Surf Sci* **2017**, *399*, 375–386. <https://doi.org/10.1016/j.apsusc.2016.12.083>.
- (3) Ho, J. C.; Yerushalmi, R.; Jacobson, Z. A.; Fan, Z.; Alley, R. L.; Javey, A. Controlled Nanoscale Doping of Semiconductors via Molecular Monolayers. *Nat Mater* **2008**, *7* (1), 62–67. <https://doi.org/10.1038/nmat2058>.
- (4) Veerbeek, J.; Huskens, J. Applications of Monolayer-Functionalized H-Terminated Silicon Surfaces: A Review. *Small Methods* **2017**, *1* (4), 1700072. <https://doi.org/10.1002/smt.201700072>.
- (5) Tong, Q. Y.; Lee, T. H.; Gösele, U.; Reiche, M.; Ramm, J.; Beck, E. The Role of Surface Chemistry in Bonding of Standard Silicon Wafers. *J Electrochem Soc* **1997**, *144* (1), 384–389. <https://doi.org/10.1149/1.1837415>.
- (6) Haber, J. A.; Lewis, N. S. Infrared and X-Ray Photoelectron Spectroscopic Studies of the Reactions of Hydrogen-Terminated Crystalline Si(111) and Si(100) Surfaces with Br₂, I₂, and Ferrocenium in Alcohol Solvents. *Journal of Physical Chemistry B* **2002**, *106* (14), 3639–3656. <https://doi.org/10.1021/jp0102872>.
- (7) Ihm, K.; Han, J. H.; Kim, B.; Chung, S.; Hwang, C. C.; Kang, T. H.; Kim, K. J.; Jung, Y. J.; An, K. S. Selective Adsorption of Benzoic Acid Species on Patterned OH/Si(100) Surface. *J Appl Phys* **2006**, *100* (4). <https://doi.org/10.1063/1.2266035>.
- (8) Ikeda, H.; Hotta, K.; Yamada, T.; Zaima, S.; Iwano, H.; Yasuda, Y. Oxidation of H-Terminated Si(100) Surfaces Studied by High-Resolution Electron Energy Loss Spectroscopy. *J Appl Phys* **1995**, *77* (10), 5125–5129. <https://doi.org/10.1063/1.359323>.
- (9) Pavlova, T. V.; Shevlyuga, V. M.; Andryushechkin, B. V.; Eltsov, K. N. Dangling Bonds on the Cl- and Br-Terminated Si(100) Surfaces. *Appl Surf Sci* **2022**.
- (10) Frederick, E.; Dwyer, K. J.; Wang, G. T.; Misra, S.; Butera, R. E. The Stability of Cl-, Br-, and I-Passivated Si(100)-(2 × 1) in Ambient Environments for Atomically-Precise Pattern Preservation. *Journal of Physics Condensed Matter* **2021**, *33* (44). <https://doi.org/10.1088/1361-648X/ac1aa4>.

- (11) Silva-Quinones, D.; Butera, R. E.; Wang, G. T.; Teplyakov, A. V. Solution Chemistry to Control Boron-Containing Monolayers on Silicon: Reactions of Boric Acid and 4-Fluorophenylboronic Acid with H- And Cl-Terminated Si(100). *Langmuir* **2021**, *37* (23), 7194–7202. <https://doi.org/10.1021/acs.langmuir.1c00763>.
- (12) Silva-Quinones, D.; He, C.; Butera, R. E.; Wang, G. T.; Teplyakov, A. V. Reaction of BCl₃ with H- and Cl-Terminated Si(1 0 0) as a Pathway for Selective, Monolayer Doping through Wet Chemistry. *Appl Surf Sci* **2020**, 533. <https://doi.org/10.1016/j.apsusc.2020.146907>.
- (13) Silva-Quinones, D.; He, C.; Dwyer, K. J.; Butera, R. E.; Wang, G. T.; Teplyakov, A. V. Reaction of Hydrazine with Solution- And Vacuum-Prepared Selectively Terminated Si(100) Surfaces: Pathways to the Formation of Direct Si-N Bonds. *Langmuir* **2020**, *36* (43), 12866–12876. <https://doi.org/10.1021/acs.langmuir.0c02088>.
- (14) Byron, C.; Silva-Quinones, D.; Sarkar, S.; Brown, S. C.; Bai, S.; Quinn, C. M.; Grzenda, Z.; Chinn, M. S.; Teplyakov, A. V. Attachment Chemistry of 4-Fluorophenylboronic Acid on TiO₂ and Al₂O₃ Nanoparticles. *Chemistry of Materials* **2022**, *34* (23), 10659–10669. <https://doi.org/10.1021/acs.chemmater.2c02789>.
- (15) Zhang, C.; Chang, S.; Dan, Y. Advances in Physics : X Advances in Ultrashallow Doping of Silicon. *Adv Phys X* **2021**, *6* (1). <https://doi.org/10.1080/23746149.2020.1871407>.
- (16) O’Connell, J.; Biswas, S.; Duffy, R.; Holmes, J. D. Chemical Approaches for Doping Nanodevice Architectures. *Nanotechnology*. Institute of Physics Publishing July 15, 2016. <https://doi.org/10.1088/0957-4484/27/34/342002>.
- (17) Ye, L.; de Jong, M. P.; Kudernac, T.; van der Wiel, W. G.; Huskens, J. Doping of Semiconductors by Molecular Monolayers: Monolayer Formation, Dopant Diffusion and Applications. *Mater Sci Semicond Process* **2017**, *62* (October 2016), 128–134. <https://doi.org/10.1016/j.mssp.2016.12.018>.
- (18) Parsons, G. N.; Clark, R. D. Area-Selective Deposition: Fundamentals, Applications, and Future Outlook. *Chemistry of Materials* **2020**, *32* (12), 4920–4953. <https://doi.org/10.1021/acs.chemmater.0c00722>.
- (19) Schubert, E. F. *Doping in III-V Semiconductors*; 1993.
- (20) Kim, Y.; Massoud, H. Z.; Fair, R. B. The Effect of Ion-Implantation Damage on Dopant Diffusion in Silicon during Shallow-Junction Formation. *J Electron Mater* **1989**, *18* (2), 143–150. <https://doi.org/10.1007/BF02657400>.
- (21) Long, B.; Alessio Verni, G.; O’Connell, J.; Holmes, J.; Shayesteh, M.; O’Connell, D.; Duffy, R. Molecular Layer Doping: Non-Destructive Doping of Silicon and Germanium. *Proceedings of the International Conference on Ion Implantation Technology* **2014**, 1–4. <https://doi.org/10.1109/IIT.2014.6939995>.
- (22) Chuang, S.-S.; Cho, T.-C.; Sung, P.-J.; Kao, K.-H.; Chen, H. J. H.; Lee, Y.-J.; Current, M. I.; Tseng, T.-Y. Ultra-Shallow Junction Formation by Monolayer Doping Process in Single Crystalline Si and Ge for Future CMOS Devices. *ECS*

- Journal of Solid State Science and Technology* **2017**, 6 (5), P350–P355. <https://doi.org/10.1149/2.0011707jss>.
- (23) Yu, M. L.; Vitkavage, D. J.; Meyerson, B. S. Doping Reaction of PH₃ and B₂H₆ with Si(100). *J Appl Phys* **1986**, 59 (12), 4032–4037. <https://doi.org/10.1063/1.336708>.
- (24) Oviroh, P. O.; Akbarzadeh, R.; Pan, D.; Coetzee, R. A. M.; Jen, T. C. New Development of Atomic Layer Deposition: Processes, Methods and Applications. *Science and Technology of Advanced Materials*. Taylor and Francis Ltd. December 31, 2019, pp 465–496. <https://doi.org/10.1080/14686996.2019.1599694>.
- (25) Sakib, S.; Bakhshandeh, F.; Saha, S.; Soleymani, L.; Zhitomirsky, I. Surface Functionalization of Metal Oxide Semiconductors with Catechol Ligands for Enhancing Their Photoactivity. *Solar RRL*. John Wiley and Sons Inc October 1, 2021. <https://doi.org/10.1002/solr.202100512>.
- (26) Ahangaran, F.; Navarchian, A. H. Recent Advances in Chemical Surface Modification of Metal Oxide Nanoparticles with Silane Coupling Agents: A Review. *Advances in Colloid and Interface Science*. Elsevier B.V. December 1, 2020. <https://doi.org/10.1016/j.cis.2020.102298>.
- (27) Liu, F.; Quan, B.; Liu, Z.; Chen, L. Surface Characterization Study on SnO₂ Powder Modified by Thiourea. *Mater Chem Phys* **2005**, 93 (2–3), 301–304. <https://doi.org/10.1016/j.matchemphys.2005.03.058>.
- (28) Elbhiri, Z.; Chevalier, Y.; Chovelon, J.-M.; Jaffrezic-Renault, N. *Grafting of Phosphonate Groups on the Silica Surface for the Elaboration of Ion-Sensitive Field-Effect Transistors*; 2000; Vol. 52. www.elsevier.com/locate/talanta.
- (29) Hua, F.; Swihart, M. T.; Ruckenstein, E. Efficient Surface Grafting of Luminescent Silicon Quantum Dots by Photoinitiated Hydrosilylation. *Langmuir* **2005**, 21 (13), 6054–6062. <https://doi.org/10.1021/la0509394>.
- (30) Marnett, A.; Karasulu, B.; Verheijen, M. A.; Mackus, A. J. M.; Kessels, W. M. M.; Roozeboom, F. (Invited) Area-Selective Atomic Layer Deposition: Role of Surface Chemistry. *ECS Trans* **2017**, 80 (3), 39–48. <https://doi.org/10.1149/08003.0039ecst>.
- (31) Methapanon, R.; Bent, S. F. Comparative Study of Titanium Dioxide Atomic Layer Deposition on Silicon Dioxide and Hydrogen-Terminated Silicon. *Journal of Physical Chemistry C* **2010**, 114 (23), 10498–10504. <https://doi.org/10.1021/jp1013303>.
- (32) Clerix, J.-W. J.; Dianat, G.; Delabie, A.; Parsons, G. N. In Situ Analysis of Nucleation Reactions during TiCl₄/H₂O Atomic Layer Deposition on SiO₂ and H-Terminated Si Surfaces Treated with a Silane Small Molecule Inhibitor. *Journal of Vacuum Science & Technology A* **2023**, 41 (3), 032406. <https://doi.org/10.1116/6.0002493>.
- (33) Parke, T.; Silva-Quinones, D.; Wang, G. T.; Teplyakov, A. V. The Effect of Surface Terminations on the Initial Stages of TiO₂ Deposition on Functionalized Silicon. *ChemPhysChem* **2022**. <https://doi.org/10.1002/cphc.202200724>.

- (34) Nye, R. A.; Song, S. K.; Van Dongen, K.; Delabie, A.; Parsons, G. N. Mechanisms for Undesired Nucleation on H-Terminated Si and Dimethylamino-Trimethylsilane Passivated SiO₂ during TiO₂ Area-Selective Atomic Layer Deposition. *Appl Phys Lett* **2022**, *121* (8). <https://doi.org/10.1063/5.0106132>.
- (35) McDonnell, S.; Longo, R. C.; Seitz, O.; Ballard, J. B.; Mordi, G.; Dick, D.; Owen, J. H. G.; Randall, J. N.; Kim, J.; Chabal, Y. J.; Cho, K.; Wallace, R. M. Controlling the Atomic Layer Deposition of Titanium Dioxide on Silicon: Dependence on Surface Termination. *Journal of Physical Chemistry C* **2013**, *117* (39), 20250–20259. <https://doi.org/10.1021/jp4060022>.
- (36) Yasmeen, S.; Ryu, S. W.; Lee, S. H.; Lee, H. B. R. Atomic Layer Deposition Beyond Thin Film Deposition Technology. *Advanced Materials Technologies*. John Wiley and Sons Inc 2022. <https://doi.org/10.1002/admt.202200876>.
- (37) Mackus, A. J. M.; Merckx, M. J. M.; Kessels, W. M. M. From the Bottom-Up: Toward Area-Selective Atomic Layer Deposition with High Selectivity. *Chemistry of Materials* **2019**, *31* (1), 2–12. <https://doi.org/10.1021/acs.chemmater.8b03454>.
- (38) Bansal, A.; Li, X.; Yi, S. I.; Weinberg, W. H.; Lewis, N. S. Spectroscopic Studies of the Modification of Crystalline Si(111) Surfaces with Covalently-Attached Alkyl Chains Using a Chlorination/Alkylation Method. *Journal of Physical Chemistry B* **2001**, *105* (42), 10266–10277. <https://doi.org/10.1021/jp010284p>.
- (39) Trenhaile, B. R.; Agrawal, A.; Weaver, J. H. Oxygen Atoms on Si (100) - (2×1): Imaging with Scanning Tunneling Microscopy. *Appl Phys Lett* **2006**, *89* (15), 25–28. <https://doi.org/10.1063/1.2362623>.
- (40) Spencer, N. D.; Goddard, P. J.; Davies, P. W.; Kitson, M.; Lambert, R. M. A Simple, Controllable Source for Dosing Molecular Halogens in UHV. *Journal of Vacuum Science & Technology A: Vacuum, Surfaces, and Films* **1983**, *1* (3), 1554–1555. <https://doi.org/10.1116/1.572185>.
- (41) Aldao, C. M.; Weaver, J. H. Halogen Etching of Si via Atomic-Scale Processes. *Prog Surf Sci* **2001**, *68* (4–6), 189–230. [https://doi.org/10.1016/S0079-6816\(01\)00047-8](https://doi.org/10.1016/S0079-6816(01)00047-8).
- (42) Watts, J. F.; Wolstenholme, John. *Surface and Thin Film*; Wiley, 2008.
- (43) Grehl, T. *Improvement in TOF-SIMS Instrumentation for Analytical Application and Fundamental Research*; 2003.
- (44) Wehbe, N.; Houssiau, L. Comparative Study of the Usefulness of Low Energy Cs⁺, Xe⁺, and O₂⁺ Ions for Depth Profiling Amino-Acid and Sugar Films. *Anal Chem* **2010**, *82* (24), 10052–10059. <https://doi.org/10.1021/ac101696c>.
- (45) Chalmers, J. M.; Griffiths, P. R. *HANDBOOK OF VIBRATIONAL SPECTROSCOPY*; 2002.
- (46) Griffiths, P. R.; Haseth, J. A. De. *Fourier Transform Infrared Spectrometry Second Edition*.
- (47) Muller, K.; Geppi, M. *Solid State NMR*; 2021.
- (48) Hayashi, S.; Hayamizu, K. Shift References in High-Resolution Solid-State NMR. *Bull. Chem. Soc. Jpn.* **1989**, No. 62, 2429–2430.

- (49) Gaussian 09, Revision D.01, M. J. Frisch, G. W. Trucks, H. B. Schlegel, G. E. Scuseria, M. A. Robb, J. R. Cheeseman, G. Scalmani, V. Barone, B. Mennucci, G. A. Petersson, H. Nakatsuji, M. Caricato, X. Li, H. P. Hratchian, A. F. Izmaylov, J. Bloino, G. Zhe. **2013**.
- (50) McLean, A. D.; Chandler, G. S. Contracted Gaussian Basis Sets for Molecular Calculations. I. Second Row Atoms, Z=11-18. *J Chem Phys* **1980**, 72 (10), 5639–5648. <https://doi.org/10.1063/1.438980>.
- (51) Krishnan, R.; Binkley, J. S.; Seeger, R.; Pople, J. A. Self-Consistent Molecular Orbital Methods. XX. A Basis Set for Correlated Wave Functions. *J Chem Phys* **1980**, 72 (1), 650–654. <https://doi.org/10.1063/1.438955>.
- (52) Leftwich, T. R.; Teplyakov, A. V. Calibration of Computationally Predicted N 1s Binding Energies by Comparison with X-Ray Photoelectron Spectroscopy Measurements. *J Electron Spectros Relat Phenomena* **2009**, 175 (1–3), 31–40. <https://doi.org/10.1016/j.elspec.2009.07.002>.
- (53) Giesbers, M.; Marcelis, A. T. M.; Zuilhof, H. Simulation of XPS C1s Spectra of Organic Monolayers by Quantum Chemical Methods. *Langmuir* **2013**, 29 (15), 4782–4788. <https://doi.org/10.1021/la400445s>.
- (54) Kung, H.; Teplyakov, A. Selectivity and Mechanism of Thermal Decomposition of β -Diketones on ZnO Powder. *J Catal* **2015**, 330, 145–153. <https://doi.org/10.1016/j.jcat.2015.07.021>.
- (55) Zhao, J.; Gao, F.; Pujari, S. P.; Zuilhof, H.; Teplyakov, A. V. Universal Calibration of Computationally Predicted N 1s Binding Energies for Interpretation of XPS Experimental Measurements. *Langmuir* **2017**, 33 (41), 10792–10799. <https://doi.org/10.1021/acs.langmuir.7b02301>.
- (56) Gouin, X.; Bois, L.; Laurent, Y. *Characterization of the Nitridation Process of Boric Acid*; 1995; Vol. 224.
- (57) H. Kiinzli, P. Gantenbein, R. S. and P. O. Influence of B₂H₆/CH₄ and B(CH₃)₃ as Process Gas on Boron Carbide Coatings: An in Situ Photoelectron Spectroscopy Study. *Nuclear Materials* **1992**, 198, 622–626. <https://doi.org/10.1080/02670836.2018.1446775>.
- (58) Grimme, S.; Antony, J.; Ehrlich, S.; Krieg, H. A Consistent and Accurate Ab Initio Parametrization of Density Functional Dispersion Correction (DFT-D) for the 94 Elements H-Pu. *J. Chem. Phys* **2010**, No. 132, 154104. <https://doi.org/10.1063/1.3382344>.
- (59) Ford, W. E.; Abraham, F.; Scholz, F.; Nelles, G.; Sandford, G.; Wrochem, F. Von. Spectroscopic Characterization of Fluorinated Benzylphosphonic Acid Monolayers on AlO. *The Journal of Physical Chemistry C* **2017**, 121, 1690–1703. <https://doi.org/10.1021/acs.jpcc.6b11089>.
- (60) Zhao, J.; Konh, M.; Teplyakov, A. Surface Chemistry of Thermal Dry Etching of Cobalt Thin Films Using Hexafluoroacetylacetone (HfACH). *Appl Surf Sci* **2018**, 455, 438–445. <https://doi.org/10.1016/j.apsusc.2018.05.182>.
- (61) Szwajca, A.; Krzywiecki, M.; Koroniak, H. Self-Assembled Monolayers of Partially Fluorinated Alcohols on Si(0 0 1): XPS and UV-Photoemission Study.

- J Fluor Chem* **2015**, *180*, 248–256. <https://doi.org/10.1016/j.jfluchem.2015.10.009>.
- (62) Lee, C.; Yang, C.; Parr, R. G. *Development of the Colle-Salvetti Correlation-Energy Formula into a Functional of the Electron Density*; Vol. 37.
- (63) Becke, A. D. A New Mixing of Hartree-Fock and Local Density-Functional Theories. *J Chem Phys* **1993**, *98* (2), 1372–1377. <https://doi.org/10.1063/1.464304>.
- (64) Hay, P. J. Gaussian Basis Sets for Molecular Calculations. The Representation of 3d Orbitals in Transition-metal Atoms. *J. Chem. Phys* **1977**, No. 66, 4377–4384.
- (65) Wachters, A. J. H. Gaussian Basis Set for Molecular Wavefunctions Containing Third-Row Atoms. *J. Chem. Phys* **1970**, No. 66, 1033–1036.
- (66) Curtiss, L. A.; Redfern, P. C.; Rassolov, V.; Kedziora, G.; Pople, J. A. Extension of Gaussian-3 Theory to Molecules Containing Third-Row Atoms K, Ca, Ga-Kr. *Journal of Chemical Physics* **2001**, *114* (21), 9287–9295. <https://doi.org/10.1063/1.1366337>.
- (67) Raghavachari, K.; Trucks, G. W. Highly Correlated Systems. Excitation Energies of First Row Transition Metals Sc-Cu. *J Chem Phys* **1989**, *91* (2), 1062–1065. <https://doi.org/10.1063/1.457230>.
- (68) Grimme, S.; Antony, J.; Ehrlich, S.; Krieg, H. A Consistent and Accurate Ab Initio Parametrization of Density Functional Dispersion Correction (DFT-D) for the 94 Elements H-Pu. *Journal of Chemical Physics* **2010**, *132* (15). <https://doi.org/10.1063/1.3382344>.
- (69) Koopmans, Y. T. *Über Die Zuordnung von Wellenfunktionen Und Zu Den Einzelnen Elektronen Eines Atoms*; 1934.
- (70) Zhao, J.; Gao, F.; Pujari, S. P.; Zuilhof, H.; Teplyakov, A. V. Universal Calibration of Computationally Predicted N 1s Binding Energies for Interpretation of XPS Experimental Measurements. *Langmuir* **2017**, *33* (41), 10792–10799. <https://doi.org/10.1021/acs.langmuir.7b02301>.
- (71) te Velde, G.; Bickelhaupt, F. M.; Baerends, E. J.; Fonseca Guerra, C.; van Gisbergen, S. J. A.; Snijders, J. G.; Ziegler, T. Chemistry with ADF. *J Comput Chem* **2001**, *22* (9), 931–967. <https://doi.org/10.1002/jcc.1056>.
- (72) Perdew, J. P.; Burke, K.; Ernzerhof, M. *Generalized Gradient Approximation Made Simple*; 1996.
- (73) Adamo, C.; Barone, V. Toward Reliable Density Functional Methods without Adjustable Parameters: The PBE0 Model. *Journal of Chemical Physics* **1999**, *110* (13), 6158–6170. <https://doi.org/10.1063/1.478522>.
- (74) Leftwich, T. R.; Teplyakov, A. V. Chemical Manipulation of Multifunctional Hydrocarbons on Silicon Surfaces. *Surf Sci Rep* **2008**, *63* (1), 1–71. <https://doi.org/10.1016/j.surfrep.2007.08.001>.
- (75) Pujari, S. P.; Scheres, L.; Marcelis, A. T. M.; Zuilhof, H. Covalent Surface Modification of Oxide Surfaces. *Angewandte Chemie - International Edition* **2014**, *53* (25), 6322–6356. <https://doi.org/10.1002/anie.201306709>.

- (76) Perrine, K. A.; Teplyakov, A. V. Reactivity of Selectively Terminated Single Crystal Silicon Surfaces. *Chem Soc Rev* **2010**, *39* (8), 3256–3274. <https://doi.org/10.1039/b822965c>.
- (77) Puglisi, R. A.; Caccamo, S.; D’Urso, L.; Fisichella, G.; Giannazzo, F.; Italia, M.; La Magna, A. A Comprehensive Study on the Physicochemical and Electrical Properties of Si Doped with the Molecular Doping Method. *Physica Status Solidi (A) Applications and Materials Science* **2015**, *212* (8), 1685–1694. <https://doi.org/10.1002/pssa.201532030>.
- (78) Ye, L.; Pujari, S. P.; Zuilhof, H.; Kudernac, T.; De Jong, M. P.; Van Der Wiel, W. G.; Huskens, J. Controlling the Dopant Dose in Silicon by Mixed-Monolayer Doping. *ACS Appl Mater Interfaces* **2015**, *7* (5), 3231–3236. <https://doi.org/10.1021/am5079368>.
- (79) Mathey, L.; Alphazan, T.; Valla, M.; Veyre, L.; Fontaine, H.; Enyedi, V.; Yckache, K.; Danielou, M.; Kerdiles, S.; Guerrero, J.; Barnes, J. P.; Veillerot, M.; Chevalier, N.; Mariolle, D.; Bertin, F.; Durand, C.; Berthe, M.; Dendooven, J.; Martin, F.; Thieuleux, C.; Grandidier, B.; Copéret, C. Functionalization of Silica Nanoparticles and Native Silicon Oxide with Tailored Boron-Molecular Precursors for Efficient and Predictive p-Doping of Silicon. *Journal of Physical Chemistry C* **2015**, *119* (24), 13750–13757. <https://doi.org/10.1021/acs.jpcc.5b03408>.
- (80) Alphazan, T.; Mathey, L.; Schwarzwälder, M.; Lin, T. H.; Rossini, A. J.; Wischert, R.; Enyedi, V.; Fontaine, H.; Veillerot, M.; Lesage, A.; Emsley, L.; Veyre, L.; Martin, F.; Thieuleux, C.; Copéret, C. Monolayer Doping of Silicon through Grafting a Tailored Molecular Phosphorus Precursor onto Oxide-Passivated Silicon Surfaces. *Chemistry of Materials* **2016**, *28* (11), 3634–3640. <https://doi.org/10.1021/acs.chemmater.5b04291>.
- (81) Tzaguy, A.; Karadan, P.; Killi, K.; Hazut, O.; Amit, I.; Rosenwaks, Y.; Yerushalmi, R. Boron Monolayer Doping: Role of Oxide Capping Layer, Molecular Fragmentation, and Doping Uniformity at the Nanoscale. *Adv Mater Interfaces* **2020**, *7* (5). <https://doi.org/10.1002/admi.201902198>.
- (82) Wu, H.; Guan, B.; Sun, Y.; Zhu, Y.; Dan, Y. Controlled Doping by Self-Assembled Dendrimer-like Macromolecules. *Sci Rep* **2017**, *7*. <https://doi.org/10.1038/srep41299>.
- (83) Shimizu, Y.; Takamizawa, H.; Inoue, K.; Yano, F.; Nagai, Y.; Lamagna, L.; Mazzeo, G.; Perego, M.; Prati, E. Behavior of Phosphorous and Contaminants from Molecular Doping Combined with a Conventional Spike Annealing Method. *Nanoscale* **2014**, *6* (2), 706–710. <https://doi.org/10.1039/c3nr03605g>.
- (84) Oberbeck, L.; Curson, N. J.; Simmons, M. Y.; Brenner, R.; Hamilton, A. R.; Schofield, S. R.; Clark, R. G. Encapsulation of Phosphorus Dopants in Silicon for the Fabrication of a Quantum Computer. *Appl Phys Lett* **2002**, *81* (17), 3197–3199. <https://doi.org/10.1063/1.1516859>.
- (85) Ramanayaka, A. N.; Kim, H. S.; Hagmann, J. A.; Murray, R. E.; Tang, K.; Meisenkothen, F.; Zhang, H. R.; Bendersky, L. A.; Davydov, A. V.; Zimmerman,

- N. M.; Richter, C. A.; Pomeroy, J. M. Towards Superconductivity in P-Type Delta-Doped Si/Al/Si Heterostructures. *AIP Adv* **2018**, *8* (7). <https://doi.org/10.1063/1.5045338>.
- (86) Ward, D. R.; Schmucker, S. W.; Anderson, E. M.; Busmann, E.; Tracy, L.; Lu, T.; Maurer, L. N.; Baczewski, A.; Campbell, D. M.; Marshall, M. T.; Misra, S. Atomic Precision Advanced Manufacturing for Digital Electronics. *Elec. Dev. Fail. Anal* **2020**, *22*(1), 4–11.
- (87) Bansal, A.; Li, X.; Lauermann, I.; Lewis, N. S.; Yi, S. I.; Weinberg, W. H. Alkylation of Si Surfaces Using a Two-Step Halogenation/Grignard Route. *J Am Chem Soc* **1996**, *118* (30), 7225–7226. <https://doi.org/10.1021/ja960348n>.
- (88) Chopra, T. P.; Longo, R. C.; Cho, K.; Halls, M. D.; Thissen, P.; Chabal, Y. J. Ethylenediamine Grafting on Oxide-Free H-, 1/3 ML F-, and Cl-Terminated Si(111) Surfaces. *Chemistry of Materials* **2015**, *27* (18), 6268–6281. <https://doi.org/10.1021/acs.chemmater.5b03156>.
- (89) Rivillon, S.; Chabal, Y. J.; Webb, L. J.; Michalak, D. J.; Lewis, N. S.; Halls, M. D.; Raghavachari, K. Chlorination of Hydrogen-Terminated Silicon (111) Surfaces. *Journal of Vacuum Science & Technology A: Vacuum, Surfaces, and Films* **2005**, *23* (4), 1100–1106. <https://doi.org/10.1116/1.1861941>.
- (90) Lin, Y. H.; Li, H. D.; Jeng, H. T.; Lin, D. S. Energetics and Interactions of Mixed Halogen Adsorbates on the Si(100) Surface. *Journal of Physical Chemistry C* **2011**, *115* (27), 13268–13274. <https://doi.org/10.1021/jp201251j>.
- (91) Ferguson, G. A.; Aureau, D.; Chabal, Y.; Raghavachari, K. Effects of the Local Environment on Si-H Stretching Frequencies for the Mixed Coverage X/H:Si(111) Surface (X = F, Cl, Br, and I). *Journal of Physical Chemistry C* **2010**, *114* (41), 17644–17650. <https://doi.org/10.1021/jp104140u>.
- (92) Bulanin, K. M.; Shah, A. G.; Fitzgerald, D. R.; Doren, D. J.; Teplyakov, A. V. Kinetically Favored Adsorbate Ordering: Hydrogen and Iodine on the Si(100)-2 × 1 Surface. *Journal of Physical Chemistry B* **2002**, *106* (29), 7286–7289. <https://doi.org/10.1021/jp020421y>.
- (93) Herrmann, C. F.; Chen, D.; Boland, J. J. Spontaneous Roughening: Fundamental Limits in Si(100) Halogen Etch Processing. *Phys Rev Lett* **2002**, *89* (9). <https://doi.org/10.1103/PhysRevLett.89.096102>.
- (94) Ferng, S. S.; Wu, S. T.; Lin, D. S.; Chiang, T. C. Mediation of Chain Reactions by Propagating Radicals during Halogenation of H-Masked Si(100): Implications for Atomic-Scale Lithography and Processing. *Journal of Chemical Physics* **2009**, *130* (16). <https://doi.org/10.1063/1.3122987>.
- (95) Santos, H. R. R.; Ramos, M. J.; Gomes, J. A. N. F. A New Strategy to Model the Si (100) Surface. **2005**, *8*, 1461–1468. <https://doi.org/10.1016/j.crci.2004.10.033>.
- (96) Rodríguez-Reyes, J. C. F.; Teplyakov, A. V. Chemistry of Organometallic Compounds on Silicon: The First Step in Film Growth. *Chemistry - A European Journal* **2007**, *13* (33), 9164–9176. <https://doi.org/10.1002/chem.200700856>.

- (97) Perrine, K. A.; Leftwich, T. R.; Weiland, C. R.; Madachik, M. R.; Opila, R. L.; Teplyakov, A. V. Reactions of Aromatic Bifunctional Molecules on Silicon Surfaces: Nitrosobenzene and Nitrobenzene. *Journal of Physical Chemistry C* **2009**, *113* (16), 6643–6653. <https://doi.org/10.1021/jp8082826>.
- (98) Leftwich, T. R.; Madachik, M. R.; Teplyakov, A. V. Dehydrative Cyclocondensation Reactions on Hydrogen-Terminated Si(100) and Si(111): An Ex Situ Tool for the Modification of Semiconductor Surfaces. *J Am Chem Soc* **2008**, *130* (48), 16216–16223. <https://doi.org/10.1021/ja802645t>.
- (99) Nemanick, E. J.; Hurley, P. T.; Webb, L. J.; Knapp, D. W.; Michalak, D. J.; Brunschwig, B. S.; Lewis, N. S. Chemical and Electrical Passivation of Single-Crystal Silicon(100) Surfaces Through a Two-Step Chlorination/Alkylation Process. *Journal of Physical Chemistry B* **2006**, *110* (30), 14770–14778. <https://doi.org/10.1021/jp056773x>.
- (100) Fenner, D. B.; Biegelsen, D. K.; Bringans, R. D. Silicon Surface Passivation by Hydrogen Termination: A Comparative Study of Preparation Methods. *J Appl Phys* **1989**, *66* (1), 419–424. <https://doi.org/10.1063/1.343839>.
- (101) Pilli, A.; Jones, J.; Chugh, N.; Kelber, J.; Pasquale, F.; LaVoie, A. Atomic Layer Deposition of BN as a Novel Capping Barrier for B₂O₃. *Journal of Vacuum Science & Technology A* **2019**, *37* (4), 041505. <https://doi.org/10.1116/1.5092806>.
- (102) Kim, T. S.; Yang, H. Y.; Kil, Y. H.; Choi, S. S.; Jeong, T. S.; Kang, S.; Shim, K. H. Inductively-Coupled BCl₃/O₂ Plasma Etching of Germanium. *Journal of the Korean Physical Society* **2009**, *55* (5 PART 1), 1799–1802. <https://doi.org/10.3938/jkps.55.1799>.
- (103) Pilli, A.; Jones, J.; Lee, V.; Chugh, N.; Kelber, J.; Pasquale, F.; LaVoie, A. In Situ XPS Study of Low Temperature Atomic Layer Deposition of B₂O₃ Films on Si Using BCl₃ and H₂O Precursors. *Journal of Vacuum Science & Technology A* **2018**, *36* (6), 061503. <https://doi.org/10.1116/1.5044396>.
- (104) Queeney, K. T.; Weldon, M. K.; Chang, J. P.; Chabal, Y. J.; Gurevich, A. B.; Sapjeta, J.; Opila, R. L. Infrared Spectroscopic Analysis of the Si/SiO₂ Interface Structure of Thermally Oxidized Silicon. *J Appl Phys* **2000**, *87* (3), 1322–1330. <https://doi.org/10.1063/1.372017>.
- (105) Vijayakumar, A.; Todi, R. M.; Sundaram, K. B. Oxygen Annealing Characterization of Reactively Sputtered SiC_{BN} Thin Films by X-Ray Photoelectron Spectroscopy. *J Electrochem Soc* **2007**, *154* (7), H547. <https://doi.org/10.1149/1.2732166>.
- (106) Lapiano-Smith, D. A.; McFeely, F. R. The Chemisorption and Reaction of BCl₃ with Si(111). *J Appl Phys* **1992**, *72* (10), 4907–4911. <https://doi.org/10.1063/1.352057>.
- (107) Moon, O. M.; Kang, B. C.; Lee, S. B.; Boo, J. H. Temperature Effect on Structural Properties of Boron Oxide Thin Films Deposited by MOCVD Method. *Thin Solid Films* **2004**, *464–465*, 164–169. <https://doi.org/10.1016/j.tsf.2004.05.107>.

- (108) Sato, K.; Fukata, N.; Hirakuri, K. Doping and Characterization of Boron Atoms in Nanocrystalline Silicon Particles. *Appl Phys Lett* **2009**, *94* (16). <https://doi.org/10.1063/1.3120768>.
- (109) Muroi, M.; Yamada, A.; Saito, A.; Habuka, H. Deposition and Etching Behaviour of Boron Trichloride Gas at Silicon Surface. *J Cryst Growth* **2020**, *529*. <https://doi.org/10.1016/j.jcrysgr.2019.125301>.
- (110) Gao, F.; Teplyakov, A. V. Reaction of Hydrazine with a Chlorine-Terminated Si(111) Surface. *Journal of Physical Chemistry C* **2014**, *118* (48), 27998–28006. <https://doi.org/10.1021/jp5095307>.
- (111) Tian, F.; Yang, D.; Opila, R. L.; Teplyakov, A. V. Chemical and Electrical Passivation of Si(1 1 1) Surfaces. *Appl Surf Sci* **2012**, *258* (7), 3019–3026. <https://doi.org/10.1016/j.apsusc.2011.11.030>.
- (112) Yao, H.; Woollam, J. A.; Alterovitz, S. A. Spectroscopic Ellipsometry Studies of HF Treated Si (100) Surfaces. *Appl Phys Lett* **1993**, *62* (25), 3324–3326. <https://doi.org/10.1063/1.109059>.
- (113) Lengyel, I.; Jensen, K. F. A Chemical Mechanism for in Situ Boron Doping during Silicon Chemical Vapor Deposition. *Thin Solid Films* **2000**, *365* (2), 231–241. [https://doi.org/10.1016/S0040-6090\(00\)00758-6](https://doi.org/10.1016/S0040-6090(00)00758-6).
- (114) Waltenburg, H. N.; Yates, J. T. *Surface Chemistry of Silicon*; 1995; Vol. 95. <https://pubs.acs.org/sharingguidelines>.
- (115) Lu, X.; Lin, M. C. Reactions of Some [C, N, O]-Containing Molecules with Si Surfaces: Experimental and Theoretical Studies. *International Reviews in Physical Chemistry*. 2002, pp 137–184. <https://doi.org/10.1080/01442350110109658>.
- (116) Buriak, J. M. Organometallic Chemistry on Silicon and Germanium Surfaces. *Chem Rev* **2002**, *102* (5), 1271–1308. <https://doi.org/10.1021/cr000064s>.
- (117) Tian, F.; Teplyakov, A. V. Silicon Surface Functionalization Targeting Si-N Linkages. *Langmuir* **2013**, *29* (1), 13–28. <https://doi.org/10.1021/la303505s>.
- (118) Bater, C.; Sanders, M.; Craig, J. H. Ammonia as a Precursor in Electron-Enhanced Nitridation of Si(100). *Surface and Interface Analysis* **2000**, *29* (3), 208–214. [https://doi.org/10.1002/\(SICI\)1096-9918\(200003\)29:3<208::AID-SIA688>3.0.CO;2-5](https://doi.org/10.1002/(SICI)1096-9918(200003)29:3<208::AID-SIA688>3.0.CO;2-5).
- (119) Bozso, F.; Avouris, P. Photoemission Studies of the Reactions of Ammonia and N Atoms with Si(100)-(2×1) and Si(111)-(7×7) Surfaces. *Phys Rev B* **1988**, *38* (6), 3937–3942. <https://doi.org/10.1103/PhysRevB.38.3937>.
- (120) Rodríguez-Reyes, J. C. F.; Teplyakov, A. V. Role of Surface Strain in the Subsurface Migration of Adsorbates on Silicon. *Phys Rev B Condens Matter Phys* **2008**, *78* (16), 37–39. <https://doi.org/10.1103/PhysRevB.78.165314>.
- (121) Tian, F.; Cui, Y.; Teplyakov, A. V. Nitroxidation of H-Terminated Si(111) Surfaces with Nitrobenzene and Nitrosobenzene. *Journal of Physical Chemistry C* **2014**, *118* (1), 502–512. <https://doi.org/10.1021/jp4102702>.
- (122) Morita, Y.; Ishida, T.; Tokumoto, H. Monolayer Nitridation of Si(001) Surfaces. *Japanese Journal of Applied Physics, Part 1: Regular Papers and Short Notes*

- and Review Papers* **2002**, *41* (4 B), 2459–2462. <https://doi.org/10.1143/JJAP.41.2459>.
- (123) Agnihotri, O. P.; Jain, S. C.; Poortmans, J.; Szlufcik, J.; Beaucarne, G.; Nijs, J.; Mertens, R. Advances in Low Temperature Processing of Silicon Nitride Based Dielectrics and Their Applications in Surface Passivation and Integrated Optical Devices. *Semicond Sci Technol* **2000**, *15* (7). <https://doi.org/10.1088/0268-1242/15/7/201>.
- (124) MäcKel, H.; Lüdemann, R. Detailed Study of the Composition of Hydrogenated SiN_x Layers for High-Quality Silicon Surface Passivation. *J Appl Phys* **2002**, *92* (5), 2602–2609. <https://doi.org/10.1063/1.1495529>.
- (125) Kato, K.; Matsushita, D.; Muraoka, K.; Nakasaki, Y. Agglomeration and Uniform Growth of Si₃N₄ on Si(100): Experiments and First-Principles Calculations. *Phys Rev B Condens Matter Mater Phys* **2008**, *78* (8), 1–9. <https://doi.org/10.1103/PhysRevB.78.085321>.
- (126) Kuroda, R.; Suwa, T.; Teramoto, A.; Hasebe, R.; Sugawa, S.; Ohmi, T. Atomically Flat Silicon Surface and Silicon/Insulator Interface Formation Technologies for (100) Surface Orientation Large-Diameter Wafers Introducing High Performance and Low-Noise Metal-Insulator-Silicon FETs. *IEEE Trans Electron Devices* **2009**, *56* (2), 291–298. <https://doi.org/10.1109/TED.2008.2010591>.
- (127) Leftwich, T. R.; Teplyakov, A. V. Cycloaddition Reactions of Phenylazide and Benzylazide on a Si(100)-2 × 1 Surface. *Journal of Physical Chemistry C* **2008**, *112* (11), 4297–4303. <https://doi.org/10.1021/jp711367s>.
- (128) Bocharov, S.; Dmitrenko, O.; Méndez De Leo, L. P.; Teplyakov, A. V. Azide Reactions for Controlling Clean Silicon Surface Chemistry: Benzylazide on Si(100)-2 × 1. *J Am Chem Soc* **2006**, *128* (29), 9300–9301. <https://doi.org/10.1021/ja0623663>.
- (129) Glachant, A. Kinetics of Si(100) Nitridation First Stages by Ammonia: Electron-Beam-Induced Thin Film Growth at Room Temperature. *Journal of Vacuum Science & Technology B: Microelectronics and Nanometer Structures* **1985**, *3* (4), 985. <https://doi.org/10.1116/1.583027>.
- (130) Bischoff, J. L.; Lutz, F.; Bolmont, D.; Kubler, L. Use of Multilayer Techniques for XPS Identification of Various Nitrogen Environments in the Si/NH₃ System. *Surf Sci* **1991**, *251–252* (C), 170–174. [https://doi.org/10.1016/0039-6028\(91\)90975-X](https://doi.org/10.1016/0039-6028(91)90975-X).
- (131) Maillot, C.; Roulet, H.; Dufour, G. Thermal Nitridation of Silicon: An Xps and Leed Investigation. *Journal of Vacuum Science and Technology B: Microelectronics and Nanometer Structures* **1984**, *2* (3), 316–319. <https://doi.org/10.1116/1.582816>.
- (132) Tian, F.; Taber, D. F.; Teplyakov, A. V. NH- Termination of the Si(111) Surface by Wet Chemistry. *J Am Chem Soc* **2011**, *133* (51), 20769–20777. <https://doi.org/10.1021/ja205140h>.

- (133) Rodríguez-Reyes, J. C. F.; Teplyakov, A. V. Cooperative Nitrogen Insertion Processes: Thermal Transformation of N H₃ on a Si(100) Surface. *Phys Rev B Condens Matter Mater Phys* **2007**, *76* (7). <https://doi.org/10.1103/PhysRevB.76.075348>.
- (134) Gao, F.; Teplyakov, A. V. Monolayer of Hydrazine Facilitates the Direct Covalent Attachment of C₆₀ Fullerene to a Silicon Surface. *Langmuir* **2017**, *33* (35), 8632–8639. <https://doi.org/10.1021/acs.langmuir.6b03975>.
- (135) Lim, C.; Choi, C. H. Surface Reaction Mechanisms of Hydrazine on Si(100)-2×1 Surface: NH₃ Desorption Pathways. *Journal of Chemical Physics* **2004**, *120* (2), 979–987. <https://doi.org/10.1063/1.1631917>.
- (136) Bu, Y.; Lin, M. C. Surface Chemistry of N₂H₄ on Si (100) -2 x 1. **1994**, *6028*, 385–394.
- (137) Wang, H.-C.; Lin, R.-F.; Wang, X. High Temperature Nitridation Structures of the Si(111)-(7×7) Surface. *Surface Science Letters* **1987**, *188* (1–2), A357. [https://doi.org/10.1016/0167-2584\(87\)90017-x](https://doi.org/10.1016/0167-2584(87)90017-x).
- (138) Kuiper, A. E. T.; Willemsen, M. F. C.; Theunissen, A. M. L.; Van De Wijgert, W. M.; Habraken, F. H. P. M.; Tijhaar, R. H. G.; Van Der Weg, W. F.; Chen, J. T. Hydrogenation during Thermal Nitridation of Silicon Dioxide. *J Appl Phys* **1986**, *59* (8), 2765–2772. <https://doi.org/10.1063/1.336985>.
- (139) Hierlemann, A. Integrated Chemical Microsensor Systems in CMOS-Technology. *Digest of Technical Papers - International Conference on Solid State Sensors and Actuators and Microsystems, TRANSDUCERS '05* **2005**, *2*, 1134–1137. <https://doi.org/10.1109/sensor.2005.1497276>.
- (140) Escorihuela, J.; Zuilhof, H. Rapid Surface Functionalization of Hydrogen-Terminated Silicon by Alkyl Silanols. *J Am Chem Soc* **2017**, *139* (16), 5870–5876. <https://doi.org/10.1021/jacs.7b01106>.
- (141) Chopra, T. P.; Longo, R. C.; Cho, K.; Chabal, Y. J. Ammonia Modification of Oxide-Free Si(111) Surfaces. *Surf Sci* **2016**, *650*, 285–294. <https://doi.org/10.1016/j.susc.2016.01.002>.
- (142) Lange, B.; Schmidt, W. G. Ammonia Adsorption on Cl/Si(0 0 1): First-Principles Calculations. *Surf Sci* **2008**, *602* (6), 1207–1211. <https://doi.org/10.1016/j.susc.2008.01.024>.
- (143) Soria, F. A.; Patrito, E. M.; Paredes-Olivera, P. On the Mechanism of Silicon Activation by Halogen Atoms. *Langmuir* **2011**, *27* (6), 2613–2624. <https://doi.org/10.1021/la104701g>.
- (144) Pavlova, T. V.; Zhidomirov, G. M.; Eltsov, K. N. First-Principle Study of Phosphine Adsorption on Si(001)-2 × 1-Cl. *Journal of Physical Chemistry C* **2018**, *122* (3), 1741–1745. <https://doi.org/10.1021/acs.jpcc.7b11519>.
- (145) Finstad, C. C.; Thorsness, A. G.; Muscat, A. J. The Mechanism of Amine Formation on Si(1 0 0) Activated with Chlorine Atoms. *Surf Sci* **2006**, *600* (17), 3363–3374. <https://doi.org/10.1016/j.susc.2006.05.023>.
- (146) Colaianni, M. L.; Chen, P. J.; Yates, J. T. Unique Hydride Chemistry on Silicon–PH₃ Interaction with Si(100)-(2×1) . *Journal of Vacuum Science & Technology*

- A: *Vacuum, Surfaces, and Films* **1994**, *12* (6), 2995–2998. <https://doi.org/10.1116/1.578927>.
- (147) de Wijs, G.; De Vita, A. First-Principles Study of Chlorine Adsorption and Reactions on Si(100). *Phys Rev B Condens Matter Mater Phys* **1998**, *57* (16), 10021–10029. <https://doi.org/10.1103/PhysRevB.57.10021>.
- (148) Nakayama, K. S.; Graugnard, E.; Weaver, J. H. Tunneling Electron Induced Bromine Hopping on Si 100 \dagger - 2 1 \dagger . **2002**, *1* (c), 4–7. <https://doi.org/10.1103/PhysRevLett.89.266106>.
- (149) Clark, I. T.; Aldinger, B. S.; Gupta, A.; Hines, M. A. Aqueous Etching Produces Si(100) Surfaces of near-Atomic Flatness: Strain Minimization Does Not Predict Surface Morphology. *Journal of Physical Chemistry C* **2010**, *114* (1), 423–428. <https://doi.org/10.1021/jp908527e>.
- (150) Hersam, M. C.; Guisinger, N. P.; Lyding, J. W.; Thompson, D. S.; Moore, J. S. Atomic-Level Study of the Robustness of the Si(100)-2X1:H Surface Following Exposure to Ambient Conditions. *Appl Phys Lett* **2001**, *78* (7), 886–888. <https://doi.org/10.1063/1.1348322>.
- (151) Gao, F.; Teplyakov, A. V. Dehydrohalogenation Condensation Reaction of Phenylhydrazine with Cl-Terminated Si(111) Surfaces. *Journal of Physical Chemistry C* **2016**, *120* (10), 5539–5548. <https://doi.org/10.1021/acs.jpcc.5b12424>.
- (152) Gao, X.; Jang, J.; Nagase, S. Hydrazine and Thermal Reduction of Graphene Oxide: Reaction Mechanisms, Product Structures, and Reaction Design. *Journal of Physical Chemistry C* **2010**, *114* (2), 832–842. <https://doi.org/10.1021/jp909284g>.
- (153) Xu, F. J.; Cai, Q. J.; Kang, E. T.; Neoh, K. G. Surface-Initiated Atom Transfer Radical Polymerization from Halogen-Terminated Si(111) (Si-X, X = Cl, Br) Surfaces for the Preparation of Well-Defined Polymer-Si Hybrids. *Langmuir* **2005**, *21* (8), 3221–3225. <https://doi.org/10.1021/la0473714>.
- (154) Layadi, N.; Donnelly, V. M.; Lee, J. T. C. Cl₂ Plasma Etching of Si(100): Nature of the Chlorinated Surface Layer Studied by Angle-Resolved x-Ray Photoelectron Spectroscopy. *J Appl Phys* **1997**, *81* (10), 6738–6748. <https://doi.org/10.1063/1.365216>.
- (155) Donnelly, V. M.; Kornblit, A. Plasma Etching: Yesterday, Today, and Tomorrow. *Journal of Vacuum Science & Technology A: Vacuum, Surfaces, and Films* **2013**, *31* (5), 050825. <https://doi.org/10.1116/1.4819316>.
- (156) Sundaram, K. B.; Chang, H. W. Electrochemical Etching of Silicon by Hydrazine. *J Electrochem Soc* **1993**, *140* (6), 1592–1597. <https://doi.org/10.1149/1.2221607>.
- (157) Gangopadhyay, U.; Kim, K.; Dhungel, S. K.; Basu, P. K.; Yi, J. Low-Cost Texturization of Large-Area Crystalline Silicon Solar Cells Using Hydrazine Mono-Hydrate for Industrial Use. *Renew Energy* **2006**, *31* (12), 1906–1915. <https://doi.org/10.1016/j.renene.2005.10.002>.

- (158) McDonnell, T. L.; Marks, N. A.; Warschkow, O.; Wilson, H. F.; Smith, P. V.; Radny, M. W. Molecular Dissociation of Group-V Hydrides on Si(001). *Phys Rev B Condens Matter Mater Phys* **2005**, *72* (19), 1–4. <https://doi.org/10.1103/PhysRevB.72.193307>.
- (159) Kim, J. W.; Yeom, H. W. Thermal Decomposition of NH₃ on the Si(1 0 0) Surface. *Surf Sci* **2003**, *546* (2–3). <https://doi.org/10.1016/j.susc.2003.09.024>.
- (160) Widjaja, Y.; Musgrave, C. B. Ab Initio Study of the Initial Growth Mechanism of Silicon Nitride on Si(100)-(2x1) Using NH₃. *Phys Rev B Condens Matter Mater Phys* **2001**, *64* (20), 1–9. <https://doi.org/10.1103/PhysRevB.64.205303>.
- (161) Pansila, P. P.; Kanomata, K.; Ahmmad, B.; Kubota, S.; Hirose, F. Nitrogen Adsorption of Si(100) Surface by Plasma Excited Ammonia. *IEICE Transactions on Electronics* **2015**, *E98C* (5), 395–401. <https://doi.org/10.1587/transele.E98.C.395>.
- (162) Nakayama, K. S.; Graugnard, E.; Weaver, J. H. Surface Modification without Desorption: Recycling of Cl on [Formula Presented]. *Phys Rev Lett* **2002**, *88* (12), 4. <https://doi.org/10.1103/PhysRevLett.88.125508>.
- (163) Bent, S. F. Organic Functionalization of Group IV Semiconductor Surfaces: Principles, Examples, Applications, and Prospects. *Surf Sci* **2002**, *500*, 879–903.
- (164) Ciampi, S.; Harper, J. B.; Gooding, J. J. Wet Chemical Routes to the Assembly of Organic Monolayers on Silicon Surfaces via the Formation of Si-C Bonds: Surface Preparation, Passivation and Functionalization. *Chem Soc Rev* **2010**, *39* (6), 2158–2183. <https://doi.org/10.1039/b923890p>.
- (165) Longo, R. C.; Cho, K.; Hohmann, S.; Thissen, P. Mechanism of Phosphorus Transport Through Silicon Oxide during Phosphonic Acid Monolayer Doping. *Journal of Physical Chemistry C* **2018**, *122* (18), 10088–10095. <https://doi.org/10.1021/acs.jpcc.8b02545>.
- (166) Tanaka, M.; Sawaguchi, T.; Kuwahara, M.; Niwa, O. Surface Modification of Silicon Oxide with Trialkoxysilanes toward Close-Packed Monolayer Formation. *Langmuir* **2013**, *29* (21), 6361–6368. <https://doi.org/10.1021/la4009834>.
- (167) Queffelec, C.; Petit, M.; Janvier, P.; Knight, D. A.; Bujoli, B. Surface Modification Using Phosphonic Acids and Esters. *Chem Rev* **2012**, *112* (7), 3777–3807. <https://doi.org/10.1021/cr2004212>.
- (168) Gao, X.; Kolevatov, I.; Chen, K.; Guan, B.; Mesli, A.; Monakhov, E.; Dan, Y. Full Activation of Boron in Silicon Doped by Self-Assembled Molecular Monolayers Full Activation of Boron in Silicon Doped by Self-Assembled Molecular Monolayers. *ACS Appl Electron Mater* **2020**, *2* (1), 268–274. <https://doi.org/10.1021/acsaelm.9b00748>.
- (169) Guan, B.; Siampour, H.; Fan, Z.; Wang, S.; Kong, X. Y.; Mesli, A.; Zhang, J.; Dan, Y. Nanoscale Nitrogen Doping in Silicon by Self-Assembled Monolayers. *Sci Rep* **2015**, *5*, 1–9. <https://doi.org/10.1038/srep12641>.
- (170) Das, A.; Kim, D. S.; Nakayashiki, K.; Rounsaville, B.; Meemongkolkiat, V.; Rohatgi, A. Boron Diffusion with Boric Acid for High Efficiency Silicon Solar

- Cells. *J Electrochem Soc* **2010**, *157* (6), H684. <https://doi.org/10.1149/1.3392364>.
- (171) Yadav, A.; Singh, G.; Nekovei, R.; Jeyakumar, R. C-Si Solar Cells Formed from Spin-on Phosphoric Acid and Boric Acid. *Renew Energy* **2015**, *80*, 80–84. <https://doi.org/10.1016/j.renene.2015.01.055>.
- (172) Schneider, A.; Hemmerlé, J.; Allais, M.; Didierjean, J.; Michel, M.; D'Ischia, M.; Ball, V. Boric Acid as an Efficient Agent for the Control of Polydopamine Self-Assembly and Surface Properties. *ACS Appl Mater Interfaces* **2018**, *10* (9), 7574–7580. <https://doi.org/10.1021/acsami.7b08356>.
- (173) Fabre, B.; Hauquier, F. Boronic Acid-Functionalized Oxide-Free Silicon Surfaces for the Electrochemical Sensing of Dopamine. *Langmuir* **2017**, *33* (35), 8693–8699. <https://doi.org/10.1021/acs.langmuir.7b00699>.
- (174) Collins, G.; O'Dwyer, C.; Morris, M.; Holmes, J. D. Palladium-Catalyzed Coupling Reactions for the Functionalization of Si Surfaces: Superior Stability of Alkenyl Monolayers. *Langmuir* **2013**, *29* (38), 11950–11958. <https://doi.org/10.1021/la402480f>.
- (175) Kırbıyık, Ç.; Can, M.; Kuş, M. Interfacial Modification via Boronic Acid Functionalized Self-Assembled Monolayers for Efficient Inverted Polymer Solar Cells. *Mater Sci Semicond Process* **2020**, *107*. <https://doi.org/10.1016/j.mssp.2019.104860>.
- (176) Leow, W. R.; Yu, J.; Li, B.; Hu, B.; Li, W.; Chen, X. Correlating the Surface Basicity of Metal Oxides with Photocatalytic Hydroxylation of Boronic Acids to Alcohols. *Angewandte Chemie - International Edition* **2018**, *57* (31), 9780–9784. <https://doi.org/10.1002/anie.201805395>.
- (177) Qian, S.; Lin, M.; Ji, W.; Yuan, H.; Zhang, Y.; Jing, Z.; Zhao, J.; Masson, J. F.; Peng, W. Boronic Acid Functionalized Au Nanoparticles for Selective MicroRNA Signal Amplification in Fiber-Optic Surface Plasmon Resonance Sensing System. *ACS Sens* **2018**, *3* (5), 929–935. <https://doi.org/10.1021/acssensors.7b00871>.
- (178) Kanayama, N.; Kitano, H. Interfacial Recognition of Sugars by Boronic Acid-Carrying Self-Assembled Monolayer. *Langmuir* **2000**, *16* (2), 577–583. <https://doi.org/10.1021/la990182e>.
- (179) Cui, Y.; Tian, F.; Gao, F.; Teplyakov, A. V. Building Organic Monolayers Based on Fluorinated Amines on the Si(111) Surface. *Journal of Physical Chemistry C* **2014**, *118* (46), 26721–26728. <https://doi.org/10.1021/jp507158x>.
- (180) Wang, F.; Wang, L.; Xue, Q. Fluorine and Sulfur Co-Doped Amorphous Carbon Films to Achieve Ultra-Low Friction under High Vacuum. *Carbon NY* **2016**, *96*, 411–420. <https://doi.org/10.1016/j.carbon.2015.09.084>.
- (181) Bulusheva, L. G.; Fedoseeva, Y. V.; Flahaut, E.; Rio, J.; Ewels, C. P.; Koroteev, V. O.; Van Lier, G.; Vyalikh, D. V.; Okotrub, A. V. Effect of the Fluorination Technique on the Surface-Fluorination Patterning of Double-Walled Carbon Nanotubes. *Beilstein Journal of Nanotechnology* **2017**, *8* (1), 1688–1698. <https://doi.org/10.3762/bjnano.8.169>.

- (182) Park, S. M.; Yu, H.; Park, M. G.; Han, S. Y.; Kang, S. W.; Park, H. M.; Kim, J. W. Quantitative Analysis of an Organic Thin Film by XPS, AFM and FT-IR. *Surface and Interface Analysis* **2012**, *44* (2), 156–161. <https://doi.org/10.1002/sia.3786>.
- (183) Shao, Y. X.; Dong, D.; Cai, Y. H.; Wang, S.; Ang, S. G.; Xu, G. Q. Switching from a [2 + 2] Cycloaddition-Like to an Ene-Like Reaction in Covalent Attachment of Halogenated Acetonitrile on Si (100) -2 × 1 : Effect of Halogen Substituent. **2010**, No. 100, 2701–2710.
- (184) Hinckley, A.; Mancheno-Posso, P.; Lai, C. S.; Muscat, A. J. Selective Removal of Native SiO₂ Using XeF₂. *ECS Trans* **2015**, *69* (7), 225–232. <https://doi.org/10.1149/06907.0225ecst>.
- (185) Yan, B.; Li, W. C.; Lu, A. H. Metal-Free Silicon Boride Catalyst for Oxidative Dehydrogenation of Light Alkanes to Olefins with High Selectivity and Stability. *J Catal* **2019**, *369*, 296–301. <https://doi.org/10.1016/j.jcat.2018.11.014>.
- (186) Lide, D. R.; Baysinger, G. CRC Handbook of Chemistry and Physics. **2003**, 84th Edition, CRC press, Florida, USA.
- (187) Badlani, M.; Wachs, I. E. *Methanol: A “Smart” Chemical Probe Molecule*; 2001; Vol. 75.
- (188) Badri, A.; Binet, C.; Lavalley, J.-C. *Use of Methanol as an IR Molecular Probe to Study the Surface of Polycrystalline Ceria*; 1997.
- (189) Tanner, R. E.; Liang, Y.; Altman, E. I. *Structure and Chemical Reactivity of Adsorbed Carboxylic Acids on Anatase TiO₂ (0 0 1)*; 2002. www.elsevier.com/locate/susc.
- (190) Balajka, J.; Hines, M. A.; DeBenedetti, W. J. I.; Komora, M.; Pavelec, J.; Schmid, M.; Diebold, U. High-Affinity Adsorption Leads to Molecularly Ordered Interfaces on TiO₂ in Air and Solution. *Science (1979)* **2018**, *361* (6404), 786–789. <https://doi.org/10.1126/science.aat6752>.
- (191) Wechsler, D.; Vensaus, P.; Tsud, N.; Steinrück, H. P.; Lytken, O.; Williams, F. J. Surface Reactions and Electronic Structure of Carboxylic Acid Porphyrins Adsorbed on TiO₂(110). *Journal of Physical Chemistry C* **2021**, *125* (12), 6708–6715. <https://doi.org/10.1021/acs.jpcc.1c01133>.
- (192) Zubavichus, Y. V.; Slovokhotov, Y. L.; Nazeeruddin, M. K.; Zakeeruddin, S. M.; Grätzel, M.; Shklover, V. Structural Characterization of Solar Cell Prototypes Based on Nanocrystalline TiO₂ Anatase Sensitized with Ru Complexes. X-Ray Diffraction, XPS, and XAFS Spectroscopy Study. *Chemistry of Materials* **2002**, *14* (8), 3556–3563. <https://doi.org/10.1021/cm020123d>.
- (193) Gakh, Y. G.; Gakh, A. A.; Gronenborn, A. M. Fluorine as an NMR Probe for Structural Studies of Chemical and Biological Systems. *Magnetic Resonance in Chemistry* **2000**, *38* (7), 551–558. [https://doi.org/10.1002/1097-458X\(200007\)38:7<551::AID-MRC686>3.0.CO;2-Q](https://doi.org/10.1002/1097-458X(200007)38:7<551::AID-MRC686>3.0.CO;2-Q).
- (194) Dürr, U. H. N.; Grage, S. L.; Witter, R.; Ulrich, A. S. Solid State ¹⁹F NMR Parameters of Fluorine-Labeled Amino Acids. Part I: Aromatic Substituents.

- Journal of Magnetic Resonance* **2008**, *191* (1), 7–15. <https://doi.org/10.1016/j.jmr.2007.11.017>.
- (195) Zhang, Y.; Tamijani, A. A.; Taylor, M. E.; Zhi, B.; Haynes, C. L.; Mason, S. E.; Hamers, R. J. Molecular Surface Functionalization of Carbon Materials via Radical-Induced Grafting of Terminal Alkenes. *J Am Chem Soc* **2020**, *141* (20), 8277–8288. <https://doi.org/10.1021/jacs.9b02369>.
- (196) Dalvit, C.; Fagerness, P. E.; Hadden, D. T. A.; Sarver, R. W.; Stockman, B. J. Fluorine-NMR Experiments for High-Throughput Screening: Theoretical Aspects, Practical Considerations, and Range of Applicability. *J Am Chem Soc* **2003**, *125* (25), 7696–7703. <https://doi.org/10.1021/ja034646d>.
- (197) Byron, C.; Bai, S.; Celik, G.; Ferrandon, M. S.; Liu, C.; Ni, C.; Mehdad, A.; Delferro, M.; Lobo, R. F.; Teplyakov, A. V. Role of Boron in Enhancing the Catalytic Performance of Supported Platinum Catalysts for the Nonoxidative Dehydrogenation of N-Butane. *ACS Catal* **2020**, *10* (2), 1500–1510. <https://doi.org/10.1021/acscatal.9b04689>.
- (198) Miyaura, N.; Yanagi, T.; Suzuki, A. The Palladium-Catalyzed Cross-Coupling Reaction Of Phenylboronic Acid With Haloarenes In The Presence Of Bases. *Synth Commun* **1981**, *11* (7), 513–519. <https://doi.org/10.1080/00397918108063618>.
- (199) Hall, D. G. Boronic Acid Catalysis. *Chemical Society Reviews*. Royal Society of Chemistry July 7, 2019, pp 3475–3496. <https://doi.org/10.1039/c9cs00191c>.
- (200) Akın Kara, D.; Kara, K.; Oylumluoglu, G.; Yigit, M. Z.; Can, M.; Kim, J. J.; Burnett, E. K.; Gonzalez Arellano, D. L.; Buyukcelebi, S.; Ozel, F.; Usluer, O.; Briseno, A. L.; Kus, M. Enhanced Device Efficiency and Long-Term Stability via Boronic Acid-Based Self-Assembled Monolayer Modification of Indium Tin Oxide in a Planar Perovskite Solar Cell. *ACS Appl Mater Interfaces* **2018**, *10* (35), 30000–30007. <https://doi.org/10.1021/acsami.8b10445>.
- (201) Zaleska, A.; Grabowska, E.; Sobczak, J. W.; Gazda, M.; Hupka, J. Photocatalytic Activity of Boron-Modified TiO₂ under Visible Light: The Effect of Boron Content, Calcination Temperature and TiO₂ Matrix. *Appl Catal B* **2009**, *89* (3–4), 469–475. <https://doi.org/10.1016/j.apcatb.2009.01.005>.
- (202) Grabowska, E.; Zaleska, A.; Sobczak, J. W.; Gazda, M.; Hupka, J. Boron-Doped TiO₂: Characteristics and Photoactivity under Visible Light. In *Procedia Chemistry*; 2009; Vol. 1, pp 1553–1559. <https://doi.org/10.1016/j.proche.2009.11.003>.
- (203) Raghunath, P.; Lin, M. C. Adsorption Configurations and Reactions of Boric Acid on a TiO₂ Anatase (101) Surface. *Journal of Physical Chemistry C* **2008**, *112* (22), 8276–8287. <https://doi.org/10.1021/jp711246b>.
- (204) Kırbıyık, Ç.; Kara, K.; Kara, D. A.; Yiğit, M. Z.; İstanbullu, B.; Can, M.; Sarıçiftci, N. S.; Scharber, M.; Kuş, M. Enhancing the C-TiO₂ Based Perovskite Solar Cell Performance via Modification by a Serial of Boronic Acid Derivative Self-Assembled Monolayers. *Appl Surf Sci* **2017**, *423*, 521–527. <https://doi.org/10.1016/j.apsusc.2017.06.189>.

- (205) Kırbyık, Ç.; Akın Kara, D.; Kara, K.; Büyükçelebi, S.; Yiğit, M. Z.; Can, M.; Kuş, M. Improving the Performance of Inverted Polymer Solar Cells through Modification of Compact TiO₂ Layer by Different Boronic Acid Functionalized Self-Assembled Monolayers. *Appl Surf Sci* **2019**, *479*, 177–184. <https://doi.org/10.1016/j.apsusc.2019.01.268>.
- (206) Kırbyık Kurukavak, C.; Yılmaz, T.; Büyükbekar, A.; Kuş, M. Surface Modification of C-TiO₂ via Different Phenyl Boronic Acid SAMs for Improved Performance of Inverted Organic Solar Cells. *Mater. Sci. Semicond. Process* **2021**, No. 106120 (135).
- (207) Kwok, Y. Y.; Ho, P. Y.; Wei, Y.; Zheng, Z.; Yiu, S. C.; Ho, C. L.; Huang, S. Molecular Engineering of Robust Starburst-Based Organic Photosensitizers for Highly Efficient Photocatalytic Hydrogen Generation from Water. *Chemistry of Materials* **2022**, *34* (12), 5522–5534. <https://doi.org/10.1021/acs.chemmater.2c00556>.
- (208) Liu, G.; Sun, C.; Yang, H. G.; Smith, S. C.; Wang, L.; Lu, G. Q.; Cheng, H. M. Nanosized Anatase TiO₂ Single Crystals for Enhanced Photocatalytic Activity. *Chemical Communications* **2010**, *46* (5), 755–757. <https://doi.org/10.1039/b919895d>.
- (209) Akshay, V. R.; Arun, B.; Mandal, G.; Mutta, G. R.; Chanda, A.; Vasundhara, M. Observation of Optical Band-Gap Narrowing and Enhanced Magnetic Moment in Co-Doped Sol-Gel-Derived Anatase TiO₂ Nanocrystals. *Journal of Physical Chemistry C* **2018**, *122* (46), 26592–26604. <https://doi.org/10.1021/acs.jpcc.8b06646>.
- (210) Zheng, D.; Pang, X.; Wang, M.; He, Y.; Lin, C.; Lin, Z. Unconventional Route to Hairy Plasmonic/Semiconductor Core/Shell Nanoparticles with Precisely Controlled Dimensions and Their Use in Solar Energy Conversion. *Chemistry of Materials* **2015**, *27* (15), 5271–5278. <https://doi.org/10.1021/acs.chemmater.5b01422>.
- (211) Nur, A. S. M.; Funada, E.; Kiritoshi, S.; Matsumoto, A.; Kakei, R.; Hinokuma, S.; Yoshida, H.; Machida, M. Phase-Dependent Formation of Coherent Interface Structure between PtO₂ and TiO₂ and Its Impact on Thermal Decomposition Behavior. *Journal of Physical Chemistry C* **2018**, *122* (1), 662–669. <https://doi.org/10.1021/acs.jpcc.7b10858>.
- (212) Miyoshi, A.; Nishioka, S.; Maeda, K. Water Splitting on Rutile TiO₂-Based Photocatalysts. *Chemistry - A European Journal*. Wiley-VCH Verlag December 10, 2018, pp 18204–18219. <https://doi.org/10.1002/chem.201800799>.
- (213) Gao, C.; Wei, T.; Zhang, Y.; Song, X.; Huan, Y.; Liu, H.; Zhao, M.; Yu, J.; Chen, X. A Photoresponsive Rutile TiO₂ Heterojunction with Enhanced Electron–Hole Separation for High-Performance Hydrogen Evolution. *Advanced Materials* **2019**, *31* (8). <https://doi.org/10.1002/adma.201806596>.
- (214) Vásquez, G. C.; Peche-Herrero, M. A.; Maestre, D.; Cremades, A.; Ramírez-Castellanos, J.; González-Calbet, J. M.; Piqueras, J. Effects of Transition Metal Doping on the Growth and Properties of Rutile TiO₂ Nanoparticles. *Journal of*

- Physical Chemistry C* **2013**, *117* (4), 1941–1947. <https://doi.org/10.1021/jp3101656>.
- (215) Singh, J.; Sharma, S.; Sharma, S.; Chand Singh, R. Effect of Tungsten Doping on Structural and Optical Properties of Rutile TiO₂ and Band Gap Narrowing. *Optik (Stuttg)* **2019**, No. 182, 538–547.
- (216) Wang, S.; Liu, H.; Yuan, S.; Fu, R. Sol-Gel Method on the Preparation of Boron-Doped Activated Alumina. In *IOP Conference Series: Earth and Environmental Science*; IOP Publishing Ltd, 2021; Vol. 714. <https://doi.org/10.1088/1755-1315/714/3/032057>.
- (217) Ha, M. A.; Baxter, E. T.; Cass, A. C.; Anderson, S. L.; Alexandrova, A. N. Boron Switch for Selectivity of Catalytic Dehydrogenation on Size-Selected Pt Clusters on Al₂O₃. *J Am Chem Soc* **2017**, *139* (33), 11568–11575. <https://doi.org/10.1021/jacs.7b05894>.
- (218) Aly, M.; Fornero, E. L.; Leon-Garzon, A. R.; Galvita, V. V.; Saeys, M. Effect of Boron Promotion on Coke Formation during Propane Dehydrogenation over Pt/γ-Al₂O₃ Catalysts. *ACS Catal* **2020**, *10* (9), 5208–5216. <https://doi.org/10.1021/acscatal.9b05548>.
- (219) ChemAxon. Chemicalize. <https://Chemicalize.Com> (Accessed 2022-08-01).
- (220) Ong, C. W.; Huang, H.; Zheng, B.; Kwok, R. W. M.; Hui, Y. Y.; Lau, W. M. X-Ray Photoemission Spectroscopy of Nonmetallic Materials: Electronic Structures of Boron and BxO_y. *J Appl Phys* **2004**, *95* (7), 3527–3534. <https://doi.org/10.1063/1.1651321>.
- (221) Kung, H.; Duan, Y.; Williams, M. G.; Teplyakov, A. V. Transmetalation Process as a Route for Preparation of Zinc-Oxide-Supported Copper Nanoparticles. *Langmuir* **2016**, *32* (28), 4029–7037. <https://doi.org/10.1021/acs.langmuir.6b00061>.
- (222) Bessada, C.; Anghel, E. M. ¹¹B, ²³Na, ²⁷Al, and ¹⁹F NMR Study of Solid and Molten Na₃AlF₆-Na₂B₄O₇. *Inorg Chem* **2003**, *42* (12), 3884–3890. <https://doi.org/10.1021/ic026074o>.
- (223) Anghel, E. M.; Florian, P.; Bessada, C. Structural Description of the Na₂B₄O₇-Na₃AlF₆-TiO₂ System. 1. IR and Raman Study of the Solidified Melts. *Journal of Physical Chemistry B* **2007**, *111* (5), 962–967. <https://doi.org/10.1021/jp061977e>.
- (224) Trzeciak, K.; Kaźmierski, S.; Druźbicki, K.; Potrzebowski, M. J. Mapping of Guest Localization in Mesoporous Silica Particles by Solid-State NMR and Ab Initio Modeling: New Insights into Benzoic Acid and p-Fluorobenzoic Acid Embedded in MCM-41 via Ball Milling. *Journal of Physical Chemistry C* **2021**, *125* (18), 10096–10109. <https://doi.org/10.1021/acs.jpcc.1c01675>.
- (225) Solís, D.; Ferraro, M. B. Solid-State Nuclear Magnetic Resonance: Performance of Point-Charge Distributions to Model Intermolecular Effects in ¹⁹F Chemical Shifts. *Theor Chem Acc* **2000**, *104* (3–4), 323–326. <https://doi.org/10.1007/s002140000145>.

- (226) Wu, C. Y.; Tu, K. J.; Deng, J. P.; Lo, Y. S.; Wu, C. H. Markedly Enhanced Surface Hydroxyl Groups of TiO₂ Nanoparticles with Superior Water-Dispersibility for Photocatalysis. *Materials* **2017**, *10* (5). <https://doi.org/10.3390/ma10050566>.
- (227) Kakuma, Y.; Nosaka, A. Y.; Nosaka, Y. Difference in TiO₂ Photocatalytic Mechanism between Rutile and Anatase Studied by the Detection of Active Oxygen and Surface Species in Water. *Physical Chemistry Chemical Physics* **2015**, *17* (28), 18691–18698. <https://doi.org/10.1039/c5cp02004b>.
- (228) Adiga, S. P.; Zapol, P.; Curtiss, L. A. Structure and Morphology of Hydroxylated Amorphous Alumina Surfaces. *Journal of Physical Chemistry C* **2007**, *111* (20), 7422–7429. <https://doi.org/10.1021/jp0701035>.
- (229) Tsyganenko, A. A.; Mardilovichb, P. P. *Structure of Alumina Surfaces*; 1996.
- (230) *Convergence of More Moore, More than Moore, and beyond Moore: Materials, Devices, and Nanosystems*; Deleonibus, S., Ed.; Jenny Stanford Publishing, 2020; Vol. 4.
- (231) Zhang, J.; Li, Y.; Cao, K.; Chen, R. Advances in Atomic Layer Deposition. *Nanomanufacturing and Metrology*. Springer Science and Business Media B.V. September 1, 2022, pp 191–208. <https://doi.org/10.1007/s41871-022-00136-8>.
- (232) Yarbrough, J.; Shearer, A. B.; Bent, S. F. Next Generation Nanopatterning Using Small Molecule Inhibitors for Area-Selective Atomic Layer Deposition. *Journal of Vacuum Science & Technology A* **2021**, *39* (2), 021002. <https://doi.org/10.1116/6.0000840>.
- (233) Jiang, X.; Bent, S. F. Area-Selective ALD with Soft Lithographic Methods: Using Self-Assembled Monolayers to Direct Film Deposition. *Journal of Physical Chemistry C* **2009**, *113* (41), 17613–17625. <https://doi.org/10.1021/jp905317n>.
- (234) Liu, T. L.; Zeng, L.; Nardi, K. L.; Hausmann, D. M.; Bent, S. F. Characterizing Self-Assembled Monolayer Breakdown in Area-Selective Atomic Layer Deposition. *Langmuir* **2021**, *37* (39), 11637–11645. <https://doi.org/10.1021/acs.langmuir.1c02211>.
- (235) Bobb-Semple, D.; Zeng, L.; Cordova, I.; Bergsman, D. S.; Nordlund, D.; Bent, S. F. Substrate-Dependent Study of Chain Orientation and Order in Alkylphosphonic Acid Self-Assembled Monolayers for ALD Blocking. *Langmuir* **2020**, *36* (43), 12849–12857. <https://doi.org/10.1021/acs.langmuir.0c01974>.
- (236) Nye, R. A.; Van Dongen, K.; De Simone, D.; Oka, H.; Parsons, G. N.; Delabie, A. Enhancing Performance and Function of Polymethacrylate Extreme Ultraviolet Resists Using Area-Selective Deposition. *Chemistry of Materials* **2023**, *35* (5), 2016–2026. <https://doi.org/10.1021/acs.chemmater.2c03404>.
- (237) Poonkottil, N.; Rijckaert, H.; Rajendran, K.; Petit, R. R.; Martin, L. I. D. J.; Van Thourhout, D.; Van Driessche, I.; Detavernier, C.; Dendooven, J. Low Temperature Area Selective Atomic Layer Deposition of Ruthenium Dioxide

- Thin Films Using Polymers as Inhibition Layers. *Adv Mater Interfaces* **2023**, *10* (9). <https://doi.org/10.1002/admi.202201934>.
- (238) Mameli, A.; Teplyakov, A. V. Selection Criteria for Small-Molecule Inhibitors in Area-Selective Atomic Layer Deposition: Fundamental Surface Chemistry Considerations. *Acc Chem Res* **2023**, *56* (15), 2084–2095. <https://doi.org/10.1021/acs.accounts.3c00221>.
- (239) Bronneberg, A. C.; Höhn, C.; Van De Krol, R. Probing the Interfacial Chemistry of Ultrathin ALD-Grown TiO₂ Films: An In-Line XPS Study. *Journal of Physical Chemistry C* **2017**, *121* (10), 5531–5538. <https://doi.org/10.1021/acs.jpcc.6b09468>.
- (240) Longo, R. C.; McDonnell, S.; Dick, D.; Wallace, R. M.; Chabal, Y. J.; Owen, J. H. G.; Ballard, J. B.; Randall, J. N.; Cho, K. Selectivity of Metal Oxide Atomic Layer Deposition on Hydrogen Terminated and Oxidized Si(001)-(2×1) Surface. *Journal of Vacuum Science & Technology B, Nanotechnology and Microelectronics: Materials, Processing, Measurement, and Phenomena* **2014**, *32* (3), 03D112. <https://doi.org/10.1116/1.4864619>.
- (241) Haber, J. A.; Lewis, N. S. Infrared and X-Ray Photoelectron Spectroscopic Studies of the Reactions of Hydrogen-Terminated Crystalline Si(111) and Si(100) Surfaces with Br₂, I₂, and Ferrocenium in Alcohol Solvents. *Journal of Physical Chemistry B* **2002**, *106* (14), 3639–3656. <https://doi.org/10.1021/jp0102872>.

Appendix A

SUPPLEMENTARY INFORMATION FOR CHAPTER 3

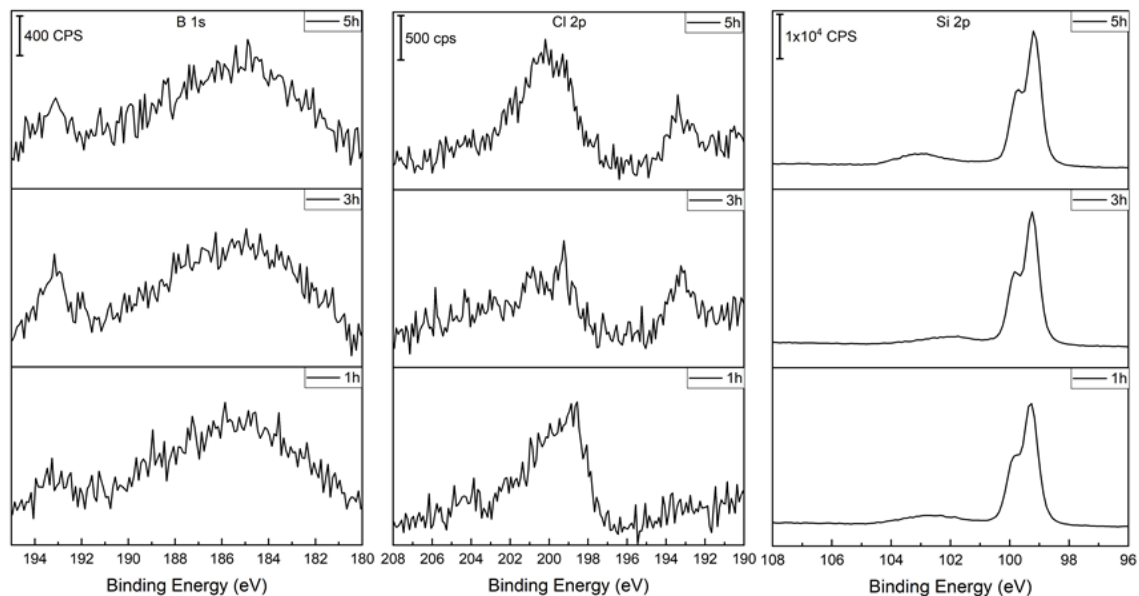


Figure A1: XPS spectra of Cl 2p, B 1s and Si 2p for the optimization of the time of the BCl_3 reaction with Cl terminated-Si (100) for 1, 3 and 5 hours.

The optimization for the reaction time of boron trichloride with Cl-terminated Si (100) shows that at 1h, 3h and 5h there is a B 1s peak observed around 193.5 eV. The highest intensity obtained was at 3 hours of reaction. The Cl 2p feature shows that the lowest intensity occurs at 3 hours of the reaction. The Si 2p feature shows the peak at 103 eV corresponding to $(\text{Si-O})_x$ bond at 5 hours of reaction, and a peak at around 102 (corresponding to Si-B bond) eV clearly observed at 3 hours of reaction. According to the results, the best conditions to perform this reaction is at 70°C for 3 hours.

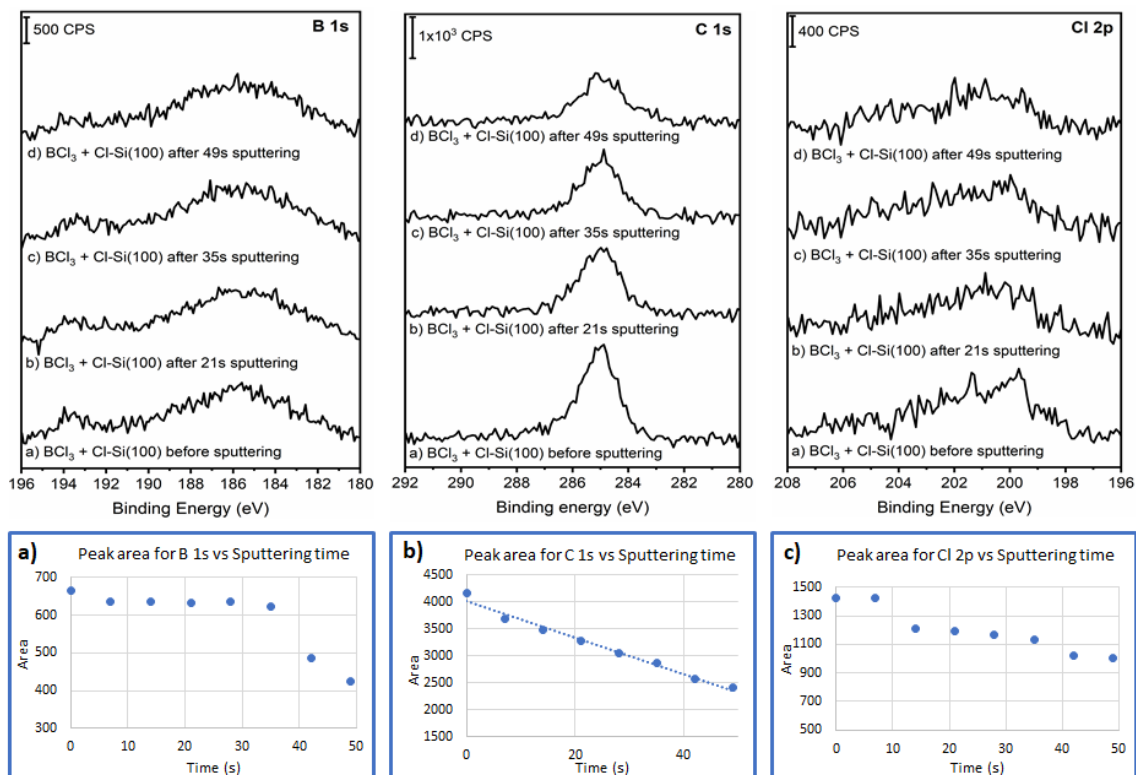


Figure A2. The top three panels show the XPS spectra of Cl 2p, B 1s and Si 2p results of the sputtering with Ar^+ monoatomic mode on the Cl-terminated Si (100) after reaction with BCl_3 for a) 0 seconds, b) 21 seconds, c) 35 seconds, and d) 49 seconds of sputtering. And the bottom three panels show the peak area versus the time of sputtering for a) Boron, b) Carbon and c) Chlorine.

Figure A2 shows the results for the sputtering of the Cl terminated-Si(100) after the reaction with BCl_3 with Ar^+ monoatomic mode (200 eV) in 7 steps of 7 seconds. The boron signal does not decrease noticeably until approximately 40 second sputtering time, but the carbon contamination decreases linearly nearly and reduced by half by the same sputtering time. The chlorine signal appears to decrease but within the signal-to-noise of these experiments, insignificantly. Thus, this sputtering approach can be optimized to remove impurities but not the monolayer B-containing species.

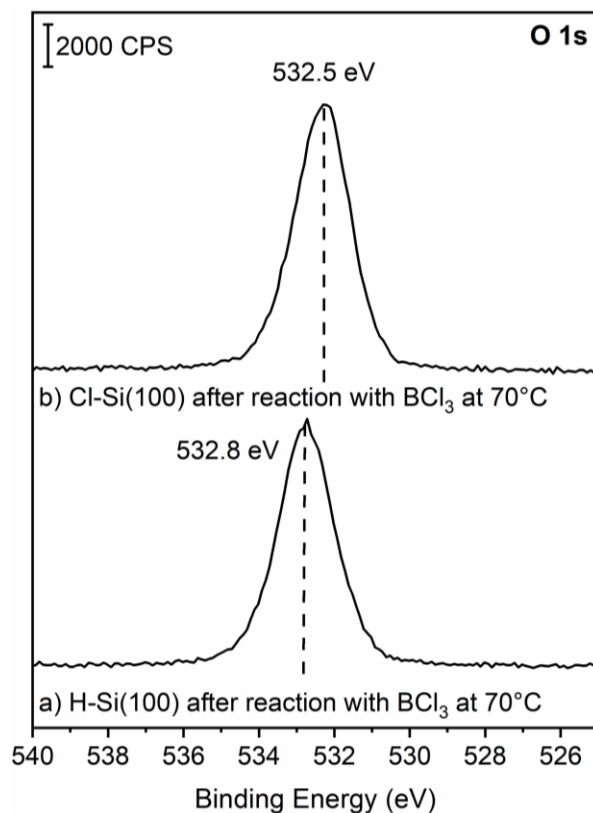
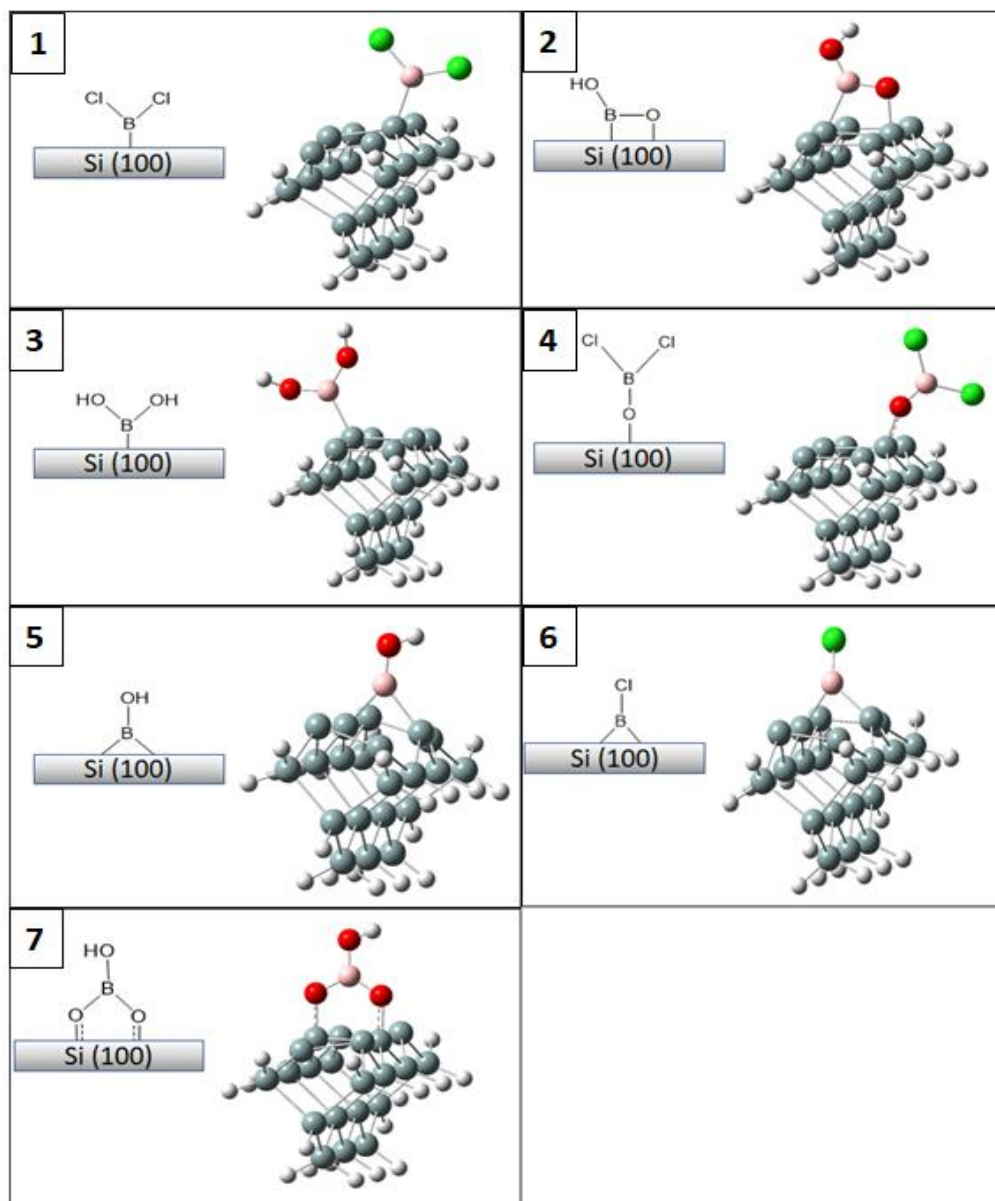


Figure A3. XPS spectra of O 1s for the reaction of BCl₃ at 70°C with a) H terminated-Si(100), and b) Cl terminated-Si(100)

The O 1s spectra shows a small shift of 0.3 eV in the H-Si(100) compared to the Cl-Si(100) surface, which agree with the assumption that in the H-Si(100) the species formed is mostly B-O-Si having the oxygen a higher binding energy, while in the Cl-Si(100) the species on the surface is B-Si and the oxygen is on the top of this monolayer having a lower binding energy. Of course, both observations are also hindered by the adventitious O-containing species.

Figure A4: Scheme A1. Models used for the DFT calculations performed with Gaussian 09 suite utilizing B3LYP functional and 6-311G+(d,p) basis set.



Appendix B

SUPPLEMENTARY INFORMATION FOR CHAPTER 4

Overlayer model equations:

The overlayer model²⁴¹ was used to calculate the surface coverages of chlorine, bromine and nitrogen with the assumption that chlorine, bromine and nitrogen-containing molecules are within a monolayer on the silicon substrate, and the adventitious carbon and oxygen layer is on top of them.

The monolayer coverage (Φ) was calculated using the following equations:

$$\Phi = \left[\left(\frac{\lambda \sin\theta}{a_{ov}} \right) \left(\frac{SF_{Si}}{SF_{ov}} \right) \left(\frac{\rho_{Si}}{\rho_{ov}} \right) \left(\frac{I_{ov}}{I_{Si}} \right) \right] \quad (\text{Eq. B1})$$

$$a_{ov} = \left(\frac{A_{ov}}{\rho_{ov} N_A} \right)^{1/3} \quad (\text{Eq. B2})$$

Where λ is the penetration depth (4.0 nm in the instrument used); θ is the photoelectron takeoff angle with respect to the analyzer (35.3° in the instrument used); SF is the sensitivity factor, ρ is the density in g/cm³; a_{ov} is the atomic diameter of the overlayer species. A_{ov} is the atomic weight of the overlayer species in g/mol. N_A is Avogadro's constant. And I is the integrated area under the substrate peaks, calculated by Casa XPS software (version 2.3.16).

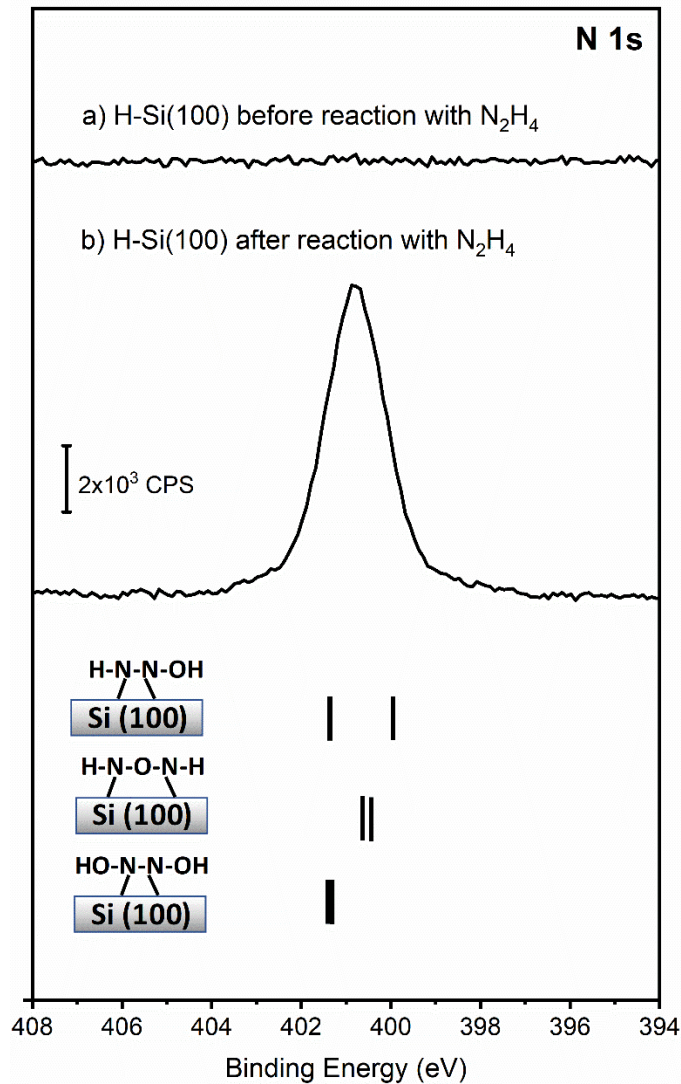


Figure B1. XPS spectra of the N 1s spectral region for H-Si(100) surface before (a) and after (b) reaction with hydrazine. The computationally predicted values for the oxidized species indicated are shown as black solid bars underneath the experimental spectra.

Figure B1 compares the experimental N 1s XPS spectra and the computationally predicted positions of the species indicated underneath the experimental data for the reaction of H-Si(100) with hydrazine. The predicted N 1s binding energies for Si-N(OH)-N(OH)-Si are expected to produce features at 401.3 eV for both nitrogen atoms. The model corresponding to Si-NH-N(OH)-Si was predicted to yield features at 399.9 and 401.4 eV. The last model corresponding to Si-NH-O-NH-Si is expected to have

features at 400.5 and 400.6 eV. Although Si-NH-O-NH-Si model appears to be consistent with the experimental data, it is also the least likely to form, since it will require a selective oxidation of N-N bond. Si-NH-N(OH)-Si model would be expected to result in a much broader peak than that observed experimentally.

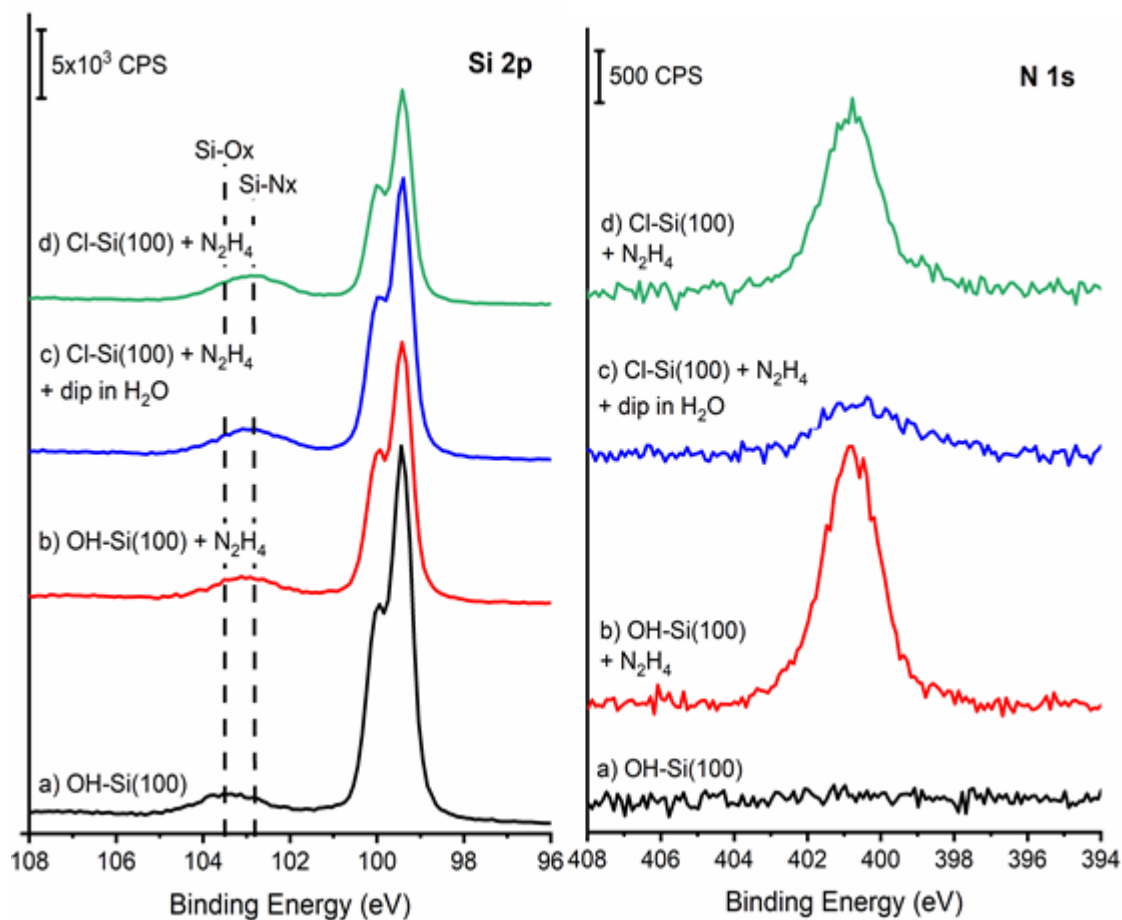


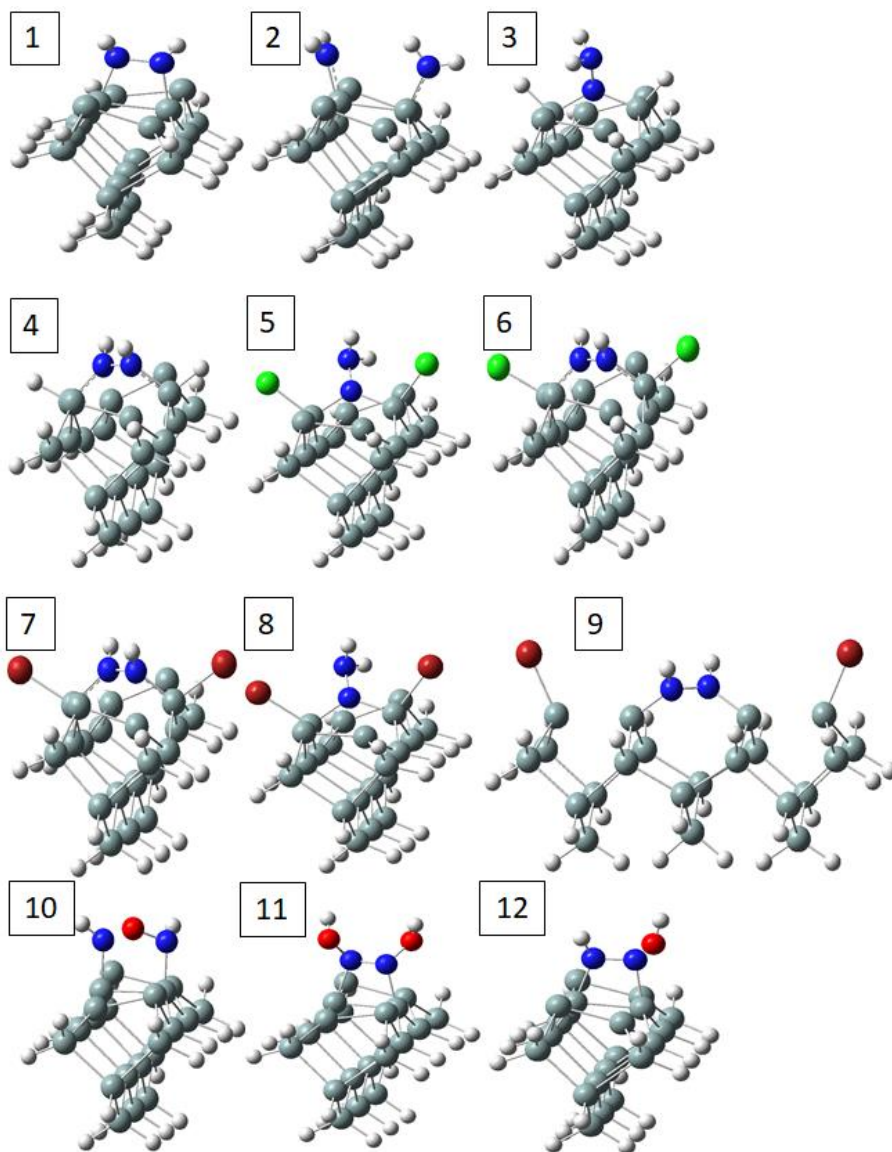
Figure B2. XPS spectra of Si 2p and N1 spectral regions comparing the reactivity of a) OH terminated-Si (100) before reaction with hydrazine, b) OH terminated-Si (100) after reaction with hydrazine, c) Cl terminated-Si(100) after reaction with hydrazine followed by a dip in H₂O and d) Cl terminated-Si(100) after reaction with hydrazine.

Figure B2 shows that the hydrazine reaction also works with OH-Si(100), although the resulting interface is oxidized, as would be expected. This figure also demonstrates that the hydrazine-terminated Si(100) survives complete oxidation and nitrogen removal even following a dip into deionized water.

Table 8.1 Thermodynamic requirements for the reaction of hydrazine with single-dimer (Si_9H_{12}), two-dimer ($\text{Si}_{21}\text{H}_{24}$) and three-dimer ($\text{Si}_{21}\text{H}_{20}$) clusters monochloride and monobromide-terminated.

Reaction	Cluster model	Energy (KJ/mol)
	Si_9H_{12}	128.2
	Si_9H_{12}	144.3
	$\text{Si}_{21}\text{H}_{24}$	109.0
	$\text{Si}_{21}\text{H}_{24}$	122.0
	$\text{Si}_{21}\text{H}_{20}$	144.8
	$\text{Si}_{21}\text{H}_{20}$	143.0

Figure B3. Nitrogen-containing species attached to the silicon surface modeled in Gaussview and used for the DFT calculations performed with Gaussian 09 suite utilizing B3LYP functional and 6-311G+(d,p) basis set.



Appendix C

SUPPLEMENTARY INFORMATION FOR CHAPTER 5

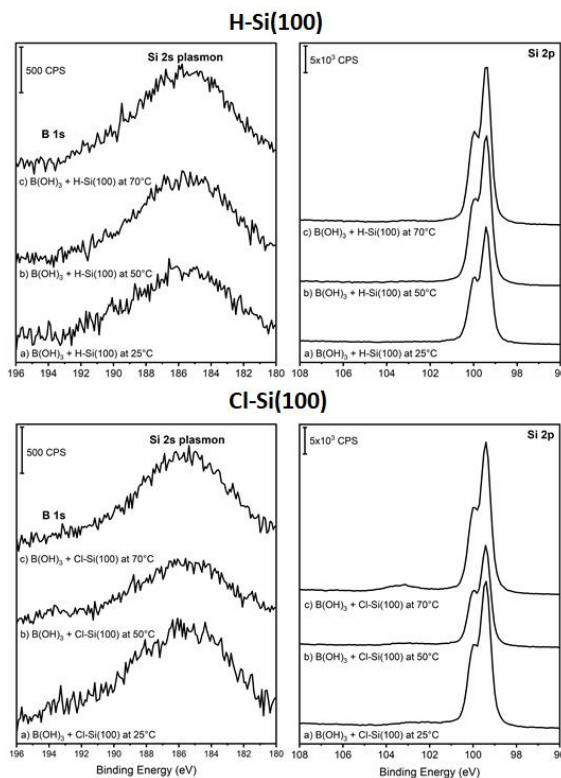


Figure C1: The top two panels show the XPS spectra of B 1s and Si 2p spectral region for reaction of boric acid with H-Si(100) at a) 25°C, b) 50°C and c) 70°C. And the two bottom panels shows the XPS spectra of B 1s and Si 2p spectral region for reaction of boric acid with Cl-Si(100) at a) 25°C, b) 50°C and c) 70°C

Figure C1 shows the temperature optimization for the reaction of boric acid with H-Si(100) and Cl-Si(100), where it can be seen that the reaction occurs only in the Cl terminated surface and the optimal temperature is 50°C where the introduction of boron is higher.

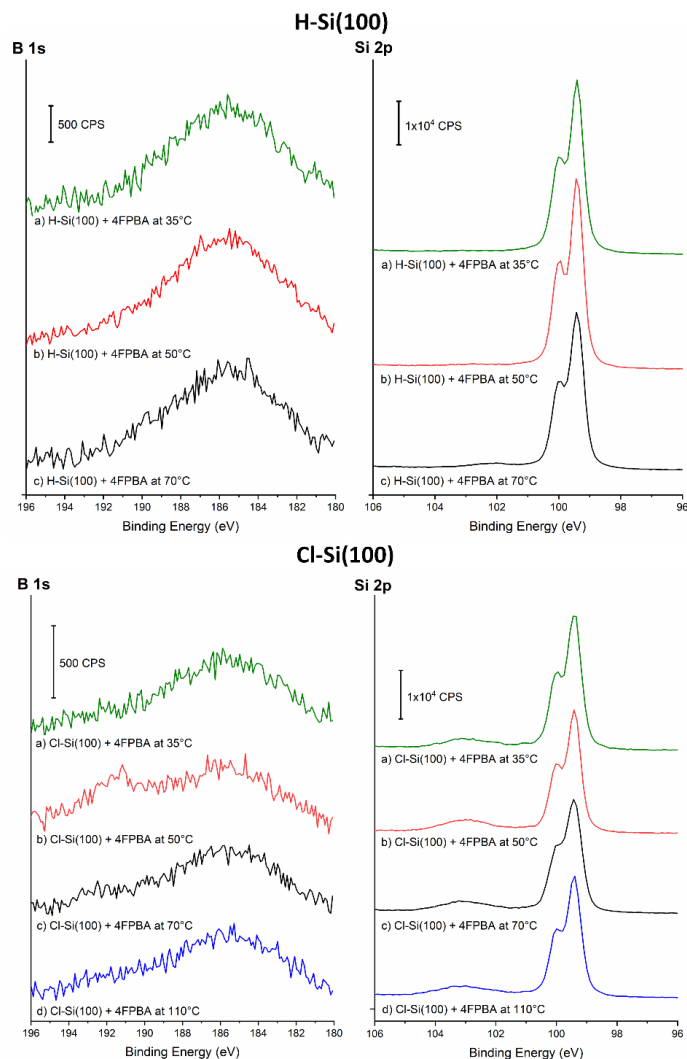


Figure C2. Top two panels show the XPS spectra of B 1s and Si 2p spectral region for reaction of 4-fluorophenylboronic acid with H-Si(100) at a) 35°C, b) 50°C, and c) 70°C. And the two bottom panels show the XPS spectra of B 1s and Si 2p spectral region for reaction of 4-fluorophenylboronic acid with Cl-Si(100) at a) 35°C, b) 50°C, c) 70°C and d) 110°C.

Figure C2 shows the temperature optimization for the reaction of 4-fluorophenylboronic acid with H-Si(100) and Cl-Si(100), where it can be seen that that the reaction occurs only in the Cl terminated surface and the optimal temperature is 50°C where the introduction of boron is higher.

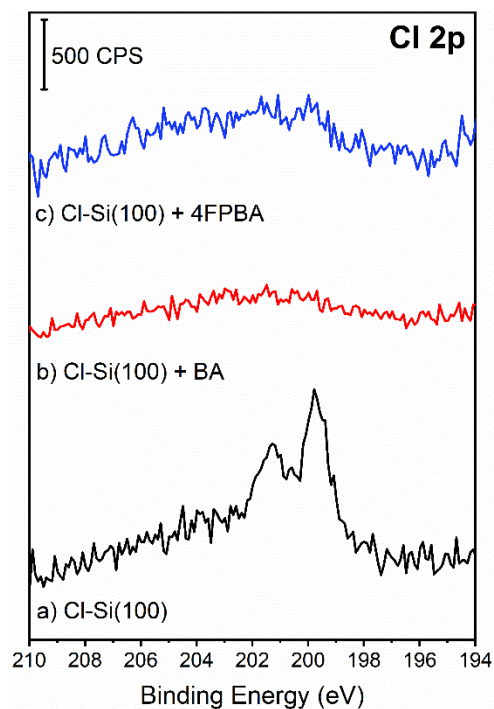


Figure C3. XPS spectra of Cl 2p spectral region for the a) Cl-terminated Si(100) as the starting point, b) Cl-Si(100) after the reaction with boric acid at 50°C for 3h and, c) Cl-Si(100) after the reaction with 4-fluorophenylboronic acid at 50°C for 3h.

Figure C3 shows the Cl 2p spectral region at the starting point where the two peaks corresponding to Cl 2p_{3/2} and 2p_{1/2} at 199.6 and 201.1 eV, respectively are initially present and after the reaction with BA and 4FBA we see that there is not chlorine present on the surface.

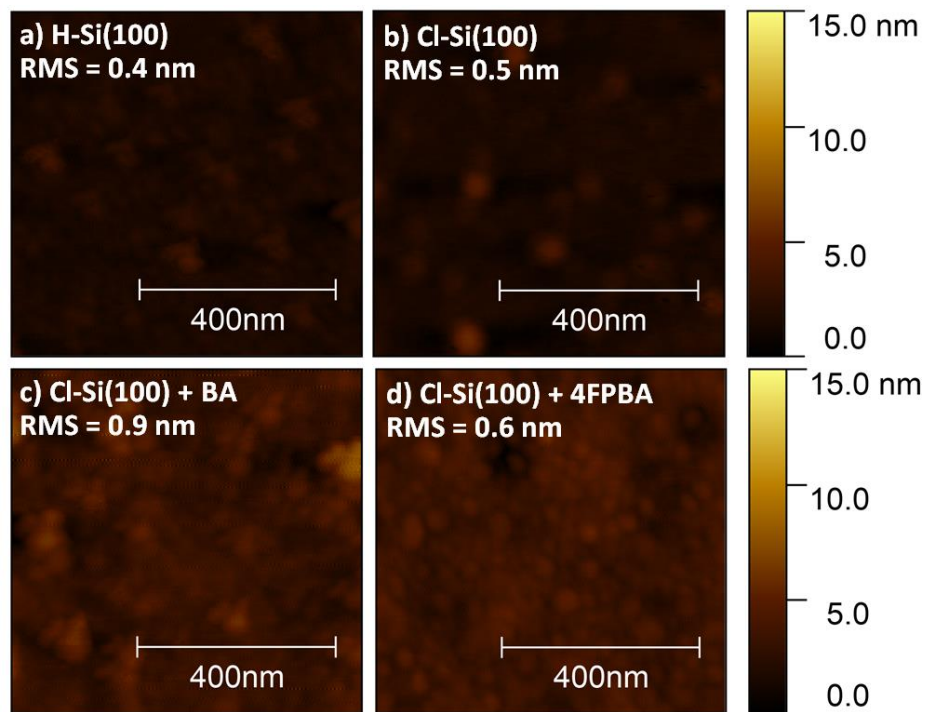


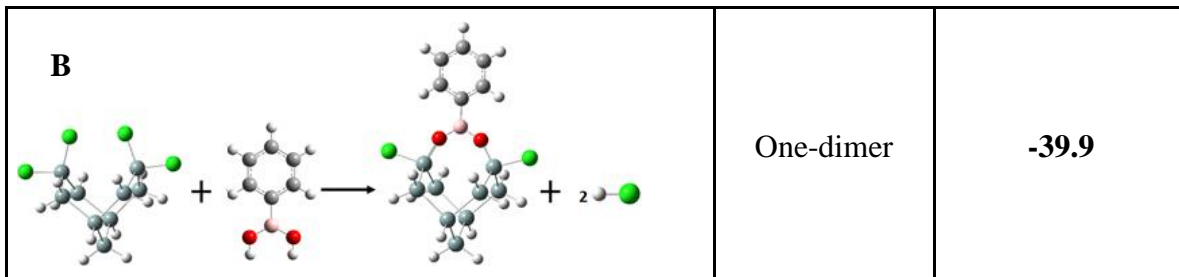
Figure C4. AFM images of the a) H-terminated Si(100), b) Cl-terminated Si(100), c) Cl-terminated Si(100) after the reaction with boric acid and d) Cl-terminated Si(100) after the reaction with 4-fluorophenylboronic acid with Cl-Si(100)

Table 8.2. Thermodynamic requirements for the reaction of 4-fluorophenylboronic acid (SA and SB) and boric acid (SC and SD) with two-dimer cluster.

Reaction		Energy (kJ/mol)
SA		-119.2
SB		-165.6
SC		-98.7
SD		-126.5

Table 8.3. Comparison of the thermodynamic requirements for the reaction of 4-fluorophenylboronic acid (A) and phenylboronic acid (B) with Cl-terminated Si(100).

Reaction	Cluster model	Energy(kJ/mol)
	One-dimer	-39.6



Appendix D

SUPPLEMENTARY INFORMATION FOR CHAPTER 6

1. XPS of varying 4FPBA weight loadings

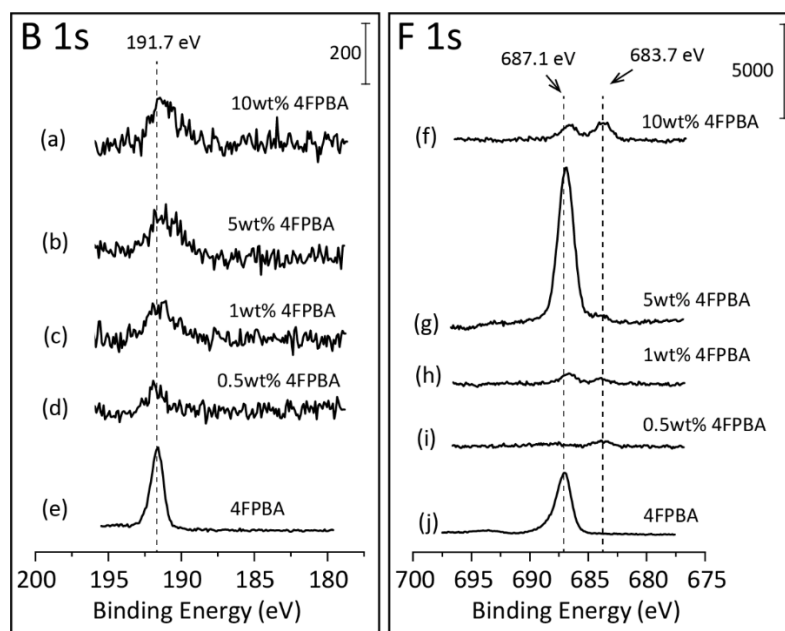


Figure D1. XPS spectra of boron 1s (left) and fluorine 1s (right) regions for weight loadings (a, f) 10wt%, (b, g) 5wt%, (c, h) 1wt%, and (d, i) 0.5wt% of 4-fluorophenylboronic acid on anatase TiO_2 , as well as (e, j) pure 4-fluorophenylboronic acid for comparison. The peak recorded at 683.7 eV for F 1s spectral region is the result of XPS-induced decomposition.

2. Transmission electron microscopy methods

Transmission electron microscopy (TEM) was performed to confirm the nanoparticle size of purchased materials at the Keck Center for Advanced Microscopy

at the University of Delaware using a Talos F200C TEM (Thermo Fischer Scientific, Waltham, MA) connected to a Thermo Fisher Scientific Ceta 16 M camera (Thermo Fischer Scientific, Waltham, MA). The nanopowder samples were dusted onto a copper grid with lacey carbon support and loaded into the TEM, which operated at an accelerating voltage of 200 keV to obtain bright field images. It was confirmed that the metal oxide nanoparticle sizes were consistent with manufacturer specifications.

3. XRD of as received and reacted samples

X-ray powder diffraction (XRD) was performed at the Advanced Materials Characterization Lab at the University of Delaware using a Bruker D8 Discover XRD (Bruker, Billerica, MA) with a Cu K α radiation source ($\lambda=1.5418 \text{ \AA}$), and measurements were taken at angles between 5° and 35° . Experimental data was compared with powder diffraction standards. Anatase TiO₂ matched with index data of JCPDS 00-001-0562, rutile TiO₂ matched with index data of JCPDS 01-078-4189, and gamma Al₂O₃ matched with index data of JCPDS 29-0063.

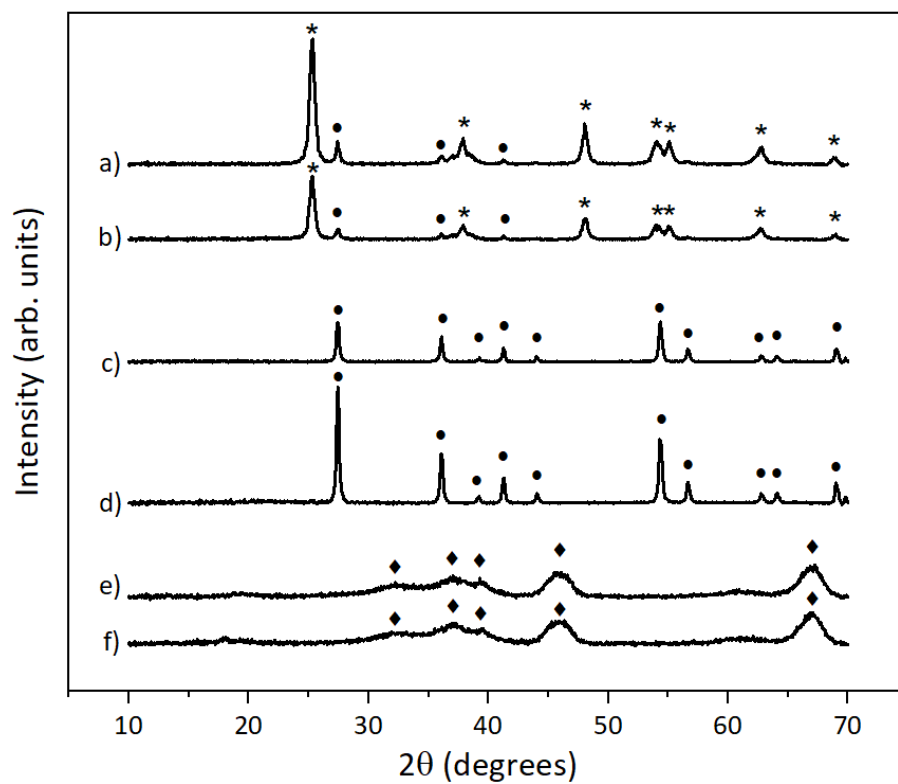


Figure D2. XRD spectra of anatase TiO₂ as received a), FPBA/anatase TiO₂ b), rutile TiO₂ as received c), FPBA/rutile TiO₂ d), γ -Al₂O₃ as received e), and FPBA/ γ -Al₂O₃. Distinct peaks for anatase TiO₂ (*), rutile TiO₂ (•), and γ -Al₂O₃ (◆) are indicated.

4. ADF predicted chemical shifts

4.1 TiO₂ monodentate

Atom	Local environment	Label number	Calculated chemical shifts (ppm)	Reference (ppm)	Calibrated chemical shifts (ppm)
C	C-F	20	13.66	189.05	175.39
	C-B	13	49.94	189.05	139.11
	C-H	16	68.05	189.05	121.00
	C-H	14	46.68	189.05	142.37
	C-H	15	43.87	189.05	145.18
	C-H	18	68.70	189.05	120.35
B	C-B-O	12	72.49	80.4	7.91
F	F-C	23	303.03	195.72	-107.31

Table 8.4. Calculated ¹³C, ¹¹B, and ¹⁹F chemical shifts (ppm) for monodentate 4FPBA on TiO₂

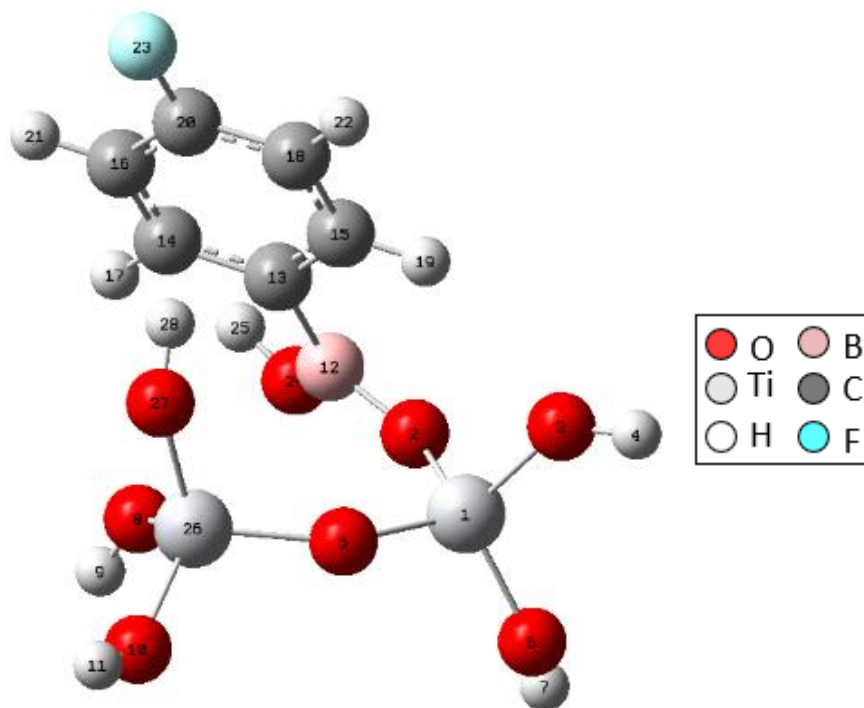


Figure D3. Structure of monodentate 4FPBA on TiO₂

4.2 TiO₂ bidentate bridging

Atom	Local environment	Label number	Calculated chemical shifts (ppm)	Reference (ppm)	Calibrated chemical shifts (ppm)
C	C-F	22	11.22	189.05	177.83
	C-B	15	58.07	189.05	130.98
	C-H	18	68.87	189.05	120.18
	C-H	16	44.91	189.05	144.14
	C-H	17	44.92	189.05	144.13
	C-H	20	68.88	189.05	120.17
B	C-B-O	14	72.39	80.4	8.01
F	F-C	25	301.66	195.72	-105.94

Table 8.5. Calculated ¹³C, ¹¹B, and ¹⁹F chemical shifts (ppm) for bidentate bridging 4FPBA on TiO₂

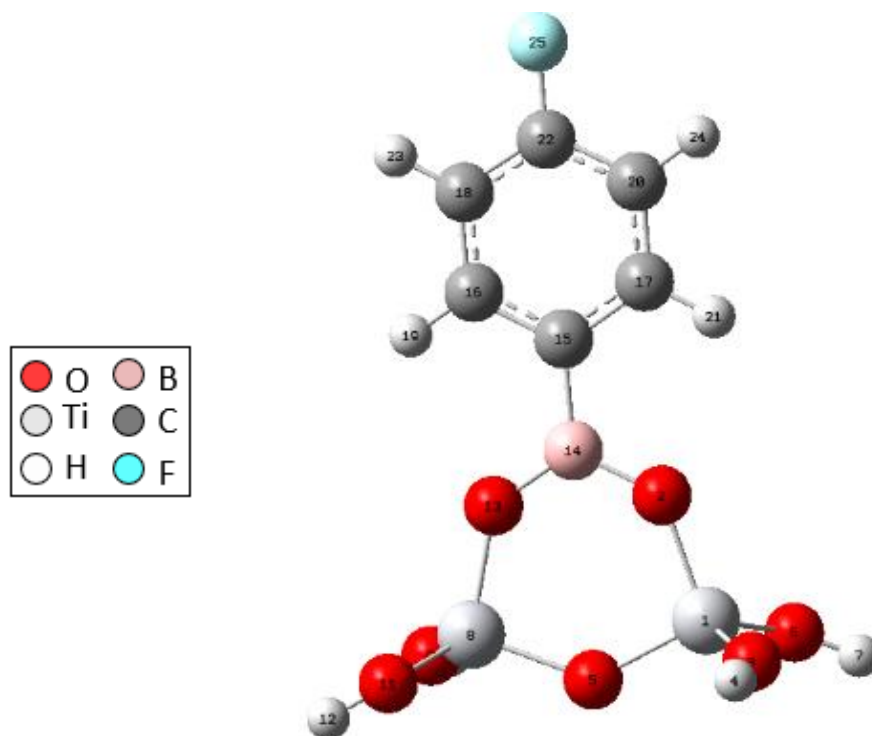


Figure D4. Structure of bidentate bridging 4FPBA on TiO₂

4.3 TiO₂ bidentate

Atom	Local environment	Label number	Calculated chemical shift (ppm)	Reference (ppm)	Calibrated chemical shifts (ppm)
C	C-F	18	10.99	189.05	178.06
	C-B	11	59.34	189.05	129.71
	C-H	14	68.59	189.05	120.46
	C-H	12	45.64	189.05	143.41
	C-H	16	68.62	189.05	120.43
	C-H	13	45.77	189.05	143.28
B	C-B-O	22	73.13	80.4	7.27
F	F-C	21	299.93	195.72	-104.21

Table 8.6. Calculated ¹³C, ¹¹B, and ¹⁹F chemical shifts (ppm) for bidentate 4FPBA on TiO₂

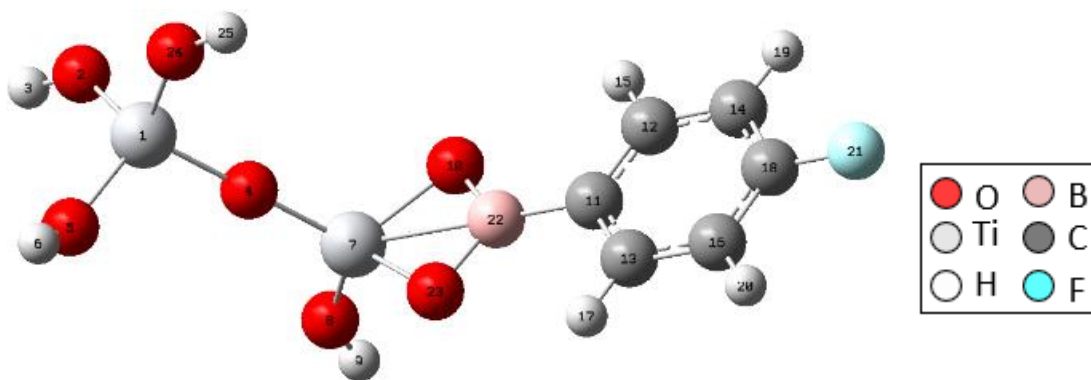


Figure D5. Structure of bidentate 4FPBA on TiO₂

4.4 Al₂O₃ monodentate

Atom	Local environment	Label number	Calculated chemical shift (ppm)	Reference (ppm)	Calibrated chemical shift (ppm)
C	C-F	9	5.24	189.05	183.81
	C-B	6	51.43	189.05	137.62
	C-H	7	46.86	189.05	142.19
	C-H	8	66.00	189.05	123.05
	C-H	10	65.49	189.05	123.56
	C-H	11	42.82	189.05	146.23
B	C-B-O	19	75.79	80.4	4.61
F	F-C	24	289.06	195.72	-93.34

Table 8.7. Calculated ¹³C, ¹¹B, and ¹⁹F chemical shifts (ppm) for monodentate 4FPBA on Al₂O₃

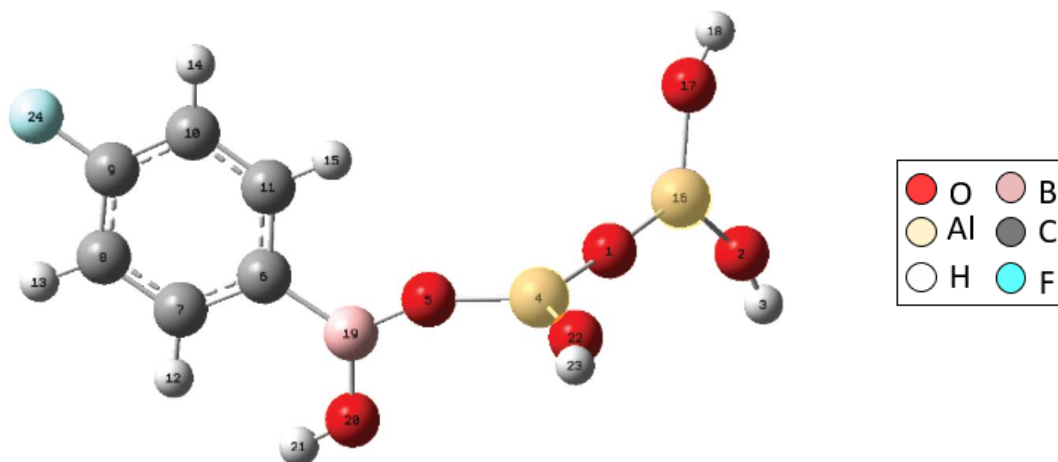


Figure D6. Structure of monodentate 4FPBA on Al₂O₃

4.5 Al₂O₃ bidentate bridging

Atom	Local environment	Label number	Calculated chemical shift (ppm)	Reference (ppm)	Calibrated chemical shift (ppm)
C	C-F	13	4.81	189.05	184.24
	C-B	10	50.82	189.05	138.23
	C-H	11	42.46	189.05	146.59
	C-H	12	66.70	189.05	122.35
	C-H	14	66.70	189.05	122.35
	C-H	15	42.45	189.05	146.60
B	C-B-O	20	72.16	80.4	8.24
F	F-C	21	289.62	195.72	-93.9

Table 8.8. Calculated ¹³C, ¹¹B, and ¹⁹F chemical shifts (ppm) for bidentate bridging 4FPBA on Al₂O₃

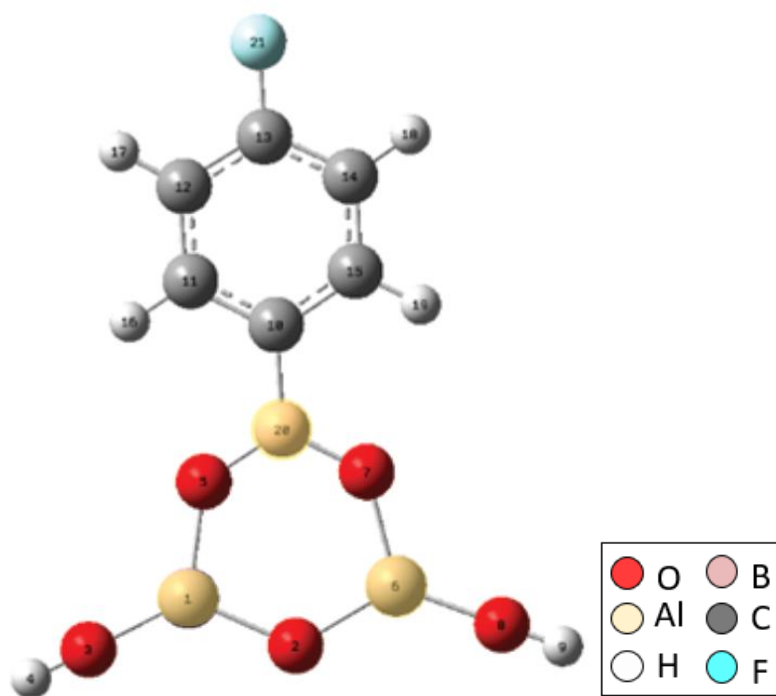


Figure D7. Structure of bidentate bridging 4FPBA on Al₂O₃

4.6 Al₂O₃ bidentate

Atom	Local environment	Label number	Calculated chemical shift (ppm)	Reference (ppm)	Calibrated chemical shift (ppm)
C	C-F	10	4.59	189.05	184.46
	C-B	7	55.95	189.05	133.10
	C-H	8	41.49	189.05	147.56
	C-H	9	66.3	189.05	122.75
	C-H	11	66.31	189.05	122.74
	C-H	12	41.5	189.05	147.55
B	C-B-O	17	65.22	80.4	15.18
F	F-C	21	287.95	195.72	-92.23

Table 8.9. Calculated ¹³C, ¹¹B, and ¹⁹F chemical shifts (ppm) for bidentate 4FPBA on Al₂O₃

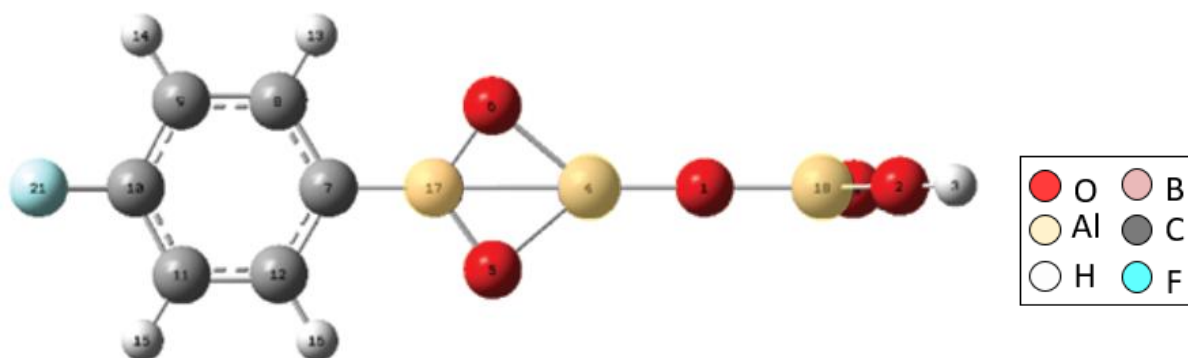


Figure D8. Structure of bidentate 4FPBA on Al₂O₃

4.7 4FPBA molecule

Atom	Local environment	Label number	Calculated chemical shift (ppm)	Reference (ppm)	Calibrated chemical shift (ppm)
C	C-F	5	11.52	189.05	177.53
	C-B	2	57.07	189.05	131.98
	C-H	4	68.95	189.05	120.10
	C-H	6	68.96	189.05	120.09
	C-H	3	46.27	189.05	142.78
	C-H	1	46.28	189.05	142.77
B	C-B-O	12	74.44	80.4	5.96
F	F-C	11	287.66	195.72	-91.94

Table 8.10. Calculated ^{13}C , ^{11}B , and ^{19}F chemical shifts (ppm) for 4FPBA molecule

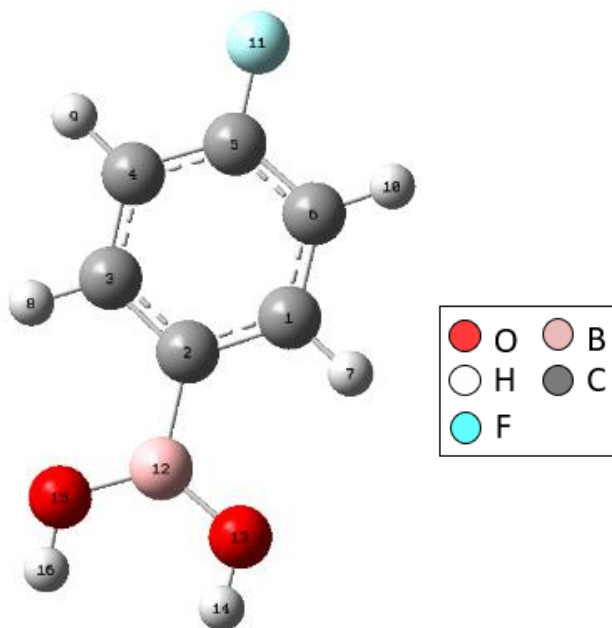


Figure D9. Structure of 4FPBA molecule

Appendix E

SUPPLEMENTARY INFORMATION FOR CHAPTER 7

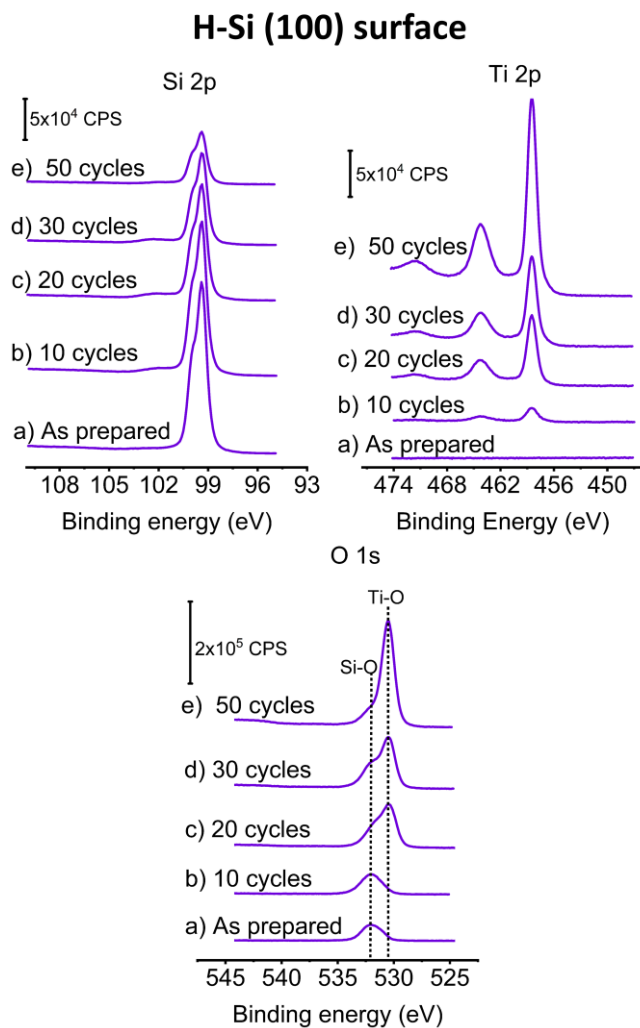


Figure E1: Si2p, Ti2p, and O 1s XPS spectral regions of (a) H-Si(100) as prepared, (b) H-Si(100) after 10, (c) 20, (d) 30, and (e) 50 ALD cycles of TiO₂.

FPBA-Si (100) surface

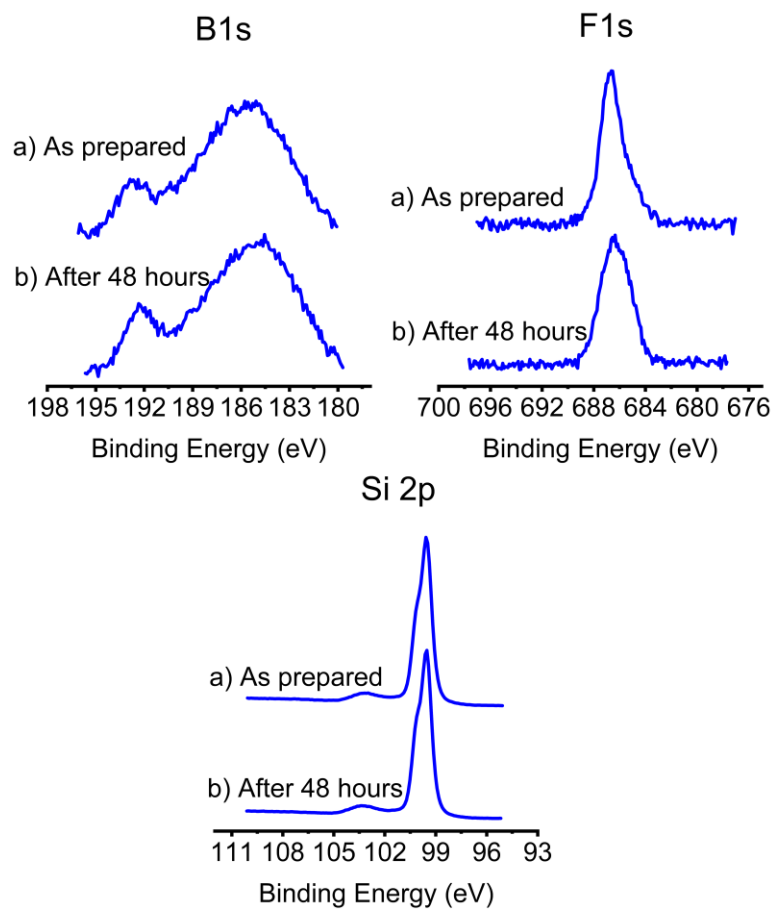


Figure E2: B 1s, F 1s and Si 2p XPS spectral regions of FPBA-Si(100) as prepared a), and after 48 hours b).

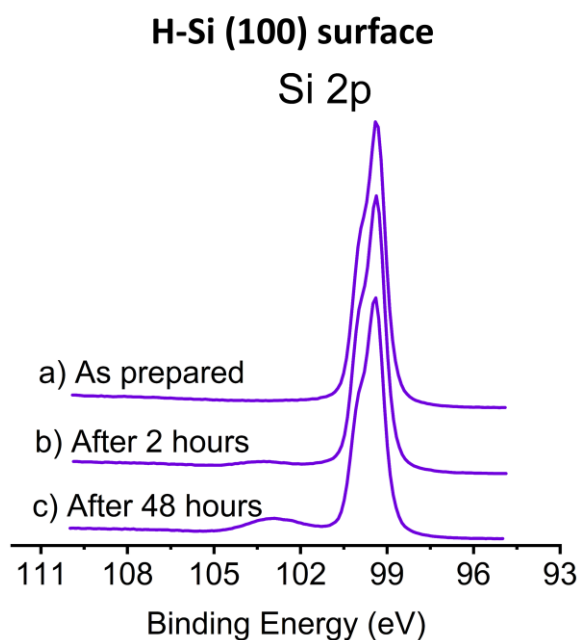


Figure E3: Si 2p XPS spectral region of H-Si(100) as prepared a), after 2 hours b), and 48 hours c).

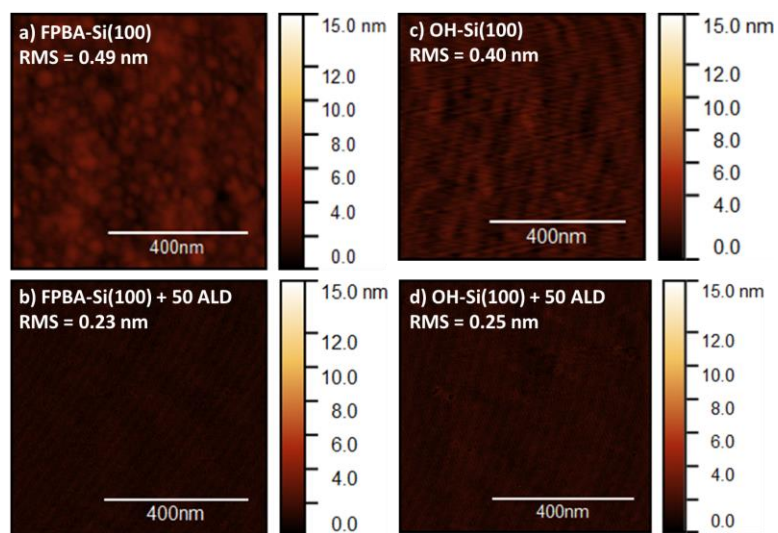


Figure E4: AFM images of the a) FPBA-Si(100), b) FPBA- Si(100) after 50 TiO₂ ALD cycles, c) OH-terminated Si(100), and d) OH-terminated Si(100) after 50 TiO₂ cycles

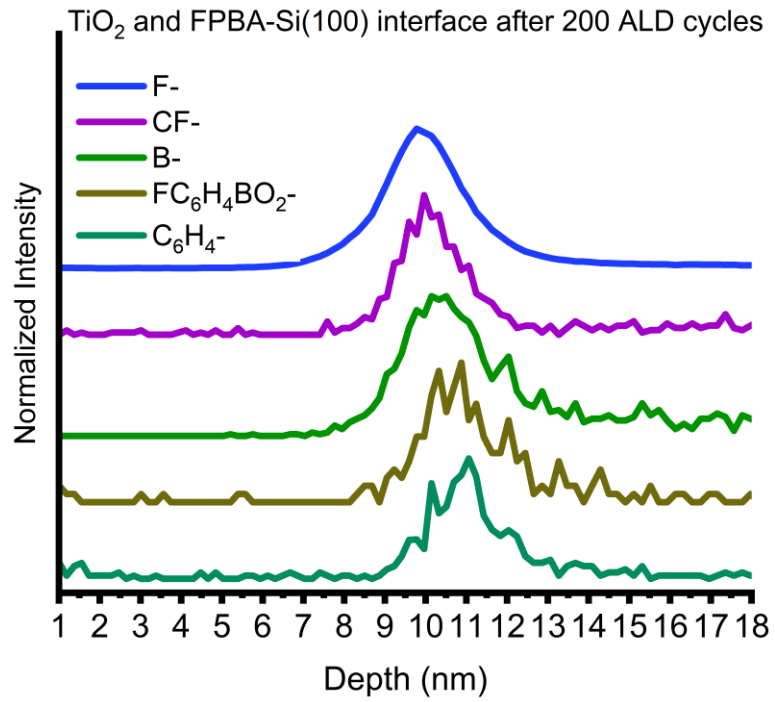


Figure E5: ToF-SIMS depth profile showing the intensity of the F⁻, CF⁻, B⁻, FC₆H₄BO₂⁻ and C₆H₄⁻ fragments at the interface of TiO₂ layer and FPBA-Si(100) after 200 ALD cycles.

Appendix F

COPYRIGHT PERMISSIONS



Reaction of BCl₃ with H- and Cl-terminated Si(100) as a pathway for selective, monolayer doping through wet chemistry
Author: Dhamelyz Silva-Quinones, Chuan He, Robert E. Butera, George T. Wang, Andrew V. Teplyakov
Publication: Applied Surface Science
Publisher: Elsevier
Date: 15 December 2020
© 2020 Elsevier B.V. All rights reserved.

Journal Author Rights

Please note that, as the author of this Elsevier article, you retain the right to include it in a thesis or dissertation, provided it is not published commercially. Permission is not required, but please ensure that you reference the journal as the original source. For more information on this and on your other retained rights, please visit: <https://www.elsevier.com/about/our-business/policies/copyright#Author-rights>

[BACK](#) [CLOSE WINDOW](#)



Reaction of Hydrazine with Solution- and Vacuum-Prepared Selectively Terminated Si(100) Surfaces: Pathways to the Formation of Direct Si-N Bonds
Author: Dhamelyz Silva-Quinones, Chuan He, Kevin J. Dwyer, et al
Publication: Langmuir
Publisher: American Chemical Society
Date: Nov 1, 2020
Copyright © 2020, American Chemical Society

PERMISSION/LICENSE IS GRANTED FOR YOUR ORDER AT NO CHARGE

This type of permission/license, instead of the standard Terms and Conditions, is sent to you because no fee is being charged for your order. Please note the following:

- Permission is granted for your request in both print and electronic formats, and translations.
- If figures and/or tables were requested, they may be adapted or used in part.
- Please print this page for your records and send a copy of it to your publisher/graduate school.
- Appropriate credit for the requested material should be given as follows: "Reprinted (adapted) with permission from {COMPLETE REFERENCE CITATION}. Copyright (YEAR) American Chemical Society." Insert appropriate information in place of the capitalized words.
- One-time permission is granted only for the use specified in your RightsLink request. No additional uses are granted (such as derivative works or other editions). For any uses, please submit a new request.

If credit is given to another source for the material you requested from RightsLink, permission must be obtained from that source.

[BACK](#) [CLOSE WINDOW](#)



Solution Chemistry to Control Boron-Containing Monolayers on Silicon: Reactions of Boric Acid and 4-Fluorophenylboronic Acid with H- and Cl-terminated Si(100)

Author: Dhameilyz Silva-Quinones, Robert E. Butera, George T. Wang, et al

Publication: Langmuir

Publisher: American Chemical Society

Date: Jun 1, 2021

Copyright © 2021, American Chemical Society

PERMISSION/LICENSE IS GRANTED FOR YOUR ORDER AT NO CHARGE

This type of permission/license, instead of the standard Terms and Conditions, is sent to you because no fee is being charged for your order. Please note the following:

- Permission is granted for your request in both print and electronic formats, and translations.
- If figures and/or tables were requested, they may be adapted or used in part.
- Please print this page for your records and send a copy of it to your publisher/graduate school.
- Appropriate credit for the requested material should be given as follows: "Reprinted (adapted) with permission from (COMPLETE REFERENCE CITATION). Copyright (YEAR) American Chemical Society." Insert appropriate information in place of the capitalized words.
- One-time permission is granted only for the use specified in your RightsLink request. No additional uses are granted (such as derivative works or other editions). For any uses, please submit a new request.

If credit is given to another source for the material you requested from RightsLink, permission must be obtained from that source.

[BACK](#)

[CLOSE WINDOW](#)



Attachment Chemistry of 4-Fluorophenylboronic Acid on TiO₂ and Al₂O₃ Nanoparticles

Author: Carly Byron, Dhameilyz Silva-Quinones, Sucharita Sarkar, et al

Publication: Chemistry of Materials

Publisher: American Chemical Society

Date: Dec 1, 2022

Copyright © 2022, American Chemical Society

PERMISSION/LICENSE IS GRANTED FOR YOUR ORDER AT NO CHARGE

This type of permission/license, instead of the standard Terms and Conditions, is sent to you because no fee is being charged for your order. Please note the following:

- Permission is granted for your request in both print and electronic formats, and translations.
- If figures and/or tables were requested, they may be adapted or used in part.
- Please print this page for your records and send a copy of it to your publisher/graduate school.
- Appropriate credit for the requested material should be given as follows: "Reprinted (adapted) with permission from (COMPLETE REFERENCE CITATION). Copyright (YEAR) American Chemical Society." Insert appropriate information in place of the capitalized words.
- One-time permission is granted only for the use specified in your RightsLink request. No additional uses are granted (such as derivative works or other editions). For any uses, please submit a new request.

If credit is given to another source for the material you requested from RightsLink, permission must be obtained from that source.

[BACK](#)

[CLOSE WINDOW](#)